Virus-Mimetic Nanoparticles for the Therapy of Mesangial Cells in Diabetic Nephropathy

Dissertation to obtain the Degree of Doctor of Natural Sciences

(Dr. rer. nat.)

From the Faculty of Chemistry and Pharmacy

University of Regensburg

Presented by

Daniel Fleischmann

from Furth im Wald

March 2021

Daniel Fleischmann

Virus-Mimetic Nanoparticles for the Therapy of Mesangial Cells in Diabetic Nephropathy

Virus-Mimetic Nanoparticles for the Therapy of Mesangial Cells in Diabetic Nephropathy

Dissertation to obtain the Degree of Doctor of Natural Sciences

(Dr. rer. nat.)

From the Faculty of Chemistry and Pharmacy

University of Regensburg

Presented by

Daniel Fleischmann

from Furth im Wald

March 2021

This work was carried out from July 2017 until March 2021 at the Department of Pharmaceutical Technology of the University of Regensburg.

The thesis was prepared under supervision of Prof. Dr. Achim Göpferich.

To my dear ones.

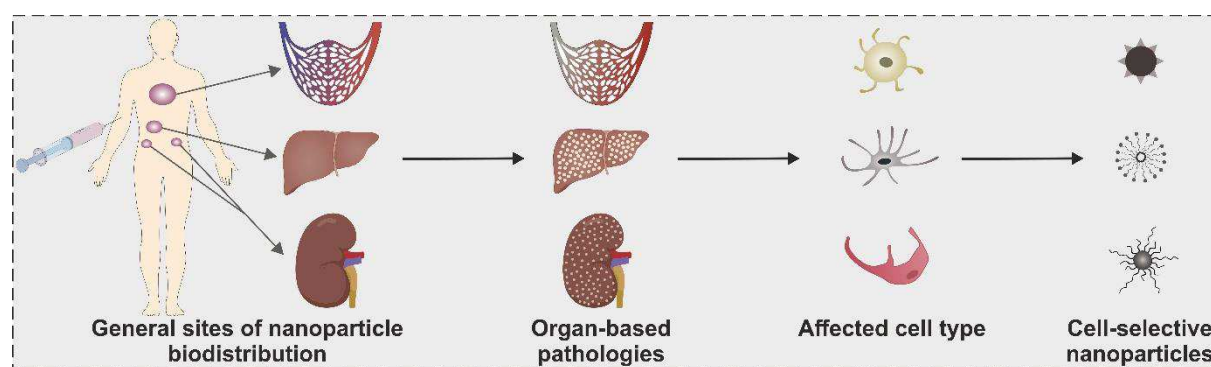*"If we knew what we were doing, it wouldn't be called research."*

Albert Einstein

Table of contents

Chapter 1

Introduction - General Sites of Nanoparticle Biodistribution As a Novel Opportunity for Nanomedicine

Abstract

The development of nanomedical devices has led to a considerable number of clinically applied nanotherapeutics. Yet, the overall poor translation of nanoparticular concepts into marketable systems has not met the initial expectations and led to increasing criticism in recent years. Most novel nano approaches thereby use highly refined formulations including a plethora of active targeting sequences, but ultimately fail to reach their target due to a generally high off-target deposition in organs such as the liver or kidney. In that regard, we propose a novel research strategy, arguing that the initial focus of nanoparticle (NP) development should not exclusively lie on formulation aspects, but also analyze general sites of mostly undesirable NP *in vivo* deposition and assess how accumulation in these organs or tissues can be harnessed to develop therapies for site-related pathologies. In that regard, we give a comprehensive overview of existing nanotherapeutic targeting strategies for specific cell types within three of the usual suspects, i.e. the liver, kidney, and the vascular system. We discuss the physiological surroundings and relevant pathologies of described tissues as well as the implications for NP-mediated drug delivery. Additionally, successful cell-selective NP concepts using active targeting strategies are assessed. By bringing together both (patho)physiological aspects and concepts for cell-selective NP formulations, we hope to show a novel opportunity for the development of more promising nanotherapeutic devices.

General sites of nanoparticle biodistribution | Organ-based pathologies | Affected cell type | Cell-selective nanoparticles

1   Introduction

When it comes to the field of nanomedicine, i.e. the design of materials in the nanometer size range to treat any form of disease, authors frequently mention Paul Ehrlich´s concept of a "magic bullet", that is able to "chemically aim" at its intended target within the body.[1] Thereby, the underlying principle is to equip nanomaterials with suitable surface functionalities enabling the specific recognition of distinct cell types, that require therapy. The applied vehicles such as liposomes or polymeric nanoparticles (NPs) should thereby act as a sort of shuttle, that transports pharmacologically active substances specifically to the intended target, while off-target sites remain unaffected. In that regard, several approaches already showed their potential to significantly improve existing therapy options and in several cases even reached marketability.[2] Especially when it comes to the treatment of cancerous diseases, many publications were able to demonstrate, that (non-)targeted NP systems can substantially increase therapeutic efficacy and/or decrease unfavorable side-effects of administered substances. Most concepts thereby focused on the differences between tumors and healthy tissues regarding morphology, cell metabolism or the expression of cell surface markers. Yet, while many of these approaches showed a considerable potential for tumor-specific targeting, the overall transferability of nanoparticulate systems from bench to bedside still remains at a poor level and has been one of the central points of criticism over the years. In that context, Wilhelm *et al.* found in 2016 in an intensively discussed meta-study, that the overall bioavailability of tumor-targeted nanomaterials was merely 0.7%.[3] When they assessed the average amount of NPs, that reached not only the tumor tissue, but also the actual cancer cell, results were even more sobering with only 14 out of 1 million administered NPs accumulating in their respective target cell on average.[4] Taking into account these observations and the general lack of clinically translated nanomedicine approaches, Kinam Park recently postulated "the beginning of the end of the nanomedicine hype", arguing that the overall benefits of nanotherapy concepts were not sufficient to justify further funding.[5] He additionally criticized the fact, that the vast majority of published studies focused on the targeting of tumor cells and cancerous diseases while non-cancerous pathologies were generally neglected, even though these account for far more deaths worldwide.[6] Despite the fact that some aspects of the general critique of nanomaterials need to be put into perspective[7], it is undoubted, that the overall poor transferability of nanoparticulate concepts into clinical applications calls for fundamental improvement. In that regard, an excellent review by Hua *et al.* discussed the most critical impediments for a successful bed-to-bedside transition of nanomedicine (NNM) approaches. One key aspect, that they identified, was that "traditionally, NNM development has been based on a formulation-driven approach, whereby novel delivery systems are firstly engineered and characterized from a physicochemical perspective".[8] In many cases, novel NP concepts would then fail to perform under physiological and, more importantly, pathological *in vivo* conditions. In this context, Wilhelm *et al.* also argued that, "our inability to control the nanoparticle transport inside the

body presents a major limitation for using nanotechnology"[3] and should therefore be included much more profoundly during the development of NP concepts. One critical obstacle that the authors

mentioned, was the oftentimes substantial clearance of administered nanomaterials by the mononuclear phagocyte system (MPS), i.e. the uptake of opsonized NPs by phagocytic macrophages or monocytes and subsequent accumulation in MPS organs such as the spleen and, in part, the liver.[9,10] Trying to overcome this limitation, numerous approaches tried to extend NP blood circulation by equipping nanomaterials with additional "stealth" elements such as poly-(ethylene glycol) (PEG) surface groups.[11–14] But although these strategies proved to be beneficiary to some extent, the predominant portion of administered NPs is generally still accumulating in the usual suspects, i.e. the kidney, liver, spleen and lungs.[3] This is not surprising, as all these organs share a strong blood supply and a considerable number of circulating NPs will always be deposited due to unspecific binding, uptake or extravasation out of the blood vessels. To our estimation, it is therefore rather surprising, that, compared to the field of tumor targeting, only a limited number of approaches have tried to turn this generally "undesired" accumulation in respective organs into possible strategies to target pathologically remodeled cell types in these tissues. In our view, combination of the described inevitable passive NP accumulation with additional active targeting elements for the specific cell type could potentially open a new field of nanomedicine, that has only been poorly investigated in the past.

However, as already mentioned above, a NP-assisted therapy of described tissues will only be successful, if it does not only include the necessary formulation parameters but also considers the actual *in vivo* conditions, that NPs are going to face upon target site accumulation.[3,8] Consequently, this review aims to cover both the (patho)physiological aspects of above discussed organs or tissues and their implications on NP concepts using both active and passive targeting.

We will therefore analyze currently existing concepts for nanotherapy of cell types in the kidney, liver, and the vascular system in general (mainly the lungs and atherosclerotic areas). We decided to exclude the above-mentioned spleen, as NP accumulation in this organ is mainly due to described MPS uptake of NPs. For each organ or tissue, we will focus on four essential aspects: 1. The (patho)physiological structure and function of the respective area. 2. The implication for passive NP accumulation. 3. Possible active targeting strategies for cell-specific NP deposition. 4. Applications of described NP concepts to treat non-cancerous, organ-based pathologies. Taken together, this analysis should help to develop novel strategies for nanomedicine-assisted therapy concepts, as it provides the necessary insights into the physiological surrounding, that administered NPs are exposed to.

2 Kidney targeting

2.1 Renal Structure

Within the human organism, the kidneys serve as the major excretory organs, facilitating the elimination of both metabolic products and partly toxic xenobiotics. The entire blood volume is thereby filtrated for approximately 300 times a day, generating up to 180 liters of primary urine that is then further concentrated. Apart from this excretory function, the kidneys are also able to regulate blood pressure and electrolyte homeostasis through described filtration and further control elements such as the renin-angiotensin-aldosterone system (RAAS). Additionally, the organ has an essential endocrine function in the formation of vital hormones such as renin or erythropoietin. Although renal pathologies are usually underrepresented in public perception, chronic kidney disease (CKD) shows a striking global prevalence of more than 13%[15], with high blood pressure and poorly managed diabetes ranking among the most common causes.[16,17]

Within the kidney, roughly 1-1.5 million *nephrons* act as the actual functional units[18], consisting of a renal corpuscle (*glomerulus*), where blood is filtrated into primary urine, and a connected tubular system, where the primary urine is concentrated and modified *via* several resorptive and secretory processes.[19] The glomerulus itself consists of a complex capillary system and several highly differentiated cell types that form the renal filter (**Figure 1**). For a successful passage of this filter and excretion into the tubular lumen, intracapillary substances thereby have to cross the so-called *glomerular filtration barrier* (GFB), which is a highly sophisticated network of fenestrated vascular endothelial cells, a densely structured glomerular basement membrane (GBM) and visceral epithelial cells (podocytes) with their numerous foot processes.[20–22] Located in the glomerular center, mesangial cells (MCs) provide structural support of the capillary loops by secreting and controlling the turnover of the extracellular matrix.[23,24] During CKD, renal fibrosis is gradually increasing and accompanied by elevated levels of inflammation, mesangial hyperproliferation and glomerulosclerosis.[25–29] As a consequence, endothelial cells and podocytes eventually lose their functional integrity, leading to an irreversible decline in glomerular filtration rate (GFR), proteinuria and a generally impaired kidney function.[17] Currently predominant therapeutic options mainly focus on the systemic control of the RAAS, effective diabetes management or, in the case of more advanced kidney damage, the application of anti-inflammatory or immunomodulatory drugs. Especially in the latter case, nanotherapeutic options could provide a more refined transport of highly potent substances to their site of action.[30,31]

Due to the kidney´s immense blood supply, circulating NPs will mandatorily be subject to renal passage, where they either are freely filtrated into the urine, extravasate into kidney-resident cells or leave the kidney without deposition. In this regard, Du *et al.* provided an excellent discussion of possible NP routes within the kidney.[32] Targeting specific cell types within the kidney is thereby dependent on a whole plethora of factors including NP size and surface characteristics but also the equipment with suitable targeting sequences.
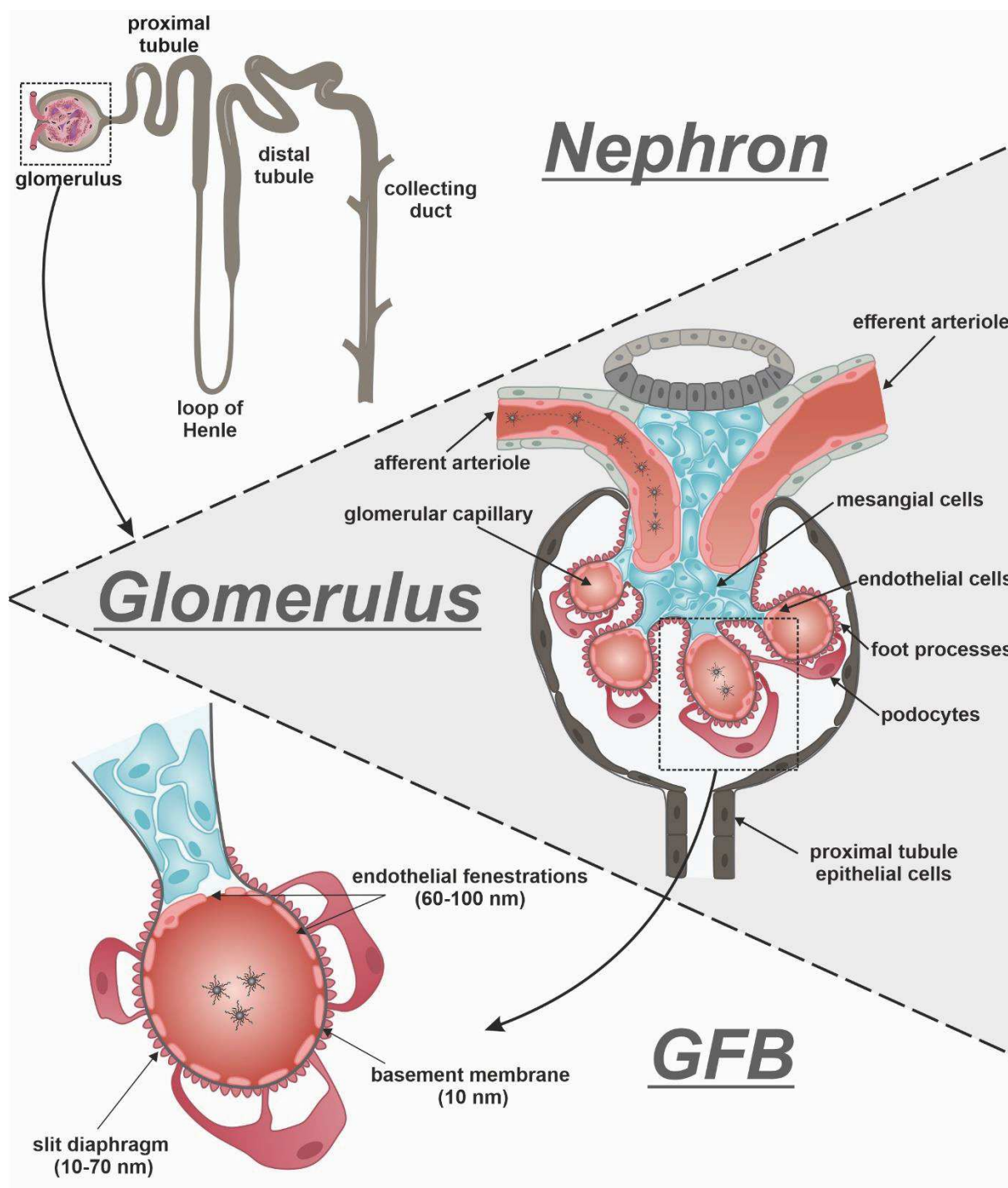
Figure 1. The physiology of renal filtration. Within each of the nephrons, blood is initially filtrated in the glomerulus. Resulting primary urine is subsequently concentrated and modified *via* a plethora of absorptive and secretory processes both in the proximal and the distal tubule, until it is collected and transported to the ureter. The glomerulus itself consists of a highly complex network of capillaries, structurally stabilizing mesangial cells and the glomerular filtration barrier (GFB), which consists of fenestrated vascular endothelial cells, a meshwork-like glomerular basement membrane as well as a slit diaphragm formed by the numerous foot processes of visceral podocytes. Consequently, the accessibility of each glomerular cell component is highly dependent on the size and physicochemical characteristics of the respective nanomaterial. Adapted with permission from[33]. Copyright 2020, Advanced Chemical Society.

2.2   Mesangial Cells

As described above, glomerular MCs play a vital role in preserving the functional integrity of the renal corpuscle by secretion and control of the extracellular matrix, which is essential for structural support of the renal filter. Besides, they also show extensive crosstalk with all adjacent cell types and thereby greatly influence proper function of the glomerular tuft.[34] However, since the mesangium is essential for glomerular homeostasis, it also greatly contributes to pathological remodeling during kidney diseases such as diabetic nephropathy.[29] MCs thereby oftentimes undergo a significant myofibroblast differentiation and show increasing profibrotic and proinflammatory signaling.[27,35] Consequently, targeted therapy of MCs would be a viable option for a more refined therapy of various pathologies.

Within the nephron, the mesangium is only accessible *via* passage through endothelial fenestrations with a diameter of approximately 60 - 100 nm.[36,37] Therefore, targeted nanomaterials need to be manufactured below respective size threshold to guarantee effective accumulation at the site of interest. Despite this limitation, the actual location of the mesangium also offers a chance for a highly effective passive targeting strategy comparable to the EPR effect (enhanced permeation and retention), which has been successfully exploited in the application of various tumor targeted nanomaterials.[38]

Choi *et al.* analyzed the possibility to transfer this targeting principle to the mesangium and concluded, that PEGylated gold NPs with a diameter of 75 ± 25 nm were able to efficiently accumulate in the mesangium, even if they did not carry any additional active targeting sequences.[37] In accordance with this assessment, Li *et al.* recently showed, that dexamethasone-loaded PEG- poly(lactic-co-glycolic acid) (PEG-PLGA) particles with a diameter of 90 nm also had a significantly enhanced intraglomerular accumulation compared to bigger NPs of 110 nm, which they explained with a successful extravasation into mesangial regions.[39] Guo *et al.* described a similar effect, using albumin-based nanoparticles containing anti-inflammatory agent celastrol to treat mesangioproliferative glomerulonephritis.[40] They found that NP species with a diameter of 95 nm showed maximum levels of intra-mesangial accumulation, compared to NPs of 130 nm. In a rat nephritis model, celastrol-carrying NPs could significantly reduce mesangial hyperproliferation and fibrosis. Additionally, celastrol-loaded particles showed a far lower toxicity and accumulation in off-target regions compared to the free drug. Interestingly, Li and Guo also used smaller NP species with a diameter of around 70 nm, which in both cases showed lower deposition in the kidney and mesangium, respectively. While Li *et al.* concluded that this observation was due to a lower stability of smaller nanoparticles, Guo *et al.* stated that NPs of 95 nm had a greater potential to benefit from various endocytosis pathways such as micropinocytosis, caveolae- and clathrin-mediated endocytosis. In this context, it is noteworthy that the actual size of endothelial fenestrations can significantly vary, depending on the animal type and, most importantly, the used disease model.[36,41]

While the aforementioned concepts were mainly based on successful extravasation of NPs through the fenestrated endothelium, various other approaches tried to expand this passive targeting by equipping particles (< 100 nm) with additional active targeting sequences in order to further enhance intra-

mesangial accumulation of nanomaterials. Since smooth muscle cells and the closely related MCs have been reported to exhibit elevated surface levels of negatively charged chondroitin sulfate proteoglycans[42,43], Harigai *et al.* developed liposomes of 100 nm carrying a special cationic lipid (TRX-20), that significantly increased surface attachment to both smooth muscle and MCs *in vitro*.[44] The authors additionally stated that binding to endothelial cells was thereby minimal because here, heparan sulfate proteoglycans were predominant, which were not bound by TRX-20. In a follow-up study, Liao *et al.* encapsulated prednisolone phosphate into TRX-20 liposomes, that were able to efficiently accumulate in glomerular areas in an IgA nephropathy mouse model.[45] Drug-loaded particles thereby also showed a higher efficiency in limiting glomerular expansion compared to free prednisolone. Morimoto *et al.* subsequently showed, that kidney deposition of prednisolone-loaded TRX-20 liposomes was generally elevated in a nephritis rat model compared to a healthy control, whereas nanoparticles almost exclusively accumulated in glomerular areas within the cortex.[46] Additionally, drug-loaded TRX-20 liposomes showed a greater efficiency in their antiproliferative effect compare to unmodified PEG liposomes. Recently, Yuan *et al.* tried to refine the targeting principle by lowering the surface density of TRX-20, thereby reducing toxic effects on the target MCs. Encapsulation of anti-inflammatory and immunosuppressing drug triptolide into TRX-20 liposomes could additionally improve the therapeutic effect in a nephropathy rat model.[47]

While TRX-20 was used as a rather unspecific binding facilitator, Tuffin *et al.* used Thy1.1 antigen (CD90), which is commonly used to induce glomerulonephritis disease models[48], as a promising candidate for highly selective mesangial targeting[49,50]. When they coupled a corresponding monoclonal antibody against Thy1.1 (OX7) to liposomes with a diameter of 100 nm, a significant increase in intraglomerular accumulation was detected, compared to untargeted liposomes. Interestingly, this effect could be significantly reduced by co-application of free OX-7, thereby proving the Thy1.1-related targeting effect. As a further proof of concept, the encapsulation of cytotoxic doxorubicin into targeted immunoliposomes led to a visible glomerular damage. In a follow-up study, Suana *et al.* successfully prepared OX-7 immunoliposomes carrying immunosuppressant mycophenolat mofetil to treat anti-Thy1.1 nephritis.[51]

In contrast to the predominant use of liposomes as nanocarriers, Zuckerman *et al.* manufactured polycationic cyclodextrin nanoparticles, that successfully delivered encapsulated siRNA into renal glomeruli *in vivo*. In a second step, they added targeting ligands for either the mannose receptor, which is expressed exclusively by MCs within the kidney, or the transferrin receptor, which can be found in various other tissues as well. Both targeted siRNA NPs showed an increase in glomerular deposition, however results varied to some extent.[52]

Since MCs also play an important role in the production and regulation of extracellular matrix (ECM) components, targeting integrins could also be a viable option as they are essential in facilitating cell-ECM adhesion. In that regard, Scindia *et al.* equipped liposomes with an antibody against integrin α8, which was shown to be present on the mesangial cell surface both in healthy and nephritic mice.

Manufactured immunoliposomes showed a significantly enhanced intraglomerular accumulation with low off-target tissue deposition except for CD11b-positive macrophages.[53]

While all described targeting strategies for MCs were based on the addition of merely one targeting sequence, our working group was able to develop a multi-ligand NP concept, thereby mimicking viral cell infiltration strategies, that usually include several surface recognition sequences.[54] We therefore manufactured polymeric PEG-poly(lactic acid)/PLGA (PEG-PLA/PLGA) nanoparticles in a size range of 70-80 nm, that carried pro-ligand Angiotensin I (AT-I) on their surface. Mimicking influenza A virus cell entry[55], particles thereby initially bound angiotensin converting enzyme (ACE) on the mesangial surface whereupon enzymatic conversion would transform AT-I into secondary ligand AT-II, that only then activated G-Protein coupled angiotensin II receptor type 1 (AT1r), initiating NP endocytosis. The stepwise particle-cell interaction with two distinct surface structures led to a significantly enhanced target cell selectivity in an *in vitro* co-culture assay.[56] In a follow-up study, particles were additionally equipped with a potent AT1r inhibitor (EXP3174) in order to increase initial cell surface binding. Resulting triple-targeted nanoparticles showed a highly selective intra-mesangial accumulation *in vivo* compared to both untargeted and mono-targeted control NPs, thereby proving the virus-mimetic concept.[57]

Building on this observation, we recently presented a related targeting concept, which was inspired by the cell infiltration process of human adenovirus and is independent from any previous enzymatic activation.[58] Particles thereby also initially bind mesangial AT1r, but finalize particle endocytosis *via* a previously sterically hidden agonist for the $\alpha_v\beta_3$ integrin, which is highly expressed by MCs.[59,60] Resulting NPs showed a significant accumulation in the mesangium *in vivo* with no off-target deposition in any other cell type within the kidney (**Figure 2**).[33] Remarkably, NP uptake was maximal for hetero-functional particle types that profited from a sequential ligand presentation. To our estimation, this outcome showed that NPs can only sufficiently profit from a functionalization with targeting sequences, if their cell-particle interplay is thereby realistically mimicking natural models such as viruses.[54] In a recent follow-up study, we were also able to load this NP system with cinaciguat, a promising anti-fibrotic drug candidate, whose pharmaceutical potency for its intracellular enzymatic target could be substantially enhanced *via* a more efficient transport into the mesangial cell cytosol.[61]
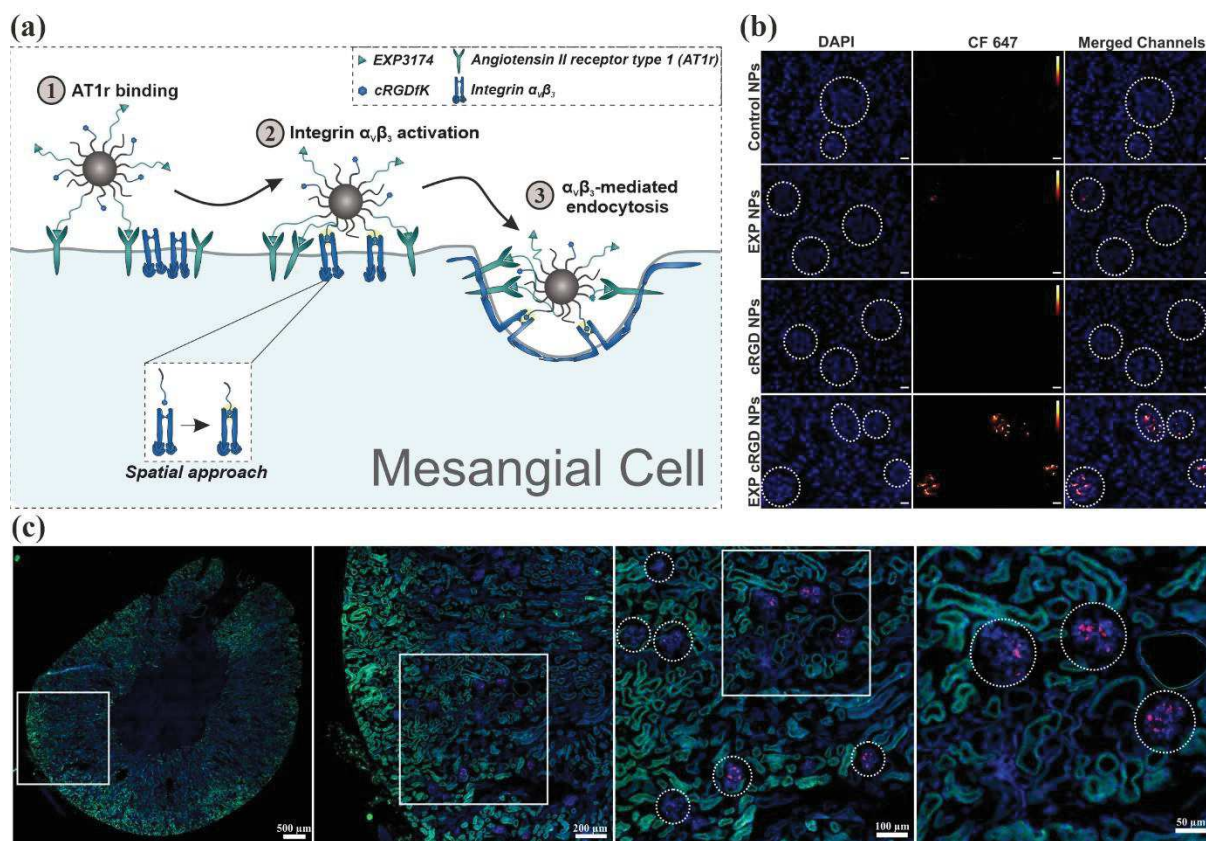
Figure 2. Adenovirus-inspired targeting of mesangial cells. (a) Virus-mimetic NPs present their ligands in a sterically controlled manner, leading to a sequential and thus highly selective particle-cell interplay. **(b)** In contrast to homo-functional or non-functionalized NPs (row 1-3), hetero-functional EXPcRGD NPs (bottom row) showed a drastically increased glomerular *in vivo* deposition. **(c)** Within the renal system, adenovirus-mimetic NPs exclusively targeted mesangial structures while no tubular deposition was visible. Adapted with permission from [33]. Copyright 2020, Advanced Chemical Society.

2.3   Glomerular endothelial cells and podocytes

Apart from the glomerular basement membrane, the GFB is mainly composed of vascular endothelial cells with the already described intracellular fenestrations and viscerally located podocytes, that form a slit diaphragm with their foot processes (Figure 1). Consequently, excessive damage and pathologic remodeling of endothelial cells and/or podocytes can quickly lead to renal dysfunctions such as a reduced glomerular filtration rate or proteinuria.[62] Due to their close proximity, both cell types thereby also greatly influence each other during renal disease progression, which generally includes advancing loss of endothelial integrity and podocyte function.[63]

For a possible cell-directed therapy of these pathologies, glomerular endothelial cells would generally be readily accessible for targeted NPs due to the strong intraglomerular supply of blood. However, nanocarriers can also be washed away much more easily due to the immediate impact of the bloodstream. Therefore, applied NPs need to quickly induce sufficient binding to the endothelium to enable satisfactory target accumulation. One possible approach is to exploit the role of endothelial cells in attracting leukocytes during inflammatory processes within the nephron.[64] In that regard, Ásgeirsdóttir *et al.* presented a liposomal nanocarrier system for anti-inflammatory dexamethasone, that uses an

antibody targeting cell adhesion molecule E-selectin.[65,66] In a glomerulonephritis mouse model, drug-loaded immunoliposomes significantly improved renal function. Although free dexamethasone showed a comparable effect, the authors stated, that systemic side effects were significantly lower for the nanocarrier system.

Located on the visceral side of the GFB, podocytes create a slit diaphragm of 10 - 70 nm with their numerous interdigitated foot processes.[67] Consequently, podocyte injury and subsequent foot process effacement or cell apoptosis is one of the major causes for proteinuria and critical loss of glomerular filtration capacity during CKD.[68,69] Targeting podocytes requires nanomaterials to cross both vascular endothelial cells and the underlying negatively charged GBM with a size cut-off of approximately 10 nm.[19,21] To that regard, Bruni *et al.* synthesized PEGylated nanocarriers in a size range from 5-30 nm, whose hydrophobic polycaprolactone core could be loaded with anti-inflammatory dexamethasone.[70] Apart from their positive effect on podocyte repair *in vitro*, nanoparticles could also cross the glomerular filter and were found in the urine. Thereby, clearance was significantly increasing in a nephropathy model, possibly due to an advanced damage of the glomerular filter and a consequently higher size cut-off. In that context, Wu *et al.* also stated, that under nephritic conditions, glomerular permeability for usually non-filtered albumin is significantly enhanced and therefore synthesized an albumin-methylprednisolone complex that could be able to cross the GFB and be recognized by podocytes *via* the neonatal Fc receptor.[71] The complex showed a significantly enhanced *in vitro* uptake into podocytes and could ameliorate drug-induced cell apoptosis. In a biodistribution study, the nanoconjugate accumulated mainly in the liver and the kidney, which the authors explained with a deposition in glomerular podocytes upon glomerular filtration.

Pollinger *et al.* identified $\alpha_v\beta_3$ integrin as a further possible candidate for a selective podocyte targeting.[72] PEGylated Qdots were therefore functionalized with integrin activator cyclo(-Arg-Gly-Asp-D-Phe-Cys) (cRGDfC) and showed a significantly increased uptake in receptor-positive podocytes *in vitro* as well as a selective accumulation in podocyte regions of *ex vivo* cultured glomeruli. In an approach for further recognition structures, Visweswaran *et al.* describe an upregulation of vascular cell adhesion molecule 1 (VCAM-1) in podocytes upon stimulation with TNF-α, which they used to mimic inflammatory conditions during glomerulopathy. As this surface receptor can facilitate receptor-mediated endocytosis, a lipid-based SAINT-O-some carrying a corresponding VCAM-1 antibody was manufactured.[73] Following up on this, the working group encapsulated rapamycin, a potent inhibitor for the mechanistic target of rapamycin (mTOR), which had previously been shown to be associated with podocyte injury. Drug-loaded nanocarriers showed a beneficial effect on inflammation-activated podocytes *in vitro*, however *in vivo* biodistribution was not assessed, which would have been particularly interesting, regarding the considerable lipid carrier size of 120 nm.

Finally, Colombo *et al.* analyzed the impact of particle size and physicochemical characteristics on the *in vitro* uptake behavior of untargeted PCL nanoparticles in podocytes.[74] In a follow-up experiment, they used a more realistic 3D *in vitro* system, in which they co-cultured endothelial cells and podocytes

and induced podocyte damage with adriamycin, followed by enhanced permeability for albumin. The application of dexamethasone-loaded NPs led to a significant podocyte repair and decreased levels of albumin permeability.

Many of described approaches showed a noteworthy targeting potential for podocytes. Also, encapsulated substances oftentimes significantly reduced podocyte injury. However, so far, only Bruni and Wu *et al.* could show an actual *in vivo* deposition of nanomaterials in podocyte regions. Interestingly, those two nanocarrier systems were below the size-cutoff of the healthy GFB while all other concepts worked with nanoparticulate systems that were too large for renal passage under normal conditions. Although authors stated that the permeability of the renal filter is enhanced under pathological conditions, it is questionable whether a nanotherapeutic invention at this advanced stage of illness would still have a significant effect on slowing disease progression as podocyte injury in most cases is an irreversible process.[75]

2.4 Tubular cells

After passage of the renal filter, primary urine is largely reabsorbed in the proximal tubular system, which is able to precisely steer excretion and reuptake of substances through various absorptive and secretory mechanisms. During CKD, fibrotic remodeling and inflammatory injury of tubular epithelial cells can significantly contribute to a worsening of renal function.[76] Many approaches therefore try to harness endocytic mechanisms of proximal epithelial cells to selectively treat tubulus-associated pathologies.[77] Most concepts are thereby based on the application of low molecular weight peptides or proteins as carriers, as these can easily cross the GFB. One frequently exploited peptide is lysozyme, which is freely filtrated into the tubular lumen where it is reabsorbed by epithelial cells *via* the megalin receptor.[78] In several studies, coupling of lysozyme to pharmacologically active substances led to a significant increase in target concentration and drug efficacy.[79–82] Apart from that, further low molecular weight carriers such as chitosan have been identified as promising candidates for an efficient drug delivery to proximal tubulus cells.[83–85] While these studies show the potential of the megalin receptor as a promising candidate for cell-selective NP targeting, the application of nanocarriers is significantly limited due to the size-cutoff of the GFB. In that regard, Nair *et al.* successfully proved the general applicability of nanomaterials in this area, showing that dextran- and dendrimer-nanoparticles < 10 nm efficiently accumulated in renal tubular cells *in vivo* with megalin expression significantly increasing upon NP injection.[86] Oroojalian *et al.* concluded, that *in vivo* transfection efficiency of siRNA-containing PEI nanoparticles was significantly increased by introduction of polymyxin B as targeting ligand for the megalin receptor of proximal tubule epithelial cells.[87] However, they did not discuss the exact transport mechanism of the NPs, whose size of 150 nm was too large for passage of the renal filter. In that regard, Williams *et al.* reported a highly interesting finding. So-called "mesoscale" PEGylated PLGA nanoparticles with a diameter of 400 nm showed a surprisingly high *in vivo* accumulation in renal proximal tubule cells, even though they most certainly could not cross the GFB. The authors explain

this finding with a possible uptake of NPs *via* peritubular capillaries, which they could reach due to their physicochemical characteristics, that minimized MPS clearance. According to the authors, particles were endocytosed by peritubular endothelial cells and subsequently transported to the basolateral membrane of the tubulus cells, resulting in a significantly increased kidney accumulation compared to other organs.[88]

Table 1 summarizes described targeting approaches for a cell-selective kidney nanotherapy. Most nanoparticular concepts can thereby be found for the glomerular mesangium, as it is more easily accessible through endothelial fenestrations. However, as described above, promising studies have also been reported for other components of the nephron.

Table 1. Kidney-targeted nanomaterials.

Cell type	NP type	Size (nm)	Ligands	Targets	Drug delivery	*In vivo*	Ref.
Mesangial Cells	PEG-PLGA	90	-	-	Dexamethasone acetate	+	39
	Albumin-based	95	-	-	Celastrol	+	40
	Liposomes	100	TRX-20	Proteoglycans	Prednisolone phosphate	+	44–46
	Liposomes	110	TRX-20	Proteoglycans	Triptolide	+	47
	Liposomes	100	OX-7	Thy1.1	Mycophenolate mofetil	+	49–51
	Cyclodextrin	70	Mannose/Transferrin	M..-/T.-receptor	siRNA	+	52
	Liposomes	100	Anti-Integrin α8	Integrin α8	-	+	53
	PEG-PLA/PLGA	70-80	Angiotensin I	ACE	-	-	56
			Angiotensin II	AT1r			
	PEG-PLA/PLGA	70-80	EXP3174	AT1r	-	+	57
			Angiotensin I	ACE			
			Angiotensin II	AT1r			
	PEG-PLA/PLGA	60	EXP3174	AT1r	Cinaciguat	+	33,61
			cRGDfK	Integrin $\alpha_v\beta_3$			
Endothelium	Liposomes	110	Anti-E-Selectin	E-Selectin	Dexamethasone	+	65,66
Podocytes	PEG-PCL	5-30	-	-	Dexamethasone	+	70
	Albumin	10	Albumin	FcRn	Methylprednisolone	+	71
	QDots	10	cRGDfC	Integrin $\alpha_v\beta_3$	-	-	72
	SAINT-O-Somes	120	Anti-VCAM-1	VCAM-1	Rapamycin	-	73
	PEG-PCL	30/60/120	-	-	Dexamethasone	-	74
Tubular Cells	Dextran/Dendrimer	5-10	-	Megalin receptor	-	+	86
	PEI	150	Polymyxin B	"-"	siRNA	+	87
	PEG-PLGA	400	-	-	-	+	88

3 Liver targeting

3.1 Hepatic Structure

As the key metabolic organ, the liver is involved in the breakdown, synthesis as well as storage of a variety of vital substances. It thereby precisely steers the homeostasis of glucose, fats and proteins in the human organism *via* a highly coordinated system of regulatory processes such as gluconeogenesis or lipogenesis.[89] Apart from that, it also has a central role in the degradation and detoxification of both metabolic and xenobiotic substances *via* a versatile system of different enzymatic reactions. Consequently, exposure to detrimental substances such as pollutants, alcohol or even pharmacological substances oftentimes initially leads to liver damage, before other organs are affected.[90] In many cases, these injuries can lead to progredient liver fibrosis or even cirrhosis and, in the long-term, cause liver failure and call for organ transplantation.[91]

Within the liver, hepatic lobules act as the functional unit (**Figure 3**). Within these hexagonal structures, blood from the portal venule and hepatic arteriole is transported within the so-called liver sinusoids towards the central vein. As described above for the glomerular endothelium, liver sinusoidal endothelial cells (LSECs) also possess fenestrations of 50 - 150 nm.[92] Due to this large pore size and the lack of a basement membrane, the endothelium is highly permeable which is essential for the efficient passage of metabolic substances to the underlying hepatocytes, where the majority of liver processes such as the enzymatic conversion takes place. However, liver-residential macrophages (Kupffer cells) within the sinusoidal vessel act as a gatekeeper and phagocytose possibly harmful blood cargoes. As a central element of the MPS, Kupffer cells also show excessive uptake of nanomaterials, especially after previous opsonization, i.e. the adsorption of blood plasma proteins.[93] Consequently, most nanotherapeutic approaches try to minimize MPS recognition and resulting liver uptake by equipping NPs with above mentioned stealth elements such as PEGylated surfaces. However, hepatic accumulation of NPs can also be harnessed to deliver potent pharmacological substances for a more beneficial therapy of liver diseases such as fibrosis. To that regard, administered NPs would not only have to passively accumulate in hepatic regions, but also be able to specifically steer further NP-cell interaction with additional targeting elements such as ligands for cell-selective surface receptors.
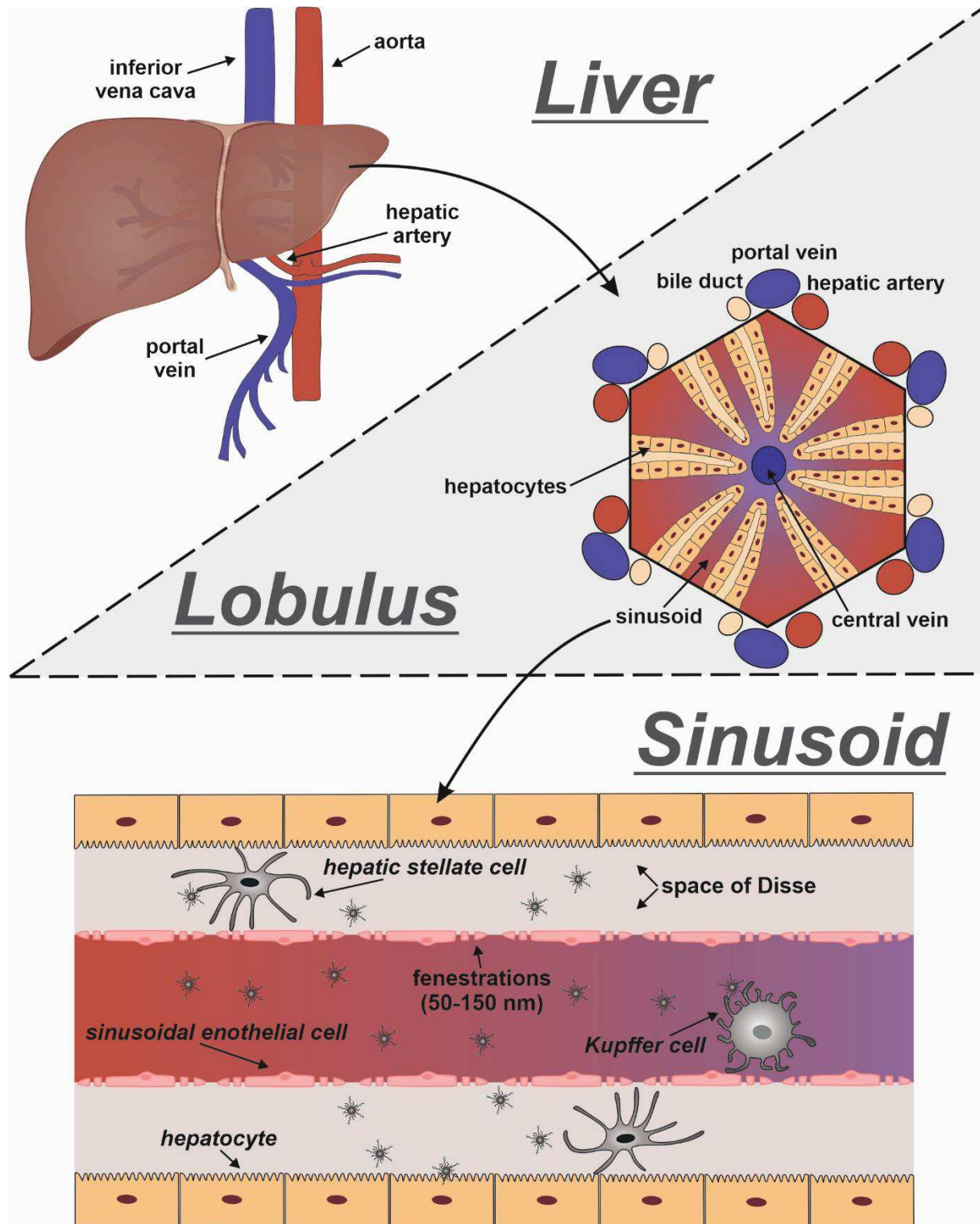
Figure 3. Hepatic cell physiology. The liver is supplied with oxygen-rich blood from the hepatic artery as well as nutrient-rich blood from the portal vein. Within the organ, hexagonal hepatic lobuli act as the functional units, where arterial and venous blood is mixed and transported through sinusoidal capillaries, that eventually merge into a central vein. Thereby, blood components can extravasate through endothelial cell fenestrations into the perisinusoidal space of Disse, where they finally reach metabolically active hepatocytes, that account for the majority of liver-related processes. Within the sinusoidal capillaries, phagocytic Kupffer cells act as highly sensitive sentinels for possible pathogens such as bacteria or other xenobiotics.

3.2   Hepatic stellate cells

When it comes to liver fibrosis, perisinusoidal hepatic stellate cells (HSCs) play a central role in disease progression. Being located in the space of Disse between the endothelium and the underlying hepatocytes, inactive HSCs mainly store nutrients in their cytosol under healthy conditions. However, progressive hepatic injury can activate HSCs to become contractile myofibroblasts, that significantly contribute to inflammation and fibrotic remodeling of the sinusoid *via* an altered secretion of extracellular matrix components as well as regulatory proteins such as transforming or hepatocyte growth factor.[94] Cell-selective delivery of pharmacological substances would significantly increase therapeutic success as the untargeted application of anti-fibrotic substances can also cause side-effects in off-target regions.[95]

Already in 1999, Beljaars *et al.* identified the Mannose 6-phosphate (M6P) / insulin like growth factor II receptor as a potential target for M6P-carrying albumin (M6P-HSA), as it is involved in the activation of pro-fibrotic transforming growth factor β (TGF-β) and overexpressed in HSCs during liver fibrosis.[96] Building on that finding, several follow-up studies successfully coupled various pharmacologically promising substances such as antiproliferative doxorubicin (Greupink *et al.*), anti-inflammatory pentoxifylline (Gonzalo *et al.*), as well as rho kinase or TGF-β receptor inhibitors (van Beuge *et al.*) to M6P-HSA and selectively targeted HSCs *in vivo,* which led to significant therapeutic effects in different fibrosis models.[97–100] Adrian *et al.* refined this concept by incorporating M6P-HSA into liposomes.[101] This targeted carrier was later fused with hemagglutinating virus of Japan (HVJ) to selectively transfect HSCs with a plasmid DNA *in vitro.*[102] In that regard, Patel *et al.* used a comparable M6P-HSA coupled liposomal carrier to encapsulate peroxisome proliferator-activated receptor γ (PPARγ) agonist rosiglitazone, which – apart from its antidiabetic effect – also has been shown to inhibit HSC proliferation and activation in fibrosis. M6P-targeted liposomes thereby displayed an enhanced accumulation in HSCs and could significantly improve various fibrosis parameters.[103] As under healthy conditions, HSCs mainly store vitamin A (retinol) in intracellular droplets, the corresponding retinol binding protein receptor (RBPR) has also been used to implement a HSC-selective nanotherapy. Sato *et al.* manufactured vitamin A-coupled liposomes containing siRNA against heat shock protein 47, which is involved in collagen excretion of activated HSCs. In three different cirrhosis models, siRNA-loaded liposomes drastically reduced liver injury and prolonged survival rate of tested animals.[104] Duong *et al.* used a comparable concept by covalently attaching both vitamin A and nitric oxide (NO) donor S-nitrosoglutathione to a diblock copolymer, resulting in RBPR-targeted, NO-delivering NPs with a size of 35 nm. Particles thereby efficiently accumulated in HSCs both *in vitro* and *in vivo* and significantly reduced portal hypertension - a major secondary symptom of liver fibrosis – due to the release of vasorelaxing and anti-fibrotic NO.[105] While the RBPR is also expressed in dormant HSCs, Li F. *et al.* decided to target mainly activated HSCs, using the plateled-derived growth factor receptor (PDGFR), which is a prominent mediator of fibrosis progression in various tissues.[106] Therefore, liposomal carriers were modified with a cyclic peptide with a previously demonstrated high affinity for the PDGFR[107], and

loaded with interferon-γ (IFN- γ), that had been shown to slow hepatic fibrosis. Liposomal IFN-γ showed a significantly prolonged circulation half-life as well as an enhanced intrahepatic accumulation, leading to a considerable therapeutic effect *in vivo*.[108] As liver fibrosis is accompanied by an excessive excretion of highly contractile extracellular matrix proteins such as collagen, targeting the corresponding receptors with suitable cyclic peptides has also proven to facilitate HSC targeting.[109] Especially the already above mentioned (cyclic) amino acid sequence RGD provided excellent affinity for the collagen VI receptor, which is upregulated in HSCs during fibrosis.[110] In that regard, both Chai *et al.* and Yang *et al.* encapsulated oymatrine, a promising antifibrotic alkaloid, into either liposomes or PEG-poly(caprolactone) (PEG-PCL) nanoparticles, that were modified with an RGD sequence. Both nanoparticulate systems showed a significantly enhanced HSC targeting and could decrease fibrosis in an *in vivo* disease model.[111,112]   Li *et al.* analogically used cRGD-modified liposomes carrying hepatocyte growth factor to substantially ameliorate liver parameters in a cirrhosis model.[113] Finally, several studies suggest the implementation of hyaluronic acid (HA) as active targeting element, since the corresponding receptor CD44 also plays a vital role in fibrotic HSC activation and proliferation. While Chen *et al.* encapsulated anti-inflammatory curcumin in HA-modified PLA NPs and reached a promising therapeutic effect *in vivo*[114], Thomas *et al.* could significantly reduce fibrosis parameters *in vivo* with HA micelles containing AT1r antagonist losartan.[115] However, it is unclear whether the latter effect was mainly due to HSC inactivation as the prepared HA micelles had a diameter of 300 nm and should, in theory, not be able to extravasate into the perisinusoidal space to reach activated HSCs.

3.3   Hepatocytes

As described above, nanotherapeutic concepts for HSCs are mainly focused on the targeting of surface receptors, that are involved in the pro-fibrotic activation and proliferation of activated stellate cells. Although hepatocytes also play a significant role during fibrosis, their primary role – especially under healthy conditions – lies in the performance of metabolic processes for the liver. Consequently, most concepts to target hepatocytes are based on the exploitation of suitable surface receptors for metabolic products. In that context, the asialoglycoprotein receptor (ASGPR) plays a central role for many hepatocyte-directed approaches. While the ASGPR is essential for the clearance of a multitude of blood components such as IgA or apoptotic cells, there is also evidence that viruses such as Hepatitis virus B (HBV) use the receptor to induce cell uptake.[116] ASGPR-mediated endocytosis itself is initiated *via* binding of terminal galactose or structurally similar groups that are exposed due to a previous cleavage of sialic acid groups of various glycoproteins. Analogically, nanotherapeutic concepts try to facilitate ASGPR-mediated hepatocyte targeting by equipping NPs with suitable surface groups such as galactose.[117] Mandal *et al.* successfully encapsulated antioxidant quercetin into galactose-modified liposomes, that were able to significantly ameliorate hepatic injury after exposure to sodium arsenite, a widespread pollutant in developing countries.[118] Jiang *et al.* used a comparable system of galactose-modified, siRNA carrying liposomes, that were able to efficiently silence expression of hepatocyte-

associated toll-like receptor 4 (TLR-4), which is a key contributor to hepatic injury after liver transplantation (ischemia-reperfusion injury), resulting in a beneficial therapeutic effect in an *in vivo* model.[119] Arima *et al.* as well as Motoyama *et al.* identified lactose as another suitable surface group to initiate ASGPR-mediated hepatocyte targeting, thereby modifying circular polyamidoamine (PAMAM)-cyclodextrin with a size of approximately 160 nm as a nanoparticular vector for a plasmid DNA.[120,121] In a follow-up study, Hayashi *et al.* complexed the described lactosylated cyclodextrin with siRNA against the amyloidogenic transthyretin (ATTR) gene, which is expressed in hepatocytes and associated with amyloidotic polyneuropathy. Targeted NPs showed an efficient uptake in HepG2 cell *in vitro* and could significantly decrease TTR expression *in vivo*.[122] Wang *et al.* presented a diblock copolymer NP system, that was modified with N-acetyl-D-galactosamine (NAcGal) as another possible targeting sequence for hepatocyte ASGPR.[123] Resulting NPs showed a significantly enhanced *in vivo* accumulation in the liver compared to untargeted NPs. Besides, encapsulated siRNA successfully silenced liver-specific apolipoprotein B expression. However, fluorescently labeled siRNA could also be found in the kidney, which could indicate insufficient stability of the NPs and subsequent renal clearance of the remnants. In a highly promising study, Sato *et al.* used the same NAcGal sequence to manufacture targeted lipid NPs carrying HBV-inhibitory siRNA.[124] While untargeted NPs showed a considerable toxicity on off-target LSECs, introduction of NAcGal significantly increased hepatocyte selectivity, leading to both a reduction in LSEC injury and a sufficient inhibitory effect on HBV levels. Apart from the ASGPR, only a few other approaches to target hepatocytes exist so far. Jin *et al.* suggested harnessing the hepatocyte LDL receptor by incorporating cholesterol-coupled siRNA into purified LDL nanoparticles.[125] Although HepG2 uptake and gene silencing were promising *in vitro*, no *in vivo* studies have yet been presented. In that context, one obstacle could be the significant LDL receptor expression in almost all cell types. As HBV possesses a considerable liver/hepatocyte selectivity, Yamada *et al.* suggested to harness HBV infiltration by preparing so-called L particles, that consist of one of the envelope proteins of HBV.[126] L particles thereby showed a significant, cell-selective delivery of a green fluorescent protein (GFP) plasmid both *in vitro* and *in vivo*. In that context, we propose, that mimicry of viral cell recognition patterns could possibly also offer a considerable increase in hepatic cell selectivity and should therefore be investigated far more intensively.[54]

3.4 Liver sinusoidal endothelial cells

Under healthy conditions, LSECs control the intrahepatic blood flow and act as sieve plates that enable the fluid exchange between sinusoidal capillaries and the metabolically active hepatocytes. However, as LSECs have been found to play a considerable role in stellate cell activation and increasing hepatic resistance during liver fibrosis as well, nanotherapeutic approaches to target LSECs would also be of great importance.[92] Even though they possess the highest vascular permeability among all endothelial cell types due to their intracellular fenestrations, LSECs also have a significant endocytotic capacity, thereby contributing to hepatic waste clearance of liver residential Kupffer cells. One example of

substances, that are degraded by LSECs is the extracellular matrix component hyaluronic acid. In that context, the corresponding HA receptor was found a promising target for LSEC-selective nanomaterials.[127,128] Kren *et al.* manufactured poly(ethylene imine)-DNA (PEI-DNA) nanoparticles of approximately 25 nm, that contained the transposon system *Sleeping Beauty* to treat hemophilia A, a bleeding disorder due to lack of Factor VIII. HA-modified NPs thereby efficiently accumulated in LSECs and showed a considerable therapeutic effect *in vivo.*[129] Interestingly, the authors also used NPs that carried a natural ligand for the above mentioned ASGPR. These otherwise identical nanocarriers could be found in ASGPR-expressing hepatocytes, thereby proving, that the same nanomaterial can be directed to two different cell types in imminent proximity just by the usage of different targeting ligands. However, targeted receptors thereby need to be sufficiently characteristic for the respective cell type. In that context, Akhter *et al.* had originally equipped PEGylated liposomes with a peptide sequence that should facilitate hepatocyte-selective NP targeting *via* the above-mentioned LDL receptor. However, NPs were found both in LSECs and hepatocytes *in vitro* and almost entirely accumulated in LSECs *in vivo*.[130] Even though the experienced effect was used in a follow-up study to selectively deliver siRNA to LSECs *in vivo*[131], the addressed LDL receptor might not be optimal for cell-selective drug delivery, as already mentioned above. Trying to maximize endothelial cell selectivity for sufficient gene delivery to LSECs, Abel *et al.* described an interesting approach of equipping lentiviral gene vectors of 80 - 100 nm with a single-chain variable fragment against endothelial cell surface marker endoglin (CD105).[132] Targeted vectors thereby exhibited a remarkable *in vivo* LSEC transduction selectivity, which could also be used for drug delivery approaches. The authors explain the experienced selectivity with the significantly enhanced CD105 expression of LSECs compared to other endothelial cell types but also state, that factors like accessibility and blood circulation kinetics played a decisive role.

3.5 Kupffer cells

In contrast to circulating macrophages, stationary Kupffer cells (KCs) are permanently located in the liver sinusoid under healthy conditions, acting as sentinels for possible pathogens or other xenobiotics. As central part of the MPS, KCs have a remarkable phagocytic activity, thereby degrading cellular debris or possibly liver-damaging substances.[133] Consequently, almost all nanotherapeutic approaches try to minimize MPS recognition and subsequent phagocytosis of administered NPs by equipping nanocarriers with described "stealth" elements or optimizing surface charge and size.[93]

However, NP phagocytosis into KCs could also be harnessed for various therapeutic concepts since KCs play a crucial role in a multitude of liver pathologies. For instance, progredient liver fibrosis and cirrhosis are in part initiated by the activation of Kupffer cells and subsequent secretion of pro-inflammatory cytokines, that in turn stimulate stellate cells to become pro-fibrotic myofibroblasts.[90] As KCs possess the above described phagocytic activity for many nanoparticulate systems, several approaches successfully target KC passively without equipping NPs with additional active targeting ligands. Di Mascolo *et al.* describe a PLGA-polyvinyl alcohol (PLGA-PVA) NP system that contained

PPARγ agonist rosiglitazone to treat obesity-induced macrophage inflammation.[134] Systemic application of rosiglitazone NPs led to a significant decrease of inflammation levels and thereby showed fewer side effects compared to the free drug. In a very detailed study, Dolina *et al.* presented lipid NPs that contained siRNA silencing the expression of PD-L1 in Kupffer cells.[135] *Via* activation of corresponding PD-1 protein, this ligand plays a critical role in suppression of immune responses by natural killer (NK) and CD8$^+$ T cells during certain virus infections. Manufactured siRNA-carrying NPs were selectively endocytosed by KCs, leading to a significant PD-L1 silencing, which in turn, enhanced NK and CD8$^+$ T cell activation in an adenovirus/cytomegalovirus *in vivo* model. Since KCs contribute to the phagocytosis of harmful microorganisms such as bacteria, they are equipped with various receptors to recognize specific lipopolysaccharides on the bacterial cell surface, among which the mannose receptor (MR) plays a central role. In that regard, equipping nanoparticulate structures with mannose sequences has been found to further enhance KC accumulation.[136] He *et al.* analogically encapsulated anti-TNF-α siRNA into mannose-modified chitosan NPs to reduce liver inflammation and subsequent damage in an *in vivo* model of acute hepatic injury.[137] Remarkably, NPs in this and a follow-up study were orally applied, showing sufficient stability and intestinal permeation.[138] Jing *et al.* presented a dual liver targeting system, where solid lipid nanoparticles were modified with either KC-targeting mannose or HepG2 tumor targeting transferrin.[139] Containing GFP plasmid, mannose-modified NPs thereby showed a significantly enhanced KC transfection efficiency *in vivo* while transferrin-NPs mainly transfected HepG2 cells.

Table 2 provides an overview of discussed liver cell-selective targeting approaches. Especially for hepatic stellate cells, many approaches have successfully manufactured nanomaterials, that were equipped with selective targeting elements and carried pharmacological substances, that could significantly reduce pathologies such as hepatic fibrosis.

Table 2. Targeting concepts for hepatic cells.

Cell type	NP type	Size (nm)	Ligands	Targets	Drug delivery	*In vivo*	Ref.
Stellate Cells	HSA	30-40*	M6P	M6P receptor	Doxorubcicin/pentoxifylline rho kinase/ALK5 (-)	+	97–100
	HVJ-liposomes	200	"-"	"-"	-	-	102
	Liposomes	135	"-"	"-"	Rosiglitazone	+	103
	Liposomes	150	Vitamin A	RBPR	siRNA	+	104
	Diblock copolymer NPs	35	"-"	"-"	S-nitrosoglutathione	+	105
	Liposomes	80	cSRNLIDC	PDGFR	IFN- γ	+	108
	Liposomes	n.a.	cRGD	Col VI receptor	Oxymatrine	+	111
	PEG-PCL	95	RGD	"-"	"-"	+	112
	Liposomes	90	cRGD	"-"	Hepatocyte growth factor	+	113
	PLA	60	HA	HA rec.	Curcumin	+	114
	HA micelles	300	"-"	"-"	Losartan	+	115
Hepatocytes	Liposomes	n.a.	Galactose	ASGPR	Quercetin	+	118
	Liposomes	140	"-"	"-"	siRNA	+	119
	PAMAM-cyclodextrin	160	Lactose	"-"	pDNA/siRNA	+	120–122
	Diblock copolymer NPs	50-100	NAcGal	"-"	siRNA	+	123
	Lipid NPs	50-70	NAcGal	"-"	siRNA	+	124
	PEI NPs	20	Asialoorosomucoid	"-"	DNA	+	129
	LDL	25	LDL	LDL rec.	siRNA	-	125
	HBV L particles	80	L protein	HBV rec.	-	+	126
LSECs	Poly-Lysin/PLA	50	HA	HA rec.	-	-	127
	PEI	25	"-"	"-"	DNA	+	129
	Liposomes	100	Peptide sequence	LDL rec.	siRNA	+	130,131
	Lentivirus	80-100	Anti-CD105	CD105	-	+	132
Kupffer Cells	PLGA/PVA	200	-	-	Rosiglitazone	+	134
	Lipid NPs	70-80	-	-	siRNA	+	135
	HSA	30-40*	Mannose	Mannose rec.	Dexamethasone	+	136
	Chitosan	150	"-"	"-"	siRNA	+	137,138
	Lipid NPs	200	"-"	"-"	-	+	139

*The authors did not present data on the size distribution of HSA-NPs. We therefore estimated the size according to the approximate diameter of HSA. (n.a.: data not available)

4 Vascular targeting

4.1 General aspects of the vasculature

Even if nanomaterials are not administered intravenously, almost any application strategy eventually leads to a NP transfer to the bloodstream, followed by circulation through the vascular system. Consequently, exposure to the vasculature greatly influences eventual bioavailability and possible off-target accumulation. Even though the phagocytic activity of vascular endothelial cells (VECs) is considerably lower than for the components of the MPS, the sheer scale of endothelial cell number and surface, that NPs are exposed to, can play a decisive role in NP targeting. Under a physiological aspect, the vasculature is – apart from the heart – the central key player to guarantee proper blood circulation. Consequently, damage or impaired function of the vascular system is regarded as the most critical pathology with ischemic heart disease and stroke as the two leading causes of death worldwide.[6] These vascular complications are mostly caused by atherosclerosis (**Figure 4**), i.e. the progredient development of subendothelial plaques due to the accumulation of low-density lipoprotein (LDL) cholesterol followed by increasing levels of inflammation and possible rupture of the plaque.[140] Yet, an impaired endothelial function also plays a significant role in a variety of other diseases such as pulmonary inflammation during chronic obstructive pulmonary disease (COPD) or asthma, two diseases that also affect millions of patients worldwide.[141] As described for renal or hepatic diseases, cell-selective therapy of the pathologically remodeled endothelium could therefore also dramatically improve current medical options.
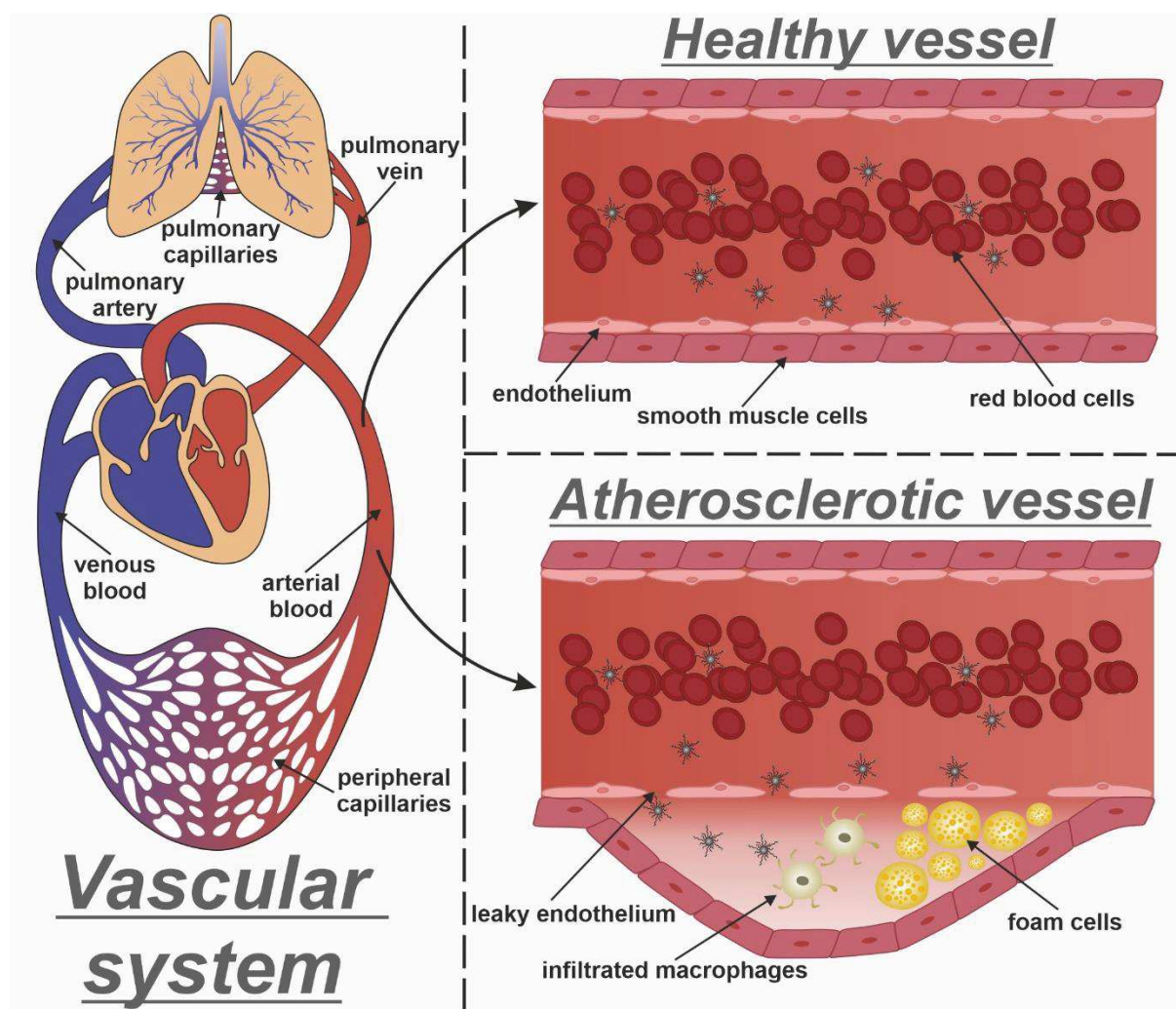
Figure 4. Vascular physiology. The vasculature is generally divided into the venous and arterial system, whereas oxygen- and nutrient- rich arterial blood is compartmentalized into the capillary system which subsequently merges into the venous pool, that is then transported back to the heart and the pulmonal system, where gas exchange takes place. Apart from direct uptake into endothelial cells or extravasation in above discussed hepatic or renal as well as splenic areas, circulating NPs cannot leave the vessel under physiological conditions, which is due to the continuous connection of endothelial cells by impermeable tight junctions. However, pathological changes such as atherosclerotic remodeling can increase the leakiness of the endothelium, thereby facilitating NP extravasation and accumulation in pathological sites of interest such as an atherosclerotic plaque.

4.2   Vascular endothelial cells

For a successful targeting of the vasculature, it is essential for NPs to initially bind to the cell surface of endothelial cells. Thereby, blood flow and resulting shear stress as well as red blood cells and other blood components have been shown to strongly influence and oftentimes decrease efficient NP margination from the vessel interior to the marginal endothelial cell layer.[142–145] In order to increase endothelial binding of circulating NPs, most approaches therefore use various cell adhesion molecules (CAMs), that are usually involved in the attraction of blood components such as platelets, leukocytes or monocytes.[146] In that context, Dziubla *et al.* successfully targeted platelet-endothelial cell adhesion molecule-1 (PECAM-1) with antibody-functionalized PEG-PLGA NPs that carried the antioxidant

enzyme catalase.[147] NPs thereby showed significant endothelial binding *in vitro,* leading to an excellent protection against oxidative stress due to the effects of encapsulated catalase. In an *in vivo* biodistribution study, NP accumulation could mainly be found in the lungs, where a high proportion (~30%) of endothelial cell surface is present. In a highly insightful study, Han *et al.* refined this concept and assessed the impact of anti-PECAM-1 ligand density as well as the flow dynamics on the vascular targeting capacity of polystyrene NPs. The authors concluded that PECAM-1 mediated endocytosis is significantly enhanced, when NPs are functionalized with a greater number of antibodies (50 vs. 200), as these NPs could benefit from a multivalency effect. Additionally, they found, that *in vitro* exposure of endothelial cells to a constant flow significantly decreased NP uptake, which they explained with an observed actin reorganization and consequently, a reduced endocytic capacity. Interestingly, *in vivo* analysis of pulmonary NP biodistribution showed a corresponding trend with NPs predominantly accumulating in smaller capillaries, where blood flow is significantly lower compared to larger arterioles.[148,149]

Intercellular adhesion molecule (ICAM) was found to be another highly promising target for efficient EC targeting. The glycoprotein is involved in intercellular contacts but also facilitates leukocyte attachment and transmigration, especially under pathological conditions such as inflammation or atherosclerosis. Muro *et al.* found, that anti-ICAM functionalized polymer NPs efficiently targeted ECs, both under static and flow conditions *in vitro*.[150] Additionally, isolated rat mesenteric vessels were perfused with anti-ICAM NPs, which showed a significant endothelial deposition within 30 minutes of perfusion. Finally, *in vivo* biodistribution analysis showed maximum NP deposition in the lung, thereby further proving the concept of EC-directed targeting. While several studies successfully harnessed the concept of ICAM-mediated EC targeting[151–153], VCAM-1 was additionally identified as a potent targeting sequence, as it is also involved in a variety of EC binding processes and drastically upregulated in various vascular pathologies such as atherosclerosis. Homem de Bittencourt *et al.* manufactured a VCAM-1 targeted, liposomal carrier system for an antiproliferative cyclopentenone (CP) prostaglandin, which significantly ameliorated disease parameters in LDL-receptor deficient and thus highly atherosclerotic mice.[154] Calin *et al.* presented a comparable approach by equipping liposomes with a VCAM-1 targeting peptide sequence to treat activated endothelial cells with an encapsulated chemokine receptor antagonist, that should prevent excessive monocyte transmigration during atherosclerosis.[155] In an *in situ* model of atherosclerosis-prone apolipoprotein E (ApoE) - deficient mice, targeted NPs showed an enhanced accumulation in mice aortas. Remarkably, NP-mediated delivery of the encapsulated CC chemokine receptor (CCR) antagonist significantly decreased the adhesion of monocytes to the vessel wall. Papademetriou *et al.* combined the above described targeting of cellular adhesion molecules and functionalized polystyrene NPs with different combinations of antibodies against either ICAM, PECAM or VCAM.[156] NP accumulation was assessed both *in vitro* and in an *in vivo* mouse model of lipopolysaccharide-induced vascular inflammation. Although results did not provide an ultimately optimal NP composition, combination of two or three CAM-targeting sequences showed beneficial

effects on the targeting capacity. In the context of mimicking physiological mechanisms of endothelial cell binding, Xu *et al.* presented another, highly interesting approach of PLGA NPs imitating the platelet adhesion process onto ECs.[157] To facilitate initial particle binding, NPs were thereby functionalized with glycoprotein 1b (GP1b), which mediates adhesion to activated (inflamed/injured) endothelial cells *via* P-selectin and von Willebrand Factor (vWF). To enable a sufficient subsequent internalization, NPs were additionally functionalized with transactivating transcriptional activator (TAT), a widely used cell penetrating peptide (CPP), which led to a significant endothelial uptake of targeted NPs under flow conditions. Additionally, NPs carrying anti-inflammatory dexamethasone showed a considerable decrease of arterial stenosis in an *in vivo* injury model. Finally, several approaches identified excessive VEC-mediated angiogenesis, which is an important factor during atherosclerosis progression[158], as a possible target to both image and treat pathologically remodeled endothelial sites. In that regard, Winter *et al.* provided a dual approach of magnetic resonance imaging (MRI) as well as treatment of aortic plaque angiogenesis in atherosclerotic rabbits.[159,160] The authors manufactured paramagnetic perfluorocarbon NPs with an RGD functionality to target $\alpha_v\beta_3$ integrin, which is drastically upregulated under angiogenic conditions. Targeted NPs additionally carried anti-angiogenic drug fumagillin and showed a considerable accumulation in angiogenic areas *in vivo*. Interestingly, one week after treatment, areas with a previously high MRI signal showed a significant decrease, indicating the therapeutic effect of the encapsulated drug and a subsequent decrease of integrin expression. Vader *et al.* used a similar approach to silence vascular endothelial growth factor receptor 2 (VEGFR-2) expression of $\alpha_v\beta_3$ integrin-positive endothelial cells *in vitro,* using cRGD-modified liposomal siRNA carriers.[161]

4.3   Plaque-associated macrophages

Apart from an activated endothelium, infiltrating monocytes play a central role in atherosclerotic plaque development. Once these progenitor cells are converted to macrophages, they endocytose excessive oxidized LDL (oxLDL) and eventually become so-called foam cells, that form the later plaque. Targeting these activated macrophages is therefore a viable option to both image atherosclerotic areas in the vessel wall and treat pathologically remodeled sites. NPs could thereby passively accumulate in the target site *via* extravasation from both the affected larger arteries such as the aorta and the vasa vasorum, i.e. smaller vessels, that supply the vasculature. The reason for this is, that the endothelial cells of these vascular components often show enhanced permeability during atherosclerosis and the associated angiogenesis as well as neovascularization.[162,163]As the described uptake of LDL is mainly mediated *via* different forms of scavenger receptor (SR or CD36), targeting of SRs is mostly used to facilitate macrophage-specific delivery of therapeutic or diagnostic materials. Nie *et al.* manufactured liposomal nanovesicles, that carried oxidized phosphatidylcholine (oxPC), which can also be found on the surface of oxidized LDL and is assumed to be a ligand for CD36. Targeted NPs thereby showed excellent macrophage endocytosis *in vitro* as well as accumulation in atherosclerotic lesions *in vivo*.[164]

Apart from (oxidized) LDL, high-density lipoprotein (HDL) can also interact with the macrophage SR. However, HDL uptake into vascular macrophages does not lead to the describe atherosclerotic effects but facilitates cholesterol removal and hepatic excretion and is therefore regarded beneficial. In that context, Sanchez-Gaytan *et al.* presented hybrid NPs consisting of a PLGA core and a surrounding phospholipid corona with the physicochemical characteristics of HDL. Particles thereby significantly increased cholesterol efflux from targeted macrophages *in vitro* and showed considerable levels of accumulation in atherosclerotic vessels of ApoE knockout mice *in vivo*.[165] Duivenvoorden *et al.* presented a similar concept to deliver anti-inflammatory simvastatin to atherosclerotic plaques using HDL-lipid NPs.[166] Macrophage content as well as inflammation levels in an ApoE KO model could thereby be significantly reduced, both in a one-week high-dose and a three-month low dose i.v. treatment. Iverson *et al.* investigated an alternative approach of macrophage SR targeting by manufacturing amphiphilic polymer NPs with physicochemical characteristics, that facilitate efficient interaction with SR A-1.[167] NPs additionally delivered an agonist for liver receptor X, which regulates the above described efflux of cholesterol from activated macrophages. Both drug-loaded NPs and NPs themselves thereby showed beneficial therapeutic effects *in vivo*, lowering levels of accumulated cholesterol and decreasing macrophage activity. Further approaches have harnessed described phagocytic activity of SRs for a macrophage- and plaque-selective targeting by manufacture of NPs carrying either described HDL functionalities or structural components with a comparably high SR affinity (**Table 3**).[168–170] Again, it is especially the combination of described passive extravasation and active targeting that seems to play a key role for the described effects.

Table 3. Vascular targeting approaches.

Cell type	NP type	Size (nm)	Ligands	Targets	Drug delivery	*In vivo*	Ref.
VECs	PEG-PLGA	170	Anti-PECAM-1	PECAM-1	Catalase	+	147
	Polystyrene	180-200	"-"	"-"	-	+	148,149
	Polystyrene/PLGA	200	Anti-ICAM	ICAM	-	-	150
	PLGA	220	"-"	"-"	-	-	152
	Polystyrene	180	"-"	"-"	-	+	153
	PLGA	175	Peptide sequence	"-"	-	+	151
	Liposomes	n.a.	Anti-VCAM-1	VCAM-1	CP-prostaglandin	+	154
	"-"	130	Peptide sequence	"-"	CCR2-agonist	+	155
	Polystyrene	200-300	Anti-PECAM-1 Anti-ICAM-1 Anti-VCAM-1	PECAM-1 ICAM-1 VCAM-1	-	+	156
	PLGA	240	GP1b TAT	P-selectin/vWF -	Dexamethasone	+	157
	Paramagnetic NPs	175-220	RGD	Integrin αvβ3	Fumagillin	+	159,160
	Liposomes	200	cRGD	"-"	siRNA	-	161
Macrophages	Liposomes	100	oxPC	Scavenger receptor	-	+	164
	HDL-PLGA	40-80	HDL	"-"	-	+	165
	HDL-lipid NPs	30	"-"	"-"	Simvastatin	+	166
	HDL polymer NPs	100-200	"-"	"-"	-	+	169
	Amphiphilic NPs	100	Polymer characteristics	"-"	Liver X rec. agonist	+	167
	"-"	100-200	"-"	"-"	-	-	170
	"-"	100-400	"-"	"-"	-	+	168

5 Implications for future nanotherapeutic approaches

In this review, our goal was to give a comprehensive overview over existing nanotherapeutic strategies to target specific cell types located in organs or tissues with a usually inevitable NP deposition such as the kidney or liver. While the presented concepts thereby used various nanomaterials and incorporated a great number of different pharmaceutically active substances, one trend became obvious during our assessment: All NP concepts, that showed considerable targeting potential for the intended cell type, profited not only from a functionalization with suitable active recognition patterns but to a large extent also from harnessing their general passive accumulation at the respective sites. For instance, NP accumulation in glomerular mesangial cells was successful with various active targeting principles but was in all cases also largely based on the fact, that applied nanomaterials could profit from an extravasation into mesangial regions due to their size. Accordingly, NP targeting of vascular endothelial cells and the therapy of related pathologies could be significantly enhanced by actively exploiting surface structures such as CAMs. However, NP uptake would have been dramatically lower, if the vasculature was not also generally subject to a considerable particle exposition.

In this context, tumor-targeted nanomaterials show a comparable phenomenon. While the EPR effect was seen as a groundbreaking option to dramatically enhance NP tumor accumulation and therapy, there is growing evidence, that not all malignant tissues share the same extent of morphological traits, that the effect is based on. Consequently, NP-mediated therapy of primary or metastatic tumors with actively targeting nanomaterials is also largely dependent on the magnitude of vascular accessibility, which differs not only between distinct tumor types, but to some extent even within one heterogeneous tumor itself.[171]

Taking into consideration these observations, we argue that future NP developments need to change their focus in order to sustainably increase the clinical translation of nanomedical devices. In classic approaches, complex nanomaterials - oftentimes equipped with highly selective recognition sequences – are mostly designed with regard to their capacity to target one specific cell type within the body. While target uptake or selectivity is thereby initially tested *in* vitro, *in vivo* biodistribution and target accumulation are only tested in a second step, whereas off-target deposition is generally regarded as an unavoidable drawback of nanomaterials, that can be minimized at the most.

In contrast, we believe that novel nanotherapeutic studies should initially put a much greater emphasis on general sites of *in vivo* NP accumulation and only then analyze, which cell types or pathologies within these deposition sites could be treated with nanomaterials (**Figure 5**). When it then comes to the final target cell-selective NP uptake, plentiful strategies already exist for the majority of cell types in organs or tissues such as the kidney, liver and vasculature (Tables 1-3). These technologies could then be used and modified in order to reach a sufficient targeting of respective tissues, however with a generally enhanced *in vivo* accumulation due to the previous assessment of general NP biodistribution. Apart from this change of procedure, a much greater focus should also be placed on the actual practicability of

developed nanomaterials, i.e. the required routes of administration and dosing intervals. In that regard, approaches such as a controlled release of NPs from biodegradable hydrogels or concepts for an oral administration of nanomaterials could be valuable options to further expand therapeutic NP options.[172–175] Lastly, we regard it as essential that the final nanotherapeutic devices are manufactured not only with a narrow focus on the chosen target cell or tissue, but still also take into account remaining off-target sites, that inevitably will always be subject to a significant dose of administered NPs. In those regions, both the utilized NP materials and the chosen pharmaceutical agent should therefore show minimal toxicity or adverse effects that could potentially decrease therapeutic success.
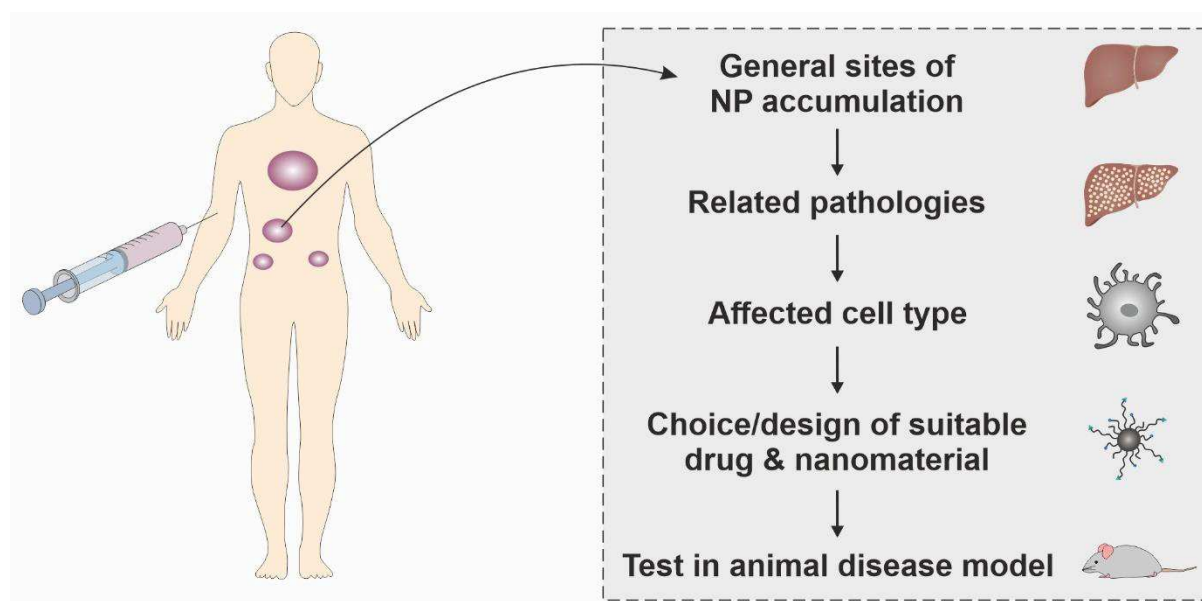
Figure 5. Proposal for a novel nanoparticle design. New nanotherapeutic approaches should be designed with an initial focus on general sites of NP *in vivo* accumulation, that could then be harnessed to develop more promising cell-selective nanomaterials.

6 Conclusion and outlook

There is hardly any other biomedical topic, that has seen such a dramatic shift from initial enthusiastic expectations to harsh criticism than the field of nanomedical devices. To our estimation, both extreme views do not reflect the realistic potential of NP-assisted therapy options. While numerous nanoparticular concepts have already reached clinical translation and marketability, it is also undoubted, that the experienced success rate has been disappointing so far. In our view, current nanomedicine research therefore needs to take a step backwards and rethink, why and most importantly in which cases the implementation of a NP system can make sense. In this case, the general criticism of a considerable off-target accumulation of most administered NPs has to be accepted and most importantly harnessed for potential therapies instead of developing more and more refined concepts, that show excellent *in vitro* behavior and ultimately fail to translate into an *in vivo* setting.

References

(1) Strebhardt, K.; Ullrich, A. Paul Ehrlich's magic bullet concept: 100 years of progress. *Nature reviews. Cancer* **2008**, *8*, 473–480.

(2) Weissig, V.; Pettinger, T. K.; Murdock, N. Nanopharmaceuticals (part 1): products on the market. *International journal of nanomedicine* **2014**, *9*, 4357–4373. DOI: 10.2147/IJN.S46900.

(3) Wilhelm, S.; Tavares, A. J.; Dai, Q.; Ohta, S.; Audet, J.; Dvorak, H. F.; Chan, W. C. W. Analysis of Nanoparticle Delivery to Tumours. *Nature Reviews Materials* **2016**, *1* (5), 16014. DOI: 10.1038/natrevmats.2016.14.

(4) Dai, Q.; Wilhelm, S.; Ding, D.; Syed, A. M.; Sindhwani, S.; Zhang, Y.; Chen, Y. Y.; MacMillan, P.; Chan, W. C. W. Quantifying the Ligand-Coated Nanoparticle Delivery to Cancer Cells in Solid Tumors. *ACS nano* **2018**, *12* (8), 8423–8435. DOI: 10.1021/acsnano.8b03900.

(5) Park, K. The beginning of the end of the nanomedicine hype. *Journal of controlled release : official journal of the Controlled Release Society* **2019**, *305*, 221–222. DOI: 10.1016/j.jconrel.2019.05.044.

(6) World Health Organization. World health statistics 2019: monitoring health for the SDGs, sustainable development goals. **2019**.

(7) Cheng, Y.-H.; He, C.; Riviere, J. E.; Monteiro-Riviere, N. A.; Lin, Z. Meta-Analysis of Nanoparticle Delivery to Tumors Using a Physiologically Based Pharmacokinetic Modeling and Simulation Approach. *ACS nano* **2020**, *14* (3), 3075–3095. DOI: 10.1021/acsnano.9b08142.

(8) Hua, S.; Matos, M. B. C. de; Metselaar, J. M.; Storm, G. Current Trends and Challenges in the Clinical Translation of Nanoparticulate Nanomedicines: Pathways for Translational Development and Commercialization. *Front. Pharmacol.* **2018**, *9*, 790. DOI: 10.3389/fphar.2018.00790.

(9) Yang, B.; Han, X.; Ji, B.; Lu, R. Competition Between Tumor and Mononuclear Phagocyte System Causing the Low Tumor Distribution of Nanoparticles and Strategies to Improve Tumor Accumulation. *Current Drug Delivery* **2016** (13), 1261–1274.

(10) Zhou, Y.; Dai, Z. New Strategies in the Design of Nanomedicines to Oppose Uptake by the Mononuclear Phagocyte System and Enhance Cancer Therapeutic Efficacy. *Chemistry, an Asian journal* **2018**, *13* (22), 3333–3340. DOI: 10.1002/asia.201800149.

(11) Gref, R.; Minamitake, Y.; Peracchia, M. T.; Trubetskoy, V.; Torchilin, V.; Langer, R. Biodegradable long-circulating polymeric nanospheres. *Science* **1994**, *263* (5153), 1600–1603. DOI: 10.1126/science.8128245.

(12) Knop, K.; Hoogenboom, R.; Fischer, D.; Schubert, U. S. Poly(ethylene glycol) in drug delivery:Pros and cons as well as potential alternatives. *Angewandte Chemie (International ed. in English)* **2010**, *49* (36), 6288–6308. DOI: 10.1002/anie.200902672.

(13) Gulati, N. M.; Stewart, P. L.; Steinmetz, N. F. Bioinspired Shielding Strategies for Nanoparticle Drug Delivery Applications. *Molecular pharmaceutics* **2018**, *15* (8), 2900–2909. DOI: 10.1021/acs.molpharmaceut.8b00292.

(14) Alexis, F.; Pridgen, E.; Molnar, L. K.; Farokhzad, O. C. Factors Affecting the Clearance and Biodistribution of Polymeric Nanoparticles. *Molecular pharmaceutics* **2008**, *5* (4), 505–515. DOI: 10.1021/mp800051m.

(15) Hill, N. R.; Fatoba, S. T.; Oke, J. L.; Hirst, J. A.; O'Callaghan, C. A.; Lasserson, D. S.; Hobbs, F. D. R. Global Prevalence of Chronic Kidney Disease - A Systematic Review and Meta-Analysis. *PloS one* **2016**, *11* (7), e0158765. DOI: 10.1371/journal.pone.0158765.

(16) Levey, A. S.; Coresh, J. Chronic kidney disease. *The Lancet* **2012**, *379* (9811), 165–180. DOI: 10.1016/S0140-6736(11)60178-5.

(17) Webster, A. C.; Nagler, E. V.; Morton, R. L.; Masson, P. Chronic Kidney Disease. *The Lancet* **2017**, *389* (10075), 1238–1252. DOI: 10.1016/S0140-6736(16)32064-5.

(18) Bertram, J. F.; Douglas-Denton, R. N.; Diouf, B.; Hughson, M. D.; Hoy, W. E. Human nephron number: implications for health and disease. *Pediatric nephrology (Berlin, Germany)* **2011**, *26* (9), 1529–1533. DOI: 10.1007/s00467-011-1843-8.

(19) Scott, R. P.; Quaggin, S. E. The Cell Biology of Renal Filtration. *J. Cell Biol.* **2015**, *209* (2), 199–210. DOI: 10.1083/jcb.201410017.

(20) Miner, J. H. The Glomerular Basement Membrane. *Exp. Cell Res.* **2012**, *318* (9), 973–978. DOI: 10.1016/j.yexcr.2012.02.031.

(21) Haraldsson, B.; Nyström, J.; Deen, W. M. Properties of the Glomerular Barrier and Mechanisms of Proteinuria. *Physiol. Rev.* **2008**, *88* (2), 451–487. DOI: 10.1152/physrev.00055.2006.

(22) Haraldsson, B.; Jeansson, M. Glomerular filtration barrier. *Current opinion in nephrology and hypertension* **2009**, *18* (4), 331–335. DOI: 10.1097/MNH.0b013e32832c9dba.

(23) Vaughan, M. R.; Quaggin, S. E. How do mesangial and endothelial cells form the glomerular tuft? *Journal of the American Society of Nephrology : JASN* **2008**, *19* (1), 24–33. DOI: 10.1681/ASN.2007040471.

(24) Schlöndorff, D. Roles of the Mesangium in Glomerular Function. *Kidney Int.* **1996**, *49* (6), 1583–1585. DOI: 10.1038/ki.1996.229.

(25) Liu, Y. Renal fibrosis: new insights into the pathogenesis and therapeutics. *Kidney International* **2006**, *69* (2), 213–217. DOI: 10.1038/sj.ki.5000054.

(26) Humphreys, B. D. Mechanisms of Renal Fibrosis. *Annual review of physiology* **2018**, *80*, 309–326. DOI: 10.1146/annurev-physiol-022516-034227.

(27) Arora, M. K.; Singh, U. K. Molecular mechanisms in the pathogenesis of diabetic nephropathy:An update. *Vascular pharmacology* **2013**, *58* (4), 259–271. DOI: 10.1016/j.vph.2013.01.001.

(28) Barutta, F.; Bruno, G.; Grimaldi, S.; Gruden, G. Inflammation in diabetic nephropathy:Moving toward clinical biomarkers and targets for treatment. *Endocrine* **2015**, *48* (3), 730–742. DOI: 10.1007/s12020-014-0437-1.

(29) Scindia, Y. M.; Deshmukh, U. S.; Bagavant, H. Mesangial Pathology in Glomerular Disease:Targets for Therapeutic Intervention. *Adv. Drug Delivery Rev.* **2010**, *62* (14), 1337–1343. DOI: 10.1016/j.addr.2010.08.011.

(30) Umanath, K.; Lewis, J. B. Update on Diabetic Nephropathy: Core Curriculum 2018. *Am. J. Kidney Dis.* **2018**, *71* (6), 884–895. DOI: 10.1053/j.ajkd.2017.10.026.

(31) Ruggenenti, P.; Cravedi, P.; Remuzzi, G. Mechanisms and treatment of CKD. *Journal of the American Society of Nephrology : JASN* **2012**, *23* (12), 1917–1928. DOI: 10.1681/ASN.2012040390.

(32) Du, B.; Yu, M.; Zheng, J. Transport and interactions of nanoparticles in the kidneys. *Nat. Rev. Mater.* **2018**, *3* (10), 358–374. DOI: 10.1038/s41578-018-0038-3.

(33) Fleischmann, D.; Maslanka Figueroa, S.; Beck, S.; Abstiens, K.; Witzgall, R.; Schweda, F.; Tauber, P.; Goepferich, A. Adenovirus-Mimetic Nanoparticles: Sequential Ligand-Receptor Interplay as a Universal Tool for Enhanced In Vitro/In Vivo Cell Identification. *ACS applied materials & interfaces* **2020**, *12* (31), 34689–34702. DOI: 10.1021/acsami.0c10057. Published Online: Jul. 22, 2020.

(34) Schlöndorff, D.; Banas, B. The Mesangial Cell Revisited:No Cell Is an Island. *J. Am. Soc. Nephrol.* **2009**, *20* (6), 1179–1187. DOI: 10.1681/ASN.2008050549.

(35) Barnes, J. L.; Gorin, Y. Myofibroblast differentiation during fibrosis: role of NAD(P)H oxidases. *Kidney International* **2011**, *79* (9), 944–956. DOI: 10.1038/ki.2010.516.

(36) Satchell, S. C.; Braet, F. Glomerular Endothelial Cell Fenestrations: an Integral Component of the Glomerular Filtration Barrier. *Am. J. Physiol. Renal Physiol.* **2009**, *296* (5), 947-956. DOI: 10.1152/ajprenal.90601.2008.

(37) Choi, C. H. J.; Zuckerman, J. E.; Webster, P.; Davis, M. E. Targeting kidney mesangium by nanoparticles of defined size. *Proceedings of the National Academy of Sciences of the United States of America* **2011**, *108* (16), 6656–6661. DOI: 10.1073/pnas.1103573108.

(38) Kalyane, D.; Raval, N.; Maheshwari, R.; Tambe, V.; Kalia, K.; Tekade, R. K. Employment of enhanced permeability and retention effect (EPR): Nanoparticle-based precision tools for targeting of therapeutic and diagnostic agent in cancer. *Materials science & engineering. C, Materials for biological applications* **2019**, *98*, 1252–1276. DOI: 10.1016/j.msec.2019.01.066.

(39) Li, S.; Zeng, Y.-C.; Peng, K.; Liu, C.; Zhang, Z.-R.; Zhang, L. Design and evaluation of glomerulus mesangium-targeted PEG-PLGA nanoparticles loaded with dexamethasone acetate. *Acta pharmacologica Sinica* **2019**, *40* (1), 143–150. DOI: 10.1038/s41401-018-0052-4.

(40) Guo, L.; Luo, S.; Du, Z.; Zhou, M.; Li, P.; Fu, Y.; Sun, X.; Huang, Y.; Zhang, Z. Targeted delivery of celastrol to mesangial cells is effective against mesangioproliferative glomerulonephritis. *Nature communications* **2017**, *8* (1), 878. DOI: 10.1038/s41467-017-00834-8.

(41) Jourde-Chiche, N.; Fakhouri, F.; Dou, L.; Bellien, J.; Burtey, S.; Frimat, M.; Jarrot, P.-A.; Kaplanski, G.; Le Quintrec, M.; Pernin, V.; Rigothier, C.; Sallée, M.; Fremeaux-Bacchi, V.; Guerrot, D.; Roumenina, L. T. Endothelium structure and function in kidney health and disease. *Nature reviews. Nephrology* **2019**, *15* (2), 87–108. DOI: 10.1038/s41581-018-0098-z.

(42) Yaoita, E.; Oguri, K.; Okayama, E.; Kawasaki, K.; Kobayashi, S.; Kihara, I.; Okayama, M. Isolation and Characterization of Proteoglycans Synthesized by Cultured Mesangial Cells. *The Journal of biological chemistry* **1990** (265), 522–531.

(43) Thogersen, V. B.; Heickendorff, L.; Ledet, T. A Quantitative Method for Analysis of Radiolabelled Proteoglycans Synthesized By Cultured Human Artetial Smooth Muscle Cells. *International Journal of Biochemistry* **1994** (26), 55–59.

(44) Harigai, T.; Kondo, M.; Isozaki, M.; Kasukawa, H.; Hagiwara, H.; Uchiyama, H.; Kimura, J. Preferential Binding of Polyethylene Glycol-Coated Liposomes Containing a Novel Cationic Lipid, TRX-20, to Human Subendthelial Cells via Chondroitin Sulfate. *Pharmaceutical research* **2001**, *18* (9).

(45) Liao, J.; Hayashi, K.; Horikoshi, S.; Ushijima, H.; Kimura, J.; Tomino, Y. Effect of Steroid-Liposome on Immunohistopathology of IgA Nephropathy in ddY Mice. *Nephron* **2001** (89), 194–200.

(46) Morimoto, K.; Kondo, M.; Kawahara, K.; Ushijima, H.; Tomino, Y.; Miyajima, M.; Kimura, J. Advances in targeting drug delivery to glomerular mesangial cells by long circulating cationic liposomes for the treatment of glomerulonephritis. *Pharm Res* **2007**, *24* (5), 946–954. DOI: 10.1007/s11095-006-9213-0.

(47) Yuan, Z.-X.; Jia, L.; Lim, L. Y.; Lin, J.-C.; Shu, G.; Zhao, L.; Ye, G.; Liang, X.-X.; Ji, H.; Fu, H.-L. Renal-targeted delivery of triptolide by entrapment in pegylated TRX-20-modified liposomes. *International journal of nanomedicine* **2017**, *12*, 5673–5686. DOI: 10.2147/IJN.S141095.

(48) Bagchus, W. M.; Hoedemaeker, P. J.; Rozing, J.; Bakker, W. W. Glomerulonephritis induced by monoclonal anti-Thy 1.1 antibodies. A sequential histological and ultrastructural study in the rat. *Laboratory investigation; a journal of technical methods and pathology* **1986**, *55* (6), 680–687.

(49) Tuffin, G.; Huwyler, J.; Waelti, E.; Hammer, C.; Marti, H.-P. Drug targeting using OX7-immunoliposomes: correlation between Thy1.1 antigen expression and tissue distribution in the rat. *Journal of drug targeting* **2008**, *16* (2), 156–166. DOI: 10.1080/10611860701848944.

(50) Tuffin, G.; Waelti, E.; Huwyler, J.; Hammer, C.; Marti, H.-P. Immunoliposome targeting to mesangial cells: a promising strategy for specific drug delivery to the kidney. *Journal of the American Society of Nephrology : JASN* **2005**, *16* (11), 3295–3305. DOI: 10.1681/ASN.2005050485.

(51) Suana, A. J.; Tuffin, G.; Frey, B. M.; Knudsen, L.; Mühlfeld, C.; Rödder, S.; Marti, H.-P. Single application of low-dose mycophenolate mofetil-OX7-immunoliposomes ameliorates experimental mesangial proliferative glomerulonephritis. *The Journal of pharmacology and experimental therapeutics* **2011**, *337* (2), 411–422. DOI: 10.1124/jpet.110.176222.

(52) Zuckerman, J. E.; Gale, A.; Wu, P.; Ma, R.; Davis, M. E. siRNA delivery to the glomerular mesangium using polycationic cyclodextrin nanoparticles containing siRNA. *Nucleic acid therapeutics* **2015**, *25* (2), 53–64. DOI: 10.1089/nat.2014.0505.

(53) Scindia, Y.; Deshmukh, U.; Thimmalapura, P.-R.; Bagavant, H. Anti-alpha8 integrin immunoliposomes in glomeruli of lupus-susceptible mice: a novel system for delivery of therapeutic agents to the renal glomerulus in systemic lupus erythematosus. *Arthritis and rheumatism* **2008**, *58* (12), 3884–3891. DOI: 10.1002/art.24026.

(54) Maslanka Figueroa, S.; Fleischmann, D.; Goepferich, A. Biomedical nanoparticle design: What we can learn from viruses. *Journal of controlled release : official journal of the Controlled Release Society* **2020.** DOI: 10.1016/j.jconrel.2020.09.045.

(55) Dou, D.; Revol, R.; Östbye, H.; Wang, H.; Daniels, R. Influenza A Virus Cell Entry, Replication, Virion Assembly and Movement. *Frontiers in immunology* **2018**, *9,* 1581. DOI: 10.3389/fimmu.2018.01581.

(56) Maslanka Figueroa, S.; Veser, A.; Abstiens, K.; Fleischmann, D.; Beck, S.; Goepferich, A. Influenza A Virus Mimetic Nanoparticles Trigger Selective Cell Uptake. *Proc. Natl. Acad. Sci. U. S. A.States of America* **2019.** DOI: 10.1073/pnas.1902563116.

(57) Maslanka Figueroa, S.; Fleischmann, D.; Beck, S.; Tauber, P.; Witzgall, R.; Schweda, F.; Goepferich, A. Nanoparticles Mimicking Viral Cell Recognition Strategies Are Superior Transporters into Mesangial Cells. *Adv. Sci.* **2020**, 1903204. DOI: 10.1002/advs.201903204.

(58) Luisoni, S.; Greber, U. F. Biology of Adenovirus Cell Entry. In *Adenoviral Vectors for Gene Therapy*; pp 27–58. DOI: 10.1016/B978-0-12-800276-6.00002-4.

(59) Fleischmann, D.; Maslanka Figueroa, S.; Goepferich, A. Steric Shielding of cRGD-Functionalized Nanoparticles from Premature Exposition to Off-Target Endothelial Cells under a Physiological Flow. *ACS Appl. Bio Mater.* **2021**, *4* (1), 640–650. DOI: 10.1021/acsabm.0c01193.

(60) Fischer, E. G. Glomerular mesangial cell adhesion to fibrinogen is mediated by alphavbeta3 integrin. *Biochemistry and cell biology = Biochimie et biologie cellulaire* **2004**, *82* (5), 597–601. DOI: 10.1139/o04-051.

(61) Fleischmann, D.; Harloff, M.; Maslanka Figueroa, S.; Schlossmann, J.; Goepferich, A. Targeted Delivery of Soluble Guanylate Cyclase (sGC) Activator Cinaciguat to Renal Mesangial Cells via Virus-Mimetic Nanoparticles Potentiates Anti-Fibrotic Effects by cGMP-Mediated Suppression of the TGF-β Pathway. *IJMS* **2021**, *22* (5), 2557. DOI: 10.3390/ijms22052557.

(62) Kitching, A. R.; Hutton, H. L. The Players: Cells Involved in Glomerular Disease. *Clinical journal of the American Society of Nephrology : CJASN* **2016**, *11* (9), 1664–1674. DOI: 10.2215/CJN.13791215.

(63) Daehn, I. S. Glomerular Endothelial Cell Stress and Cross-Talk With Podocytes in Early corrected Diabetic Kidney Disease. *Frontiers in medicine* **2018**, *5*, 76. DOI: 10.3389/fmed.2018.00076.

(64) Ulbrich, H.; Eriksson, E. E.; Lindbom, L. Leukocyte and endothelial cell adhesion molecules as targets for therapeutic interventions in inflammatory disease. *Trends in pharmacological sciences* **2003**, *24* (12), 640–647. DOI: 10.1016/j.tips.2003.10.004.

(65) Asgeirsdóttir, S. A.; Kamps, J. A. A. M.; Bakker, H. I.; Zwiers, P. J.; Heeringa, P.; van der Weide, K.; van Goor, H.; Petersen, A. H.; Morselt, H.; Moorlag, H. E.; Steenbergen, E.; Kallenberg, C. G.; Molema, G. Site-specific inhibition of glomerulonephritis progression by targeted delivery of dexamethasone to glomerular endothelium. *Molecular pharmacology* **2007**, *72* (1), 121–131. DOI: 10.1124/mol.107.034140.

(66) Asgeirsdóttir, S. A.; Zwiers, P. J.; Morselt, H. W.; Moorlag, H. E.; Bakker, H. I.; Heeringa, P.; Kok, J. W.; Kallenberg, C. G. M.; Molema, G.; Kamps, J. A. A. M. Inhibition of proinflammatory genes in anti-GBM glomerulonephritis by targeted dexamethasone-loaded AbEsel liposomes. *American journal of physiology. Renal physiology* **2008**, *294* (3), F554-61. DOI: 10.1152/ajprenal.00391.2007.

(67) Reiser, J.; Altintas, M. M. Podocytes. *F1000Research* **2016**, *5*. DOI: 10.12688/f1000research.7255.1.

(68) Mallipattu, S. K.; He, J. C. The podocyte as a direct target for treatment of glomerular disease? *American journal of physiology. Renal physiology* **2016**, *311* (1), F46-51. DOI: 10.1152/ajprenal.00184.2016.

(69) Li, J. J.; Kwak, S. J.; Jung, D. S.; Kim, J.-J.; Yoo, T.-H.; Ryu, D.-R.; Han, S. H.; Choi, H. Y.; Lee, J. E.; Moon, S. J.; Kim, D. K.; Han, D. S.; Kang, S.-W. Podocyte biology in diabetic nephropathy. *Kidney international. Supplement* **2007** (106), S36-42. DOI: 10.1038/sj.ki.5002384.

(70) Bruni, R.; Possenti, P.; Bordignon, C.; Li, M.; Ordanini, S.; Messa, P.; Rastaldi, M. P.; Cellesi, F. Ultrasmall polymeric nanocarriers for drug delivery to podocytes in kidney glomerulus. *Journal of controlled release : official journal of the Controlled Release Society* **2017**, *255*, 94–107. DOI: 10.1016/j.jconrel.2017.04.005.

(71) Wu, L.; Chen, M.; Mao, H.; Wang, N.; Zhang, B.; Zhao, X.; Qian, J.; Xing, C. Albumin-based nanoparticles as methylprednisolone carriers for targeted delivery towards the neonatal Fc receptor in glomerular podocytes. *International journal of molecular medicine* **2017**, *39* (4), 851–860. DOI: 10.3892/ijmm.2017.2902.

(72) Pollinger, K.; Hennig, R.; Breunig, M.; Tessmar, J.; Ohlmann, A.; Tamm, E. R.; Witzgall, R.; Goepferich, A. Kidney Podocytes as Specific Targets for Cyclo(RGDfC)-Modified Nanoparticles. *Small* **2012**, *8* (21), 3368–3375. DOI: 10.1002/smll.201200733.

(73) Visweswaran, G. R. R.; Gholizadeh, S.; Ruiters, M. H. J.; Molema, G.; Kok, R. J.; Kamps, J. A. A. M. Targeting Rapamycin to Podocytes Using a Vascular Cell Adhesion Molecule-1 (VCAM-1)-Harnessed SAINT-Based Lipid Carrier System. *PloS one* **2015**, *10* (9), e0138870. DOI: 10.1371/journal.pone.0138870.

(74) Colombo, C.; Li, M.; Watanabe, S.; Messa, P.; Edefonti, A.; Montini, G.; Moscatelli, D.; Rastaldi, M. P.; Cellesi, F. Polymer Nanoparticle Engineering for Podocyte Repair: From in Vitro Models to New

Nanotherapeutics in Kidney Diseases. *ACS omega* **2017**, *2* (2), 599–610. DOI: 10.1021/acsomega.6b00423.

(75) Reiser, J.; Sever, S. Podocyte biology and pathogenesis of kidney disease. *Annual review of medicine* **2013**, *64*, 357–366. DOI: 10.1146/annurev-med-050311-163340.

(76) Liu, B.-C.; Tang, T.-T.; Lv, L.-L. How Tubular Epithelial Cell Injury Contributes to Renal Fibrosis. In *Renal Fibrosis: Mechanisms and Therapies,* 1st ed. 2019; Liu, B.-C., Lan, H.-Y., Lv, L.-L., Eds.; Advances in Experimental Medicine and Biology; Springer Singapore, 2019; pp 233–252. DOI: 10.1007/978-981-13-8871-2_11.

(77) Christensen, E. I.; Birn, H.; Storm, T.; Weyer, K.; Nielsen, R. Endocytic receptors in the renal proximal tubule. *Physiology (Bethesda, Md.)* **2012**, *27* (4), 223–236. DOI: 10.1152/physiol.00022.2012.

(78) Christensen, E. I.; Birn, H. Megalin and cubilin:Multifunctional endocytic receptors. *Nature reviews. Molecular cell biology* **2002**, *3* (4), 256–266. DOI: 10.1038/nrm778.

(79) Prakash, J.; Borst, M. H. de; van Loenen-Weemaes, A. M.; Lacombe, M.; Opdam, F.; van Goor, H.; Meijer, D. K. F.; Moolenaar, F.; Poelstra, K.; Kok, R. J. Cell-specific delivery of a transforming growth factor-beta type I receptor kinase inhibitor to proximal tubular cells for the treatment of renal fibrosis. *Pharmaceutical research* **2008**, *25* (10), 2427–2439. DOI: 10.1007/s11095-007-9515-x.

(80) Zhang, Z.; Zheng, Q.; Han, J.; Gao, G.; Liu, J.; Gong, T.; Gu, Z.; Huang, Y.; Sun, X.; He, Q. The targeting of 14-succinate triptolide-lysozyme conjugate to proximal renal tubular epithelial cells. *Biomaterials* **2009**, *30* (7), 1372–1381. DOI: 10.1016/j.biomaterials.2008.11.035.

(81) Prakash, J.; Borst, M. H. de; Lacombe, M.; Opdam, F.; Klok, P. A.; van Goor, H.; Meijer, D. K. F.; Moolenaar, F.; Poelstra, K.; Kok, R. J. Inhibition of renal rho kinase attenuates ischemia/reperfusion-induced injury. *Journal of the American Society of Nephrology : JASN* **2008**, *19* (11), 2086–2097. DOI: 10.1681/ASN.2007070794.

(82) Prakash, J.; van Loenen-Weemaes, A. M.; Haas, M.; Proost, J. H.; Meijer, D. K. F.; Moolenaar, F.; Poelstra, K.; Kok, R. J. Renal-selective delivery and angiotensin-converting enzyme inhibition by subcutaneously administered captopril-lysozyme. *Drug metabolism and disposition: the biological fate of chemicals* **2005**, *33* (5), 683–688. DOI: 10.1124/dmd.104.002808.

(83) Yuan, Z.-X.; Zhang, Z.-R.; Di Zhu; Sun, X.; Gong, T.; Liu, J.; Luan, C.-t. Specific renal uptake of randomly 50% N-acetylated low molecular weight chitosan. *Molecular pharmaceutics* **2009**, *6* (1), 305–314. DOI: 10.1021/mp800078a.

(84) Qiao, H.; Sun, M.; Su, Z.; Xie, Y.; Chen, M.; Zong, L.; Gao, Y.; Li, H.; Qi, J.; Zhao, Q.; Gu, X.; Ping, Q. Kidney-specific drug delivery system for renal fibrosis based on coordination-driven assembly of catechol-derived chitosan. *Biomaterials* **2014**, *35* (25), 7157–7171. DOI: 10.1016/j.biomaterials.2014.04.106.

(85) Kodaira, H.; Tsutsumi, Y.; Yoshioka, Y.; Kamada, H.; Kaneda, Y.; Yamamoto, Y.; Tsunoda, S.-i.; Okamoto, T.; Mukai, Y.; Shibata, H.; Nakagawa, S.; Mayumi, T. The targeting of anionized

polyvinylpyrrolidone to the renal system. *Biomaterials* **2004**, *25* (18), 4309–4315. DOI: 10.1016/j.biomaterials.2003.10.097.

(86) Nair, A. V.; Keliher, E. J.; Core, A. B.; Brown, D.; Weissleder, R. Characterizing the interactions of organic nanoparticles with renal epithelial cells in vivo. *ACS nano* **2015**, *9* (4), 3641–3653. DOI: 10.1021/acsnano.5b00428.

(87) Oroojalian, F.; Rezayan, A. H.; Mehrnejad, F.; Nia, A. H.; Shier, W. T.; Abnous, K.; Ramezani, M. Efficient megalin targeted delivery to renal proximal tubular cells mediated by modified-polymyxin B-polyethylenimine based nano-gene-carriers. *Materials science & engineering. C, Materials for biological applications* **2017**, *79*, 770–782. DOI: 10.1016/j.msec.2017.05.068.

(88) Williams, R. M.; Shah, J.; Ng, B. D.; Minton, D. R.; Gudas, L. J.; Park, C. Y.; Heller, D. A. Mesoscale nanoparticles selectively target the renal proximal tubule epithelium. *Nano letters* **2015**, *15* (4), 2358–2364. DOI: 10.1021/nl504610d.

(89) Rui, L. Energy metabolism in the liver. *Comprehensive Physiology* **2014**, *4* (1), 177–197. DOI: 10.1002/cphy.c130024.

(90) Hernandez-Gea, V.; Friedman, S. L. Pathogenesis of liver fibrosis. *Annual review of pathology* **2011**, *6*, 425–456. DOI: 10.1146/annurev-pathol-011110-130246.

(91) Schuppan, D.; Afdhal, N. H. Liver cirrhosis. *The Lancet* **2008**, *371* (9615), 838–851. DOI: 10.1016/S0140-6736(08)60383-9.

(92) Poisson, J.; Lemoinne, S.; Boulanger, C.; Durand, F.; Moreau, R.; Valla, D.; Rautou, P.-E. Liver sinusoidal endothelial cells: Physiology and role in liver diseases. *Journal of hepatology* **2017**, *66* (1), 212–227. DOI: 10.1016/j.jhep.2016.07.009.

(93) Gustafson, H. H.; Holt-Casper, D.; Grainger, D. W.; Ghandehari, H. Nanoparticle Uptake: The Phagocyte Problem. *Nano today* **2015**, *10* (4), 487–510. DOI: 10.1016/j.nantod.2015.06.006.

(94) Puche, J. E.; Saiman, Y.; Friedman, S. L. Hepatic stellate cells and liver fibrosis. *Comprehensive Physiology* **2013**, *3* (4), 1473–1492. DOI: 10.1002/cphy.c120035.

(95) Prud´homme, G. J. Pathobiology of transforming growth factor b in cancer, fibrosis and immunologic disease, and therapeutic considerations. *Laboratory investigation; a journal of technical methods and pathology* **2007**, *87*, 1077–1091.

(96) Beljaars, L.; Molema, G.; Weert, B.; Bonnema, H.; Olinga, P.; Groothuis, G. M. M.; Meijer, D. K. F.; Poelstra, K. Albumin Modified With Mannose 6-Phosphate: A Potential Carrier for Selective Delivery of Antifibrotic Drugs to Rat and Human Hepatic Stellate Cells. *Hepatology* **1999**, *29* (5), 1487–1493.

(97) Greupink, R.; Bakker, H. I.; Bouma, W.; Reker-Smit, C.; Meijer, D. K. F.; Beljaars, L.; Poelstra, K. The antiproliferative drug doxorubicin inhibits liver fibrosis in bile duct-ligated rats and can be selectively delivered to hepatic stellate cells in vivo. *The Journal of pharmacology and experimental therapeutics* **2006**, *317* (2), 514–521. DOI: 10.1124/jpet.105.099499.

(98) Gonzalo, T.; Talman, E. G.; van de Ven, A.; Temming, K.; Greupink, R.; Beljaars, L.; Reker-Smit, C.; Meijer, D. K. F.; Molema, G.; Poelstra, K.; Kok, R. J. Selective targeting of pentoxifylline to hepatic stellate cells using a novel platinum-based linker technology. *Journal of Controlled Release* **2006**, *111* (1-2), 193–203. DOI: 10.1016/j.jconrel.2005.12.010.

(99) van Beuge, M. M.; Prakash, J.; Lacombe, M.; Gosens, R.; Post, E.; Reker-Smit, C.; Beljaars, L.; Poelstra, K. Reduction of fibrogenesis by selective delivery of a Rho kinase inhibitor to hepatic stellate cells in mice. *The Journal of pharmacology and experimental therapeutics* **2011**, *337* (3), 628–635. DOI: 10.1124/jpet.111.179143.

(100) van Beuge, M. M.; Prakash, J.; Lacombe, M.; Post, E.; Reker-Smit, C.; Beljaars, L.; Poelstra, K. Enhanced effectivity of an ALK5-inhibitor after cell-specific delivery to hepatic stellate cells in mice with liver injury. *PloS one* **2013**, *8* (2), e56442. DOI: 10.1371/journal.pone.0056442.

(101) Adrian, J. E.; Kamps, J. A. A. M.; Scherphof, G. L.; Meijer, D. K. F.; van Loenen-Weemaes, A.-m.; Reker-Smit, C.; Terpstra, P.; Poelstra, K. A novel lipid-based drug carrier targeted to the non-parenchymal cells, including hepatic stellate cells, in the fibrotic livers of bile duct ligated rats. *Biochimica et biophysica acta* **2007**, *1768* (6), 1430–1439. DOI: 10.1016/j.bbamem.2007.03.027.

(102) Adrian, J. E.; Kamps, J. A. A. M.; Poelstra, K.; Scherphof, G. L.; Meijer, D. K. F.; Kaneda, Y. Delivery of viral vectors to hepatic stellate cells in fibrotic livers using HVJ envelopes fused with targeted liposomes. *Journal of drug targeting* **2007**, *15* (1), 75–82. DOI: 10.1080/10611860601141481.

(103) Patel, G.; Kher, G.; Misra, A. Preparation and evaluation of hepatic stellate cell selective, surface conjugated, peroxisome proliferator-activated receptor-gamma ligand loaded liposomes. *Journal of drug targeting* **2012**, *20* (2), 155–165. DOI: 10.3109/1061186X.2011.610800.

(104) Sato, Y.; Murase, K.; Kato, J.; Kobune, M.; Sato, T.; Kawano, Y.; Takimoto, R.; Takada, K.; Miyanishi, K.; Matsunaga, T.; Takayama, T.; Niitsu, Y. Resolution of liver cirrhosis using vitamin A-coupled liposomes to deliver siRNA against a collagen-specific chaperone. *Nature biotechnology* **2008**, *26* (4), 431–442. DOI: 10.1038/nbt1396.

(105) Duong, H. T. T.; Dong, Z.; Su, L.; Boyer, C.; George, J.; Davis, T. P.; Wang, J. The use of nanoparticles to deliver nitric oxide to hepatic stellate cells for treating liver fibrosis and portal hypertension. *Small (Weinheim an der Bergstrasse, Germany)* **2015**, *11* (19), 2291–2304. DOI: 10.1002/smll.201402870.

(106) Klinkhammer, B. M.; Floege, J.; Boor, P. PDGF in organ fibrosis. *Molecular aspects of medicine* **2018**, *62*, 44–62. DOI: 10.1016/j.mam.2017.11.008.

(107) Bansal, R.; Prakash, J.; Ruijter, M. de; Beljaars, L.; Poelstra, K. Peptide-modified albumin carrier explored as a novel strategy for a cell-specific delivery of interferon gamma to treat liver fibrosis. *Molecular pharmaceutics* **2011**, *8* (5), 1899–1909. DOI: 10.1021/mp200263q.

(108) Li, F.; Li, Q.-h.; Wang, J.-y.; Zhan, C.-y.; Xie, C.; Lu, W.-y. Effects of interferon-gamma liposomes targeted to platelet-derived growth factor receptor-beta on hepatic fibrosis in rats. *Journal of*

controlled release : official journal of the Controlled Release Society **2012**, *159* (2), 261–270. DOI: 10.1016/j.jconrel.2011.12.023.

(109) Beljaars, L.; Molema, G.; Schuppan, D.; Geerts, A.; Bleser, P. J. de; Weert, B.; Meijer, D. K. F.; Poelstra, K. Successful Targeting to Rat Hepatic Stellate Cells Using Albumin Modified with Cyclic Peptides That Recognize the Collagen Type VI Receptor. *The Journal of biological chemistry* **2000**, *275* (17), 12743–12751.

(110) Du, S.-L.; Pan, H.; Lu, W.-y.; Wang, J.; Wu, J.; Wang, J.-y. Cyclic Arg-Gly-Asp peptide-labeled liposomes for targeting drug therapy of hepatic fibrosis in rats. *The Journal of pharmacology and experimental therapeutics* **2007**, *322* (2), 560–568. DOI: 10.1124/jpet.107.122481.

(111) Chai, N.-L.; Fu, Q.; Shi, H.; Cai, C.-H.; Wan, J.; Xu, S.-P.; Wu, B.-Y. Oxymatrine liposome attenuates hepatic fibrosis via targeting hepatic stellate cells. *World journal of gastroenterology* **2012**, *18* (31), 4199–4206. DOI: 10.3748/wjg.v18.i31.4199.

(112) Yang, J.; Hou, Y.; Ji, G.; Song, Z.; Liu, Y.; Dai, G.; Zhang, Y.; Chen, J. Targeted delivery of the RGD-labeled biodegradable polymersomes loaded with the hydrophilic drug oxymatrine on cultured hepatic stellate cells and liver fibrosis in rats. *European journal of pharmaceutical sciences : official journal of the European Federation for Pharmaceutical Sciences* **2014**, *52*, 180–190. DOI: 10.1016/j.ejps.2013.11.017.

(113) Li, F.; Sun, J.-Y.; Wang, J.-y.; Du, S.-L.; Lu, W.-y.; Liu, M.; Xie, C.; Shi, J.-Y. Effect of hepatocyte growth factor encapsulated in targeted liposomes on liver cirrhosis. *Journal of controlled release : official journal of the Controlled Release Society* **2008**, *131* (1), 77–82. DOI: 10.1016/j.jconrel.2008.07.021.

(114) Chen, Y.-N.; Hsu, S.-L.; Liao, M.-Y.; Liu, Y.-T.; Lai, C.-H.; Chen, J.-F.; Nguyen, M.-H. T.; Su, Y.-H.; Chen, S.-T.; Wu, L.-C. Ameliorative Effect of Curcumin-Encapsulated Hyaluronic Acid-PLA Nanoparticles on Thioacetamide-Induced Murine Hepatic Fibrosis. *International journal of environmental research and public health* **2016**, *14* (1). DOI: 10.3390/ijerph14010011.

(115) Thomas, R. G.; Moon, M. J.; Kim, J. H.; Lee, J. H.; Jeong, Y. Y. Effectiveness of Losartan-Loaded Hyaluronic Acid (HA) Micelles for the Reduction of Advanced Hepatic Fibrosis in C3H/HeN Mice Model. *PloS one* **2015**, *10* (12), e0145512. DOI: 10.1371/journal.pone.0145512.

(116) Roggenbuck, D.; Mytilinaiou, M. G.; Lapin, S. V.; Reinhold, D.; Conrad, K. Asialoglycoprotein receptor (ASGPR): a peculiar target of liver-specific autoimmunity. *Auto- immunity highlights* **2012**, *3* (3), 119–125. DOI: 10.1007/s13317-012-0041-4.

(117) Managit, C.; Kawakami, S.; Yamashita, F.; Hashida, M. Effect of galactose density on asialoglycoprotein receptor-mediated uptake of galactosylated liposomes. *Journal of Pharmaceutical Sciences* **2005**, *94* (10), 2266–2275. DOI: 10.1002/jps.20443.

(118) Mandal, A. K.; Das, S.; Basu, M. K.; Chakrabarti, R. N.; Das, N. Hepatoprotective activity of liposomal flavonoid against arsenite-induced liver fibrosis. *The Journal of pharmacology and experimental therapeutics* **2007**, *320* (3), 994–1001. DOI: 10.1124/jpet.106.114215.

(119) Jiang, N.; Zhang, X.; Zheng, X.; Chen, D.; Zhang, Y.; Siu, L. K. S.; Xin, H.-B.; Li, R.; Zhao, H.; Riordan, N.; Ichim, T. E.; Quan, D.; Jevnikar, A. M.; Chen, G.; Min, W. Targeted gene silencing of TLR4 using liposomal nanoparticles for preventing liver ischemia reperfusion injury. *American journal of transplantation : official journal of the American Society of Transplantation and the American Society of Transplant Surgeons* **2011**, *11* (9), 1835–1844. DOI: 10.1111/j.1600-6143.2011.03660.x.

(120) Arima, H.; Yamashita, S.; Mori, Y.; Hayashi, Y.; Motoyama, K.; Hattori, K.; Takeuchi, T.; Jono, H.; Ando, Y.; Hirayama, F.; Uekama, K. In vitro and in vivo gene delivery mediated by Lactosylated dendrimer/alpha-cyclodextrin conjugates (G2) into hepatocytes. *Journal of controlled release : official journal of the Controlled Release Society* **2010**, *146* (1), 106–117. DOI: 10.1016/j.jconrel.2010.05.030.

(121) Motoyama, K.; Mori, Y.; Yamashita, S.; Hayashi, Y.; Jono, H.; Ando, Y.; Hirayama, F.; Uekama, K.; Arima, H. In vitro gene delivery mediated by lactosylated dendrimer (generation 3, G3)/α-cyclodextrin conjugates into hepatocytes. *J Incl Phenom Macrocycl Chem* **2011**, *70* (3-4), 333–338. DOI: 10.1007/s10847-010-9842-0.

(122) Hayashi, Y.; Mori, Y.; Yamashita, S.; Motoyama, K.; Higashi, T.; Jono, H.; Ando, Y.; Arima, H. Potential use of lactosylated dendrimer (G3)/α-cyclodextrin conjugates as hepatocyte-specific siRNA carriers for the treatment of familial amyloidotic polyneuropathy. *Molecular pharmaceutics* **2012**, *9* (6), 1645–1653. DOI: 10.1021/mp200654g.

(123) Wang, H.-X.; Xiong, M.-H.; Wang, Y.-C.; Zhu, J.; Wang, J. N-acetylgalactosamine functionalized mixed micellar nanoparticles for targeted delivery of siRNA to liver. *Journal of controlled release : official journal of the Controlled Release Society* **2013**, *166* (2), 106–114. DOI: 10.1016/j.jconrel.2012.12.017.

(124) Sato, Y.; Matsui, H.; Yamamoto, N.; Sato, R.; Munakata, T.; Kohara, M.; Harashima, H. Highly specific delivery of siRNA to hepatocytes circumvents endothelial cell-mediated lipid nanoparticle-associated toxicity leading to the safe and efficacious decrease in the hepatitis B virus. *Journal of controlled release : official journal of the Controlled Release Society* **2017**, *266*, 216–225. DOI: 10.1016/j.jconrel.2017.09.044.

(125) Jin, H.; Lovell, J. F.; Chen, J.; Lin, Q.; Ding, L.; Ng, K. K.; Pandey, R. K.; Manoharan, M.; Zhang, Z.; Zheng, G. Mechanistic insights into LDL nanoparticle-mediated siRNA delivery. *Bioconjugate chemistry* **2012**, *23* (1), 33–41. DOI: 10.1021/bc200233n.

(126) Yamada, T.; Iwasaki, Y.; Tada, H.; Iwabuki, H.; Chuah, M. K. L.; VandenDriessche, T.; Fukuda, H.; Kondo, A.; Ueda, M.; Seno, M.; Tanizawa, K.; Kuroda, S.'i. Nanoparticles for the delivery of genes and drugs to human hepatocytes. *Nature biotechnology* **2003**, *21* (8), 885–890.

(127) Ohya, Y.; Takeda, S.; Shibata, Y.; Ouchi, T.; Kano, A.; Iwata, T.; Mochizuki, S.; Taniwaki, Y.; Maruyama, A. Evaluation of polyanion-coated biodegradable polymeric micelles as drug delivery vehicles. *Journal of controlled release : official journal of the Controlled Release Society* **2011**, *155* (1), 104–110. DOI: 10.1016/j.jconrel.2010.11.008.

(128) Toriyabe, N.; Hayashi, Y.; Hyodo, M.; Harashima, H. Synthesis and Evaluation of Stearylated Hyaluronic Acid for the Active Delivery of Liposomes to Liver Endothelial Cells. *Biological Pharmacy Bulletin* **2011**, *34* (7), 1084–1089.

(129) Kren, B. T.; Unger, G. M.; Sjeklocha, L.; Trossen, A. A.; Korman, V.; Diethelm-Okita, B. M.; Reding, M. T.; Steer, C. J. Nanocapsule-delivered Sleeping Beauty mediates therapeutic Factor VIII expression in liver sinusoidal endothelial cells of hemophilia A mice. *The Journal of clinical investigation* **2009**, *119* (7), 2086–2099. DOI: 10.1172/JCI34332.

(130) Akhter, A.; Hayashi, Y.; Sakurai, Y.; Ohga, N.; Hida, K.; Harashima, H. A liposomal delivery system that targets liver endothelial cells based on a new peptide motif present in the ApoB-100 sequence. *International journal of pharmaceutics* **2013**, *456* (1), 195–201. DOI: 10.1016/j.ijpharm.2013.07.068.

(131) Akhter, A.; Hayashi, Y.; Sakurai, Y.; Ohga, N.; Hida, K.; Harashima, H. Ligand density at the surface of a nanoparticle and different uptake mechanism: two important factors for successful siRNA delivery to liver endothelial cells. *International journal of pharmaceutics* **2014**, *475* (1-2), 227–237. DOI: 10.1016/j.ijpharm.2014.08.048.

(132) Abel, T.; El Filali, E.; Waern, J.; Schneider, I. C.; Yuan, Q.; Münch, R. C.; Hick, M.; Warnecke, G.; Madrahimov, N.; Kontermann, R. E.; Schüttrumpf, J.; Müller, U. C.; Seppen, J.; Ott, M.; Buchholz, C. J. Specific gene delivery to liver sinusoidal and artery endothelial cells. *Blood* **2013**, *122* (12), 2030–2038. DOI: 10.1182/blood-2012-11-468579.

(133) Tacke, F. Targeting hepatic macrophages to treat liver diseases. *Journal of hepatology* **2017**, *66* (6), 1300–1312. DOI: 10.1016/j.jhep.2017.02.026.

(134) Di Mascolo, D.; J Lyon, C.; Aryal, S.; Ramirez, M. R.; Wang, J.; Candeloro, P.; Guindani, M.; Hsueh, W. A.; Decuzzi, P. Rosiglitazone-loaded nanospheres for modulating macrophage-specific inflammation in obesity. *Journal of controlled release : official journal of the Controlled Release Society* **2013**, *170* (3), 460–468. DOI: 10.1016/j.jconrel.2013.06.012.

(135) Dolina, J. S.; Sung, S.-S. J.; Novobrantseva, T. I.; Nguyen, T. M.; Hahn, Y. S. Lipidoid Nanoparticles Containing PD-L1 siRNA Delivered In Vivo Enter Kupffer Cells and Enhance NK and CD8(+) T Cell-mediated Hepatic Antiviral Immunity. *Molecular therapy. Nucleic acids* **2013**, *2*, e72. DOI: 10.1038/mtna.2012.63.

(136) Melgert, B. N.; Olinga, P.; van der Laan, J. M.; Weert, B.; Cho, J.; Schuppan, D.; Groothuis, G. M.; Meijer, D. K.; Poelstra, K. Targeting dexamethasone to Kupffer cells: effects on liver inflammation and fibrosis in rats. *Hepatology (Baltimore, Md.)* **2001**, *34* (4 Pt 1), 719–728. DOI: 10.1053/jhep.2001.27805.

(137) He, C.; Yin, L.; Tang, C.; Yin, C. Multifunctional polymeric nanoparticles for oral delivery of TNF-α siRNA to macrophages. *Biomaterials* **2013**, *34* (11), 2843–2854. DOI: 10.1016/j.biomaterials.2013.01.033.

(138) Chu, S.; Tang, C.; Yin, C. Effects of mannose density on in vitro and in vivo cellular uptake and RNAi efficiency of polymeric nanoparticles. *Biomaterials* **2015**, *52*, 229–239. DOI: 10.1016/j.biomaterials.2015.02.044.

(139) Jing, F.; Li, J.; Liu, D.; Wang, C.; Sui, Z. Dual ligands modified double targeted nano-system for liver targeted gene delivery. *Pharmaceutical biology* **2013**, *51* (5), 643–649. DOI: 10.3109/13880209.2012.761245.

(140) Falk, E. Pathogenesis of atherosclerosis. *Journal of the American College of Cardiology* **2006**, *47* (8 Suppl), C7-12. DOI: 10.1016/j.jacc.2005.09.068.

(141) Harkness, L. M.; Kanabar, V.; Sharma, H. S.; Westergren-Thorsson, G.; Larsson-Callerfelt, A.-K. Pulmonary vascular changes in asthma and COPD. *Pulmonary pharmacology & therapeutics* **2014**, *29* (2), 144–155. DOI: 10.1016/j.pupt.2014.09.003.

(142) Namdee, K.; Thompson, A. J.; Charoenphol, P.; Eniola-Adefeso, O. Margination propensity of vascular-targeted spheres from blood flow in a microfluidic model of human microvessels. *Langmuir : the ACS journal of surfaces and colloids* **2013**, *29* (8), 2530–2535. DOI: 10.1021/la304746p.

(143) Myerson, J. W.; Braender, B.; Mcpherson, O.; Glassman, P. M.; Kiseleva, R. Y.; Shuvaev, V. V.; Marcos-Contreras, O.; Grady, M. E.; Lee, H.-S.; Greineder, C. F.; Stan, R. V.; Composto, R. J.; Eckmann, D. M.; Muzykantov, V. R. Flexible Nanoparticles Reach Sterically Obscured Endothelial Targets Inaccessible to Rigid Nanoparticles. *Advanced materials (Deerfield Beach, Fla.)* **2018**, *30* (32), e1802373. DOI: 10.1002/adma.201802373.

(144) Müller, K.; Fedosov, D. A.; Gompper, G. Understanding particle margination in blood flow - A step toward optimized drug delivery systems. *Medical engineering & physics* **2016**, *38* (1), 2–10. DOI: 10.1016/j.medengphy.2015.08.009.

(145) Mehrabadi, M.; Ku, D. N.; Aidun, C. K. Effects of shear rate, confinement, and particle parameters on margination in blood flow. *Physical review. E* **2016**, *93* (2), 23109. DOI: 10.1103/PhysRevE.93.023109.

(146) Langer, H. F.; Chavakis, T. Leukocyte-endothelial interactions in inflammation. *Journal of cellular and molecular medicine* **2009**, *13* (7), 1211–1220. DOI: 10.1111/j.1582-4934.2009.00811.x.

(147) Dziubla, T.; Shuvaev, V. V.; Hong, N. K.; Hawkins, B. J.; Muniswamy, M.; Takano, H.; Simone E.; Nakada, M. T.; Fisher, A.; Albelda, S. M.; Muzykantov, V. R. Endothelial Targeting of Semi-permeable Polymer Nanocarriers for Enzyme Therapies. *Biomaterials* **2008**, *29* (2), 215–227.

(148) Han, J.; Shuvaev, V. V.; Davies, P. F.; Eckmann, D. M.; Muro, S.; Muzykantov, V. R. Flow shear stress differentially regulates endothelial uptake of nanocarriers targeted to distinct epitopes of PECAM-1. *Journal of controlled release : official journal of the Controlled Release Society* **2015**, *210*, 39–47. DOI: 10.1016/j.jconrel.2015.05.006.

(149) Han, J.; Zern, B. J.; Shuvaev, V. V.; Davies, P. F.; Muro, S.; Muzykantov, V. Acute and chronic shear stress differently regulate endothelial internalization of nanocarriers targeted to platelet-endothelial cell adhesion molecule-1. *ACS nano* **2012**, *6* (10), 8824–8836. DOI: 10.1021/nn302687n.

(150) Muro, S.; Dziubla, T.; Qiu, W.; Leferovich, J.; Cui, X.; Berk, E.; Muzykantov, V. R. Endothelial targeting of high-affinity multivalent polymer nanocarriers directed to intercellular adhesion molecule 1. *The Journal of pharmacology and experimental therapeutics* **2006**, *317* (3), 1161–1169. DOI: 10.1124/jpet.105.098970.

(151) Zhang, N.; Chittasupho, C.; Duangrat, C.; Siahaan, T. J.; Berkland, C. PLGA nanoparticle--peptide conjugate effectively targets intercellular cell-adhesion molecule-1. *Bioconjugate chemistry* **2008**, *19* (1), 145–152. DOI: 10.1021/bc700227z.

(152) Garnacho, C.; Dhami, R.; Simone, E.; Dziubla, T.; Leferovich, J.; Schuchman, E. H.; Muzykantov, V.; Muro, S. Delivery of acid sphingomyelinase in normal and niemann-pick disease mice using intercellular adhesion molecule-1-targeted polymer nanocarriers. *The Journal of pharmacology and experimental therapeutics* **2008**, *325* (2), 400–408. DOI: 10.1124/jpet.107.133298.

(153) Bhowmick, T.; Berk, E.; Cui, X.; Muzykantov, V. R.; Muro, S. Effect of flow on endothelial endocytosis of nanocarriers targeted to ICAM-1. *Journal of controlled release : official journal of the Controlled Release Society* **2012**, *157* (3), 485–492. DOI: 10.1016/j.jconrel.2011.09.067.

(154) Homem de Bittencourt, P. I.; Lagranha, D. J.; Maslinkiewicz, A.; Senna, S. M.; Tavares, A. M. V.; Baldissera, L. P.; Janner, D. R.; Peralta, J. S.; Bock, P. M.; Gutierrez, L. L. P.; Scola, G.; Heck, T. G.; Krause, M. S.; Cruz, L. A.; Abdalla, D. S. P.; Lagranha, C. J.; Lima, T.; Curi, R. LipoCardium: endothelium-directed cyclopentenone prostaglandin-based liposome formulation that completely reverses atherosclerotic lesions. *Atherosclerosis* **2007**, *193* (2), 245–258. DOI: 10.1016/j.atherosclerosis.2006.08.049.

(155) Calin, M.; Stan, D.; Schlesinger, M.; Simion, V.; Deleanu, M.; Constantinescu, C. A.; Gan, A.-M.; Pirvulescu, M. M.; Butoi, E.; Manduteanu, I.; Bota, M.; Enachescu, M.; Borsig, L.; Bendas, G.; Simionescu, M. VCAM-1 directed target-sensitive liposomes carrying CCR2 antagonists bind to activated endothelium and reduce adhesion and transmigration of monocytes. *European journal of pharmaceutics and biopharmaceutics : official journal of Arbeitsgemeinschaft fur Pharmazeutische Verfahrenstechnik e.V* **2015**, *89*, 18–29. DOI: 10.1016/j.ejpb.2014.11.016.

(156) Papademetriou, I.; Tsinas, Z.; Hsu, J.; Muro, S. Combination-targeting to multiple endothelial cell adhesion molecules modulates binding, endocytosis, and in vivo biodistribution of drug nanocarriers and their therapeutic cargoes. *Journal of controlled release : official journal of the Controlled Release Society* **2014**, *188*, 87–98. DOI: 10.1016/j.jconrel.2014.06.008.

(157) Xu, H.; Kona, S.; Su, L.-C.; Tsai, Y.-T.; Dong, J.-F.; Brilakis, E. S.; Tang, L.; Banerjee, S.; Nguyen, K. T. Multi-ligand poly(L-lactic-co-glycolic acid) nanoparticles inhibit activation of endothelial cells. *Journal of cardiovascular translational research* **2013**, *6* (4), 570–578. DOI: 10.1007/s12265-013-9460-5.

(158) Camaré, C.; Pucelle, M.; Nègre-Salvayre, A.; Salvayre, R. Angiogenesis in the atherosclerotic plaque. *Redox biology* **2017**, *12*, 18–34. DOI: 10.1016/j.redox.2017.01.007.

(159) Winter, P. M.; Neubauer, A. M.; Caruthers, S. D.; Harris, T. D.; Robertson, J. D.; Williams, T. A.; Schmieder, A. H.; Hu, G.; Allen, J. S.; Lacy, E. K.; Zhang, H.; Wickline, S. A.; Lanza, G. M. Endothelial alpha(v)beta3 integrin-targeted fumagillin nanoparticles inhibit angiogenesis in atherosclerosis. *Arteriosclerosis, thrombosis, and vascular biology* **2006**, *26* (9), 2103–2109. DOI: 10.1161/01.ATV.0000235724.11299.76.

(160) Winter, P. M.; Caruthers, S. D.; Zhang, H.; Williams, T. A.; Wickline, S. A.; Lanza, G. M. Antiangiogenic synergism of integrin-targeted fumagillin nanoparticles and atorvastatin in atherosclerosis. *JACC. Cardiovascular imaging* **2008**, *1* (5), 624–634. DOI: 10.1016/j.jcmg.2008.06.003.

(161) Vader, P.; Crielaard, B. J.; van Dommelen, S. M.; van der Meel, R.; Storm, G.; Schiffelers, R. M. Targeted delivery of small interfering RNA to angiogenic endothelial cells with liposome-polycation-DNA particles. *Journal of controlled release : official journal of the Controlled Release Society* **2012**, *160* (2), 211–216. DOI: 10.1016/j.jconrel.2011.09.080.

(162) Moreno, P. R.; Purushothaman, K.-R.; Sirol, M.; Levy, A. P.; Fuster, V. Neovascularization in human atherosclerosis. *Circulation* **2006**, *113* (18), 2245–2252. DOI: 10.1161/CIRCULATIONAHA.105.578955.

(163) Sedding, D. G.; Boyle, E. C.; Demandt, J. A. F.; Sluimer, J. C.; Dutzmann, J.; Haverich, A.; Bauersachs, J. Vasa Vasorum Angiogenesis: Key Player in the Initiation and Progression of Atherosclerosis and Potential Target for the Treatment of Cardiovascular Disease. *Frontiers in immunology* **2018**, *9*, 706. DOI: 10.3389/fimmu.2018.00706.

(164) Nie, S.; Zhang, J.; Martinez-Zaguilan, R.; Sennoune, S.; Hossen, M. N.; Lichtenstein, A. H.; Cao, J.; Meyerrose, G. E.; Paone, R.; Soontrapa, S.; Fan, Z.; Wang, S. Detection of atherosclerotic lesions and intimal macrophages using CD36-targeted nanovesicles. *Journal of controlled release : official journal of the Controlled Release Society* **2015**, *220* (Pt A), 61–70. DOI: 10.1016/j.jconrel.2015.10.004.

(165) Sanchez-Gaytan, B. L.; Fay, F.; Lobatto, M. E.; Tang, J.; Ouimet, M.; Kim, Y.; van der Staay, S. E. M.; van Rijs, S. M.; Priem, B.; Zhang, L.; Fisher, E. A.; Moore, K. J.; Langer, R.; Fayad, Z. A.; Mulder, W. J. M. HDL-mimetic PLGA nanoparticle to target atherosclerosis plaque macrophages. *Bioconjugate chemistry* **2015**, *26* (3), 443–451. DOI: 10.1021/bc500517k.

(166) Duivenvoorden, R.; Tang, J.; Cormode, D. P.; Mieszawska, A. J.; Izquierdo-Garcia, D.; Ozcan, C.; Otten, M. J.; Zaidi, N.; Lobatto, M. E.; van Rijs, S. M.; Priem, B.; Kuan, E. L.; Martel, C.; Hewing, B.; Sager, H.; Nahrendorf, M.; Randolph, G. J.; Stroes, E. S. G.; Fuster, V.; Fisher, E. A.; Fayad, Z. A.; Mulder, W. J. M. A statin-loaded reconstituted high-density lipoprotein nanoparticle inhibits atherosclerotic plaque inflammation. *Nature communications* **2014**, *5*, 3065. DOI: 10.1038/ncomms4065.

(167) Iverson, N. M.; Plourde, N. M.; Sparks, S. M.; Wang, J.; Patel, E. N.; Shah, P. S.; Lewis, D. R.; Zablocki, K. R.; Nackman, G. B.; Uhrich, K. E.; Moghe, P. V. Dual use of amphiphilic macromolecules

as cholesterol efflux triggers and inhibitors of macrophage athero-inflammation. *Biomaterials* **2011**, *32* (32), 8319–8327. DOI: 10.1016/j.biomaterials.2011.07.039.

(168) Lewis, D. R.; Petersen, L. K.; York, A. W.; Zablocki, K. R.; Joseph, L. B.; Kholodovych, V.; Prud'homme, R. K.; Uhrich, K. E.; Moghe, P. V. Sugar-based amphiphilic nanoparticles arrest atherosclerosis in vivo. *Proceedings of the National Academy of Sciences of the United States of America* **2015**, *112* (9), 2693–2698. DOI: 10.1073/pnas.1424594112.

(169) Marrache, S.; Dhar, S. Biodegradable synthetic high-density lipoprotein nanoparticles for atherosclerosis. *Proceedings of the National Academy of Sciences of the United States of America* **2013**, *110* (23), 9445–9450. DOI: 10.1073/pnas.1301929110.

(170) Petersen, L. K.; York, A. W.; Lewis, D. R.; Ahuja, S.; Uhrich, K. E.; Prud'homme, R. K.; Moghe, P. V. Amphiphilic nanoparticles repress macrophage atherogenesis: novel core/shell designs for scavenger receptor targeting and down-regulation. *Molecular pharmaceutics* **2014**, *11* (8), 2815–2824. DOI: 10.1021/mp500188g.

(171) Maeda, H. Toward a full understanding of the EPR effect in primary and metastatic tumors as well as issues related to its heterogeneity. *Advanced Drug Delivery Reviews* **2015**, *91*, 3–6. DOI: 10.1016/j.addr.2015.01.002.

(172) Pridgen, E. M.; Alexis, F.; Farokhzad, O. C. Polymeric nanoparticle drug delivery technologies for oral delivery applications. *Expert opinion on drug delivery* **2015**, *12* (9), 1459–1473. DOI: 10.1517/17425247.2015.1018175.

(173) Reinholz, J.; Landfester, K.; Mailänder, V. The challenges of oral drug delivery via nanocarriers. *Drug Delivery* **2018**, *25* (1), 1694–1705. DOI: 10.1080/10717544.2018.1501119.

(174) Wang, Y.; Zhang, S.; Benoit, D. S. W. Degradable poly(ethylene glycol) (PEG)-based hydrogels for spatiotemporal control of siRNA/nanoparticle delivery. *Journal of controlled release : official journal of the Controlled Release Society* **2018**, *287*, 58–66. DOI: 10.1016/j.jconrel.2018.08.002.

(175) Mauri, E.; Negri, A.; Rebellato, E.; Masi, M.; Perale, G.; Rossi, F. Hydrogel-Nanoparticles Composite System for Controlled Drug Delivery. *Gels (Basel, Switzerland)* **2018**, *4* (3). DOI: 10.3390/gels4030074.

Chapter 2

Goals of the Thesis – How to Profit from Viral Mimicry

The majority of existing pathologies can nowadays be detected more quickly and efficiently with the help of increasingly precise diagnostic tools as well as a constantly growing medical expertise. Additionally, development of highly potent pharmaceutical substances or also vaccines has reached a pace, that seemed unimaginable only a few years ago.[1] Nevertheless, many therapeutic approaches with new drug candidates fail due to an old problem: insufficient distribution to the site of action within the organism. In this regard, drugs oftentimes provide an excellent target efficacy, but do not reach therapy-relevant tissues in sufficient quantities after their application. Treatment with respective substances therefore requires the administration of higher doses, which often leads to side effects or even the discontinuation of therapy due to toxic events. For this handicap of modern drug therapy, already known to Paul Ehrlich, he had a "simple" solution: "...we must learn to aim, learn to aim chemically!".[2]

For him, "chemical aiming" consisted of giving active substances a modified structure that does not impair their efficacy, but at the same time leads to a higher accumulation in the target tissue. In reality, unfortunately, such approaches often fail because it is not possible to optimize both described drug properties independently by merely changing the chemical structure of a molecule. Nanotherapy offers a key to solving this problem. It aims to exchange unfavorable physicochemical properties of a drug for more favorable characteristics of a transport vehicle. To this end, NPs with a typical size of 10 to 100 nm are loaded with potent active ingredients. These drug ferries are designed to deliver the substance in a targeted manner to the intended site of action, which it otherwise cannot reach sufficiently under its own power. The transport thereby ideally leads to an increased concentration at the target tissue, combined with enhanced efficacy and fewer side effects, which is often referred to in the literature as the "targeting effect".[3]

Despite the development of a wide range of such targeting concepts, it has become apparent that nanotherapeutics often show only insufficient final accumulation in the target cells and thus do not offer the hoped-for advantage over a conventional therapy with free drugs.[4] For example, although nanoparticles can often accumulate passively in tissues such as tumors due to the EPR effect, they generally fail in a subsequent selective recognition of their target cells on site. Even the provision of special ligands to bind receptor proteins in the cell membrane often does little to improve the ability of nanotherapeutics to selectively recognize their target cells, as these receptors are usually found on a variety of other cell types as well.

For viruses as natural NPs, on the other hand, cell identification and differentiation pose no problems. Viral particles depend on the selective infiltration of their respective target cells for successful reproduction and therefore, in the course of evolution, have developed a variety of highly efficient mechanisms for specific cell recognition and uptake. The basis of viral cell entry is thereby the ability to recognize several characteristic structures on the cell surface in a precisely "programmed" sequence and use them to overcome the cell membrane barrier.[5]

Unlike human cells, viruses do not possess a metabolism and therefore depend on the infection of a host cell for replication. Viral particles consist of a short sequence of nucleic acids (DNA or RNA) that carry

the viral genetic information and, in most cases, are surrounded by an individually adapted protein envelope. The common goal of all viruses is the rapid replication of this genetic information and the formation of new virus particles. However, the host cell tools required for this are located inside the cell, so that viruses depend on the uptake into the cell for a successful reproduction. At the same time, many viruses are oftentimes specialized on individual cell types due to their transmission and reproduction pathway and therefore additionally rely on a prior recognition of the respective target cell. Numerous viruses therefore use membrane-bound receptor proteins both for cell identification and for internalization by endocytosis. In doing so, they usually harness already existing transport pathways and thus achieve a highly effective cell uptake without provoking possible host cell defense reactions.[6]

For example, the uptake of cholesterol into the cell interior of hepatocytes occurs through attachment to low-density lipoprotein (LDL), which in turn binds to the LDL receptor and is transported into the cell by the latter. The hepatitis C virus uses this transport process, which is essential for the cell, to penetrate hepatocytes by also binding to the LDL receptor with the aid of its specially structured viral envelope. However, as almost all other cells also express this receptor, the virus would be unable to specifically recognize hepatocytes merely by the attachment to this surface structure. In order to still be selectively taken up by the target cell, hepatitis C, like many other viruses, uses the already described concept of "chemical aiming".[7]

It does this by using additional, well-defined chemical structures to sequentially scan the cell surface for the presence of specific receptors or enzymes. In each case, binding to the next structure requires successful binding to a previous structure. The procedure is thereby similar to a cascade of "if-then" decisions used in programming algorithms. In total, the hepatitis C virus binds to at least 4 other membrane-bound receptors before internalization ultimately occurs. To make these sequential logical decisions, the virus "programs" its interface. Strictly defined chemical structures are used by the virus for each of its decisions as to whether the appropriate "chemical lock" for the respective "chemical key" is present on the cell membrane under investigation. Only in case of success, i.e. a logical "yes", the next key is shown.

Viral targeting thus not only means the use of several specific molecular interactions for cell recognition, but at the same time the strict control of their sequence. It presupposes that the chemical makeup of the virus particle's surface enables it to interact with biological interfaces and change its surface structure in a success-dependent manner, thereby making multiple if-then decisions.

Human adenoviruses have a particularly sophisticated form of this recognition and infection principle, which can cause, among other things, mild to moderate respiratory diseases. In a highly selective multistep process, adenoviruses bind various membrane receptors of the cell to be infected and even move along the cell surface together with the already bound receptors (**Figure 1**).[8]
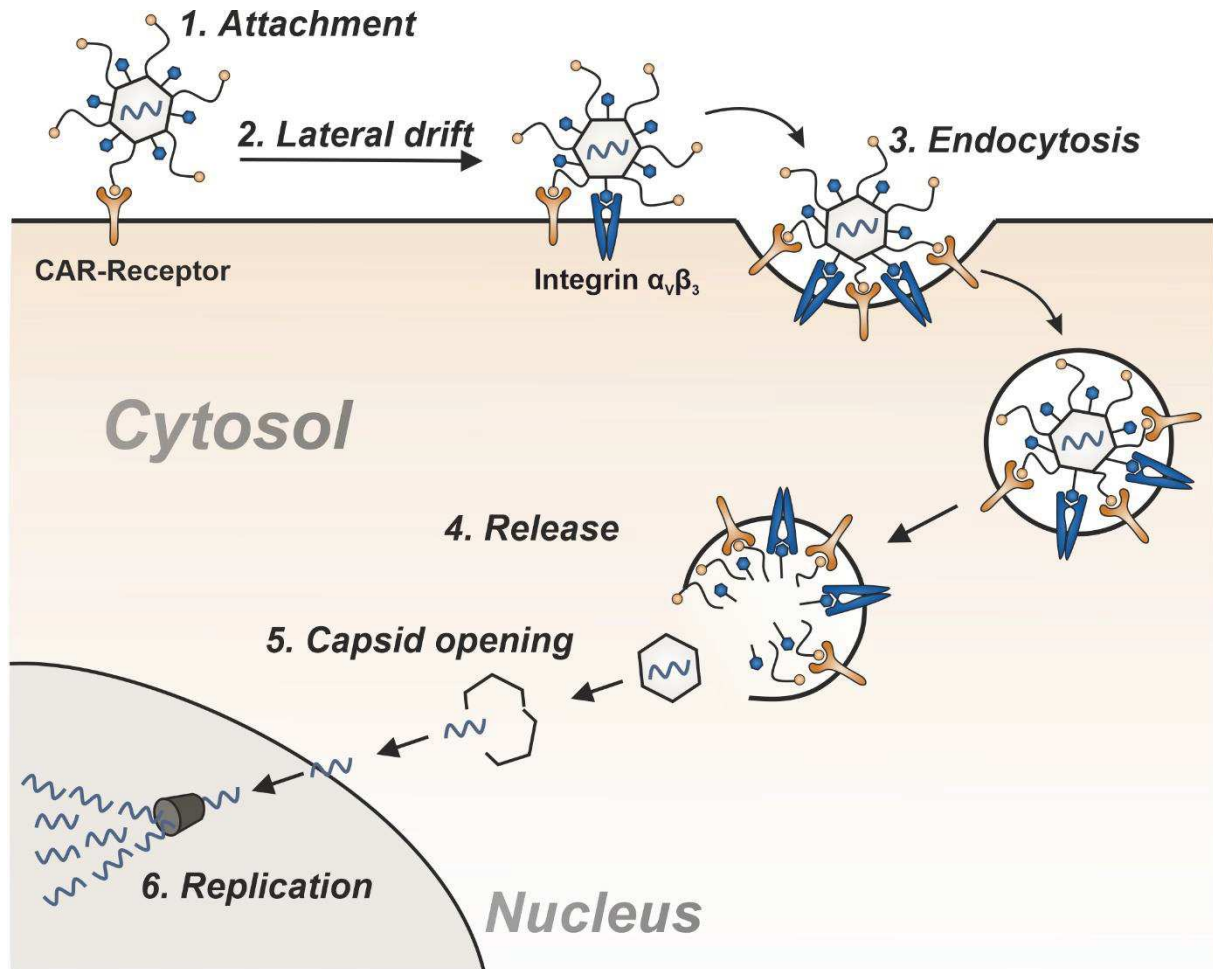
Figure 1. Cell recognition and uptake of human adenovirus type 2 (AdV2). Initially, AdV2 attaches to the membrane-anchored coxsackie and adenovirus receptor (CAR) *via* button-like end linkers of fiber proteins that protrude from the virus capsule (capsid). The "docked" virus then moves laterally along the cell membrane together with the CAR (lateral drift), now presenting a previously shielded protein structure integrated into the viral envelope. Only if this recognition sequence can bind the $\alpha_v\beta_3$-integrin, receptor-mediated endocytosis occurs. As a consequence, the virus is taken up into the cell interior together with the bound receptors in a newly formed endosome. Further virus-induced reactions eventually lead to the rupture of the endosome and the entry of the viral capsid into the cytosol. Finally, the viral capsid opens and releases the previously protected viral genetic information in the form of a linear DNA strand. This DNA is finally introduced into the nucleus of the infected cell, where it is amplified by the cell's own enzymes, ultimately leading to the formation of new virus particles.

Inspired by the highly complex infection strategy of AdV2, the goal of this work was trying to transfer described adenoviral traits to a NP system, which should also be able to identify target cells by means of a programmed sequence of different recognition steps.

The physiological focus of research was thereby in the area of the kidney, where - in the context of a targeted treatment - drug-loaded NPs should reach renal mesangial cells. These play a crucial role in the filtration apparatus of the kidney by maintaining the structure of the vascular tangles (glomeruli) embedded in the mesangium, in which the continuous filtration of blood takes place.[9,10] However, a plethora of diseases such as diabetes can cause severe pathological changes within the complex microarchitecture of these glomeruli, whereby mesangial cells act as a key player in facilitating a pro-fibrotic turnover of various extracellular matrix components as well as interacting with glomerular

endothelial cells and podocytes.[11] Caused by these pathological changes, the kidney progrediently loses its filtrating function, which in the worst case can lead to an irreversible renal failure.[12]

Although a wide range of drugs exist, that would possess a high therapeutic potential in the context of described diseases, they oftentimes do not sufficiently reach mesangial cells due to disadvantageous physicochemical properties or an unfavorable distribution in the organism. Selective treatment of mesangial cells with targeted and drug-loaded nanoparticles could therefore offer a decisive advantage over currently available therapeutic options.[13]

To make this possible, the surfaces of the designed NPs, i.e. the interfaces between the particles and their cellular environment, must be capable of selectively distinguishing mesangial cells from other cells *in vivo*. The nanotherapeutic approach of this work was thereby to create NPs that, like the above-described viral models, scan the surface of potential target cells for relevant recognition structures in order to decide whether or not to induce endocytosis. Therefore, a ligand-mediated strategy of a sequential mesangial cell recognition was established.

The concept is based on an initial binding to angiotensin II receptor type 1 (AT1r), a membrane-bound protein that is increasingly present on the cell membrane of mesangial cells in the course of described renal diseases.[13,14] The NP-cell contact is thereby enabled by AT1r inhibitor EXP3174, which is covalently attached to the particle surface. This allows the particles to bind to the cell membrane *via* the receptor, however without an immediate uptake due to the antagonistic features of the ligand.

For a subsequent mesangial identity verification including final cell endocytosis, the integrin receptor $\alpha_v\beta_3$ already described above for AdV2 infection was selected, as it is also present on the surface of mesangial cells. For integrin recognition, the nanoparticles were therefore equipped with a cyclic amino acid sequence (cRGDfK), whose binding to the $\alpha_v\beta_3$ receptor initiates particle uptake. However, to enable the mandatorily stepwise recognition process, cRGDfK was attached in closer proximity to the particle core, thus spatially shielded and initially not visible for the receptor (steric shielding effect).

The first focus of the project lay in the manufacturing process of a NP species that was equipped with above-described ligands and could actually present them in a sterically controlled manner (**Chapter 3**). In this regard, all necessary polymeric components were initially synthesized to form hetero-multivalent block co-polymer nanoparticles functionalized with EXP3174 as well as cRGDfK. In a next step, the impact of both ligands to bind the AT1r and subsequently induce integrin-mediated endocytosis was assessed. Here, a central aspect lay in the confirmation of a sequential ligand presentation *via* the described steric shielding concept. After testing the mesangial cell specificity of resulting NPs in an *in vitro* co-culture assay with two off-target cell types, the robustness of the NP system to reach mesangial sites was finally assessed in a more realistic *in vivo* setting.

In this regard, it became obvious that the intravascular transport of NPs after a systemic administration also plays a decisive role for the ligand-receptor interaction of NPs, the above-described shielding concept as well as an unfavorable off-target deposition in vascular endothelial cells. Therefore, an *in vitro* system of endothelial cell culture and subsequent NP incubation under more realistic dynamic flow

conditions was implemented to study the impact on the described virus-mimetic approach (**Chapter 4**). In this context, NPs with varying compositions of cRGDfK targeting and shielding elements were manufactured and analyzed regarding their interaction with endothelial cells under different flow conditions.

Finally, the successfully tested adenovirus-mimetic NP system was loaded with cinaciguat (CCG), an activator of the soluble guanylate cyclase (sGC), which had previously shown great potential in the therapy of renal pathologies such as diabetic nephropathy (**Chapter 5**).[15,16] Therefore the optimal parameters for an efficient and reproducible encapsulation process were initially determined. It was then tested whether resulting NPs still provided the necessary mesangial targeting features and drug-loaded NPs were subsequently analyzed for their capacity to potentiate the pharmacological effect of encapsulated CCG *via* a drug delivery effect. Finally, a TGF-β induced fibrosis model was implemented, and the anti-fibrotic potential of the NP system was assessed.

References

(1) Polack, F. P.; Thomas, S. J.; Kitchin, N.; Absalon, J.; Gurtman, A.; Lockhart, S.; Perez, J. L.; Pérez Marc, G.; Moreira, E. D.; Zerbini, C.; Bailey, R.; Swanson, K. A.; Roychoudhury, S.; Koury, K.; Li, P.; Kalina, W. V.; Cooper, D.; Frenck, R. W.; Hammitt, L. L.; Türeci, Ö.; Nell, H.; Schaefer, A.; Ünal, S.; Tresnan, D. B.; Mather, S.; Dormitzer, P. R.; Şahin, U.; Jansen, K. U.; Gruber, W. C. Safety and Efficacy of the BNT162b2 mRNA Covid-19 Vaccine. *The New England journal of medicine* **2020**, *383* (27), 2603–2615. DOI: 10.1056/NEJMoa2034577. Published Online: Dec. 10, 2020.

(2) Strebhardt, K.; Ullrich, A. Paul Ehrlich's magic bullet concept: 100 years of progress. *Nature reviews. Cancer* **2008**, *8*, 473–480.

(3) Blanco, E.; Shen, H.; Ferrari, M. Principles of Nanoparticle Design for Overcoming Biological Barriers to Drug Delivery. *Nat. Biotechnol.* **2015**, *33* (9), 941–951. DOI: 10.1038/nbt.3330.

(4) Wilhelm, S.; Tavares, A. J.; Dai, Q.; Ohta, S.; Audet, J.; Dvorak, H. F.; Chan, W. C. W. Analysis of Nanoparticle Delivery to Tumours. *Nature Reviews Materials* **2016**, *1* (5), 16014. DOI: 10.1038/natrevmats.2016.14.

(5) Marsh, M.; Helenius, A. Virus Entry:Open Sesame. *Cell* **2006**, *124* (4), 729–740. DOI: 10.1016/j.cell.2006.02.007.

(6) Grove, J.; Marsh, M. The Cell Biology of Receptor-Mediated Virus Entry. *J. Cell Biol.* **2011**, *195* (7), 1071–1082. DOI: 10.1083/jcb.201108131.

(7) Ploss, A.; Evans, M. J. Hepatitis C Virus Host Cell Entry. *Curr. Opin. Virol.* **2012**, *2* (1), 14–19. DOI: 10.1016/j.coviro.2011.12.007.

(8) Luisoni, S.; Greber, U. F. Biology of Adenovirus Cell Entry. In *Adenoviral Vectors for Gene Therapy*; pp 27–58. DOI: 10.1016/B978-0-12-800276-6.00002-4.

(9) Schlöndorff, D.; Banas, B. The Mesangial Cell Revisited:No Cell Is an Island. *J. Am. Soc. Nephrol.* **2009**, *20* (6), 1179–1187. DOI: 10.1681/ASN.2008050549.

(10) Scott, R. P.; Quaggin, S. E. The Cell Biology of Renal Filtration. *J. Cell Biol.* **2015**, *209* (2), 199–210. DOI: 10.1083/jcb.201410017.

(11) Dronavalli, S.; Duka, I.; Bakris, G. L. The pathogenesis of diabetic nephropathy. *Nature clinical practice. Endocrinology & metabolism* **2008**, *4* (8), 444–452. DOI: 10.1038/ncpendmet0894.

(12) Webster, A. C.; Nagler, E. V.; Morton, R. L.; Masson, P. Chronic Kidney Disease. *The Lancet* **2017**, *389* (10075), 1238–1252. DOI: 10.1016/S0140-6736(16)32064-5.

(13) Scindia, Y. M.; Deshmukh, U. S.; Bagavant, H. Mesangial Pathology in Glomerular Disease:Targets for Therapeutic Intervention. *Adv. Drug Delivery Rev.* **2010**, *62* (14), 1337–1343. DOI: 10.1016/j.addr.2010.08.011.

(14) Miura, S.-i.; Karnik, S. S.; Saku, K. Review:Angiotensin II Type 1 Receptor Blockers: Class Effects Versus Molecular Effects. *J. Renin Angiotensin Aldosterone Syst.* **2011**, *12* (1), 1–7. DOI: 10.1177/1470320310370852.

(15) Czirok, S.; Fang, L.; Radovits, T.; Szabó, G.; Szénási, G.; Rosivall, L.; Merkely, B.; Kökény, G. Cinaciguat ameliorates glomerular damage by reducing ERK1/2 activity and TGF-ß expression in type-1 diabetic rats. *Scientific reports* **2017**, *7* (1), 11218. DOI: 10.1038/s41598-017-10125-3.

(16) Beyer, C.; Zenzmaier, C.; Palumbo-Zerr, K.; Mancuso, R.; Distler, A.; Dees, C.; Zerr, P.; Huang, J.; Maier, C.; Pachowsky, M. L.; Friebe, A.; Sandner, P.; Distler, O.; Schett, G.; Berger, P.; Distler, J. H. W. Stimulation of the soluble guanylate cyclase (sGC) inhibits fibrosis by blocking non-canonical TGFβ signalling. *Annals of the rheumatic diseases* **2015**, *74* (7), 1408–1416. DOI: 10.1136/annrheumdis-2013-204508.

Chapter 3

Adenovirus-Mimetic Nanoparticles: Sequential Ligand-Receptor Interplay as a Universal Tool for Enhanced *In Vitro/In Vivo* Cell Identification

Abstract

Viral infection patterns often rely on precisely coordinated sequences of distinct ligand-receptor interactions, leading in many cases to an outstanding target cell specificity. A successful mimicry of viral targeting strategies to create more site-specific nanoparticles (NPs) would therefore require particle-cell interactions to also be adequately controllable. In the present study, hetero-multivalent block-copolymer NPs present their attached ligands in a sterically controlled manner to create a sequential NP-cell interaction similar to the cell infiltration strategy of human adenovirus type 2.Targeting renal mesangial cells, particles thereby initially bind angiotensin II receptor type 1 (AT1r) on the cell surface *via* a structurally flexible AT1r antagonist. After a mandatory spatial approach, particle-endocytosis is realized *via* binding of immobile $\alpha_V\beta_3$ integrins with a previously concealed secondary ligand, thereby creating a stepwise particle-cell interplay of primary NP attachment and subsequent uptake.Manufactured adenovirus mimetic NPs show great avidity for both target motifs *in vitro*, leading to a substantial binding as well as subsequent cell uptake into target mesangial cells. Additionally, steric shielding of secondary ligand visibility leads to a highly controllable, sequential ligand-receptor interaction, whereby hetero-functional NPs activate mesangial cell surface integrins only after a successful prior binding to the AT1r. This stepwise cell identification significantly enhances mesangial cell specificity in co-culture assays with different off-target cells. Additionally, described NPs display excellent *in vivo* robustness by efficiently accumulating in the mesangium upon injection, thereby opening new paths for possible drug delivery applications.

1   Introduction

Nanomaterials for biomedical applications suffer in many cases from poor availability at the intended site of action.[1–3] A paradigm shift in material design can help to overcome poor target cell specificity, which has been identified as one of the main impediments for successful targeting.[4,5] In this context, viruses can serve as a valuable template since they are endowed with the paramount ability to distinguish between off-target and target cells.[6–8] For a successful transfer of this target specificity to novel nanoparticulate approaches, it is crucial to investigate the underlying structural characteristics of viruses and integrate them into the process of nanoparticle (NP) development. As most viral particles comprise of a multitude of targeting elements, equipping NPs with more than one targeting ligand as well could thereby be a *via*ble option. However, most viral cell recognition strategies show a considerable level of complexity with a highly orchestrated sequence of consecutive binding events to a multitude of cell surface structures.[9–12] Taking this into consideration, virus-mimetic nanomaterials should ideally also comprise targeting elements, whose course of interaction with their target structures is adequately controllable.[13,14] While many approaches using multi-ligand NP systems already exist[15–17], our focus lay not only on the manufacture of NPs with two different ligands, but the precise steerability of ligand-receptor interactions, which, in our view, is crucial for the described viral target specificity.

In that context, we recently presented influenza A mimetic NPs, that were enzymatically activated by a target cell ectoenzyme, thereby unveiling an additional ligand that triggered particle endocytosis *via* contact with its cell membrane receptor. This conditional and sequential target-cell recognition process led to a highly specific cell uptake *in vitro*, even in the presence of a 10-fold surplus of off-target cells.[18] In a follow-up study, we refined these enzymatically activated NPs to reach mesangial cells *in vivo*.[19]

The mesangium was selected as target with respect to its prominent role within the glomerulus as well as in the development of diabetic nephropathy and other related kidney diseases.[20–23] In this context, NPs accumulating in mesangial cells could possibly offer a starting point for a more rational therapy compared to the currently predominant gold standard, which is mainly based on control of blood pressure and glucose levels.[24] Even though the influenza A mimetic concept resulted in an excellent NP accumulation in the mesangium, its underlying principle mandatorily requires the presence of an ectoenzyme on the cell of interest and thus, is not broadly applicable to cells and tissues lacking respective enzymes.

Trying to overcome this major constraint, we were looking for a more versatile mechanism of endowing hetero-multivalent NPs with the ability to sequentially bind a multitude of distinct cell surface structures. In that context, we decided to mimic human adenovirus type 2 (AdV2) as a biological model. In order to infiltrate possible target cells, AdV2 initially binds to the coxsackievirus and adenovirus receptor (CAR) *via* its terminal fiber knobs.[25–27] The laterally flexible virus-receptor complex then performs drifting motions alongside the cell membrane until it binds immobile integrins *via* its penton base RGD motif that finally triggers clathrin-mediated endocytosis.[28] We were particularly interested in the

adenoviral infiltration strategy, as the initial virus-cell interactions do not involve any processing or enzymatic conversion of the virus, as it would be the case for above described influenza viruses or also SARS-CoV-2.[29] Additionally, the primary CAR binding does not initiate any endocytotic mechanisms, but merely facilitates attachment to the cellular surface. To our estimation, this sequential process of primary attachment and subsequent uptake is highly promising to further increase target specificity of nanomaterials. Trying to integrate this stepwise process into a robust NP system, the starting point of our considerations was, that the visibility of ligands tethered to a NP surface can be readily controlled by altering the ligand density, the linker length as well as the physical composition of the NP surface.[19,30] We therefore hypothesized, that the intended stepwise particle-cell interaction could be achieved by sterically controlling the ligand-receptor binding events. To facilitate initial attachment to the cellular surface, we decided to use EXP3174, a losartan metabolite and potent blocker of the angiotensin II receptor type 1 (AT1r), which is known to be significantly upregulated in mesangial cells during various kidney pathologies such as diabetic nephropathy.[22,31] Due to its antagonistic features, EXP3174 should merely facilitate initial NP binding to AT1r, yet without immediate induction of uptake.[32] Based on the above described adenoviral cell infiltration, cRGDfK (cyclo Arg-Gly-Asp-D-Phe-Lys), a well-established $\alpha_V\beta_3$ integrin agonist, was chosen to initiate integrin-mediated particle uptake of previously bound NPs.[33–35]

To enable primary AT1r binding, EXP3174 was tethered to longer block-copolymer chains, leading to the desired flexibility and consequently high availability of the AT1r antagonist. cRGDfK, in contrast, was bound to shorter block-copolymer strands and therefore only able to reach $\alpha_V\beta_3$ integrins after a mandatory first AT1r binding and subsequent spatial approach of the NP to the cell membrane (**Figure 1**). This shielding of the second ligand should not only lead to described sequential particle-cell interaction, but also prevent premature exposition to integrin-positive off-target sites such as angiogenic endothelial cells or macrophages.[36]

To investigate the feasibility of this recognition strategy, we used the same poly(ethylene glycol)-poly(lactic acid) (PEG-PLA) block-copolymer NP design and same target tissue as for our influenza A mimetic concept. By doing so, we excluded any impact of unspecific factors such as differences in geometry or surface composition on the results.[37–39]

In the present study, we first evaluated the validity of our targeting strategy *in vitro*, using mesangial cell mono-cultures, as well as co-cultures that additionally comprised a major fraction of off-target cells. In a follow-up *in vivo* experiment, adenovirus mimetic NPs were then tested for efficient accumulation in mesangial areas within the glomerulus (**Figure S1**), which should act not only as an adequate benchmark to compare our previous and new targeting concept but also as a prerequisite for a future NP-based treatment of mesangial cells.
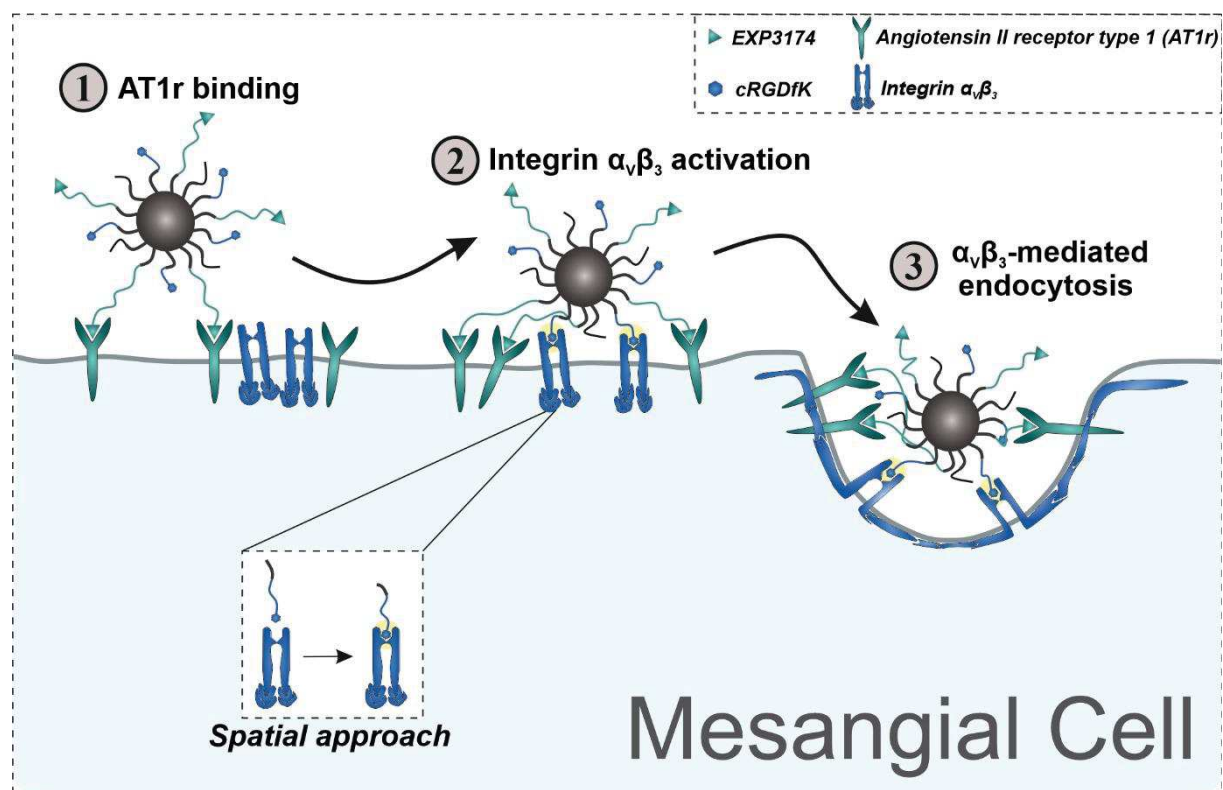
Figure 1. Adenovirus mimetic NPs enter glomerular mesangial cells *via* a sterically controlled and thus sequential particle-cell interaction. NPs thereby initially bind the AT1r *via* EXP3174. After a subsequent spatial approach of the NP, $\alpha_V\beta_3$ integrin-mediated endocytosis is finally triggered *via* previously concealed cRGDfK.

2 Materials and Methods

2.1 Materials

Heterobifunctional hydroxyl poly(ethylene glycol)carboxylic acid with a molecular mass of 2000 and 5000 g mol^{-1} (COOH-PEG$_{2k/5k}$-OH) and hydroxyl poly(ethylene glycol)Boc-amine with a molecular mass of 2000 g mol^{-1} (Boc-NH-PEG$_{2k}$-OH) were purchased from Jenkem Technology USA Inc. (Allen, TX, USA) while methoxy poly(ethylene glycol)with a molecular mass of 5000 g mol^{-1} (MeO-PEG$_{5k}$-OH) and Resomer RG 502 (PLGA, lactide:glycolide 50:50; molecular mass 13,400 g mol^{-1}) were obtained from Sigma-Aldrich (Taufkirchen, Germany). EXP3174 (also known as losartan carboxylic acid) was purchased from Santa Cruz (Heidelberg, Germany), while cyclic RGDfK (cRGDfK) was obtained from Synpeptide Co. Ltd. (Shanghai, China). AlexaFluor^{TM} 568 Hydrazide (Alexa568), CellTracker^{TM} Green Dye (CTG) and CellTracker^{TM} Deep Red Dye (CTDR) were purchased from Fisher Scientific GmbH (Schwerte, Germany).

Amine-functionalized spherical gold NPs with an average diameter of 2.2 nm (Au$_{2.2}$-NH$_2$) were obtained from Nanopartz Inc. (Loveland, CO, USA). GoldEnhance^{TM} EM Plus kit was purchased from Nanoprobes (Yaphank, NY, USA). Goat-derived Integrin α-8 antibody was obtained from R&D Systems (Minneapolis, MN, USA). All other chemicals were purchased from Sigma-Aldrich in analytical grade if not stated differently. Ultrapure water was obtained from a Milli-Q water purification system (Millipore, Billerica, MA, USA).

Rat-derived mesangial cells (rMCs) were a kind gift from Prof. Dr. Armin Kurtz (Institute of Physiology, University of Regensburg, Regensburg, Germany). NCI-H295R (CRL-2128) and HeLa (CCL-2) cells were purchased from ATCC (Manassas, VA, USA). All cell lines were cultured in RPMI 1640 medium containing 10 % fetal bovine serum, Insulin-Transferrin-Selenium (ITS) (1x) and 100 nM hydrocortisone. AT1r-YFP rMCs were generated by transfecting rMCs with a plasmid encoding the AT1r with a YFP-tag (CXN2-HA-AT1R-YFP), using Lipofectamine 2000 according to manufacturer´s instructions and as previously described.[19] For culture of AT1r-YFP rMCs, RPMI1640 medium was additionally supplemented with geneticin (600 µg mL^{-1}).

2.2 Polymer synthesis

COOH-PEG$_{2k}$-PLA$_{10k}$, Boc-NH-PEG$_{5k}$-PLA$_{10k}$ and MeO-PEG$_{5k}$-PLA$_{10k}$ block copolymers were synthesized *via* a ring-opening polymerization as previously described.[37,40] In brief, heterobifunctional PEG polymers (1 equivalent = equiv) were mixed with 3,6-dimethyl-1,4-dioxane-2,5-dione (70 equiv) and 1,8-diazabicylo [5.4.0] undec-7-ene (3 equiv). The polymer mixture was stirred for 1 hour (h) at room temperature (RT) until polymerization was quenched with benzoic acid (14 equiv). Resulting block-copolymer was precipitated in diethyl ether, isolated *via* filtration and dried under vacuum.

Molecular weight of synthesized polymers was determined in deuterated chloroform at 295 K using a Bruker Avance 300 spectrometer (Bruker BioSpin GmbH, Rheinstetten, Germany).

For preparation of cRGDfK-PEG$_{2k}$-PLA polymers, previously synthesized COOH-PEG$_{2k}$-PLA$_{10k}$ was covalently coupled to the lysine residue of cRGDfK as shown before.[30,41] In short, COOH-PEG$_{2k}$-PLA$_{10k}$ (1 equiv) was activated using 3-(ethyliminomethyleneamino)-N,N-dimethylpropan-1-amine (EDC)/ N-hydroxysuccinimide (NHS) (25 equiv) for 2 h at RT, followed by quenching with β-mercaptoethanol (BME) (30 equiv). Activated polymer was reacted with cRGDfK (3 equiv) and N,N-diisopropylethylamine (DIPEA) (10 equiv) for 24 h at RT. After precipitation of resulting cRGDfK-coupled polymer in diethyl ether/methanol (15:1 v/v), free cRGDfK and excess reactants were removed using dialysis against Millipore water (mpH$_2$O).

For EXP3174-PEG$_{5k}$-PLA$_{10k}$, the Boc-protecting group of Boc-NH-PEG$_{5k}$-PLA$_{10k}$ was initially cleaved. In brief, Boc-protected polymer was dissolved in dichloromethane (DCM)/trifluoroacetic acid (TFA) (1:1 v/v). After stirring for 30 min (min), excess TFA was neutralized using a saturated sodium hydrogen carbonate solution. The organic phase was washed with mpH$_2$O, followed by polymer isolation as described above.

Resulting NH$_2$-PEG$_{5k}$-PLA$_{10k}$ was coupled to EXP3174 *via* the carboxylic acid residue of the imidazole component. EXP3174 (3.5 equiv) was activated with N,N'-dicyclohexylcarbodiimide (DCC)/NHS (3.3 equiv) for 2 h at RT. After removal of resulting dicyclohexylurea *via* centrifugation, NH$_2$-PEG$_{5k}$-PLA$_{10k}$ (1 equiv) and DIPEA (17.5 equiv) were added and reacted for 24 h at RT. Resulting EXP3174-PEG$_{5k}$-PLA$_{10k}$ was precipitated in methanol/diethyl ether (1:5 v/v) and the product was dialyzed against ethanol/100mM borate buffer pH 8.5/water (1/1/8 v/v) for 24 h followed by mpH$_2$O for 12 h to remove unreacted EXP3174 and excess reactants.

2.3   PLGA labeling with fluorescent dyes

For particle visualization, the core forming PLGA was covalently linked to fluorescent dyes prior to NP preparation. To that end, carboxylic acid-terminated PLGA was activated for 2 h using 4-(4,6-dimethoxy-1,3,5-triazin-2-yl)-4-methylmorpholinium chloride (DMTMM) as a catalytical agent. Activated PLGA was then reacted either with AlexaFluor^{TM}568 Hydrazide or CF^{TM} 647 amine for 24 h at RT. Labeled PLGA was dialyzed against mpH$_2$O for 24 h to remove unreacted fluorescent dyes.

2.4   PLGA labeling with nanogold

For electron microscopy analysis, PLGA was conjugated to nanogold according to a method that was previously established by our group.[42] PLGA was initially activated with EDC and NHS for 2 h in DCM. After DCM removal under reduced pressure, activated PLGA was dissolved in DMSO and mixed with DIPEA and lyophilized monoamino gold NPs with an average diameter of 2.2 nm (Au$_{2.2}$-NH$_2$). After stirring at RT for 24 h, gold-conjugated PLGA was precipitated in mpH$_2$O, isolated *via* centrifugation at 2500g for 10 min and lyophilized.

2.5   NP preparation

Block-copolymer NPs were manufactured using a common solvent evaporation technique. Corresponding amounts of PEG-PLA polymers and PLGA were mixed at a ratio of 70/30 (m/m) and diluted in acetonitrile (ACN) to a final concentration of 10 mg mL^{-1}. To reach the desired ligand surface density for hetero-/homo-functional NP species, cRGDfK-PEG$_{2k}$-PLA and/or EXP3174-PEG$_{5k}$-PLA$_{10k}$ were mixed with COOH-PEG$_{2k}$-PLA$_{10k}$ according to the calibration depicted in Figure S2 g/h. The organic phase was then added dropwise to vigorously stirring 10 % Dulbecco's Phosphate-Buffered Saline (DPBS) (v/v) (7.5 mM, pH 7.4) and stirred for 3 h at RT to remove the organic solvent. Resulting NP dispersions were concentrated *via* centrifugation at 1250g for 25 min using Pall Microsep filters (molecular weight cut-off 30 kDa; Pall Corporation, NY, USA). To obtain the mass concentration of manufactured NPs, a method previously introduced by our working group was used.[30] In brief, PEG content was assessed using a colorimetric iodine complexing assay.[43] NPs were then lyophilized and gravimetrically analyzed to obtain the ratio of PEG content and NP weight. In the following experiments, this ratio was used to calculate mass concentration from the assessed PEG content for each NP species. The molar NP concentration was calculated as described before[19], taking into account the NP mass concentration, an estimated NP density of 1.25 g cm^{-3} [44] as well as the NP diameter assessed by dynamic light scattering measurements, assuming a spherical NP shape.

2.6   NP characterization

NP size and zeta potential was evaluated using a Malvern Zetasizer Nano ZS (Malvern, Herrenberg, Germany). Samples were measured with a 633 nm He-Ne laser at an angle of 173° (25 °C, RT) in 7.5 mM DPBS, using either PMAA semimicro cuvettes (DLS; Brand, Wertheim, Germany) or folded capillary cells (zeta potential; Malvern, Herrenberg, Germany), respectively. For stability analysis, NPs were prepared as described above and incubated for 24 h at 37°C in DPBS as well as RPMI 1640 medium containing 10 % fetal bovine serum. At the displayed time points, a sample was taken, and the size was evaluated as described above.

2.7   cRGDfK quantification

The level of cRGDfK on the NP surface was assessed using a previously described method that is based on the measurement of arginine.[35] In brief, 50 μL of NP samples (1 mg mL^{-1}) were mixed with 175 μL of a working solution consisting of 9,10-phenanthrenequinone (150 μM in ethanol) and 2 N NaOH (6:1 v/v). After 3 h of incubation at 60 °C, 1 equiv of sample was mixed with 1 equiv of 1 N HCl and incubated for another 1 h at RT. Finally, fluorescence was measured at a Synergy™ Neo2 Multi-Mode Microplate Reader (BioTek Instrument Inc., Winooski, VT, USA) with an excitation wavelength of 312/7 nm and an emission wavelength of 395/7 nm. Dilutions of cRGDfK (0-40 μg mL^{-1}) served as

calibration. cRGDfK molarity as well as the ratio of molar cRGDfK content and molar PEG content were determined and plotted against the theoretical value (Figure S2h).

2.8   EXP3174 quantification

To determine the surface level of EXP3174 on manufactured particles, 1 equiv of NP samples (1 mg mL^{-1}) was mixed with 10 equiv of 0.2 M acetic acid. Dilutions of EXP3174 in 0.2 M acetic acid (0-30 µM) served as calibration. Fluorescence of samples and standards was measured at a Synergy™ Neo2 Multi-Mode Microplate Reader (see above) (excitation 250/ 10 nm, emission 370/5 nm). EXP3174 molarity as well as the ratio of molar EXP3174 content and molar PEG content was determined and plotted against the theoretical value (Figure S2g).

2.9   Calcium mobilization assay

In order to investigate AT1r binding of NPs, intracellular calcium levels were measured using fura-2 as a Ca^{2+} chelator as previously described by our working group.[45] In brief, rMCs were incubated with 5 µM fura-2AM, 2.5 mM probenecid and 0.05 % Pluronics F-127 in Leibovitz′s L-15 medium for 1 h at RT. Cells were thereafter centrifuged (5 min, 200g, RT) and resuspended in Leibovitz′s medium. 45 µL of NPs or free EXP3174 at different concentrations were pipetted into 96-well plates (Greiner Bio One, Frickenhausen, Germany), followed by 45 µL of rMC suspension (2 x 10^6 cells mL^{-1}). In the following, cells were incubated with samples for 45 min at RT. After incubation, 10 µL of 30 nM AT II was added to each well to activate uninhibited AT1r and consequently induce Ca^{2+} influx into the cell cytosol. Fluorescence signal during the first 30 seconds after injection was measured using a FluoStar Omega fluorescence microplate reader (BMG Labtech, Ortenberg, Germany) with excitation filters at 340/20 nm and 380/20 nm and the emission filter at 510/20 nm, respectively. Maximal ratio of Ca^{2+} - bound to Ca^{2+} - unbound Fura-2 was evaluated by incubating loaded cells with 0.1 % Triton-X 100 and measuring fluorescence levels as described above. Analogously, minimal ratio was achieved by incubation with 0.1 % Triton-X 100 combined with 45 mM ethylene glycol-bis(2-aminoethylether)-N,N,N′,N′-tetraacetic acid (EGTA). Levels of intracellular calcium per sample was calculated using the equation of Grynkiewicz et al.[46] Half maximal inhibitory concentrations (IC$_{50}$) were calculated using GraphPad Prism (San Diego, CA, USA) and applying a sigmoidal dose-response equation (variable slope).

2.10   CLSM analysis

For a detailed analysis of NP-cell interaction, either rMCs or AT1r-YFP rMCs were seeded into 8-well slides (Ibidi, Gräfelfing, Germany) at a density of 15,000 cells well^{-1} and incubated for 24 h at 37 °C. In order to facilitate visualization of the cell cytosol, cells were stained with CTDR (25 µM, 45 min, 37 °C) in serum-free RPMI 1640 medium prior to seeding. NPs were manufactured using AlexaFluor™ 568-labeled PLGA and adjusted to 0.05 mg mL^{-1} in Leibovitz`s buffer supplemented with 0.1 % bovine

serum albumine (BSA). Mesangial cells were incubated with 250 µL of NPs for 15, 45 and 90 min at 37 °C, washed with prewarmed DPBS and fixed with 4 % paraformaldehyde (PFA) in DPBS for 10 min. AT1r-YFP rMCs were additionally stained for cell nuclei with a 1:200 dilution of 4′,6-Diamidine-2′-phenylindole dihydrochloride (DAPI) in DPBS. After a final washing step, fixed samples were analyzed using a Zeiss LSM 710 (Carl Zeiss Microscopy GmbH, Jena, Germany).

2.11   Flow cytometry

To assess mesangial cell association of NP samples, rMCs were seeded into 24-well plates (Greiner Bio One, Frickenhausen, Germany) at a density of 40,000 cells well^{-1} and incubated for 48 h at 37 °C. NPs were manufactured using CF^{TM} 647-labeled PLGA and adjusted to 0.05 mg NP mL^{-1} in Leibovitz´s buffer supplemented with 0.1 % BSA. To confirm $\alpha_V\beta_3$-dependence of NP cell entry, 300 µL of free cRGDfK (c = 500 µM) were added to the relevant cell samples for 15 min prior to NP incubation. Cells were washed with DPBS and 300 µL of prewarmed NP solutions were added for 45 min at 37 °C. For respective analysis of time-dependent uptake, cells were incubated over a time period of 120 min with NPs being removed after 0, 15, 30, 45, 60, 90 and 120 min. Cells were washed with DPBS, trypsinized and centrifuged for 5 min at 200g and 4 °C, followed by two further washing and centrifugation steps (DPBS, 200g, 5 min, 4 °C). Final samples were resuspended in DPBS and analyzed using a FACS Calibur cytometer (Becton Dickinson, Franklin Lakes, NJ, USA). NP-associated fluorescence was excited at 633 nm and corresponding emission was recorded (661/16 bandpass filter). Flow cytometry data was analyzed using Flowing software 2.5.1 (Turku Centre for Biotechnology, Turku, Finland). Within the population of *via*ble cells, geometric mean of cell-associated fluorescence was evaluated.

2.12   Transmission electron microscopy

To evaluate the cellular localization of NPs, rMCs were seeded into a 24-well plate at a density of 12,000 cells well^{-1} and incubated for 72 h. NP formulations containing nanogold-conjugated PLGA were diluted in Leibovitz`s buffer containing 0.1 % BSA and added for 45 min at a concentration of 0.05 mg mL^{-1} (V = 300 µL). After incubation, samples were washed with DPBS and prepared for electron microscopy analysis according to a pre-established protocol of our working group.[42] In brief, cells were fixed with 2.5 % PFA and 2.5 % glutaraldehyde in a 0.1 M sodium cacodylate solution (Caco buffer) for 60 min at RT, washed with Caco buffer and permeabilized with 0.1% Triton-X in DPBS for 10 min. After a washing step with mpH$_2$O, samples were gold enhanced using a GoldEnhance^{TM} EM Plus kit (Nanoprobes Inc., Yaphank, NY, USA) according to the manufacturer´s specifications, followed by further washing and post-fixation in a 2.5 % sodium thiosulfate solution in mpH$_2$O. Cells were stained with 0.5 % osmium tetroxide and dehydrated in rising concentrations of ethanol (50 – 99.5 %). For counterstaining, 2 % uranylacetate was applied for 5 min at 70 % ethanol concentration. After embedding in Epon, ultrathin sections of 150 nm were imaged using a 100 kV Zeiss Libra 120 electron microscope (Carl Zeiss NTS GmbH, Oberkochen, Germany) at a magnification of 6300x as well as

12,500x. For exact analysis of the NP size without gold-tag, EXPcRGD NPs were manufactured in mpH$_2$O as described above and adjusted to 50 µg mL^{-1}. Samples were thereafter pipetted onto carbon-coated copper grids (300 mesh; Plano, Wetzlar, Germany) and incubated for 2 min. Excess NPs were removed with a filter paper, the grids were negatively stained with 1 % uranyl acetate solution and stored in a desiccator until TEM analysis.

2.13   Co-culture experiments

In order to assess cell specificity of manufactured NPs, we used a co-culture design that had been previously implemented by our group.[18] For mono-culture NP uptake (Figure 6b), pre-seeded rMCs, NCI-H295-R or HeLa cells were incubated for 45 min with different CF^{TM} 647-labeled NP types. Cell uptake was then assessed using flow cytometry as described above.

For co-culture analysis, rMCs were seeded together with HeLa or NCI-H295R cells in 24-well plates at a density of 10,000 and 50,000/100,000 cells well^{-1} respectively and incubated for 48 h at 37 °C. To differentiate between cell types, rMCs were stained with CTG (15 µM, 45 min, 37 °C) in serum-free RPMI 1640 medium prior to seeding.

Co-cultured cells were then incubated with CF^{TM}647-labeled NPs at a concentration of 0.05 mg mL^{-1} (V = 300 µL) for 45 min. Preparation of samples and flow cytometry analysis was performed as described above. Additionally, rMC-associated fluorescence was excited at 488 nm and recorded using a 530/30 bandpass filter. During data analysis, the population of *via*ble cells was further gated for stained rMC cells and NP-associated fluorescence analyzed concerning cell specificity.

For CLSM analysis, rMC cells were CTG-stained prior to seeding as described above. To visualize all cell types, HeLa or NCI-H295R cells were also stained using CTDR (25 µM, 45 min, 37 °C). After CellTracker^{TM} incubation, rMCs were seeded into 8-well Ibidi slides together with HeLa/NCI-H295R cells at a density of 2000 and 10,000/20,000 cells well^{-1}. After 48 h of incubation at 37 °C, cell nuclei were stained with Hoechst 33258 (5 µg mL^{-1} in DPBS) for 20 min. Cells were washed twice with prewarmed DPBS and AlexaFluor^{TM}568-labeled NPs were added at a concentration of 0.05 mg mL^{-1} (V = 250 µL) for 45 min at 37 °C. After NP incubation, samples were treated as described above and analyzed using a Zeiss LSM 710 microscope.

2.14   In vivo cell targeting

Animal experiments were performed according to the national and institutional guidelines and were approved by the local authority (Regierung von Unterfranken, reference number: 55.2-2532-2-329). Female, 10-week-old NMRI mice (Charles River, Sulzfeld, Germany) acted as model animals. After analgesia with buprenorphine (0.1 mg kg body weight^{-1}), mice were anaesthetized with isoflurane and 100 µL of CF^{TM} 647-labeled NPs (c = 120 nM) were injected *via* the vena jugularis (n = 6 for each NP species). Additionally, 100 µL of the free CF^{TM} 647 dye were injected at a comparable concentration

(50 μM). Mice were kept in anesthesia and after 5 min, an initial blood sample was taken *via* i.v. puncture. After 60 min, mice were anaesthetized with ketamine/xylazine, a final blood sample was taken, and animals were killed *via* perfusion fixation. Both kidneys were removed and immediately transferred to a solution of 18 % sucrose and 1 % PFA in phosphate buffer (0.1 M pH 7.4). After 6 h, kidneys were washed with DPBS and cryoprotected at -80 °C until further processing. For cryosections, the organs were embedded in Tissue Tek® O.C.T.™ Compound (Sakura Finetek, Torrance, CA, USA), cut into 5 μm sections using a CryoStar NX70 cryotome (Thermo Fisher Scientific, Waltham, MA, USA) and fixed on Superfrost™ plus glass slides (Thermo Fisher Scientific, Schwerte, Germany).

For analysis of NP kidney deposition and glomerular fluorescence quantification, sections were rinsed in DPBS and blocked with 5 % BSA supplemented with 0.04 % Triton-X in DPBS for 10 min at RT. After further rinsing in DPBS, samples were stained for cell nuclei with a 1:400 dilution of DAPI in 0.5 % BSA and 0.04 % Triton-X in DPBS. After a final washing step in DPBS and mpH$_2$O respectively, cryosections were mounted with Mowiol mounting medium and analyzed at a Zeiss Axiovert 200M.

For image analysis, Fiji software (Madison, WI, USA) was used. Glomerular fluorescence intensities were evaluated by measuring the integrated density of areas over a certain fluorescence threshold and division by the respective glomerular area.

In order to assess the exact cellular location of NPs, kidney cryosections were prepared as described above. After washing and blocking of sections, samples were stained overnight at 4 °C with a goat-derived integrin α-8 antibody (1:200 dilution in 0.5 % BSA/0.04 % Triton-X in DPBS). Samples were thereafter washed with DPBS and stained with a 1:400 dilution of Cy2® donkey anti-goat and DAPI in 0.5 % BSA/0.04 % Triton-X in DPBS for 1h at RT. After a final washing step, samples were mounted and analyzed at a Zeiss LSM 710.

3   Results and Discussion

3.1   Preparation of hetero-multivalent EXPcRGD NPs using a modular concept

In order to create NPs with the desired adenovirus mimetic properties, we implemented a modular design that is based on the synergistic combination of different biocompatible polymer components into a hetero-multivalent particle species (**Figure 2a**). Thereby, biodegradable poly(lactic-coglycolic acid) (PLGA) forms a hydrophobic NP core that not only guarantees enhanced structural integrity in aqueous media but also allows NP visualization *via* coupling of fluorescent dyes or nanogold.[42,47] PEG-PLA block copolymers as second component offer the structural flexibility that is needed in order to implement our pursued virus-mimetic NP design.[48] In a first step, PEG-PLA polymers with either longer (PEG_{5k}-PLA_{10k}) or shorter (PEG_{2k}-PLA_{10k}) PEG chains were synthesized *via* ring-opening polymerization of cyclic lactide (**Figure S2a** and **Figures S3-S6**).[40]

Since EXP3174 was intended to initially bind the mesangial AT1r as a freely moving ligand, it was covalently coupled to the longer and thus more flexible PEG_{5k}-PLA_{10k} chains (**Figure S2b**). The second ligand (cRGDfK), in contrast, should not be able to interact with surface-bound integrins unless a first AT1r binding and subsequent spatial approach of the NP has taken place. To that regard, it was attached to shorter PEG_{2k}-PLA_{10k} (**Figure S2c**). NP surface density of both cRGDfK and EXP3174 could be tuned precisely by mixing distinct amounts of either ligand-functionalized or non-functionalized PEG-PLA polymers with PLGA prior to NP manufacture *via* nanoprecipitation (**Figure S2f-h**).

Hetero-functional EXPcRGD NPs as well as homo-functional (EXP NPs/cRGD NPs) and non-functionalized, methoxy-terminated particles (Control NPs) were manufactured below a size threshold of 60 nm (**Figure 2b**). To our estimation, this size range was optimal for efficient extravasation from intraglomerular capillaries to reach mesangial areas, as endothelial fenestrations have an average diameter of 60 - 100 nm.[49,50] Stability analysis in DPBS and cell culture medium (**Figure 2d/e**) as well as transmission electron microscopy (TEM) (**Figure S2i**) showed uniformly shaped NPs with no considerable tendency towards aggregation. Addition of unfunctionalized COOH-PEG_{2k}-PLA_{10k} to the polymer mix resulted in negative zeta potential values (**Figure 2c**). These characteristics should help to further stabilize NPs and reduce unspecific binding to off-target cells. Also, extended serum protein adsorption and subsequent phagocytic clearance should be prevented.[37,51]
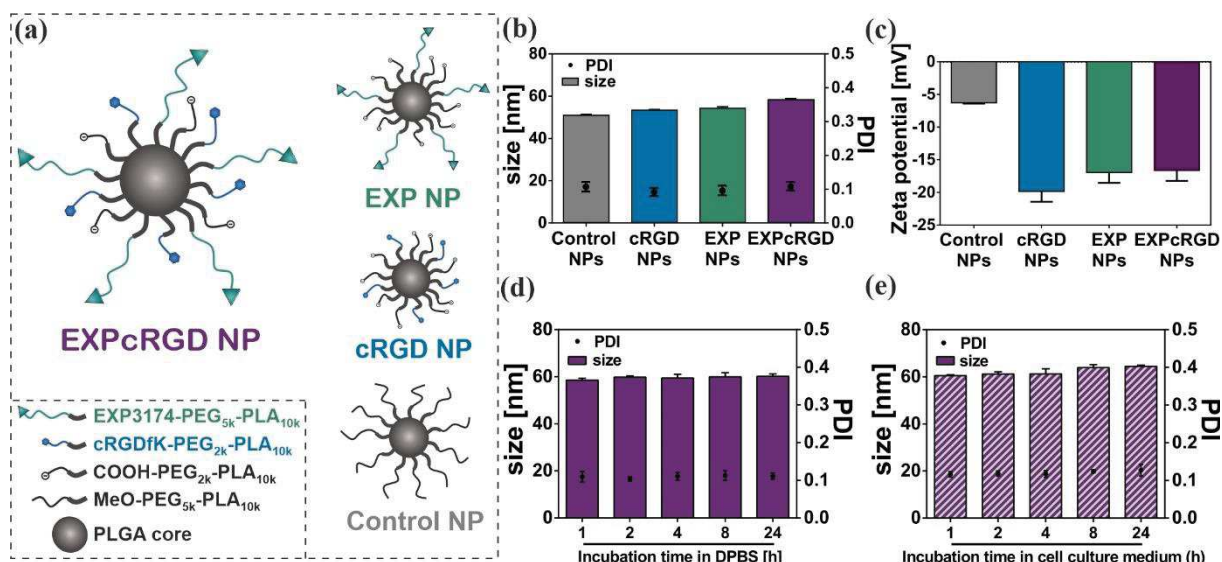
Figure 2. Characterization of different NP species. **(a)** Particle design of hetero-functional EXPcRGD NPs as well as homo-functional (EXP NPs and cRGD NPs) or non-functionalized NP species (Control NPs). **(b)** Dynamic light scattering (DLS) analysis. All particle types were manufactured below a size threshold of 60 nm without considerable aggregation. (PDI: polydispersity index.) **(c)** Zeta potential measurements. **(d)/(e)** NP stability analyzed through DLS measurements. EXPcRGD NPs underwent no significant size variation or aggregation upon incubation for 24 h at 37 °C in either **(d)** DPBS or **(e)** cell culture medium supplemented with 10 % fetal bovine serum. Results represent mean ± SD (n = 3).

3.2 Hetero-multivalent EXPcRGD NPs display excellent ligand affinity for target motifs

While it has been previously demonstrated that homo-functional EXP3174- or cRGDfK-carrying NPs can be used to effectively target cell types expressing either AT1r or $\alpha_V\beta_3$[52,53], we intended to prove, that the merger of both ligands actually results in a hetero-multivalent nanomaterial that synergistically combines both ligands' features. We therefore initially evaluated the optimal surface density for each ligand to guarantee sufficient AT1r/integrin interaction. In a first step, we prepared homo-functional NPs with different ligand densities and performed DLS analysis to exclude any impact of the size-differences on the later NP-cell interaction. As shown in **Figure S7a/b**, particle size and quality was thereby not significantly altered by the respective ligand density for both cRGD NPs and EXP NPs. We then assessed EXP3174-mediated NP binding to the AT1r expressed by rat mesangial cells (rMCs). As activation of G_q-coupled AT1r with its primary ligand angiotensin II (AT II) results in a calcium influx into the cell cytosol, intracellular Ca^{2+} levels after AT II stimulation can be used as a marker for AT1r activity after NP incubation. Thereby, low receptor activity indicates a high ratio of bound EXP3174, as the ligand itself acts as a potent antagonist.[31]

Figure 3a shows intracellular Ca^{2+} levels of AT II-stimulated rMCs that had been pre-incubated with EXP3174-functionalized NPs or free EXP3174 for 45 min. Particles thereby carried 25 % of EXP3174 on their surface, as this functionalization degree had been shown to sufficiently guarantee AT1r binding (**Figure S7c**). Both EXPcRGD NPs (**IC_{50} = 276 ± 31 pM**) and EXP NPs (**IC_{50} = 552 ± 73 pM**) showed excellent AT1r avidity, resulting in a highly effective inhibition of the receptor in the picomolar range

and consequent minimal intracytosolic Ca^{2+} levels. Furthermore, inhibition potency of EXP3174-carrying NP types was even higher than for the free ligand (**$IC_{50} = 2.7 \pm 0.9$ nM**). This strongly suggests, that EXP3174-functionalized particles were able to interact with the target receptor in a multivalent fashion, leading to an overall avidity gain, which was in line with our previous findings.[45] As IC_{50} levels of both EXPcRGD and EXP NPs were found to be in the same range, we concluded that the combination of both EXP3174 and cRGDfK in one particle type did not significantly interfere with the binding capacity of EXP3174 itself. Interestingly, AT1r inhibition potency was thereby even slightly higher for EXPcRGD NPs than for homo-functional EXP NPs. To our estimation, this effect was caused by the complete and irreversible removal of AT1 receptors from the cell surface due to the cRGDfK-mediated endocytosis of AT1r-bound NPs (Figure 1). Consequently, endocytosed receptors could no longer be (re)activated, leading to a sharper decrease in Ca^{2+} influx upon AT II stimulation. Control NPs and cRGD NPs did not show any interaction with the AT1r, resulting in a maximal Ca^{2+} signal upon receptor stimulation and confirming the assay´s specificity for the AT1r (**Figure S7d**). Additionally, intracellular Ca^{2+} levels of AT1r-deficient HeLa cells were minimal upon EXPcRGD NP incubation and AT II stimulation, thereby further supporting the AT1r binding specificity of EXPcRGD NPs (**Figure S7e**). Having verified the AT1r binding capacity of adenovirus mimetic EXPcRGD NPs, our next goal was to investigate particle uptake into rMCs *via* cRGDfK-$\alpha_V\beta_3$ interaction. As for EXP3174, we therefore initially evaluated the optimal cRGDfK ligand density for sufficient integrin-mediated NP endocytosis. As depicted in **Figure S7f**, cRGDfK-mediated rMC uptake of cRGD NPs thereby gradually increased with higher ligand surface densities. In a next step, we introduced 25 % of longer $COOH\text{-}PEG_{5k}\text{-}PLA_{10k}$ into these cRGDfK-functionalized NPs. This component should enable the above described concept of steric hindrance and result in a reduced visibility of the cRGDfK ligand (**Figure S8**), which was central for our approach of a sequential ligand-receptor interplay. As shown in **Figure S7g**, ligand-mediated endocytosis could thereby significantly be reduced for all cRGDfK densities, that we had tested before (Figure S7f). For the further course of our studies, we chose to prepare both cRGD NPs and EXPcRGD NPs with a cRGDfK density of merely 15 %, as this amount guaranteed a significantly enhanced ligand-mediated rMC uptake, but could also be sufficiently regulated by addition of respective shielding elements. As shown in **Figure 3b**, we finally compared levels of rMC uptake for the established NP compositions. As discussed above, cell uptake of cRGDfK-functionalized NPs could thereby be significantly reduced by addition of described shielding elements. Interestingly, addition of an excess of free cRGDfK (c = 500 µM) prior to NP incubation led to a comparable decrease in cell uptake of unshielded cRGD NPs, thereby both proving $\alpha_V\beta_3$-dependency of NP uptake and supporting the hypothesis, that our shielding concept can equally inhibit ligand-integrin interaction. Remarkably, addition of $EXP\text{-}PEG_{5k}\text{-}PLA_{10k}$ instead of unfunctionalized $COOH\text{-}PEG_{5k}\text{-}PLA_{10k}$ (EXPcRGD NPs) reversed the shielding effect and significantly increased rMC uptake. We therefore concluded, that hetero-functional EXPcRGD NPs initially bound the AT1r and subsequently were able to spatially approach the cell surface, thereby reaching the endocytosis-mediating integrin. This assessment was

further supported by the observation, that addition of free EXP3174 (c = 1 mM) prior to NP incubation lead to a sharp decrease of EXPcRGD NP cell uptake, as NPs were no longer able to bind the AT1r and approach the rMC surface. To additionally confirm our concept of a sequential ligand-receptor interplay, we compared the decrease of AT1r activity of rMCs due to EXP3174-mediated NP binding with the cRGDfK-mediated cell uptake of hetero-functional EXPcRGD NPs. As shown in **Figure 3c**, AT1r activity thereby sharply decreased within the first 45 min and subsequently stayed on a minimal level. NP uptake, on the contrary, gradually increased with cell-associated fluorescence levels increasing even further after 45 min. This contrary time course further proved our assumption, that hetero-functional NPs initially bound the AT1r and only then initiated cell uptake *via* integrin activation. Interestingly, AT1r activity slightly increased again at 120 min, which we explained with a possible AT1r recycling after completed uptake with bound NPs.
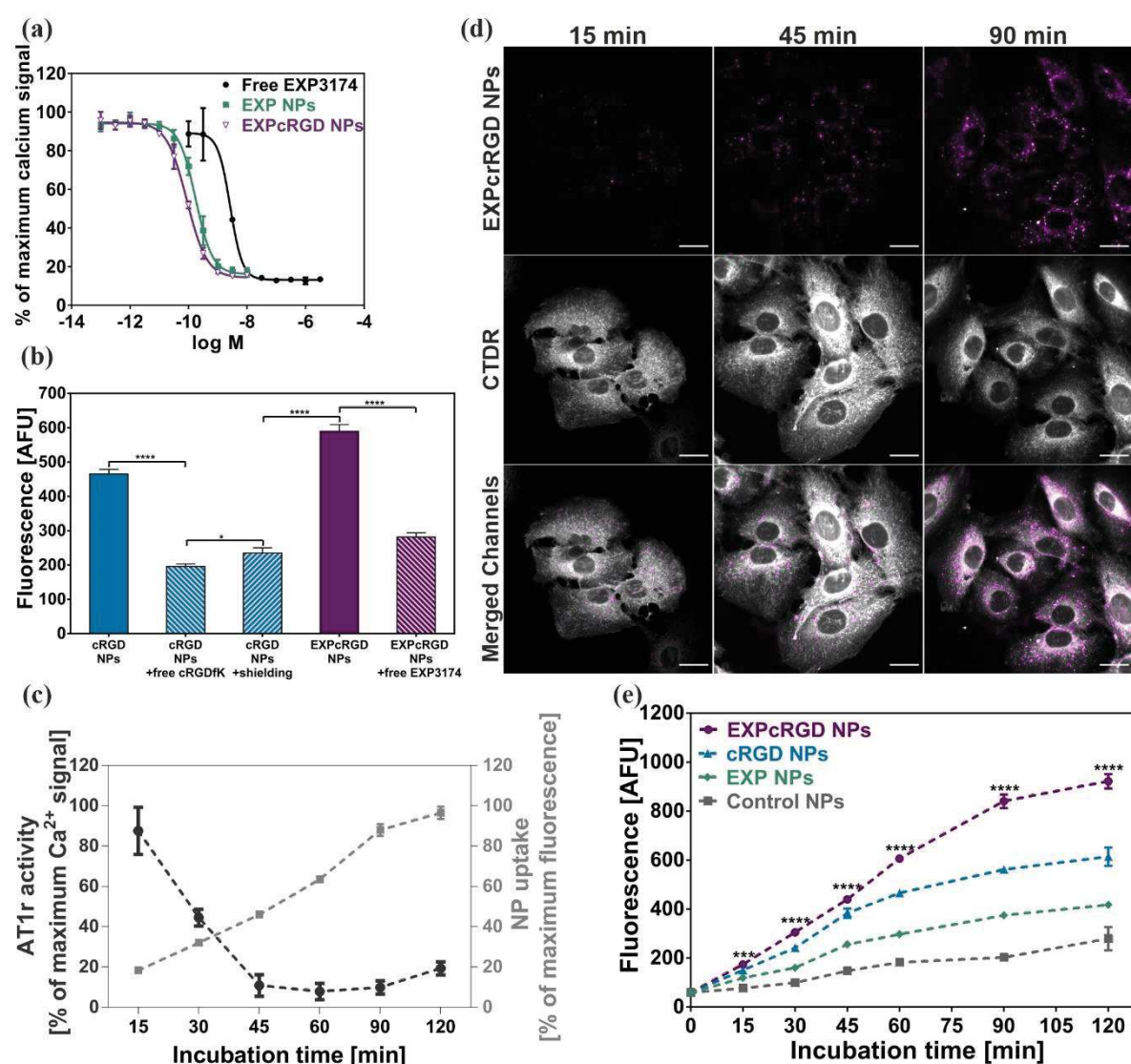
Figure 3. NP interaction with target motifs. **(a)** Intracellular calcium levels after AT1r stimulation of rMCs treated with free or particle-bound EXP3174. Both EXPcRGD NPs (**IC$_{50}$ = 276 ± 31 pM**) and EXP NPs (**IC$_{50}$ = 552 ± 73 pM**) effectively bound and thereby inhibited the AT1r. This effect was even stronger than for free EXP3174 (**IC$_{50}$ = 2.7 ± 0.9 nM**. (M = molar concentration of either NPs or free EXP3174.) **(b)** Flow cytometry analysis of rMC uptake for cRGD-carrying NPs. **(c)** Sequential NP-cell interplay. EXPcRGD NPs initially bound to the AT1r,

leading to a drastic decline in AT1r activity *via* EXP3174 receptor blockade. In contrast, $\alpha_V\beta_3$-initiated NP uptake increased mainly after 45 min. **(d)** CLSM analysis of CTDR-stained rMCs after incubation with EXPcRGD NPs. Over time, increasing levels of NP-associated fluorescence (purple) could be detected in vesicular structures within the rMC cytosol (grey). (Scale bar 20 µm.) **(e)** Flow cytometry analysis of NP uptake into rMCs over 120 min. Hetero-multivalent EXPcRGD NPs showed a substantially increased cell-uptake compared to Control NPs as well as homo-functional NPs. Results represent mean ± SD (*n* = 3).* P < 0.05, *** P < 0.001, **** P < 0.0001. **(**AFU, arbitrary fluorescence units.)

For a better visualization of the time-dependent NP uptake, mesangial cells were incubated with fluorescently labeled NPs and the cellular distribution was analyzed *via* confocal laser scanning microscopy (CLSM). To exactly assess the dimensions of the cell body, rMCs were pre-treated with CellTracker[TM] Deep Red (CTDR). **Figure 3d** shows strong intracellular accumulation of AlexaFluor[TM]568-labeled EXPcRGD NPs in spherical structures, that represent endocytotic vesicles.[54] Over time, both the number and intensity of visible accumulations increased. Especially between 45 and 90 min of incubation, vesicles appeared to considerably gain size. These findings demonstrate, that after successful AT1r binding, EXPcRGD NPs could efficiently bind to the integrin receptor, triggering internalization through integrin-mediated endocytosis and accumulation in intracellular vesicles. It is well described in literature, that these endocytic vesicles can fuse to larger endosomes and therefore gain size as well as intensity over time.[55,56] Finally, we performed flow cytometry analysis of NP-treated rMCs and determined the cell-associated fluorescence over an incubation period of 120 min. As shown in **Figure 3e**, levels of NP-derived fluorescence were highest for EXPcRGD NPs compared to all other NP species over the entire incubation period. While EXP NPs as well as Control NPs merely showed moderate fluorescence signals, substantial levels of cell-association could be detected for cRGD NPs. However, respective fluorescence levels reached a plateau after approximately 60 min, while EXPcRGD NPs´ cell-association further increased. This strongly supports our hypothesis of a sequential interaction between EXPcRGD NPs and their target cell which results in a prolonged increase in fluorescence levels compared to homo-functional cRGD NPs.

3.3   Ultrastructural analysis indicates sequential ligand-receptor interplay

To further verify the concept of sequential AT1r binding and integrin-mediated NP endocytosis, we performed time-dependent CLSM analysis of NP interaction with rMCs expressing the AT1r tagged with yellow fluorescence protein (AT1r-YFP rMCs). **Figure 4a** thereby shows a significant accumulation of EXPcRGD NPs in intracellular vesicles over time, which was similar to the results depicted in Figure 3d. Additionally, AT1r-derived fluorescence considerably increased and intensified in also mainly spherical structures. While cRGD NPs showed a comparable intracellular accumulation with increasing incubation times (**Figure 4b**), no considerably enhanced AT1r signal could be detected. For a better visualization of observed differences, we assessed the exact localization of both NP-associated and AT1r fluorescence after 45 min of incubation. As depicted in **Figure 4c**, signals for EXPcRGD NPs and the AT1r were thereby exactly colocalized, indicating, that these hetero-functional

NPs had initially bound the AT1r and only then initiated integrin-mediated endocytosis, leading to an uptake of both EXPcRGD NPs and bound AT1r into spherical endocytotic vesicles (Figure 1). Homo-functional cRGD NPs, on the contrary, merely bound the integrin and thereby initiated cell uptake, however without any interaction with the AT1r, whose fluorescence signal accordingly was not colocalized to a significant extent (**Figure 4d**). As a control, we additionally analyzed NP-cell interaction for cRGDfK-lacking EXP NPs and Control NPs (**Figure S9**).

While Control NPs did not show any significant rMC uptake or changes in AT1r signal over time (Figure S9b), considerable EXP NP-derived fluorescence was visible, however mainly located on the cell surface. This NP-associated fluorescence was colocalized with AT1r clusters, that had formed as a consequence of non-internalized, AT1r-bound NPs lacking additional cRGDfK functionalization (Figure S9a).
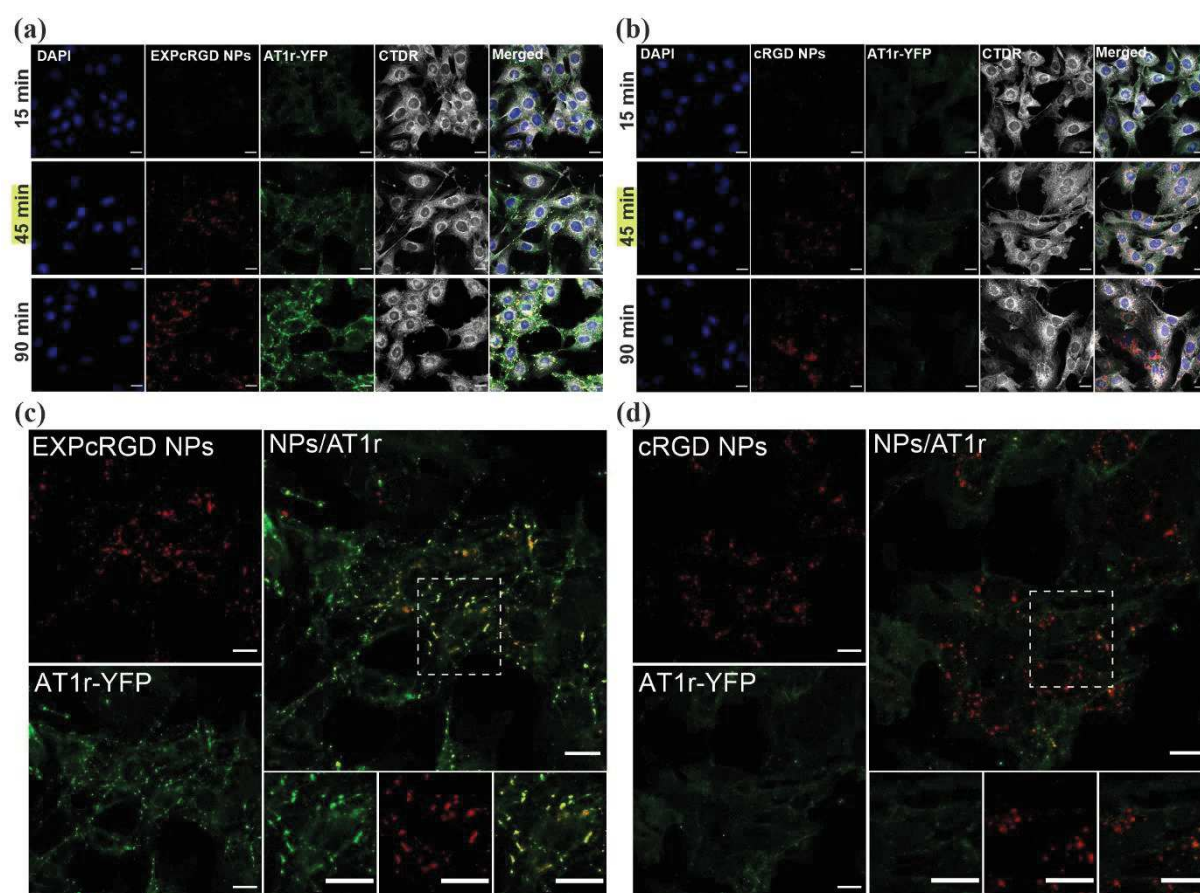
Figure 4. CLSM analysis of NP uptake (red) in rMCs (grey) transfected with YFP-tagged AT1r (green). **(a)** Time-dependent uptake of EXPcRGD NPs. Signals for both EXPcRGD NPs and AT1r-YFP significantly increased with longer incubation times. Fluorescence thereby intensified in mainly spherical structures, indicating AT1r clustering and subsequent NP/AT1r endocytosis. **(b)** Time-dependent uptake of cRGD NPs. While cRGD NP-associated fluorescence increased similarly to (a), no considerable change in AT1r-YFP signal could be detected. **(c)** EXPcRGD NP /AT1r localization after 45 min. Fluorescence signals for EXPcRGD NPs and the AT1r were exactly colocalized (yellow merged regions), proving NP-AT1r binding and subsequent endocytosis. **(d)** cRGD NP/AT1r localization after 45 min. cRGD NP-associated fluorescence showed no considerable colocalization with the AT1r signal, indicating an AT1r-independent uptake of NPs. (Scale bar 20 μm. Smaller images show zoomed-in view of the white boxes above.)

Finally, TEM analysis was performed to assess NP-cell interactions at an ultrastructural level.[57–59] Thereby, we used a NP labeling concept that we had recently established. In order to increase electron density and consequential TEM visibility of applied NPs, ultrasmall gold NPs with an average diameter of 2.2 nm were covalently coupled to PLGA which was then used for further NP manufacture (**Figure S10a**). Mesangial cells, that were incubated with these gold-tagged NPs, could then be gold-enhanced in order to intensify and thus visualize the particles´ gold core and assess their exact location. This retrospective gold-enhancement offers the substantial advantage that physicochemical characteristics of nanogold-labeled NPs do not significantly differ from unlabeled NPs (**Figure S10b**), which would not be the case for commonly used larger gold NPs.

Figure 5a shows the cell body of two mesangial cells incubated with gold-tagged EXPcRGD NPs. Within the cell cytosol, numerous circular vesicles, filled with gold-enhanced NPs, could be detected. The distribution pattern showed remarkable similarity to the previously described CLSM results (Figures 3c/4), thereby strongly supporting our hypothesis of ligand-mediated NP endocytosis. Additionally, a major fraction of particles was present at the cell border, indicating that these NPs were still bound to membrane-located surface structures that most likely represent AT1r clusters. These findings further indicate that EXPcRGD NPs interacted with the target cell in a stepwise process of prior binding to the AT1r and subsequent integrin-mediated endocytosis.

In accordance with this assessment, EXP NPs lacking the cRGDfK ligand could only be detected at the rMC membrane while no significant particle accumulations in endocytotic vesicles were found (**Figure 5b**). Additionally, cell-particle association for Control NPs was only marginal (**Figure 5c**), which was also in line with our previous findings. cRGD NPs, in contrast, did accumulate in the rMC cytosol similar to EXPcRGD NPs, but showed only marginal binding to the cell surface, as these particles lacked AT1r ligand EXP3174 (**Figure S11a**). Particle-free cells were treated and prepared equally, to demonstrate that the gold enhancement did not lead to unspecific staining (**Figure S11b**).
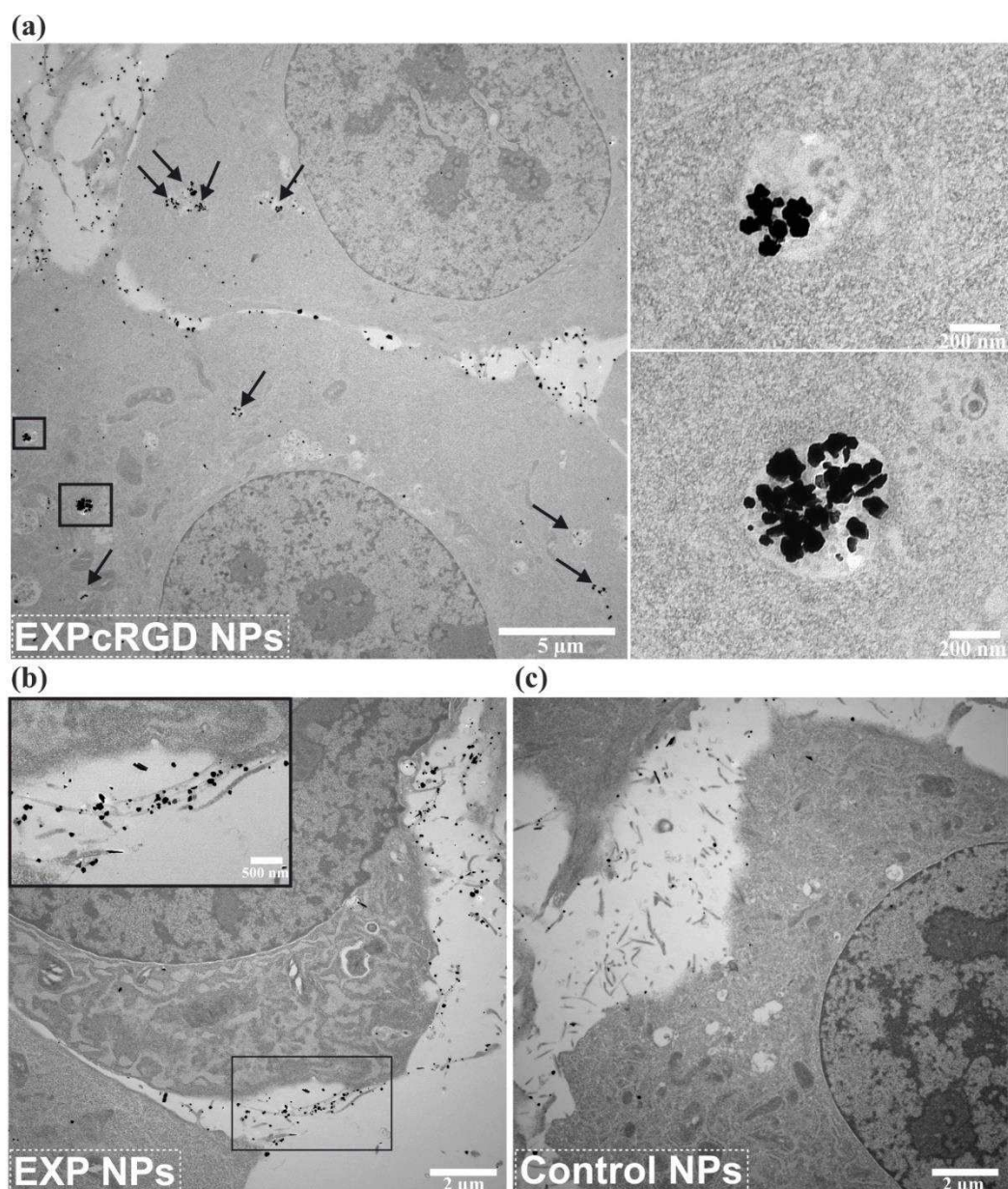
Figure 5. TEM analysis of NP interaction with mesangial cells. **(a)** EXPcRGD NPs accumulated in numerous vesicular structures (black arrows) within rMCs. Vesicles of differing sizes were present both in outer and inner parts of the cell cytosol, indicating intracellular processing and fusing into larger endosomes. Moreover, a substantial number of NPs was still located at the cell membrane, suggesting that particle underwent a stepwise process of initial cell binding and subsequent endocytosis. (Images on the right show zoomed-in view of black boxes on the left.) **(b)** EXP NPs, in contrast, merely accumulated at the cell border where they bound to distinct surface structures of rMCs, indicating a possible interaction with membrane-bound AT1r. (Image in top left corner shows zoomed-in view of black box.) **(c)** Control NPs showed only negligible interaction with rMCs with hardly any gold-enhanced NPs visible.

3.4 Virus mimetic targeting concept facilitates enhanced mesangial cell specificity *in vitro*

Having demonstrated, that hetero-multivalent EXPcRGD NPs synergistically combine both key features of their surface ligands and present them in a sterically controlled manner, we intended to demonstrate, that this design can actually be applied to increase mesangial cell specificity. We therefore implemented an *in vitro* based assay, in which target rMCs were co-cultured with a superior number (5-10-fold) of

off-target cells carrying merely one of the two target receptors. While HeLa cells express no AT1r and only low levels of $\alpha_V\beta_3$-integrin, NCI-H295R cells were chosen as they show high AT1r but no $\alpha_V\beta_3$ expression [18,52] (**Figures 6a/S12**). To test the impact of different receptor expression levels on NP uptake, all cell lines were initially cultivated in mono-culture and incubated with the different NP formulations (**Figure 6b**). Particle uptake in rMCs was in accordance with previous results, showing the highest levels of cellular internalization for EXPcRGD NPs. On the contrary, HeLa cells were only able to take up cRGD NPs efficiently. EXPcRGD NP uptake was thereby drastically reduced, which can be explained by a combined effect of the cRGDfK shielding and a missing AT1r expression. NCI-H295R cells, on the contrary, showed high levels of cell-associated fluorescence for EXP NPs and EXPcRGD NPs, as these particle species could bind the abundantly present AT1r on the cell surface. In a next step, target rMCs were co-cultured with a superior number of either HeLa or NCI-H295R cells to test the NP´s rMC specificity. To differentiate between co-cultured cells in CLSM analysis, CellTracker™ Green (CTG) was used to stain rMCs while off-target cells were marked with CTDR. After incubation with fluorescently labeled EXPcRGD NPs, cellular distribution of NPs was assessed. In the rMC/HeLa co-culture model, EXPcRGD NP-derived fluorescence could almost exclusively be detected within the areas of mesangial cells. HeLa cells, in contrast, showed merely weak interaction with NPs, resulting in marginal fluorescence levels (**Figure 6c**, top row). We accordingly concluded, that EXPcRGD NPs could specifically locate mesangial cells among HeLa cells due to the differences in AT1r expression on the cell surface. These findings were supported by flow cytometry analysis showing, that cell-associated fluorescence of EXPcRGD NPs was significantly higher in rMCs than in off-target HeLa cells, while accumulation of cRGD NPs was considerable both in HeLa cells and rMCs (**Figure 6d**).

In contrast, rMC/NCI-H295R co-culture provided a divergent particle distribution. NP-associated fluorescence could not only be found in rMCs, but also in areas covered by NCI-H295R cells. However, distribution patterns differed significantly. While fluorescence among rMCs was found in circular, vesicle-like structures as seen before, NCI-H295R-associated fluorescence was more diffuse and intensified mainly at the cell membrane (Figure 6c, bottom row). We therefore concluded, that while accumulating in endocytotic vesicles of rMCs as seen before, EXPcRGD NPs were merely able to bind AT1r present in the cell membrane of NCI-H295R cells but could not be taken up into the cytosol due to an absence of $\alpha_V\beta_3$ integrin. Additionally, flow cytometry analysis showed, that even though EXPcRGD NP-associated fluorescence for NCI-H295R cells was higher compared to HeLa cells, EXPcRGD NPs still showed a significantly enhanced signal in mesangial cells (**Figure 6e**). EXP NPs, in contrast, bound to both rMCs and NCI-H295R cells with no significant cell specificity. Interestingly, addition of an excess of free EXP3174 (c = 1 mM) prior to EXPcRGD NP incubation led to a sharp decrease of fluorescence levels for NCI-H295R cells, while cell-associated fluorescence for rMCs was still significantly higher.

In summary, the co-culture model demonstrated, that hetero-multivalent EXPcRGD NPs have the capability to effectively identify receptor-positive mesangial cells in the presence of off-target cells, that

are not only prevailing in number but even express one of the two target receptors. The sequential ligand-receptor interplay is thereby a decisive tool to minimize off-target accumulation, as NPs are only taken up into cells, that express the necessary surface characteristics. If one receptor is missing, NP uptake is drastically reduced, thereby maximizing cell specificity for receptor-positive target cells.
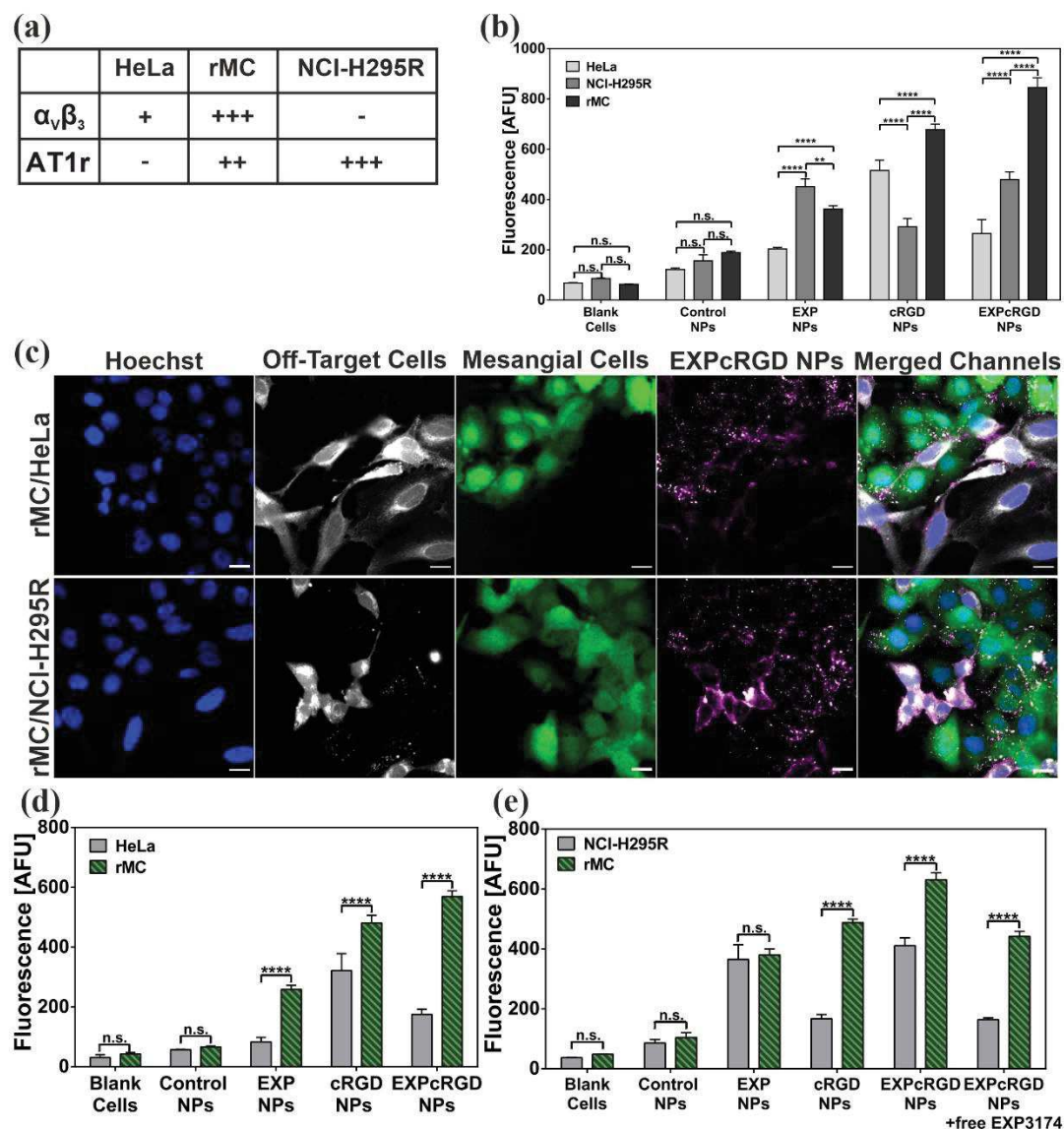

Figure 6. *In vitro* NP cell specificity in a mono- and co-culture assay. **(a)** Receptor expression of off-target HeLa and NCI-H295R cells in contrast to receptor double-positive rMCs. **(b)** Flow-cytometry analysis of NP uptake in mono-culture. EXPcRGD NPs showed maximum uptake into target rMCs **(c)** CLSM analysis of CTG-stained rMCs (green), co-cultured with CTDR-labeled HeLa or NCI-H295R cells (grey). Cell nuclei were stained with Hoechst 33258 (blue). For the rMC/HeLa co-culture (top row), NP-derived fluorescence (purple) could merely be detected within areas of rMCs. Co-culture of rMCs with AT1r-expressing NCI-H295R cells led to a diverging NP distribution (bottom row) with EXPcRGD NPs also binding to the surface of NCI-H295R cells, yet without any visible cell uptake (Scale bars 20 µm.) Flow cytometry analysis of rMCs co-cultured with either **(d)** HeLa or **(e)** NCI-H295R cells supported CLSM results as EXPcRGD NPs showed a significantly higher cell-association with rMCs in both cases. Results represent mean ± SD (*n*=3). ** P < 0.01, **** P < 0.0001. (n.s.: not significant. AFU, arbitrary fluorescence units.)

3.5   Accumulation of adenovirus mimetic EXPcRGD NPs in renal mesangial cells *in vivo*

Both rMC binding and uptake studies successfully showed that the virus-mimetic concept of sequential ligand-receptor interaction enables hetero-multivalent EXPcRGD NPs to specifically target mesangial cells *in vitro*. However, transferring *in vitro* results into a robust system with sufficient *in vivo* efficiency has been shown to be the major obstacle in NP design as many strategies fail to deliver desired target-specificity.[60] While many targeting studies oftentimes focus on the time-dependent biodistribution of targeted NPs upon administration, we were mainly interested in the question, whether our adenovirus mimetic NP species is able to specifically accumulate in mesangial cells *in vivo* or not. To our estimation, reaching mesangial areas within the glomerulus requires not only adequate passive accumulation in the target region but also described active cell uptake and is therefore an ideal benchmark to enable the comparison between our novel adenovirus NPs and the previously tested influenza A mimetic design.

To that regard, NPs were initially tested for potential cytotoxicity to guarantee pharmaceutical safety of the NP system. Both non-functionalized Control NPs and EXPcRGD NPs thereby showed no significant reduction of cell *via*bility (**Figure S13**). In a next step, fluorescently labeled NPs were injected into 10-week-old female NMRI mice. After 1 h of NP circulation, mice were sacrificed, and kidneys were extracted. Fluorescence analysis of prepared cryosections revealed, that EXPcRGD NPs effectively accumulated in glomerular areas while fluorescence in tubular parts of the kidney was neglectable (**Figure 7**). On the contrary, Control NPs as well as homo-functional EXP or cRGD NPs showed a considerably lower deposition in kidney cryosections (**Figure S14**).
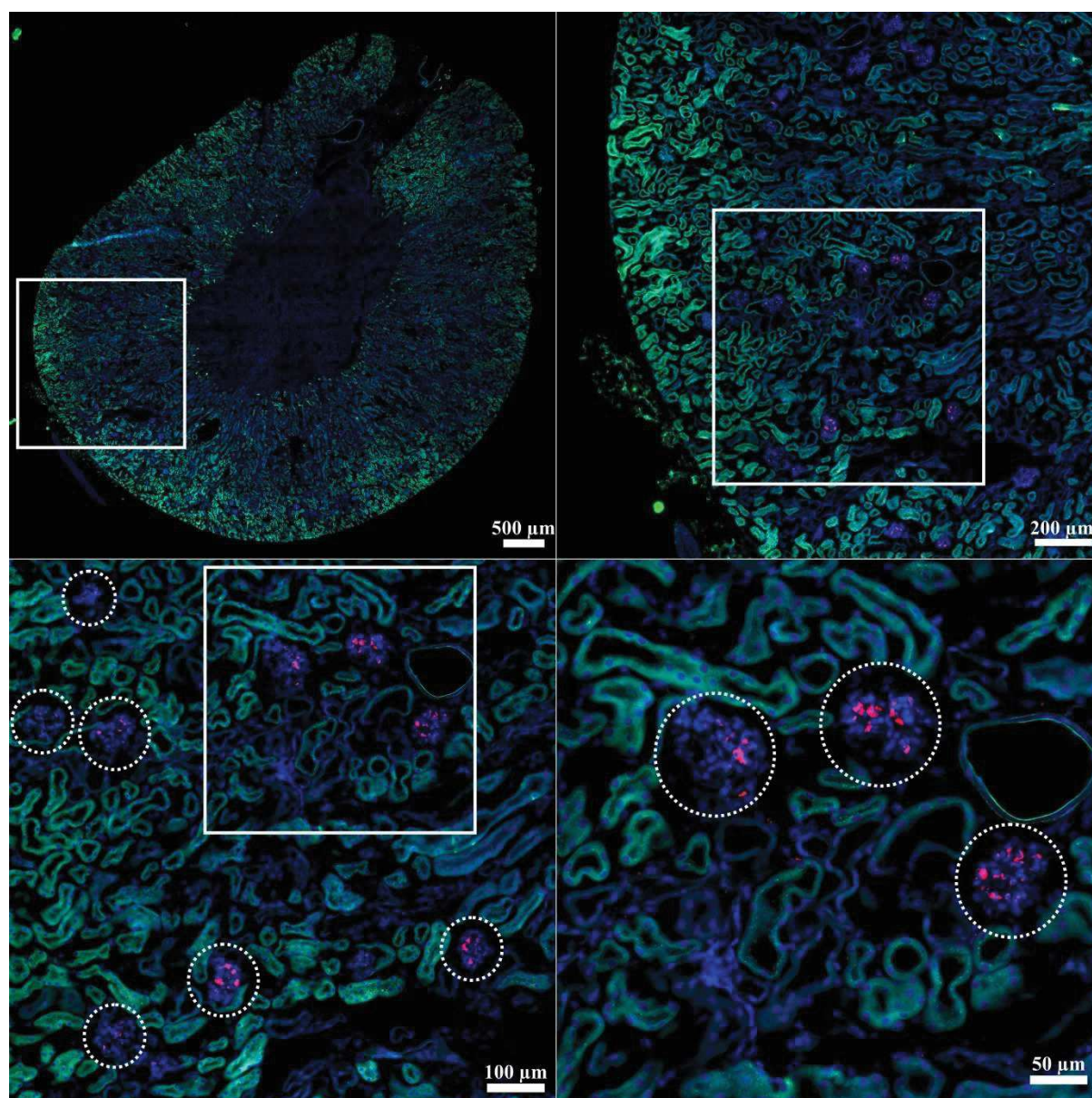
Figure 7. EXPcRGD NPs show strong intraglomerular accumulation *in vivo*. Transversal kidney cryosections were imaged using fluorescence microscopy. To facilitate histological evaluation, cell nuclei were stained with DAPI (blue) and tissue autofluorescence was recorded (green). EXPcRGD NPs (red) accumulated almost exclusively in glomerular areas of the cortex (white circles), while fluorescence in tubular areas was negligible. (From top-left to bottom-right, images show zoomed-in views of white boxes.)

To quantify observed differences, we determined glomerulus-associated fluorescence levels by assessing the glomerular fluorescence intensity per area for all NP types (**Figure 8a/b**). EXPcRGD NPs thereby showed a more than 10-fold increase in fluorescence intensity compared to Control NPs. Moreover, glomerular accumulation of hetero-multivalent NPs was significantly greater than for both homo-functional NP types. Remarkably, cRGD NP fluorescence was even lower than for non-functionalized Control NPs. We therefore hypothesized that cRGD NPs were not able to reach glomerular areas as a predominant number of particles bound $\alpha_V\beta_3$-expressing cells such as angiogenic endothelial cells shortly after injection and consequently left the bloodstream before reaching deeper areas of the kidney.[61] This hypothesis was further supported by the finding, that relative blood plasma

levels of cRGD NPs after 1 h of incubation were lowest among all particle types (**Figure S15**). In EXPcRGD NPs, on the contrary, shorter cRGDfK-functionalized PEG-PLA chains were shielded from premature exposition to $\alpha_V\beta_3$ integrins by addition of longer, EXP3174-functionalized PEG-PLA chains. Consequently, hetero-multivalent particles avoided off-target deposition and therefore successfully reached glomerular areas within the kidney. Antibody staining for mesangial cell marker integrin-α8 further revealed, that EXPcRGD NP-associated fluorescence in the glomerulus could almost entirely be found within mesangial cells (**Figure 8c**), proving our hypothesis of extravasation into the mesangial interstitium and subsequent endocytosis (Figure S1). In order to verify, that detected fluorescence in mesangial areas was derived from structurally intact NPs, we additionally injected a comparable dose of free fluorescent dye into mice and analyzed fluorescence deposition. While intraglomerular signal for these samples was negligible, tubular cells exhibited very strong fluorescence levels **(Figure S16)**. This indicated that, in contrast to injected NP species, the low-molecular dye was filtrated into the tubular system. We therefore concluded that intraglomerular fluorescence for all NP types derived from intact particles as a degradation would have led to an increase in the tubular signal, otherwise.
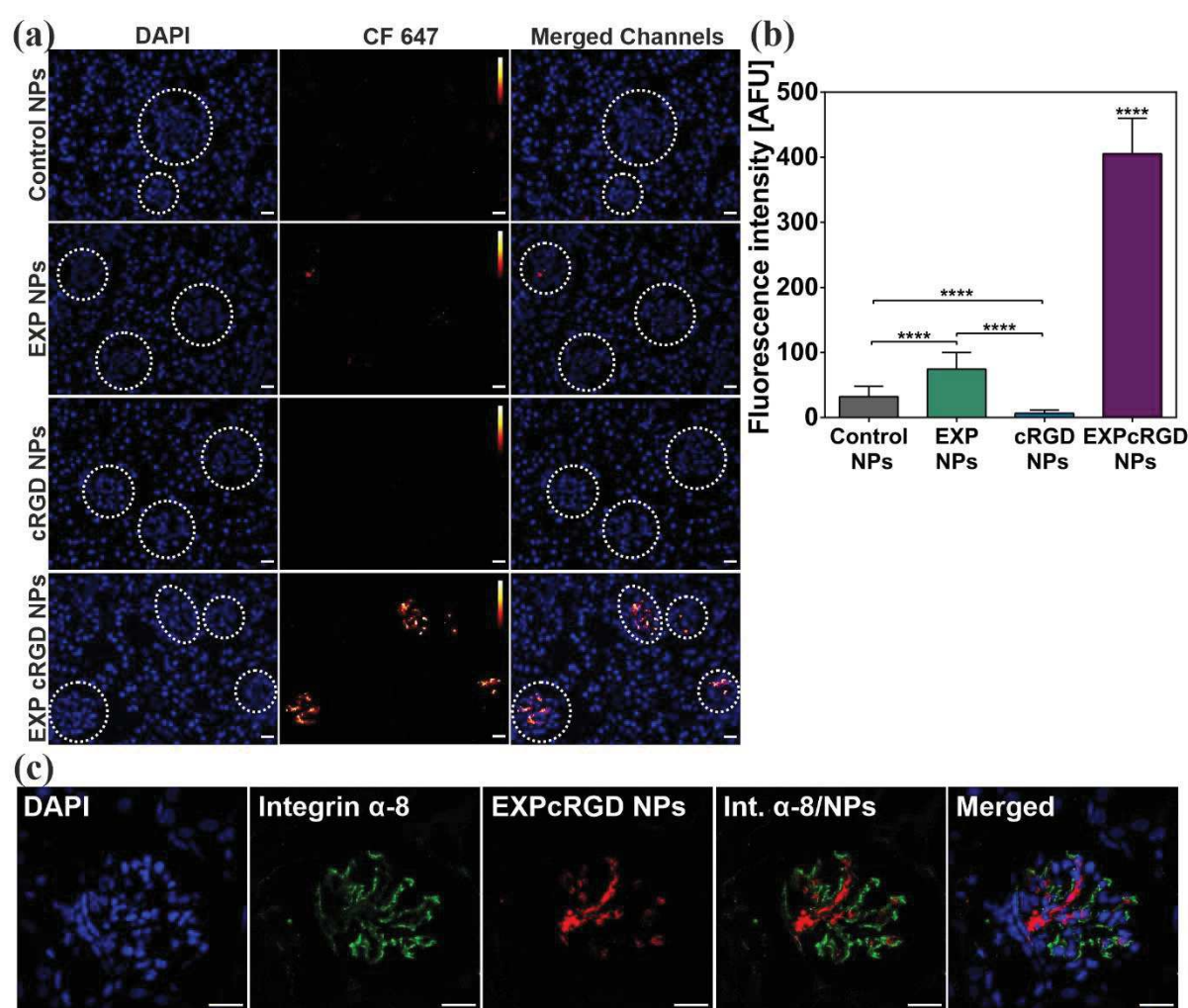
Figure 8. EXPcRGD NPs show a significantly enhanced accumulation in mesangial cells. **(a)** Fluorescence microscopy analysis revealed, that high fluorescence levels within glomeruli (white circles) could mainly be detected for EXPcRGD NPs. While EXP NPs showed a moderate accumulation in glomeruli, Control NPs and

cRGD NPs did not produce signals to any considerable extent. (Scale bar 20 µm. Calibration bar: 0 – 65535 Gray Value.) **(b)** Precise quantification of intraglomerular fluorescence intensity was achieved by assessing the integrated density per area of glomerulus for 60 glomeruli per sample. Thereby, EXPcRGD NPs showed far higher fluorescence intensities per glomerulus compared to all other particle types. Results represent mean ± SD ($n = 60$). ****P < 0.0001. (AFU, arbitrary fluorescence units.) **(c)** Antibody staining for mesangial surface marker integrin α-8 showed that EXPcRGD NP-associated fluorescence (red) was found within areas covered by mesangial cells (green), indicating that EXPcRGD NPs were able to specifically infiltrate mesangial cells *via* endocytosis. Scale bar 20 µm.

To our estimation, discussed *in vivo* studies successfully demonstrated the potential of our new, adenovirus mimetic NP design. Hetero-multivalent EXPcRGD NPs effectively accumulated in mesangial areas of the glomerulus, while homo-functional or unfunctionalized NP species failed to do so. This strongly suggests, that in order to reach sufficient levels of bioavailability, NPs do not only have to carry appropriate surface ligands but must also present them in an orchestrated fashion, that is suitable for the respective targeting strategy. Moreover, NP accumulation in the mesangium also proved that our adenovirus mimetic system of sterically controlled particle-cell interaction represents a *via*ble alternative to our previously published influenza A mimetic concept that was limited to a previous enzymatic activation.

4   Conclusion

In this study, we manufactured adenovirus-mimetic block-copolymer NPs capable of effectively targeting glomerular mesangial cells due to a sterically controlled, sequential ligand-receptor interaction, that is independent of previous enzymatic ligand activation. Hetero-multivalent NPs thereby not only showed precisely tunable physicochemical characteristics, but also displayed excellent avidity for both target motifs, leading to a substantial AT1r binding in the picomolar range and a significantly increased mesangial cell uptake compared to unfunctionalized NPs. Profiting from these features, virus-mimetic NPs could specifically target mesangial cells *in vitro*, even in a surrounding environment of off-target cells. Additionally, hetero-multivalent NPs displayed the necessary *in vivo* robustness, leading to an efficient accumulation in mesangial areas *in vivo* with only marginal off-target deposition within the kidney. Remarkably, hetero-multivalent EXPcRGD NPs thereby showed far better mesangial targeting compared to homo-functional cRGD or EXP NPs, although these previously had been found to also display substantial activity for receptor-positive cell lines *in vitro*.[30,45] These findings strongly support our conviction, that in order to exhaustively profit from their ligand features *in vivo*, nanomaterials have to utilize them in an appropriate biomimetic manner. Our new concept of sterically controlled particle-cell interaction thereby proved to be a *via*ble alternative to our previous design of enzymatic ligand activation as it also led to a significant NP accumulation in the mesangium. As we were able to target the same distinct cell type *in vivo* with two divergent virus-inspired concepts, we conclude, that mimicry of viral infection patterns can offer promising starting points for further targeting concepts and should therefore be more thoroughly investigated. Moreover, our successful mesangial cell targeting moves a more refined therapy of mesangium-related kidney pathologies within reach, as it could dramatically increase drug delivery compared to all other currently available approaches. In that regard, we could already show, that the anti-fibrotic and therefore highly promising drug candidate pirfenidone (PFD) can efficiently be encapsulated in presented block co-polymer NPs using both the above described nanoprecipitation and a novel microfluidic technique.[62] Especially when it comes to highly active substances such as PFD, drug delivery approaches using described virus-mimetic NPs could significantly decrease unfavorable off-target accumulation, thereby drastically improving currently available therapy options.

References

(1) Wilhelm, S.; Tavares, A. J.; Dai, Q.; Ohta, S.; Audet, J.; Dvorak, H. F.; Chan, W. C. W. Analysis of Nanoparticle Delivery to Tumours. *Nature Reviews Materials* **2016**, *1* (5), 16014. DOI: 10.1038/natrevmats.2016.14.

(2) Bae, Y. H.; Park, K. Targeted Drug Delivery to Tumors: Myths, Reality and Possibility. *Journal of Controlled Release* **2011**, *153* (3), 198–205. DOI: 10.1016/j.jconrel.2011.06.001.

(3) Awasthi, R.; Roseblade, A.; Hansbro, P. M.; Rathbone, M. J.; Dua, K.; Bebawy, M. Nanoparticles in Cancer Treatment: Opportunities and Obstacles. *Curr. drug targets* **2018**, *19* (14), 1696–1709. DOI: 10.2174/1389450119666180326122831.

(4) Nel, A. E.; Mädler, L.; Velegol, D.; Xia, T.; Hoek, E. M. V.; Somasundaran, P.; Klaessig, F.; Castranova, V.; Thompson, M. Understanding Biophysicochemical Interactions at the Nano-Bio Interface. *Nat. Mater.* **2009**, *8* (7), 543–557. DOI: 10.1038/nmat2442.

(5) Torrice, M. Does Nanomedicine Have a Delivery Problem? *ACS Cent. Sci.* **2016**, *2* (7), 434–437. DOI: 10.1021/acscentsci.6b00190.

(6) Ploss, A.; Evans, M. J. Hepatitis C Virus Host Cell Entry. *Curr. Opin. Virol.* **2012**, *2* (1), 14–19. DOI: 10.1016/j.coviro.2011.12.007.

(7) Wilen, C. B.; Tilton, J. C.; Doms, R. W. HIV: Cell Binding and Entry. *Cold Spring Harbor Perspect. Med.* **2012**, *2* (8). DOI: 10.1101/cshperspect.a006866.

(8) Gagliardi, M. Biomimetic and Bioinspired Nanoparticles for Targeted Drug Delivery. *Therapeutic delivery* **2017**, *8* (5), 289–299. DOI: 10.4155/tde-2017-0013.

(9) Marsh, M.; Helenius, A. Virus Entry:Open Sesame. *Cell* **2006**, *124* (4), 729–740. DOI: 10.1016/j.cell.2006.02.007.

(10) Lindenbach, B. D.; Rice, C. M. The Ins and Outs of Hepatitis C Virus Entry and Assembly. *Nat. Rev. Microbiol.* **2013**, *11* (10), 688–700. DOI: 10.1038/nrmicro3098.

(11) Boulant, S.; Stanifer, M.; Lozach, P.-Y. Dynamics of Virus-Receptor Interactions in Virus Binding, Signaling, and Endocytosis. *Viruses* **2015**, *7* (6), 2794–2815. DOI: 10.3390/v7062747.

(12) Grove, J.; Marsh, M. The Cell Biology of Receptor-Mediated Virus Entry. *J. Cell Biol.* **2011**, *195* (7), 1071–1082. DOI: 10.1083/jcb.201108131.

(13) Xiong, X.-B.; Uludağ, H.; Lavasanifar, A. Virus-Mimetic Polymeric Micelles for Targeted siRNA Delivery. *Biomaterials* **2010**, *31* (22), 5886–5893. DOI: 10.1016/j.biomaterials.2010.03.075.

(14) Ni, R.; Zhou, J.; Hossain, N.; Chau, Y. Virus-Inspired Nucleic Acid Delivery System: Linking Virus and Viral Mimicry. *Advanced Drug Delivery Reviews* **2016**, *106*, 3–26. DOI: 10.1016/j.addr.2016.07.005.

(15) Jang, C.; Lee, J. H.; Sahu, A.; Tae, G. The Synergistic Effect of Folate and RGD Dual Ligand of Nanographene Oxide on Tumor Targeting and Photothermal Therapy In Vivo. *Nanoscale* **2015**, *7* (44), 18584–18594. DOI: 10.1039/c5nr05067g.

(16) Chu, Y.; Chen, N.; Yu, H.; Mu, H.; He, B.; Hua, H.; Wang, A.; Sun, K. Topical Ocular Delivery to Laser-Induced Choroidal Neovascularization by Dual Internalizing RGD and TAT Peptide-Modified Nanoparticles. *International journal of nanomedicine* **2017**, *12*, 1353–1368. DOI: 10.2147/IJN.S126865.

(17) Li, X.; Zhou, H.; Yang, L.; Du, G.; Pai-Panandiker, A. S.; Huang, X.; Yan, B. Enhancement of Cell Recognition In Vitro by Dual-Ligand Cancer Targeting Gold Nanoparticles. *Biomaterials* **2011**, *32* (10), 2540–2545. DOI: 10.1016/j.biomaterials.2010.12.031.

(18) Maslanka Figueroa, S.; Veser, A.; Abstiens, K.; Fleischmann, D.; Beck, S.; Goepferich, A. Influenza A Virus Mimetic Nanoparticles Trigger Selective Cell Uptake. *Proc. Natl. Acad. Sci. U. S. A.States of America* **2019.** DOI: 10.1073/pnas.1902563116.

(19) Maslanka Figueroa, S.; Fleischmann, D.; Beck, S.; Tauber, P.; Witzgall, R.; Schweda, F.; Goepferich, A. Nanoparticles Mimicking Viral Cell Recognition Strategies Are Superior Transporters into Mesangial Cells. *Adv. Sci.* **2020**, 1903204. DOI: 10.1002/advs.201903204.

(20) Schlöndorff, D. Roles of the Mesangium in Glomerular Function. *Kidney Int.* **1996**, *49* (6), 1583–1585. DOI: 10.1038/ki.1996.229.

(21) Schlöndorff, D.; Banas, B. The Mesangial Cell Revisited:No Cell Is an Island. *J. Am. Soc. Nephrol.* **2009**, *20* (6), 1179–1187. DOI: 10.1681/ASN.2008050549.

(22) Scindia, Y. M.; Deshmukh, U. S.; Bagavant, H. Mesangial Pathology in Glomerular Disease:Targets for Therapeutic Intervention. *Adv. Drug Delivery Rev.* **2010**, *62* (14), 1337–1343. DOI: 10.1016/j.addr.2010.08.011.

(23) Kolset, S. O.; Reinholt, F. P.; Jenssen, T. Diabetic Nephropathy and Extracellular Matrix. *J. Histochem. Cytochem.* **2012**, *60* (12), 976–986. DOI: 10.1369/0022155412465073.

(24) Umanath, K.; Lewis, J. B. Update on Diabetic Nephropathy: Core Curriculum 2018. *Am. J. Kidney Dis.* **2018**, *71* (6), 884–895. DOI: 10.1053/j.ajkd.2017.10.026.

(25) Luisoni, S.; Greber, U. F. Biology of Adenovirus Cell Entry. In *Adenoviral Vectors for Gene Therapy*; pp 27–58. DOI: 10.1016/B978-0-12-800276-6.00002-4.

(26) Ghebremedhin, B. Human Adenovirus: Viral Pathogen with Increasing Importance. *Eur. J. Microbiol. Immunol.* **2014**, *4* (1), 26–33. DOI: 10.1556/EuJMI.4.2014.1.2.

(27) Bewley, M. C.; Springer, K.; Zhang, Y.-B.; Freimuth, P.; Flanagan, J. M. Structural Analysis of the Mechanism of Adenovirus Binding to Its Human Cellular Receptor, CAR. *Science* **1999**, *286* (286), 1579–1583.

(28) Burckhardt, C. J.; Suomalainen, M.; Schoenenberger, P.; Boucke, K.; Hemmi, S.; Greber, U. F. Drifting Motions of the Adenovirus Receptor CAR and Immobile Integrins Initiate Virus Uncoating and Membrane Lytic Protein Exposure. *Cell Host Microbe* **2011**, *10* (2), 105–117. DOI: 10.1016/j.chom.2011.07.006.

(29) Offringa, A.; Montijn, R.; Singh, S.; Paul, M.; Pinto, Y. M.; Pinto-Sietsma, S.-J. The Mechanistic Overview of SARS-CoV-2 Using Angiotensin-Converting Enzyme 2 to Enter the Cell for Replication:

Possible Treatment Options Related to the Renin-Angiotensin System. *European heart journal. Cardiovascular pharmacotherapy* **2020.** DOI: 10.1093/ehjcvp/pvaa053.

(30) Abstiens, K.; Gregoritza, M.; Goepferich, A. M. Ligand Density and Linker Length are Critical Factors for Multivalent Nanoparticle-Receptor Interactions. *ACS applied materials & interfaces* **2019**, *11* (1), 1311–1320. DOI: 10.1021/acsami.8b18843.

(31) Miura, S.-i.; Karnik, S. S.; Saku, K. Review:Angiotensin II Type 1 Receptor Blockers: Class Effects Versus Molecular Effects. *J. Renin Angiotensin Aldosterone Syst.* **2011**, *12* (1), 1–7. DOI: 10.1177/1470320310370852.

(32) Yan, Y.-D.; Kim, H.-K.; Seo, K.-H.; Lee, W. S.; Lee, G.-S.; Woo, J.-S.; Yong, C.-S.; Choi, H.-G. The Physicochemical Properties, In Vitro Metabolism and Pharmacokinetics of a Novel Ester Prodrug of EXP3174. *Molecular pharmaceutics* **2010**, *7* (6), 2132–2140. DOI: 10.1021/mp100166c.

(33) Zhan, C.; Gu, B.; Xie, C.; Li, J.; Liu, Y.; Lu, W. Cyclic RGD Conjugated Poly(ethylene glycol)-co-poly(lactic acid) Micelle Enhances Paclitaxel Anti-Glioblastoma Effect. *J. Controlled Release* **2010**, *143* (1), 136–142. DOI: 10.1016/j.jconrel.2009.12.020.

(34) Kluza, E.; van der Schaft, D. W. J.; Hautvast, P. A. I.; Mulder, W. J. M.; Mayo, K. H.; Griffioen, A. W.; Strijkers, G. J.; Nicolay, K. Synergistic Targeting of Alphavbeta3 Integrin and Galectin-1 with Heteromultivalent Paramagnetic Liposomes for Combined MR Imaging and Treatment of Angiogenesis. *Nano letters* **2010**, *10* (1), 52–58. DOI: 10.1021/nl902659g.

(35) Graf, N.; Bielenberg, D. R.; Kolishetti, N.; Muus, C.; Banyard, J.; Farokhzad, O. C.; Lippard, S. J. α(V)β(3) Integrin-Targeted PLGA-PEG Nanoparticles for Enhanced Anti-Tumor Efficacy of a Pt(IV) Prodrug. *ACS nano* **2012**, *6* (5), 4530–4539. DOI: 10.1021/nn301148e.

(36) Wilder, R. L. Integrin Alpha V Beta 3 as a Target for Treatment of Rheumatoid Arthritis and Related Rheumatic Diseases. *Annals of the rheumatic diseases* **2002**, *61 Suppl 2*, ii96-9. DOI: 10.1136/ard.61.suppl_2.ii96.

(37) Abstiens, K.; Maslanka Figueroa, S.; Gregoritza, M.; Goepferich, A. M. Interaction of Functionalized Nanoparticles with Serum Proteins and its Impact on Colloidal Stability and Cargo Leaching. *Soft Matter* **2019**, *15* (4), 709–720. DOI: 10.1039/c8sm02189a.

(38) Moghimi, S. M.; Hunter, A. C.; Andresen, T. L. Factors Controlling Nanoparticle Pharmacokinetics:An Integrated Analysis and Perspective. *Annual review of pharmacology and toxicology* **2012**, *52*, 481–503. DOI: 10.1146/annurev-pharmtox-010611-134623.

(39) Aggarwal, P.; Hall, J. B.; McLeland, C. B.; Dobrovolskaia, M. A.; McNeil, S. E. Nanoparticle Interaction with Plasma Proteins as it Relates to Particle Biodistribution, Biocompatibility and Therapeutic Efficacy. *Advanced Drug Delivery Reviews* **2009**, *61* (6), 428–437. DOI: 10.1016/j.addr.2009.03.009.

(40) Qian, H.; Wohl, A. R.; Crow, J. T.; Macosko, C. W.; Hoye, T. R. A Strategy for Control of "Random" Copolymerization of Lactide and Glycolide:Application to Synthesis of PEG-b-PLGA Block

Polymers Having Narrow Dispersity. *Macromolecules* **2011**, *44* (18), 7132–7140. DOI: 10.1021/ma201169z.

 (41) Valencia, P. M.; Hanewich-Hollatz, M. H.; Gao, W.; Karim, F.; Langer, R.; Karnik, R.; Farokhzad, O. C. Effects of Ligands with Different Water Solubilities on Self-assembly and Properties of Targeted Nanoparticles. *Biomaterials* **2011**, *32* (26), 6226–6233. DOI: 10.1016/j.biomaterials.2011.04.078.

 (42) Abstiens, K.; Fleischmann, D.; Gregoritza, M.; Goepferich, A. M. Gold-Tagged Polymeric Nanoparticles with Spatially Controlled Composition for Enhanced Detectability in Biological Environments. *ACS Applied Nano Materials* **2019**, *2* (2), 917–926. DOI: 10.1021/acsanm.8b02165.

 (43) Childs, C. E. The Determination of Polythethylene Glycol in Gamma Globulin Solutions. *Microchemical Journal* **1975**, *20*, 190–192.

 (44) Rabanel, J.-M.; Faivre, J.; Tehrani, S. F.; Lalloz, A.; Hildgen, P.; Banquy, X. Effect of the Polymer Architecture on the Structural and Biophysical Properties of PEG-PLA Nanoparticles. *ACS applied materials & interfaces* **2015**, *7* (19), 10374–10385. DOI: 10.1021/acsami.5b01423.

 (45) Hennig, R.; Pollinger, K.; Veser, A.; Breunig, M.; Goepferich, A. Nanoparticle Multivalency Counterbalances the Ligand Affinity Loss upon PEGylation. *J. Controlled Release* **2014**, *194*, 20–27. DOI: 10.1016/j.jconrel.2014.07.062.

 (46) G. Grynkiewicz, M. Poeni, R. Y. Tsien. A New Generation of Ca2+ Indicators with Greatly Improved Fluorescence Properties. *J. Biol. Chem.* **1985**, *260* (6), 3440–3450.

 (47) Makadia, H. K.; Siegel, S. J. Poly Lactic-co-Glycolic Acid (PLGA) as Biodegradable Controlled Drug Delivery Carrier. *Polymers* **2011**, *3* (3), 1377–1397. DOI: 10.3390/polym3031377.

 (48) Xiao, R. Z.; Zeng, Z. W.; Zhou, G. L.; Wang, J. J.; Li, F. Z.; Wang, A. M. Recent Advances in PEG-PLA Block Copolymer Nanoparticles. *Int. J. Nanomed.* **2010**, *5*, 1057–1065. DOI: 10.2147/IJN.S14912.

 (49) Satchell, S. C.; Braet, F. Glomerular Endothelial Cell Fenestrations: an Integral Component of the Glomerular Filtration Barrier. *Am. J. Physiol. Renal Physiol.* **2009**, *296* (5), 947-956. DOI: 10.1152/ajprenal.90601.2008.

 (50) H. Latta. An Approach to the Structure and Function of the Glomerular Mesangium. *J. Am. Soc. Nephrol.* **1992**, *2*, 65–73.

 (51) He, C.; Hu, Y.; Yin, L.; Tang, C.; Yin, C. Effects of Particle Size and Surface Charge on Cellular Uptake and Biodistribution of Polymeric Nanoparticles. *Biomaterials* **2010**, *31* (13), 3657–3666. DOI: 10.1016/j.biomaterials.2010.01.065.

 (52) Hennig, R.; Ohlmann, A.; Staffel, J.; Pollinger, K.; Haunberger, A.; Breunig, M.; Schweda, F.; Tamm, E. R.; Goepferich, A. Multivalent Nanoparticles Bind the Retinal and Choroidal Vasculature. *Journal of controlled release : official journal of the Controlled Release Society* **2015**, *220* (Pt A), 265–274. DOI: 10.1016/j.jconrel.2015.10.033.

(53) Pollinger, K.; Hennig, R.; Breunig, M.; Tessmar, J.; Ohlmann, A.; Tamm, E. R.; Witzgall, R.; Goepferich, A. Kidney Podocytes as Specific Targets for Cyclo(RGDfC)-Modified Nanoparticles. *Small* **2012**, *8* (21), 3368–3375. DOI: 10.1002/smll.201200733.

(54) Doherty, G. J.; McMahon, H. T. Mechanisms of Endocytosis. *Annual review of biochemistry* **2009**, *78*, 857–902. DOI: 10.1146/annurev.biochem.78.081307.110540.

(55) Liu, M.; Li, Q.; Le Liang; Li, J.; Wang, K.; Li, J.; Lv, M.; Chen, N.; Song, H.; Lee, J.; Shi, J.; Wang, L.; Lal, R.; Fan, C. Real-Time Visualization of Clustering and Intracellular Transport of Gold Nanoparticles by Correlative Imaging. *Nature communications* **2017**, *8*, 15646. DOI: 10.1038/ncomms15646.

(56) Sahay, G.; Alakhova, D. Y.; Kabanov, A. V. Endocytosis of Nanomedicines. *Journal of controlled release : official journal of the Controlled Release Society* **2010**, *145* (3), 182–195. DOI: 10.1016/j.jconrel.2010.01.036.

(57) Cai, W. Applications of Gold Nanoparticles in Cancer Nanotechnology. *Nanotechnol., Sci. Appl.* **2008**, *1*, 17–32. DOI: 10.2147/NSA.S3788.

(58) Llevot, A.; Astruc, D. Applications of Vectorized Gold Nanoparticles to the Diagnosis and Therapy of Cancer. *Chem. Soc. Rev.* **2012**, *41* (1), 242–257. DOI: 10.1039/c1cs15080d.

(59) Sperling, R. A.; Rivera Gil, P.; Zhang, F.; Zanella, M.; Parak, W. J. Biological Applications of Gold Nanoparticles. *Chem. Soc. Rev.* **2008**, *37* (9), 1896–1908. DOI: 10.1039/b712170a.

(60) Blanco, E.; Shen, H.; Ferrari, M. Principles of Nanoparticle Design for Overcoming Biological Barriers to Drug Delivery. *Nat. Biotechnol.* **2015**, *33* (9), 941–951. DOI: 10.1038/nbt.3330.

(61) Hodivala-Dilke, K. Alphavbeta3 Integrin and Angiogenesis: a Moody Integrin in a Changing Environment. *Current opinion in cell biology* **2008**, *20* (5), 514–519. DOI: 10.1016/j.ceb.2008.06.007.

(62) Maslanka Figueroa, S.; Fleischmann, D.; Beck, S.; Goepferich, A. Thermodynamic, Spatial and Methodological Considerations for the Manufacturing of Therapeutic Polymer Nanoparticles. *Pharm Res* **2020**, *37* (3). DOI: 10.1007/s11095-020-2783-4.

Chapter 3 – Supporting Information

Adenovirus-Mimetic Nanoparticles: Sequential Ligand-Receptor Interplay as a Universal Tool for Enhanced *In Vitro/In Vivo* Cell Identification

1 Mesangial passive targeting
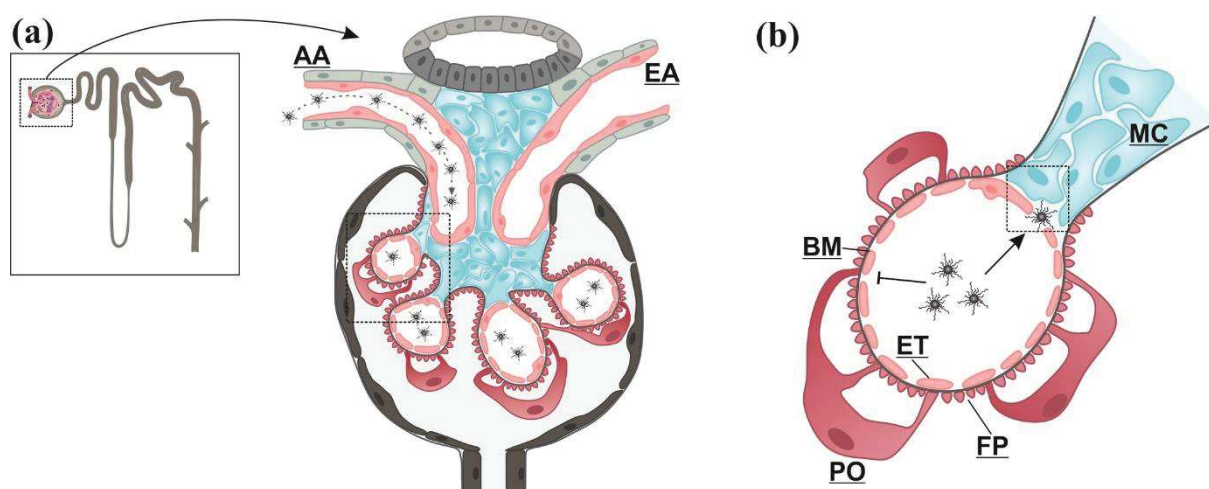
Figure S1. Mesangial accumulation of adenovirus-mimetic NPs. **(a)** Upon i.v. administration, NPs rapidly enter glomerular areas of the kidney via the afferent arteriole that then diverges into the glomerular capillary system.[1] **(b)** Within the capillaries, particles larger than approximately 10 nm cannot pass the renal filter due to its multilayer structure.[2–4] Interstitial mesangial cells, on the contrary, are easily accessible via extravasation through the fenestrated endothelium.[5,6] Having accumulated in mesangial areas, NPs can then finalize cell uptake by mimicking previously described adenoviral cell infiltration (Figure 1). (AA: afferent arteriole; EA: efferent arteriole; MC: mesangial cells; PO: podocyte; FP: foot processes; ET: endothelium; BM: basement membrane

2 Polymer synthesis and nanoparticle composition
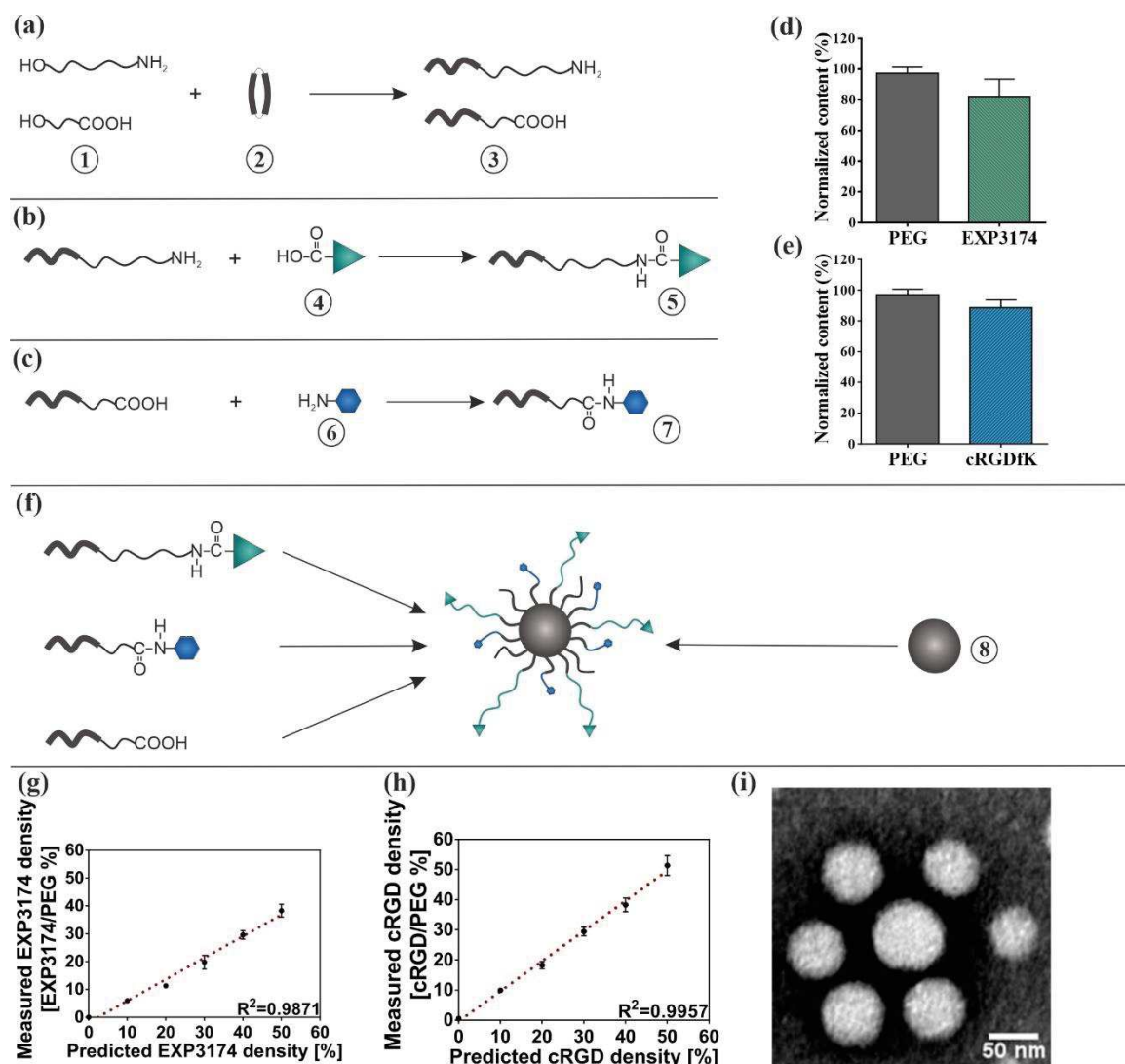
Figure S2. Synthesis concept for ligand-functionalized PEG-PLA block co-polymers. **(a)** Hetero-bifunctional PEG polymers (①) of varying chain length (2 kDa/5 kDa) were mixed with 3,6-dimethyl-1,4-dioxane-2,5-dione (②) to synthesize NH_2-PEG_{5k}-PLA_{10k} as well as COOH-PEG_{2k}-PLA_{10k} (③) via ring-opening polymerization using 1,8-diazabicyclo [5.4.0]undec-7-ene as a catalyst (please refer to the experimental section for a detailed description of the synthesis procedure). **(b)** Subsequently, NH_2-PEG_{5k}-PLA_{10k} was covalently coupled to the carboxyl group of EXP3174 (④) via DCC/NHS chemistry, resulting in EXP3174-PEG_{5k}-PLA_{10k} (⑤). **(c)** Additionally, COOH-PEG_{2k}-PLA_{10k} was attached to the lysine residue of cRGDfK (⑥) via EDC/NHS chemistry, leading to shorter cRGDfK-PEG_{2k}-PLA_{10k} (⑦). **(d)** Coupling efficiency for synthesized EXP3174-PEG_{5k}-PLA_{10k} and **(e)** cRGDfK-PEG_{2k}-PLA_{10k} was determined by independently measuring the concentration of both PEG and EXP3174. Molar concentration thereby did not significantly vary, indicating successful polymer functionalization. **(f)** EXP3174- and cRGDfK-functionalized PEG-PLA polymers were subsequently mixed with unfunctionalized COOH-PEG_{2k}-PLA_{10k} as well as PLGA (⑧) to manufacture hetero-multivalent EXPcRGD NPs. Quantification of EXP3174 **(g)** and **(h)** cRGDfK ligand surface density, respectively, after NP manufacture. Final surface content was directly proportional to the priorly added amount of ligand-functionalized polymer for both EXP3174 ($R^2 = 0.9871$) and cRGDfK ($R^2 = 0.9957$), thereby proving sufficient stability of ligand coupling to the respective polymers. **(i)** TEM imaging of EXPcRGD NPs (63,000x magnification). Results represent mean ± SD ($n = 3$).

3-6 ^{1}H-NMR spectra of synthesized polymers
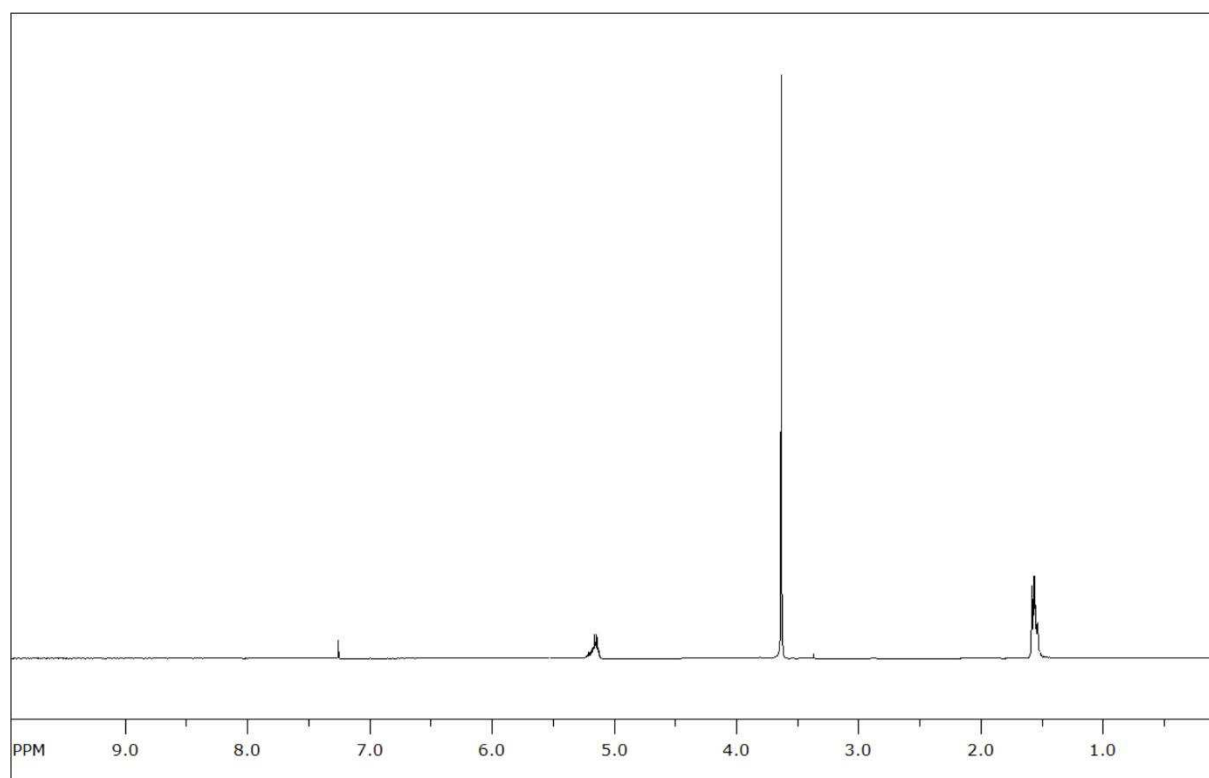
Figure S3. ^{1}H-NMR (CDCl$_3$, 400 MHz) spectra of MeO-PEG$_{5k}$-PLA$_{10k}$. δ (ppm): 1.56 ppm (-C(CH$_3$)H-), 3.37 ppm (H$_3$COCH$_2$CH$_2$-), 3.63 ppm (-OCH$_2$CH$_2$-), 4.16 (-OCH$_2$CH$_2$-O(CO)-), 5.15 ppm (-C(CH$_3$)H-), 7.26 (solvent peak).
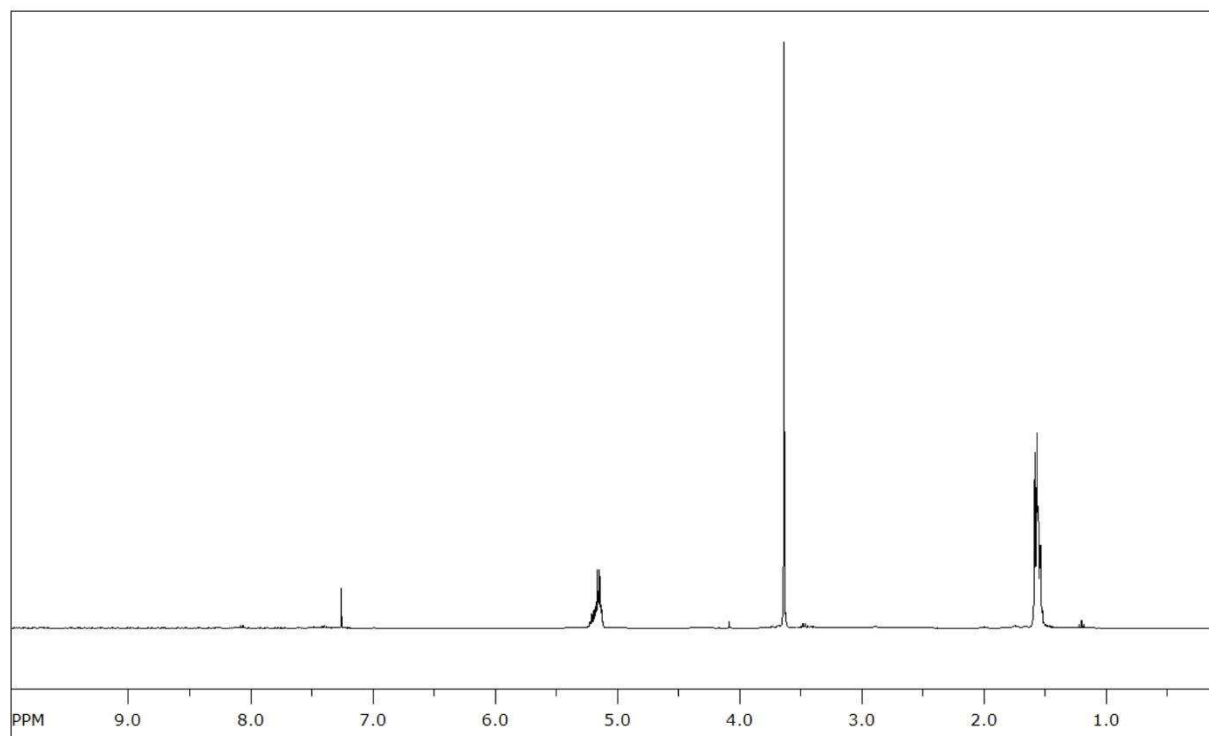
Figure S4. ^{1}H-NMR (CDCl$_3$, 400 MHz) spectra of COOH-PEG$_{2k}$-PLA$_{10k}$. δ (ppm): 1.56 ppm (-C(CH$_3$)H-), 3.40 ppm (H$_3$COCH$_2$CH$_2$-), 3.63 ppm (-OCH$_2$CH$_2$-), 4.13 (-OCH$_2$CH$_2$-O(CO)-), 5.17 ppm (-C(CH$_3$)H-), 7.26 (solvent peak).
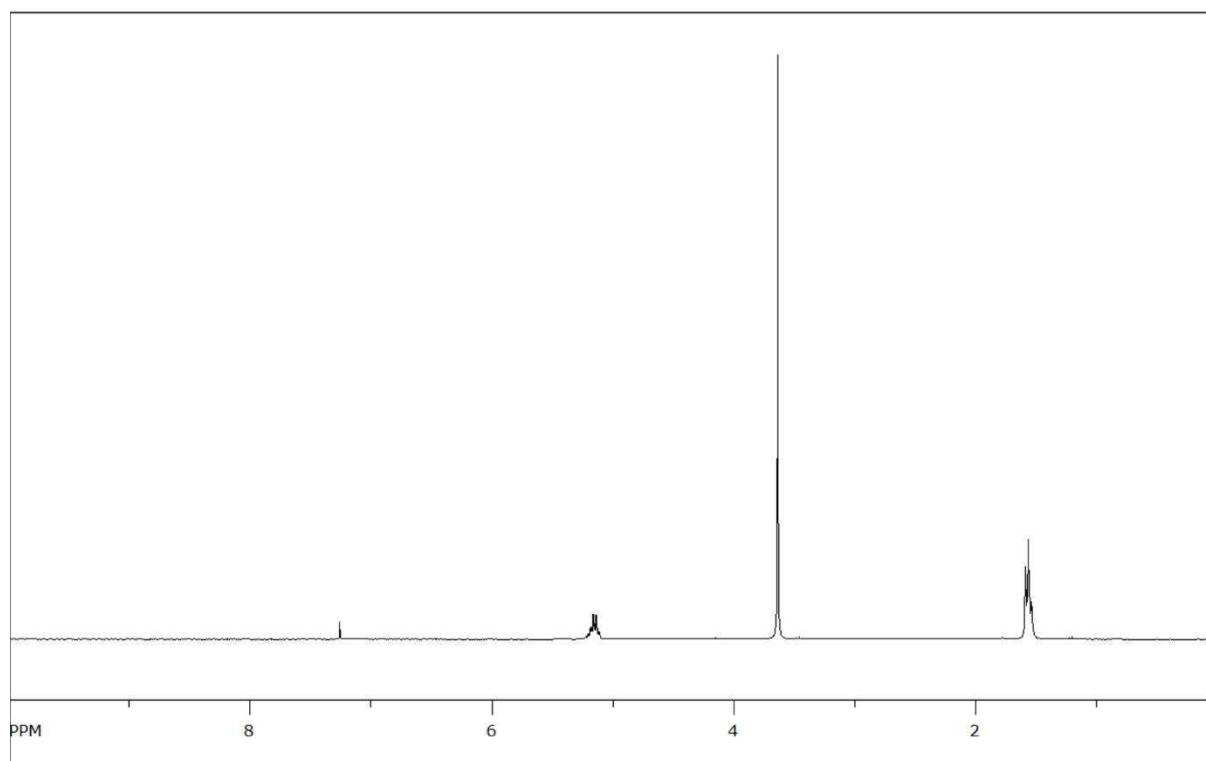
Figure S5. ^{1}H-NMR (CDCl$_3$, 400 MHz) spectra of COOH-PEG$_{5k}$-PLA$_{10k}$. δ (ppm): 1.56 ppm (-C(CH$_3$)H-), 3.43 ppm (H$_3$COCH$_2$CH$_2$-), 3.63 ppm (-OCH$_2$CH$_2$-), 4.15 (-OCH$_2$CH$_2$-O(CO)-), 5.16 ppm (-C(CH$_3$)H-), 7.26 (solvent peak).
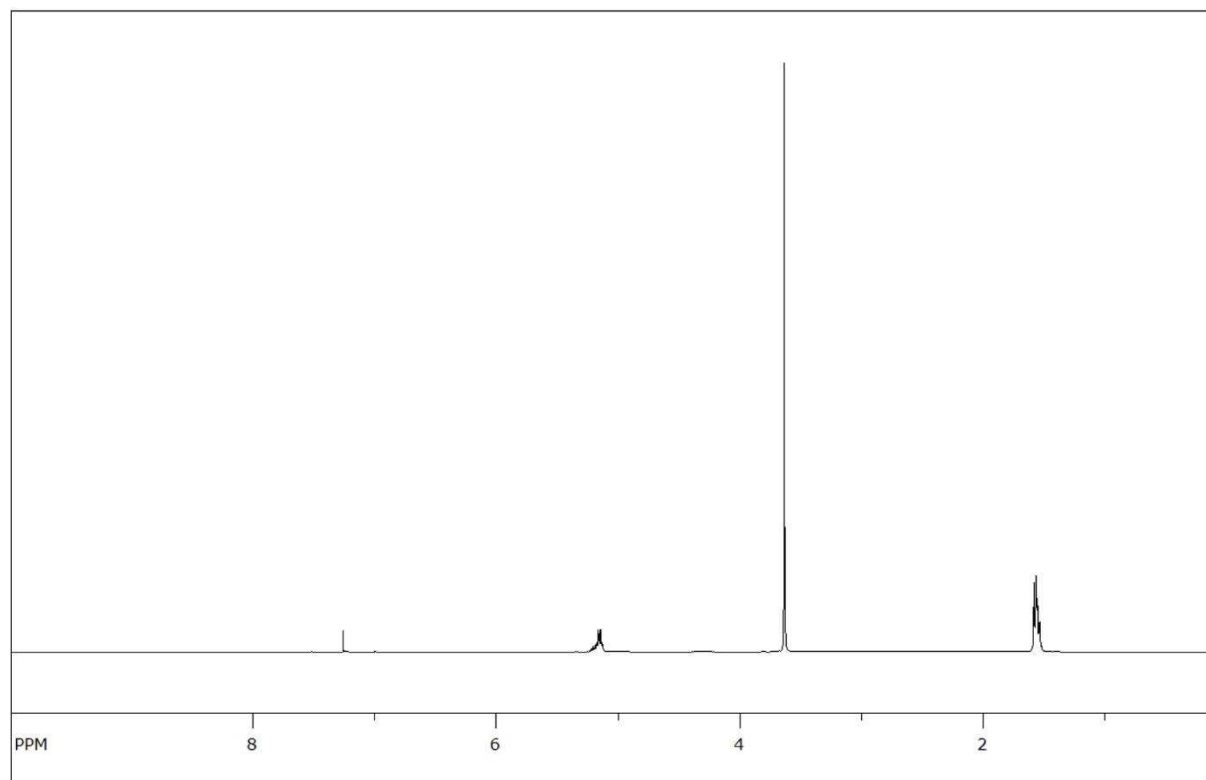
Figure S6. ^{1}H-NMR (CDCl$_3$, 400 MHz) spectra of NH$_2$-PEG$_{5k}$-PLA$_{10k}$. δ (ppm):
1.57 ppm (-C(CH$_3$)H-), 3.39 ppm (H$_3$COCH$_2$CH$_2$-), 3.61 ppm (-OCH$_2$CH$_2$-), 4.19 (-OCH$_2$CH$_2$-O(CO)-), 5.18 ppm (-C(CH$_3$)H-), 7.25 ppm (solvent peak).

7   Additional data on ligand properties
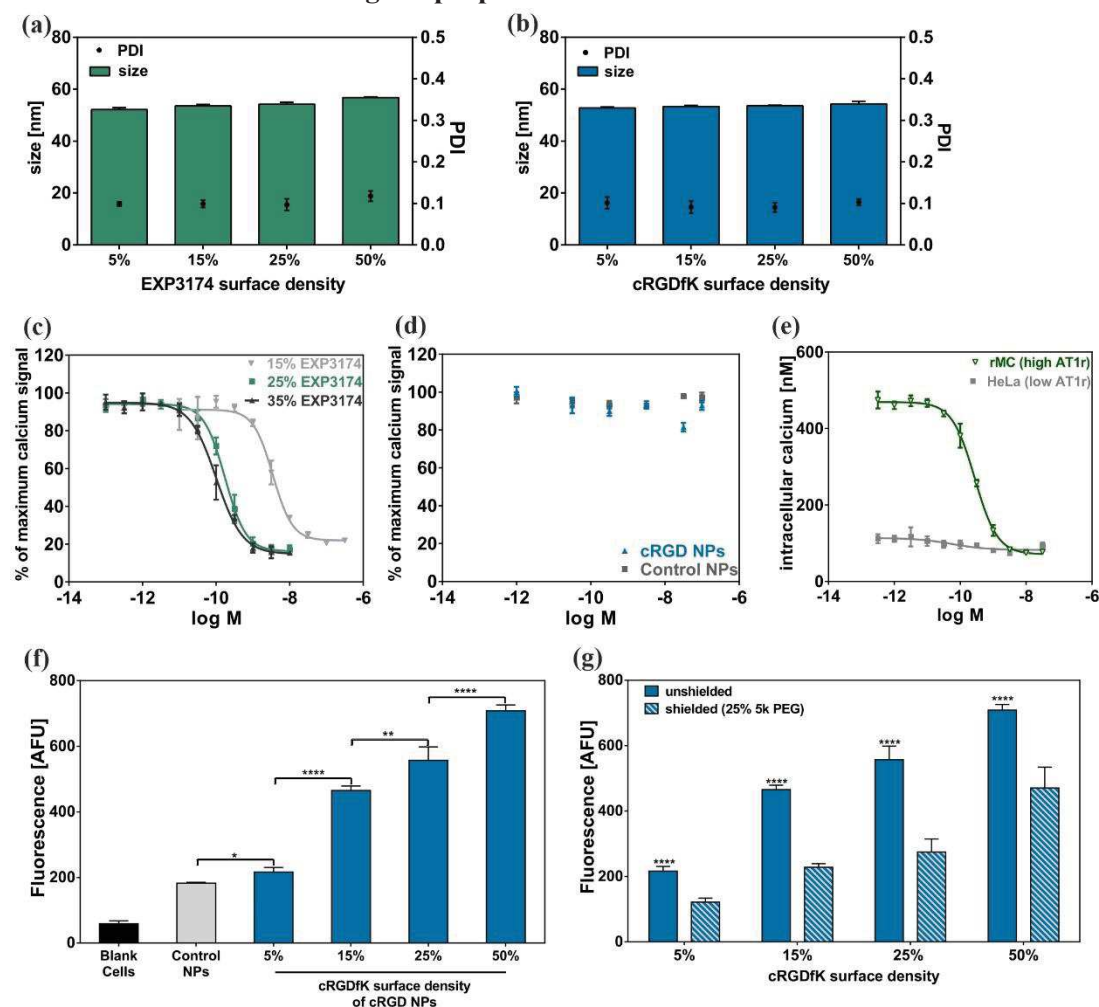
Figure S7. DLS analysis of **(a)** EXP3174-functionalized and **(b)** cRGDfK-functionalized showed no significant impact of the ligand density on the NPs´ hydrodynamic diameter or a possible tendency for aggregation. (PDI: polydispersity index.) **(c)** AT1r activity for rMCs treated with EXP NPs with varying EXP3174 surface densities. EXP NPs with 25 % and 35 % EXP3174 density showed a comparable AT1r blocking **(IC$_{50}$ (25%) = 552 ± 73 pM; IC$_{50}$ (35%) = 321 ± 81 pM)**, while a surface density of 15 % lead to a drastically reduced AT1r binding **(IC$_{50}$ (15%) = 11 ± 1 nM)**. (M = molar NP concentration.) **(d)** AT1r activity for EXP3174-free NPs. Neither unfunctionalized Control NPs nor cRGD NPs could significantly bind the AT1r, resulting in maximum calcium levels upon ATII stimulation and confirming the specificity of the assay. **(e)** Intracellular Ca^{2+} levels for either rMCs (high AT1r expression) or HeLa cells (low AT1r expression)[7] upon incubation with EXPcRGD NPs and stimulation with AT II. Measured intracellular Ca^{2+} levels in HeLa cells were far lower compared to rMCs due to the differences in AT1r expression. (M = molar NP concentration.) **(f)/(g)** Flow cytometry analysis of rMC uptake for cRGDfK-carrying NPs. **(f)** Cell uptake gradually increased with higher surface densities of cRGDfK, as described before.[8] While cRGD NPs with a ligand density of 15% still showed sufficiently enhanced levels of endocytosis, 5% cRGD NPs provided merely low internalization levels, comparable to unfunctionalized Control NPs. **(g)** By introduction of longer shielding elements (see Figure S8), respective rMC uptake could be significantly reduced for all cRGDfK ligand densities. * P < 0.05, ** P < 0.01, **** P < 0.0001. (AFU, arbitrary fluorescence units.) Results represent mean ± SD (*n* = 3).
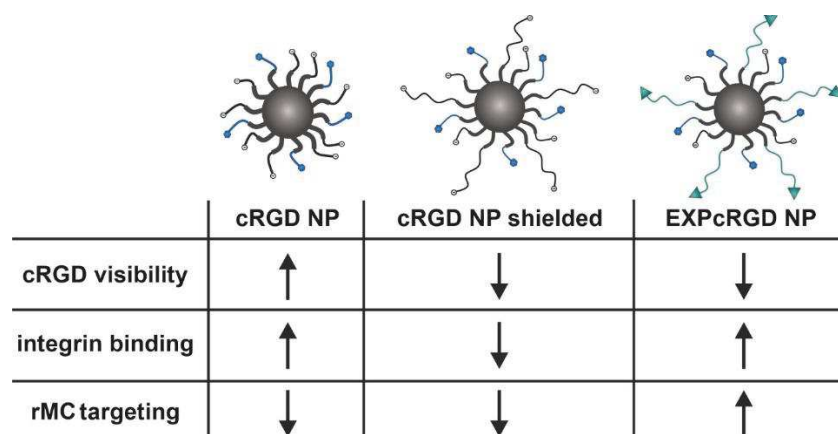
8   Shielding concept

Figure S8. Shielding concept for cRGDfK. While ligand visibility of unshielded cRGD NPs was maximum, introduction of longer COOH-PEG$_{5k}$-PLA$_{10k}$ chains significantly reduced the accessibility of the ligand due to a steric hindrance effect, leading to a decreased integrin binding and subsequent rMC uptake of shielded cRGD NPs. For EXPcRGD NPs, coupling of EXP3174 to longer PEG$_{5k}$-PLA$_{10k}$ chains provided the necessary initial binding to the rMC surface. Resulting spatial approach of the NP then lead to a sufficient integrin binding via previously hidden cRGDfK, thereby combining cell-specific targeting and satisfactory uptake.

9   CLSM images of NP-AT1r interaction

(a)

(b)
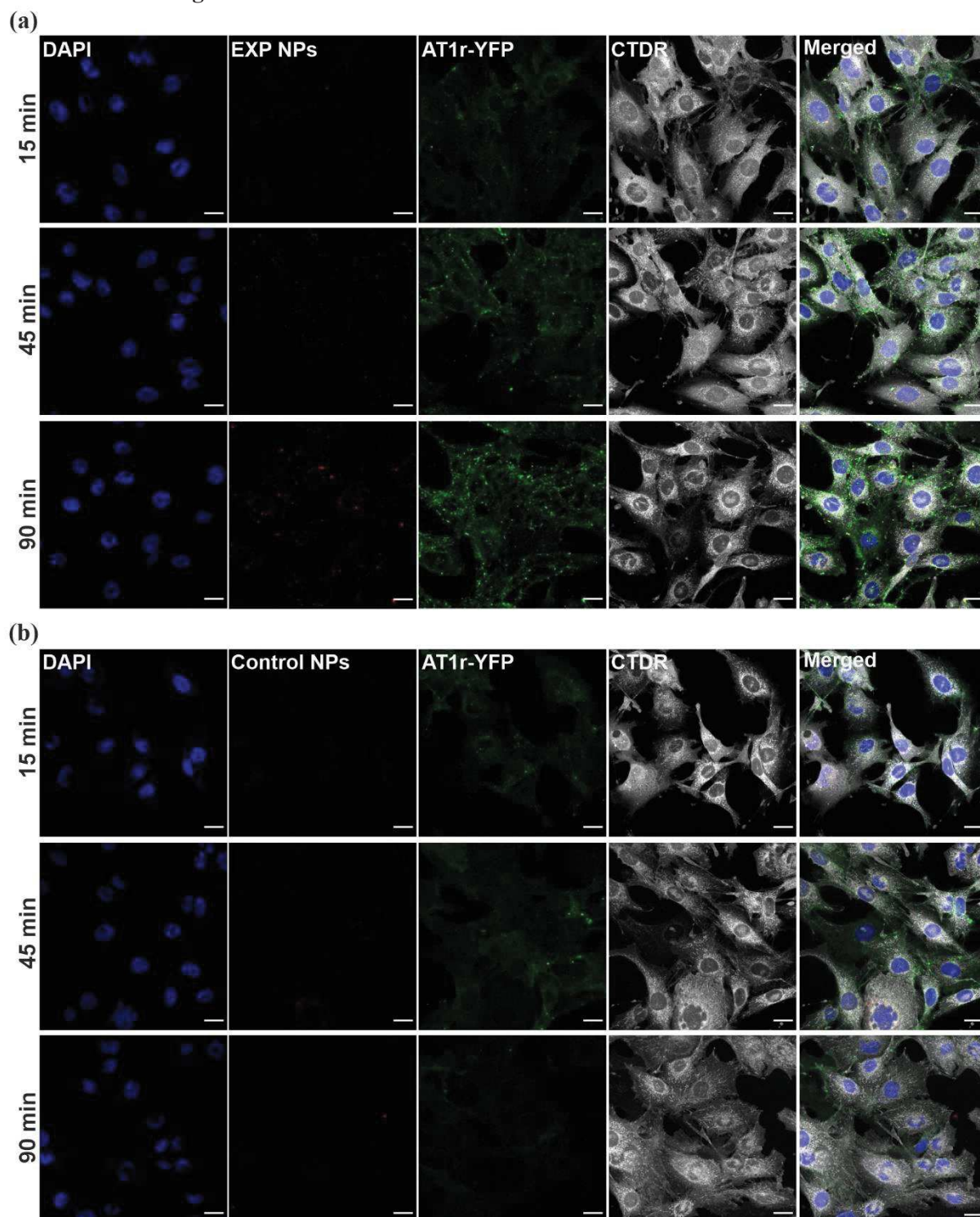
Figure S9. Time-dependent CLSM analysis of NP interaction with AT1r-YFP rMCs (grey). **(a)** For EXP NPs, AT1r signal (green) could mainly be found on the cellular surface, where large receptor clusters became visible and were colocalized with NP-associated fluorescence (red). This indicates EXP NP binding to the AT1r, however without any significant endocytosis. **(b)** Control NPs showed merely negligible levels of rMC uptake. Fluorescence levels for the AT1r were also drastically reduced, as the receptors did not merge to larger formations and remained widely spread across the entire cell surface. (Scale bar 20 μm.)

10 Gold-tagged NPs
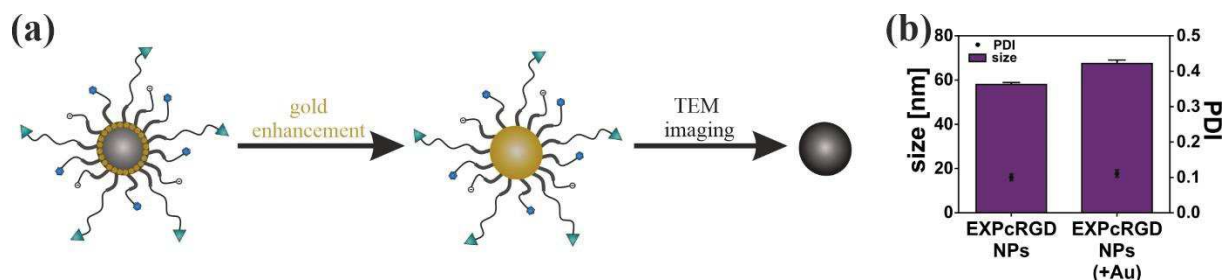
Figure S10. Gold-tagged NPs for facilitated TEM visualization. **(a)** NPs were gold-labeled by covalently attaching ultra-small gold NPs (diameter: 2.2 nm) to the carboxyl group of PLGA, prior to NP manufacturing. After incubation of rMCs with labeled NPs, the particle core was gold-enhanced by depositing further gold particles on the NP core, thereby increasing electron density of the sample and enabling visualization in TEM microscopy, where NPs appeared as dark black spots. **(b)** DLS analysis of NPs. Due to the encapsulation of gold NPs, Au-labeled EXPcRGD NPs showed a slightly increased hydrodynamic diameter with a PDI in a still acceptable range. Results represent mean ± SD (n = 3).

11 Additional TEM images
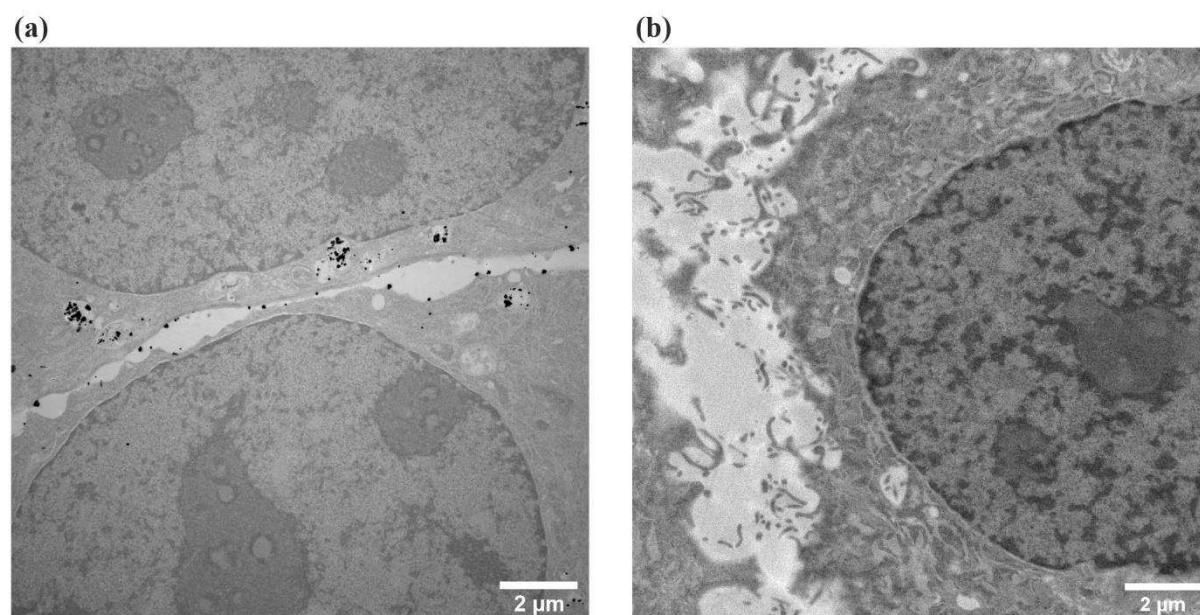
Figure S11. (a) TEM image of rMCs incubated with cRGD NPs. Comparable to EXPcRGD NPs, cRGD NPs showed significant accumulation in endocytotic vesicles within the rMC cytosol. However, NP density on the cellular surface appeared to be lower, indicating that NPs were already taken up to a large degree via integrin-mediated endocytosis. **(b)** TEM image of untreated rMCs after gold-enhancement. Control cells were treated with the same TEM preparation protocol, however without NP incubation. Consequently, no gold deposition was visible, indicating that the applied gold-enhancement did not lead to unspecific staining.
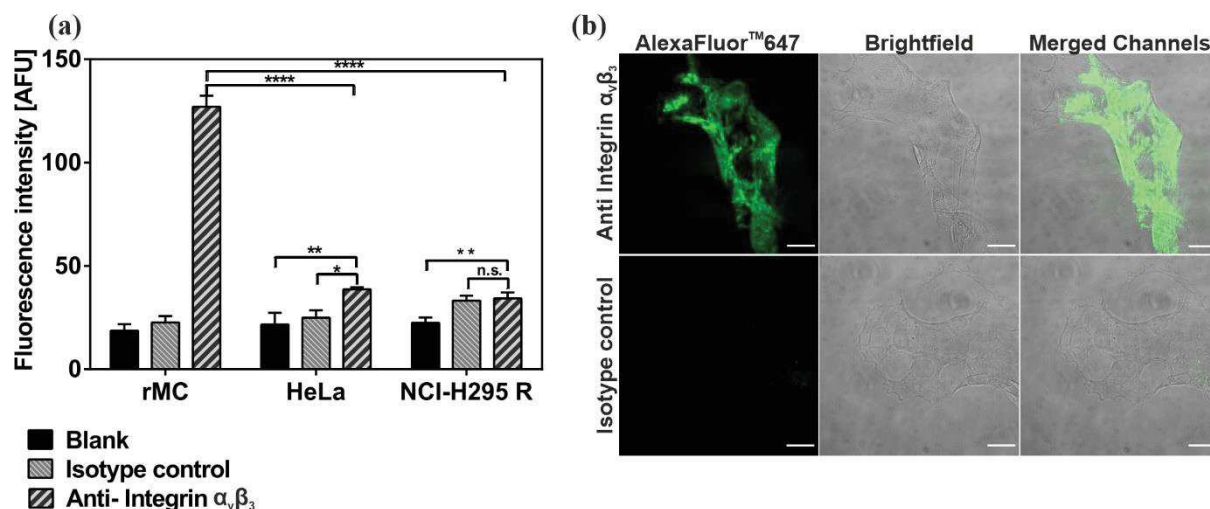
12 α$_V$β$_3$ expression

Figure S12. α$_V$β$_3$ expression by different cell types investigated by **(a)** flow cytometry and **(b)** CLSM. For cytometry analysis, unspecific binding sites were blocked with 2% BSA in DPBS and 10^5 cells were incubated for 1 h with a 1:20 dilution of AlexaFluor® anti - CD51/61 antibody in 0.1% BSA in DPBS (AlexaFluor® Mouse IgG1, κ Isotype Ctrl (FC) served as unspecific control). Thereafter, cells underwent several steps of DPBS washing and centrifugation. Finally, samples were resuspended in DPBS and analyzed using flow cytometry as previously described (FACS Calibur, excitation: 633 nm, emission: 661/16 nm bandpass filter). α$_V$β$_3$-derived fluorescence levels were thereby highest for rMCs. While NCI-H295R cells showed no significant integrin expression, HeLa cells were found to have a rather low integrin density, which, however, was still significantly greater than for the isotype control. Results represent mean ± SD (*n*=3).****P < 0.0001, **P < 0.01, *P < 0.05. (AFU, arbitrary fluorescence units.) For visualization and confirmation of flow cytometry results, rMCs were seeded into 8-well Ibidi slides (15.000 cells well^{-1}) and stained for α$_V$β$_3$ integrin as described above. Cells were then washed with DPBS, fixed with 4% PFA in DPBS and analyzed at a Zeiss LSM 710. CLSM images revealed a strong integrin signal that was co-localized with rMC cell body, indicating a substantial α$_V$β$_3$ receptor density on the surface of mesangial cells. Scale bar = 20 µm.
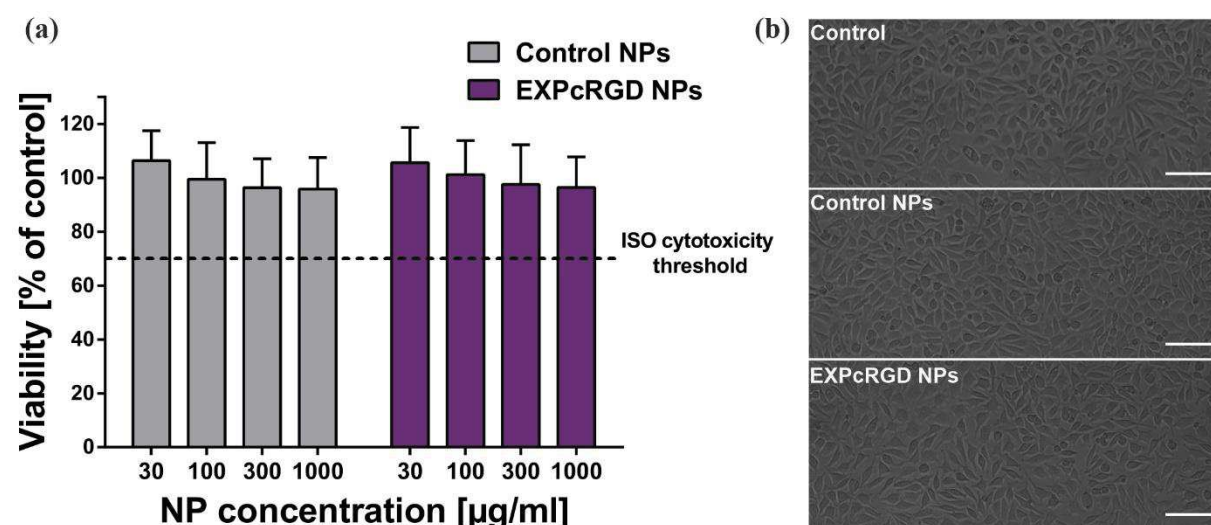
13   MTT assay

Figure S13. L-929 cell viability after 24 h of incubation with Control and EXPcRGD NPs. **(a)** Cytotoxicity of unfunctionalized and ligand-carrying NPs was tested as described before[9], using a 3-(4,5-dimethylthiazol-2-yl)-2,5-diphenyltetrazolium bromide (MTT) reduction assay according to ISO 10993 – 5:2009 (Biological evaluation of medical devices, part 5: Tests for in vitro cytotoxicity). In brief, mouse fibroblast L-929 cells were seeded at a density of 10,000 cells per well and incubated for 24 h (37 °C / 5 % CO_2). NPs were manufactured in mpH_2O under aseptic conditions. To further decrease microbial contamination, NPs were exposed to UV-light for 3 h. Samples were thereafter adjusted to concentrations from 30 to 1000 µg mL^{-1} in EMEM medium containing 10 % FCS and incubated with cells for 24 h. (Positive control: 0.1 % SDS; negative control: pure medium.) Thereafter, samples were removed and 50 µL EMEM medium containing 1.0 mg mL-1 MTT were added. After 2 h of incubation, the MTT solution was aspirated and 100 µL isopropanol was added to each well. After 30 min of incubation under gentle shaking and light exclusion, absorbance at 570 and 690 nm was measured using a FluoStar Omega fluorescence microplate reader (BMG Labtech, Ortenberg, Germany). Viability was assessed using the difference in absorbance at 570 and 690 nm and normalized to the negative control. Results represent mean ± SD (n = 6). **(b)** Brightfield images of L-929 cells incubated with either no NPs or 1000 µg mL^{-1} of Control/EXPcRGD NPs. (Scale bar 100 µm.)

14 Fluorescence analysis of kidney NP accumulation
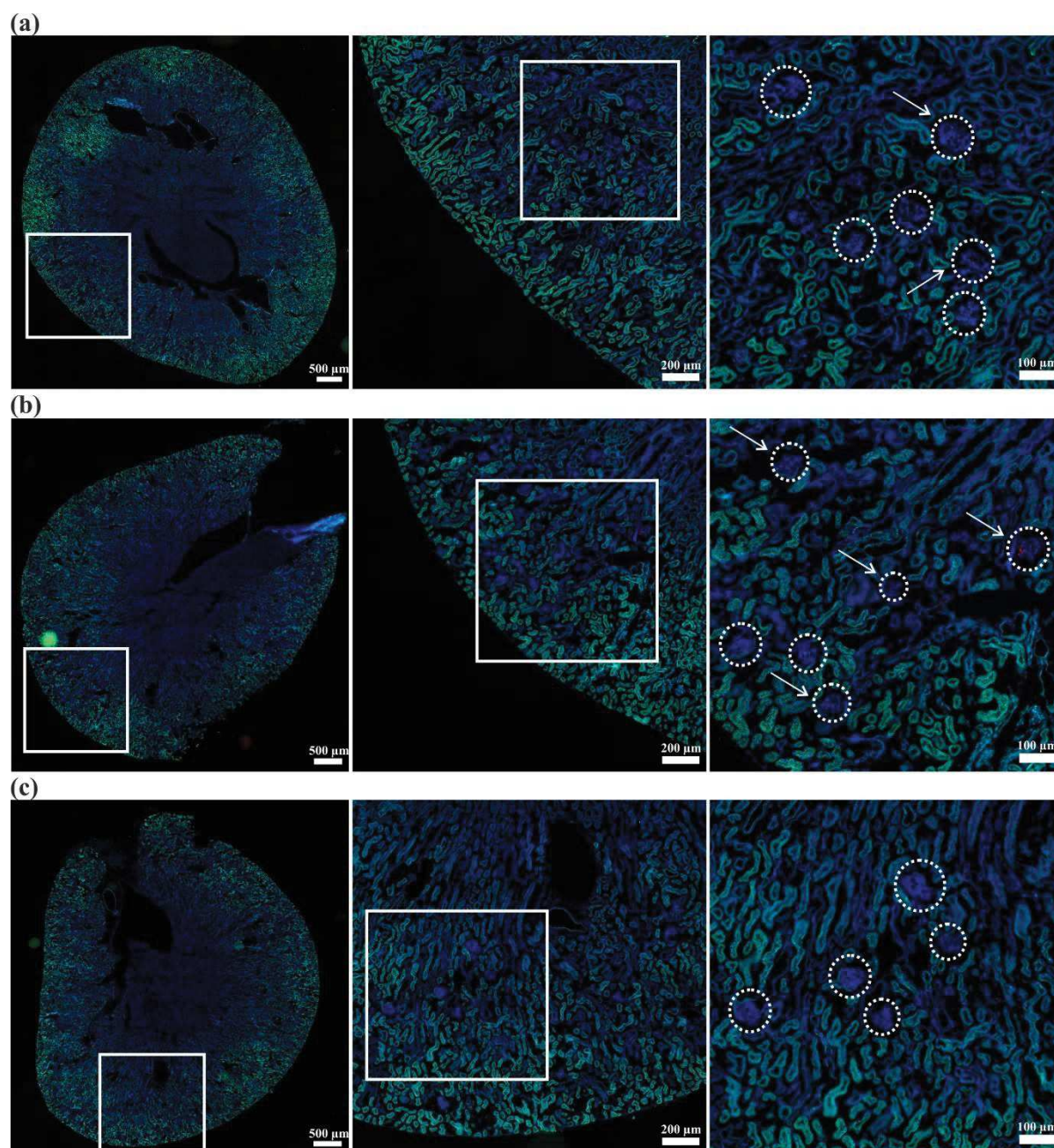
(a)

(b)

(c)

Figure S14. Fluorescence analysis of kidney cryosections. Cell nuclei were stained with DAPI (blue). Additionally, kidney autofluorescence (green) was recorded to facilitate histological evaluation of samples. NP-derived fluorescence is shown in red. **(a)** Unfunctionalized Control NPs showed only weak fluorescence levels in renal glomeruli, while EXP NPs **(b)** accumulated in a considerable amount in glomerular areas (white circles; arrows indicate fluorescence-positive glomeruli.). However, fluorescence intensity was significantly lower than for EXPcRGD NPs (Figure 7). **(c)** For cRGD NPs, fluorescence signal was minimal with no visible particle accumulation in any glomerulus. For all depicted NP species, tubular fluorescence was negligible, indicating that no renal filtration had taken place. (Images on the right show magnified sections of white boxes indicated in the respective left images.)

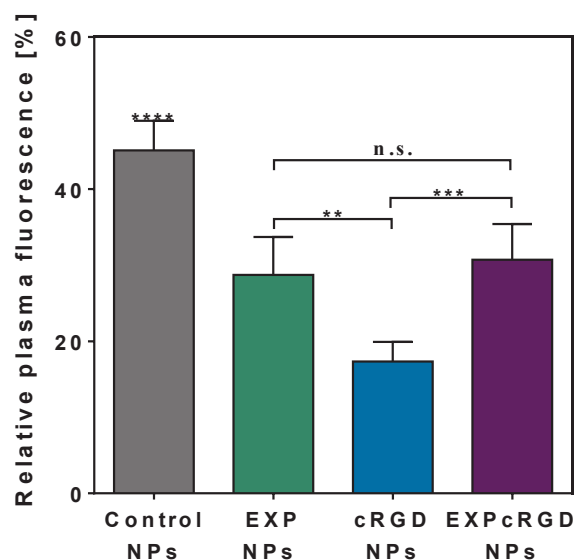## 15   Blood plasma fluorescence

Figure S15. Relative blood plasma fluorescence after NP injection. Control NPs exhibited the highest blood circulation values with almost 50% residual blood plasma fluorescence after 60 min of injection compared to the value after 5 min. In contrast to EXP NPs as well as EXPcRGD NPs, that both showed tolerable residual concentrations, cRGD NPs were rapidly cleared from the blood. Results represent mean $\pm$ SD (n=3). ****P < 0.0001, ***P < 0.001, **P < 0.01. (n.s.: not significant.)
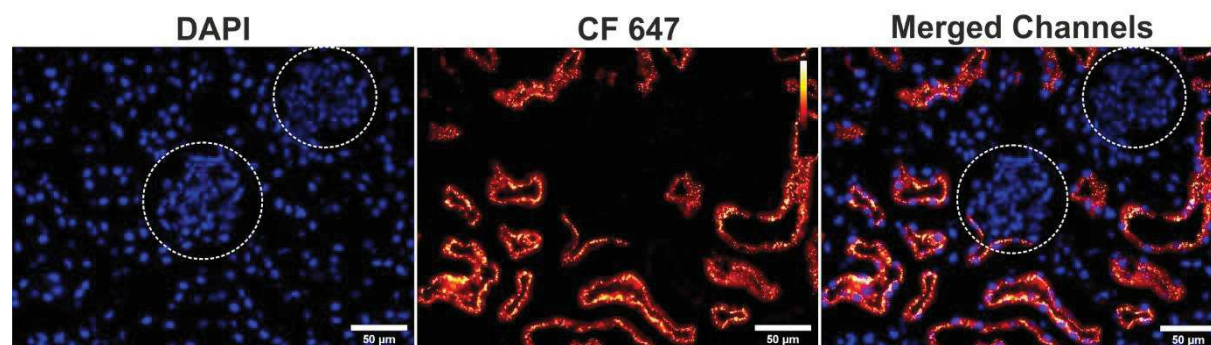
16   Kidney fluorescence distribution of free CF^{TM}647 dye

Figure S16. Fluorescence imaging of kidney cryosections after injection of free CF^{TM} 647 fluorescent dye. To visualize cell nuclei, sections were DAPI-stained (blue). After injection of a comparable molarity of free dye, strong fluorescence signals (red to white) could be detected in tubular areas of the kidney, indicating free renal filtration of the low-molecular dye. As expected, no intraglomerular accumulation could be detected (white circles). (Calibration bar: 0 - 65535 Gray Value.)

References

(1) Scott, R. P.; Quaggin, S. E. The Cell Biology of Renal Filtration. *J. Cell Biol.* **2015**, *209* (2), 199–210. DOI: 10.1083/jcb.201410017.

(2) Miner, J. H. The Glomerular Basement Membrane. *Exp. Cell Res.* **2012**, *318* (9), 973–978. DOI: 10.1016/j.yexcr.2012.02.031.

(3) Haraldsson, B.; Nyström, J.; Deen, W. M. Properties of the Glomerular Barrier and Mechanisms of Proteinuria. *Physiol. Rev.* **2008**, *88* (2), 451–487. DOI: 10.1152/physrev.00055.2006.

(4) Choi, H. S.; Liu, W.; Misra, P.; Tanaka, E.; Zimmer, J. P.; Itty Ipe, B.; Bawendi, M. G.; Frangioni, J. V. Renal Clearance of Quantum Dots. *Nat. Biotechnol.* **2007**, *25* (10), 1165–1170. DOI: 10.1038/nbt1340.

(5) H. Latta. An Approach to the Structure and Function of the Glomerular Mesangium. *J. Am. Soc. Nephrol.* **1992**, *2*, 65–73.

(6) Satchell, S. C.; Braet, F. Glomerular Endothelial Cell Fenestrations: an Integral Component of the Glomerular Filtration Barrier. *Am. J. Physiol. Renal Physiol.* **2009**, *296* (5), 947-956. DOI: 10.1152/ajprenal.90601.2008.

(7) Hennig, R.; Ohlmann, A.; Staffel, J.; Pollinger, K.; Haunberger, A.; Breunig, M.; Schweda, F.; Tamm, E. R.; Goepferich, A. Multivalent Nanoparticles Bind the Retinal and Choroidal Vasculature. *Journal of controlled release : official journal of the Controlled Release Society* **2015**, *220* (Pt A), 265–274. DOI: 10.1016/j.jconrel.2015.10.033.

(8) Abstiens, K.; Gregoritza, M.; Goepferich, A. M. Ligand Density and Linker Length are Critical Factors for Multivalent Nanoparticle-Receptor Interactions. *ACS applied materials & interfaces* **2019**, *11* (1), 1311–1320. DOI: 10.1021/acsami.8b18843.

(9) Abstiens, K.; Fleischmann, D.; Gregoritza, M.; Goepferich, A. M. Gold-Tagged Polymeric Nanoparticles with Spatially Controlled Composition for Enhanced Detectability in Biological Environments. *ACS Applied Nano Materials* **2019**, *2* (2), 917–926. DOI: 10.1021/acsanm.8b02165.

Chapter 4

Steric Shielding of cRGD-Functionalized Nanoparticles from Premature Exposition to Off-Target Endothelial Cells under a Physiological Flow

Abstract

One of the central impediments for the clinical translation of targeted nanomaterials is their extensive off-target deposition, which can be mainly attributed to addressed cellular surface structures being ubiquitously present in various other regions, such as the vascular system. This is especially important for the integrin receptor family, which is frequently addressed with ligands such as cRGD (cyclic Arg-Gly-Asp-D-Phe-Lys). Aside from upregulation during tumor progression, integrins also play a prominent physiological role in endothelial cells, to whom particles are exposed immediately after injection. However, there is a lack of understanding of how to modulate the usually undesirable interaction of nanoparticles (NPs) with these cells, especially under physiological conditions, that include the imminent impact of blood flow dynamics on NP behavior. Therefore, in this study, we introduced a steric shielding concept that is based on the addition of longer PEG chains into the NP corona, thereby individually camouflaging the ligand activity of cRGD-functionalized polymer NPs. More so, we implemented a method of endothelial cell culture and particle incubation under a constant flow, mimicking physiological conditions (shear stress = 2-14 dyn cm^{-2}). By controlling surface density (25-75 %) and length (3.5 kDa vs 5 kDa) of respective shielding elements, *in vitro* NP uptake into model endothelial cells could be precisely steered. Additionally, NP-cell interplay showed significant differences when examined under dynamic conditions, confirming the need for such investigations to improve the clinical translation of nanomaterials.

1   Introduction

Approaches for cell-specific drug delivery using nanoparticles (NPs) have become more and more sophisticated in recent years[1–4], yet the overall applicability of nanomaterials still remains at a comparably low level.[5] In an attempt to overcome this predicament, many concepts try to enhance site-selective targeting by equipping NPs with additional surface functionalities, thereby creating increasingly complex structures with oftentimes highly orchestrated cell recognition patterns.[6–9] However, the vast majority of NP targeting concepts still provides unsatisfactory bioavailability at the actual site of interest.[10,11] In many cases, NPs thereby initially show excellent levels of cell-selective *in vitro* targeting, due to the described characteristic surface structures, but fail to sufficiently transfer these features into a robust *in vivo* system. The underlying difficulty is thereby oftentimes not the actual target cell recognition, but an excessive particle clearance or off-target deposition beforehand.[12] In our view, the focus of NP targeting concepts should therefore not only lie on the final NP-target cell interaction, but the plentiful obstacles, that administered NPs have to pass before they reach their actual site of interest.[13,14]

One key impediment is thereby a possible clearance of particles *via* immunological barriers such as the mononuclear phagocyte system (MPS).[15] Yet, a frequently underestimated proportion of intravenously administered NPs fails to reach the target site not necessarily due to such active clearance patterns but rather because of a general accumulation in off-target regions that are passed through during blood circulation of NPs.[16,17] In that regard, the vasculature itself generally accounts for a considerable amount of NP deposition, mostly because of the sheer scale of vascular endothelial cells, that injected NPs are exposed to. This factor becomes even more critical, if NPs are additionally equipped with cell recognition sequences for structures that can also be expressed by endothelial cells.

Integrins, for instance, have frequently been used as a recognition motif for efficient tumor NP targeting due to their prominent role in cancer progression.[18–22] However, expression of these transmembrane receptors is not limited to malignant cells, but can also be found for the majority of cell types by facilitating a multitude of essential intra- and intercellular processes.[23–25] When it comes to vascular endothelial cells, $\alpha_v\beta_3$ integrin in particular has been found to be a key player during angiogenesis.[26,27] NPs, which carry $\alpha_v\beta_3$ integrin-targeting structures such as RGD (Arg-Gly-Asp)[28], are therefore most likely also subject to unintended off-target binding to integrin-positive endothelial cells after injection, thereby considerably reducing the prospects of satisfactory accumulation at the actual target site.

In that regard, we recently evaluated the *in vivo* accumulation of NPs functionalized with cRGD (cyclic Arg-Gly-Asp-D-Phe-Lys) in $\alpha_v\beta_3$ integrin-positive mesangial cells within renal glomeruli.[29] The targeting concept was thereby based on an initial extravasation of administered NPs through endothelial fenestrations into interstitial mesangial areas. Here, NPs would then initiate a ligand-mediated, active mesangial cell uptake which would be facilitated by a considerably decreased blood flow in respective areas.

cRGD NPs thereby showed a substantial integrin-mediated mesangial cell uptake *in vitro*, which was directly proportional to the cRGD surface density on the NP. However, despite this substantial target efficacy, the final mesangial *in vivo* accumulation of cRGD NPs was only marginal. In contrast, a hetero-functional NP species, that presented the cRGD ligand only after a spatial approach to the cell surface, mediated *via* an additional ligand, showed excellent levels of mesangial *in vivo* deposition. To our estimation, these sequentially binding NPs were protected from premature binding to integrin-positive endothelial cells by initially hiding the respective cRGD ligand. Following up on this observation, we were interested, whether these results could be used to create a novel flexible shielding concept for ligand-functionalized NPs.

In this context, most previous approaches aimed to manufacture so-called "stealth" particles covered by additional protective layers of either PEGylated polymers or other surface components[30,31], that should enable a generally low visibility for undesirable clearance routes such as the above mentioned MPS. In contrast, our concept was mainly focused on a more precise control of the actual ligand-receptor interaction (**Figure 1a**). By implementing additional shielding elements with a distinct length and surface density, excessive interaction of the cRGD ligand with off-target cell integrins should thereby be sterically hindered during initial NP circulation, while still allowing sufficient ligand-mediated NP uptake at the actual target region due to the decreased blood flow rate after extravasation. In this respect, a multitude of studies stress, that NP-cell interaction can be greatly influenced by parameters such as fluid dynamics, particle margination as well as physical forces within the vessel.[32–35] These effects are sometimes overlooked and could potentially lead to false conclusions regarding cell-particle interplay[36]. As the endothelium is directly exposed to the circulating blood[37], we considered it essential to evaluate the NP-cell interaction not only under the commonly applied static conditions, but also to assess the impact of fluid dynamics on the NP flow within the vessel and resulting cell uptake. In that regard, several studies have previously shown, that both the interaction between ligands and receptors and the spatial organization of macromolecular polymer chains can significantly be altered under flow conditions.[38,39]

For a more accurate assessment of the described shielding approach, we implemented an *in vitro* concept of both endothelial cell culture and NP incubation mimicking physiological flow conditions (**Figure 1b**). In that context, human umbilical vein endothelial cells (HUVECs) were initially cultured either under static conditions or under a constant shear stress to trigger flow-specific changes in cell morphology, that could potentially have an impact on cell-particle interactions.[35] Subsequently, cRGD-functionalized NPs containing different combinations of shielding elements were tested for endothelial cell uptake both under respective static and flow conditions.

The above mentioned shielding concept itself is based on a steric hindrance effect that has been described by a multitude of previous studies.[40,41] It relies on the scalable introduction of longer, carboxylic acid terminated poly(ethylene glycol) (PEG) chains into the surface of ligand-carrying polymeric NPs. To that end, integrin-targeting cRGD tethered to a shorter 2 kDa (2k) PEG chain was

shielded with different amounts (25-75 %) of either 3.5 k or 5 k PEG chains. As described above, these PEG shielding elements should hinder the cRGD ligand from prematurely interacting with integrins expressed by off-target endothelial cells during the initial phase of blood circulation (**Figure 1c**).

As a complete suppression of ligand activity would be counterproductive for the later intended NP uptake into the actual target cell, our goal was to realize a precise steerability of integrin-mediated NP uptake by adjusting both the density and length of respective shielding chains (**Figure 2a**). We hypothesized, that a partial shielding of cRGD visibility could potentially reduce excessive endothelial NP uptake while still guaranteeing sufficient target cell uptake due to the above described, more favorable physiological conditions as well as an overexpression of integrins at the target site.[42]

In the present study, we initially evaluated the effect of above-mentioned shielding parameters on endothelial NP uptake under static conditions. In a next step, these results were tested on their transferability to a more realistic set-up mimicking physiological flow conditions. Finally, the impact of different flow parameters on NP uptake was analyzed.
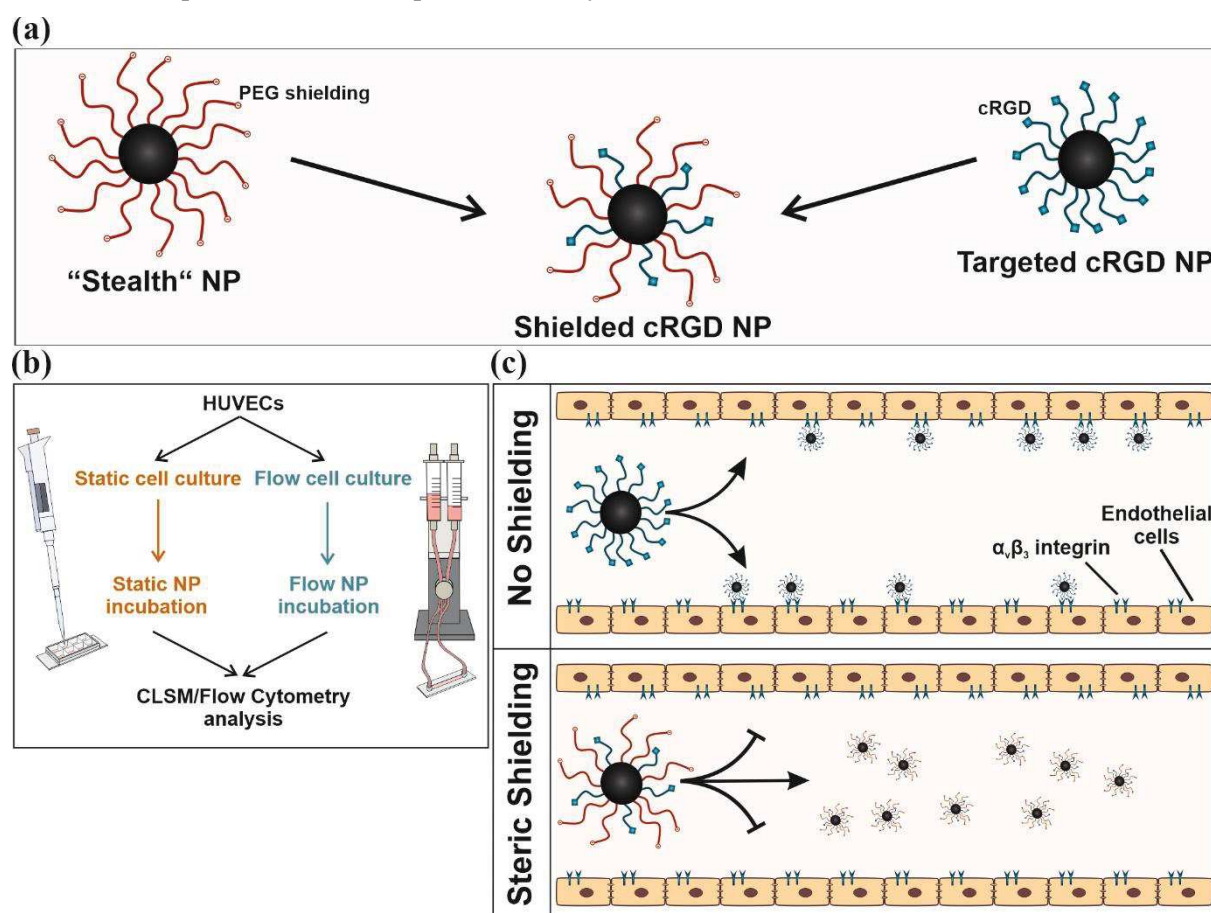

Figure 1. Experimental set-up and shielding concept. **(a)** Shielded cRGD NPs are designed to combine beneficial properties of both untargeted "stealth" and targeted cRGD NPs. **(b)** Static *vs.* dynamic cell culture and NP uptake. HUVECs were cultured for 3 days either under static conditions or under a constant shear stress of 10 dyn cm^{-2} to realistically mimic *in vivo* fluid dynamics. Subsequently, cells were incubated with different NP species, also either under static or under flow conditions (2/10/15 mL min^{-1}), and final NP uptake was assessed. **(c)** Concept of steric ligand shielding from premature exposition to off-target endothelial cells. In contrast to unshielded, cRGD-carrying NPs (top row), shielded cRGD NPs (bottom row) show a considerably reduced binding and uptake into $\alpha_v\beta_3$ integrin-positive endothelial cells.

2   Materials and Methods

2.1   Materials

Hydroxyl poly(ethylene glycol)carboxylic acid (Molecular weight: 2000, 3500 and 5000 g mol^{-1} ; COOH-PEG$_{2k/3.5k/5k}$-OH) was purchased from JenKem Technology USA Inc. (Allen, TX, USA). Resomer RG 502 (PLGA; lactide:glycolide, 50:50; molecular mass, 13,400 g mol^{-1}) was obtained from Sigma-Aldrich (Taufkirchen, Germany). Cyclic RGDfK (cRGDfK) was purchased from Synpeptide Co. Ltd. (Shanghai, China). AlexaFluor^{TM} 568 Hydrazide (Alexa568), Anti-Human CD144 AlexaFluor^{TM} 488 (Anti VE-Cadherin) and CellMask™ Deep Red Plasma Membrane Stain (CellMask DeepRed) were obtained from Fisher Scientific GmbH (Schwerte, Germany). AlexaFluor^{TM} 568 Phalloidin (Phalloidin) was purchased from Life Technologies GmbH (Darmstadt, Germany). The pump system, fluidic unit, perfusion sets, µ-slides I Luer 0.4 mm and µ-slides 8 Well were purchased from Ibidi GmbH (Planegg, Germany). All other substances were obtained from Sigma-Aldrich in analytical grade unless stated differently. Human Umbilical Vein Endothelial Cells (HUVECs) were obtained from PromoCell GmbH (Heidelberg, Germany). HUVECs were cultured in Endothelial Cell Growth Medium MV + Supplements (PromoCell GmbH) containing 10 % fetal bovine serum.

2.2   Polymer synthesis, cRGDfK coupling and PLGA fluorescent labeling

COOH-PEG$_{2k/3.5k/5k}$-PLA$_{10k}$ block polymers were synthesized *via* a previously established ring-opening polymerization of heterobifunctional PEG polymers and 3,6-dimethyl-1,4-dioxane-2,5-dione.[29,43–45] To receive ligand-functionalized polymers, synthesized COOH- PEG$_{2k/3.5k/5k}$-PLA$_{10k}$ was then linked to the lysin residue of cRGDfK as described before.[29,45,46] Resulting cRGDfK coupling efficiency as well as the later ligand surface density on prepared NPs were assessed with a pre-existing method using 9,10-phenanthrenequinone.[22,29] For a later NP visualization in CLSM and flow cytometry, NP core component PLGA was additionally coupled to either Alexa568 or CF^{TM} 647 amine as previously stated.[29,47]

2.3   NP preparation and characterization

For NP manufacture, we used a previously described solvent evaporation technique, whereby the organic phase consisted of a mix of all polymeric components (PEG-PLA/PLGA : 70/30) at a certain ratio, depending on the intended final surface amount of respective PEG chains (Figures S1 and S4). The exact preparation procedure can be found in our previous publications.[29,45,48]

2.4   NP characteristics

The hydrodynamic diameter and zeta potential levels of each NP batch were measured in 10 % (v/v) DPBS with a Malvern Zetasizer Nano ZS (Malvern, Herrenberg, Germany), using a 633 nm He-Ne laser (173° angle, 25 °C, RT).

2.5   HUVEC culture under static and flow conditions

To assess the impact of a constant media flow, HUVECs (passages 3-5) were seeded at a density of 250,000 cells slide^{-1} in a µ-slide I Luer with a channel height of 0.4 mm. After 2 h of cell attachment, the slide was connected to a red perfusion set filled with HUVEC growth medium containing 10 % fetal bovine serum. The perfusion system was connected to an Ibidi fluidic unit and the applied media flow was gradually increased for 2 h to a final shear stress of 10 dyn cm^{-2}. Cells were cultured under constant flow for 72 h at 37 °C and 5 % CO_2. For the static experiments, HUVECs were seeded in a Ibidi 8 well µ-slide at a density of 4000 cells well^{-1} and cultured without any applied flow for 72 h at 37 °C and 5 % CO_2, with media being exchanged every 24 h. Morphology changes during incubation were analyzed using a Leica DMIRB Inverted Microscope (Leica Microsystems, Wetzlar, Germany).

2.6   Immunostaining of changes in cell morphology

To compare cell morphology of HUVECs cultured under static and flow conditions, cells were cultured for 72 h as described above. Cells were thereafter washed with DPBS and fixed with 4 % paraformaldehyde (PFA) in DPBS for 10 min at RT. Samples were washed with DPBS, permeabilized with 0.1 % Triton-X 100 in DPBS for 10 min at RT, washed again and blocked for unspecific binding sites with a 1 % solution of bovine serum albumin (BSA) in DPBS for 30 min at RT. After an additional washing step with DPBS, a dilution of Phalloidin (1:200), 4′,6-Diamidine-2′-phenylindole dihydrochloride (DAPI, 1:200) and Anti VE-Cadherin (1:25) in DPBS was added for 1 h at RT. Samples were thereafter washed and analyzed at a Zeiss LSM 710 (Carl Zeiss Microscopy GmbH, Jena, Germany). For analysis of cell shape and orientation, Fiji software (Madison, WI, USA) was used. In brief, the signal for Anti VE-Cadherin staining was used to determine the shape of each cell, as VE-Cadherin acts as a junction protein located at the cell border. For each cell, the divergence angle of the central axis from a horizontal line (from -90 ° to +90 °), the ratio of major to minor axis as well as a circularity value (0-1; 1 indicates a perfect circle) were assessed.

2.7   Flow cytometry analysis of NP uptake under static conditions

To test the effect of shielding components on NP uptake into endothelial cells, HUVECs were seeded into a 24-well plate (20,000 cells well^{-1}) and incubated for 72 h at 37 °C and 5 % CO_2. NPs containing CF647-functionalized PLGA were prepared as described above and diluted to 0.1 mg NP mL^{-1} in Leibovitz´s buffer supplemented with 0.1 % BSA (LB + BSA). Cells were washed and NPs (300 µL)

were added for 45 min at 37 °C. After incubation, cells were washed, trypsinized and centrifuged for 5 min at 200 g and 4 °C. This procedure was repeated twice and final samples were resuspended and analyzed using a BD FACSCanto[TM] II (BD, Heidelberg, Germany). NP-derived fluorescence was excited at 633 nm and emission was recorded using a 660/20 nm bandpass filter. Resulting cytometry data of the gated population of viable cells was analyzed with Flowing software 2.5.1 (Turku Centre for Biotechnology, Turku, Finland).

2.8   CLSM analysis of NP uptake under static conditions

For visualization of NP uptake, HUVECs were seeded into Ibidi 8 well μ-slides at a density of 4000 cells well[-1] and cultured for 72 h at 37 °C and 5 % CO_2. NPs were manufactured as described above, however, in this case with Alexa568-modified PLGA. NP solutions were diluted to 0.1 mg NP mL^{-1} in prewarmed LB + BSA and 200 μL well[-1] were added to the cells. After 45 min of incubation, NPs were removed, cells were washed with DPBS and cells were stained with CellMask Deep Red (1:1000 in LB) for 5 min at 37 °C. Cells were thereafter washed and fixed in 4 % PFA in DPBS for 10 min at RT. After a washing step, a 1:200 dilution of DAPI in DPBS was added for 10 min at RT. Finally, cells were washed with DPBS and analyzed at the CLSM as described above.

2.9   Flow cytometry analysis of NP uptake under flow conditions

For analysis of NP deposition under constant flow, HUVECs were initially cultured in μ-slides for 72 h under a constant shear stress (10 dyn cm^{-2}) as described above. CF467-labeled NPs were adjusted to a final concentration of 0.1 mg mL^{-1} in LB + BSA. The μ-slide was disconnected from the perfusion set and washed with LB. The perfusion set was thereafter emptied, washed with LB, and filled with the NP solution. The μ-slide was connected to the perfusion set again and the NP solution was pumped through the system for 45 min at a flow rate of either 2 mL min^{-1}, 10 ml min^{-1} or 15 mL min^{-1} (shear stress = 1.8/9.2/13.8 dyn cm^{-2}). After incubation, the μ-slide was disconnected, cells were washed with DPBS, prepared for flow cytometry, and analyzed as described above.

2.10   CLSM analysis of NP uptake under flow conditions

To visualize NP deposition under flow conditions, HUVECs were cultured under a constant shear stress for 72 h as described above. Alexa568-labeled NPs were manufactured, and cells were incubated with NPs at a flow rate of 2 mL min^{-1} (shear stress = 1.8 dyn cm^{-2}) as described in the section above. Cells were thereafter prepared for CLSM imaging as already described for the static conditions.

3 Results and Discussion

3.1 Steric shielding can precisely regulate cRGD-mediated NP uptake under static conditions

For the intended shielding concept, we could build on an already established modular NP system, that is based on the combination of poly(lactic-co-glycolic acid) (PLGA) with PEG−poly(lactic acid) (PEG-PLA) block-copolymers of varying PEG chain lengths (**Figure S1**).[29] While core forming PLGA is added for enhanced NP integrity as well as for fluorescence visualization[29,47], carboxylic acid terminated PEG-PLA (COOH-PEG-PLA) polymers form a brush-like corona with protruding PEG chains due to their higher hydrophilicity. The targeting ligand cRGD was thereby covalently coupled to "short" PEG_{2k}-PLA_{10k} (cRGD-PEG_{2k}-PLA_{10k}), as previously described.[29,45] For the manufacturing of all NP types except Control NPs (100 % COOH-PEG_{2k}-PLA_{10k}), 25 % of cRGD-PEG_{2k}-PLA_{10k} were added, thereby obtaining a corresponding cRGD surface density of 25 % (**Figure 2d**). This level of ligand-functionalization was chosen as it had previously been shown to facilitate sufficient integrin-mediated NP uptake on the one hand and allow a precise control over shielding on the other hand.[29] While unshielded cRGD NPs additionally contained likewise "short" COOH-PEG_{2k}-PLA_{10k}, shielded NP species were manufactured with rising amounts of either COOH-$PEG_{3.5k}$-PLA_{10k} (3.5k shielding) or COOH-PEG_{5k}-PLA_{10k} (5k shielding) (**Figure S1**). Our assumption thereby was, that these longer PEG chains would gradually decrease the interaction between cRGD and the targeted $\alpha_v\beta_3$ integrin due to a steric hindrance effect. Despite the considerable changes in surface composition, all NP types could be manufactured in a narrow size range of 55 ± 10 nm (**Figure 2b**), thereby minimizing possible effects of size differences on the NP uptake.[49] Due to the carboxylic residues of applied COOH-PEG-PLA, NPs had a negative zeta potential of -10 ± 5 mV (**Figure 2c**), which has been shown to reduce unspecific binding to off-target cells as well as minimize plasma protein binding and possible phagocytosis.[44,50] Since the above described shielding components should primarily decrease NP interaction with integrin-positive endothelial cells, we decided to use HUVECs as a model cell type. These cells showed significant $\alpha_v\beta_3$ integrin expression as evaluated *via* immunocytochemistry using CLSM and flow cytometry (**Figure S2**).
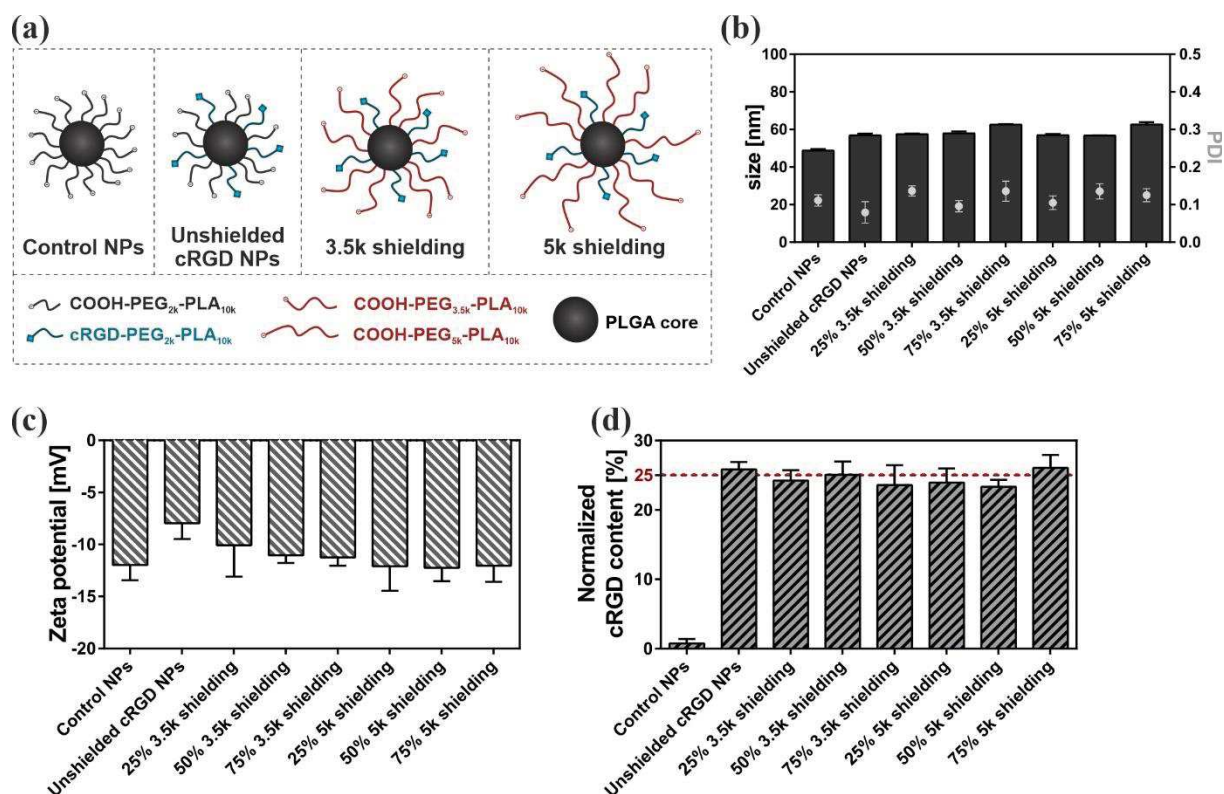
Figure 2. (a) Specification of tested NP species. **(b)** DLS analysis. **(c)** Zeta potential measurements. Due to the addition of negatively charged COOH-PEG-PLA, zeta potential values were all in a negative range of -7.5 to -12.5 mV. **(d)** cRGD quantification. cRGD surface density was evaluated by measuring the molar cRGD content per NP batch and normalizing it to the respective PEG content. Except for cRGD-free Control NPs, cRGD content was in a range of 25 ± 1.5% for all NP types. Results represent mean ± SD (n = 3).

To initially test the practicability of our shielding concept, HUVECs were cultured for 72 h under static conditions and subsequently incubated for 45 min with the above described, fluorescently labeled NP-formulations. Additionally, unshielded cRGD NPs with divergent ligand densities (5/15/35/50 %) were tested to assess whether the chosen cRGD amount of 25 % led to a satisfactory target efficacy compared to unfunctionalized NPs. Flow cytometry analysis of NP-cell interplay (**Figure 3**) revealed three major outcomes: First, NP uptake into endothelial cells gradually increased with a higher cRGD surface density, thereby proving the previously experienced endocytosis-mediating potential of the ligand (**Figure 3a**).[29] Second, as postulated above, NPs with a cRGD surface density of 25 % ("Unshielded cRGD NPs") proved to possess a satisfactory on-target efficacy, showing a 4-5-fold higher NP uptake compared to Control NPs without the respective ligand (**Figures 3a/b**). This indicates the significant impact of a sufficient cRGD functionalization on integrin-mediated NP endocytosis and was further confirmed by the observation, that addition of an excess of free cRGD (c = 500 µM) led to a drastically declined cell-associated fluorescence. Lastly, the introduction of above-described shielding components significantly reduced integrin-mediated NP uptake even though these shielded NPs carried the same cRGD surface density of 25 % (**Figure 3c**). Cell-associated fluorescence thereby gradually decreased both with higher surface densities (25-75 %) and greater length (3.5k-5k) of the shielding elements. By

adding 75 % of COOH-PEG$_{5k}$-PLA$_{10k}$ (75 % 5k shielding), NP uptake could even be reduced to a level that was no longer significantly different from the result for Control NPs.
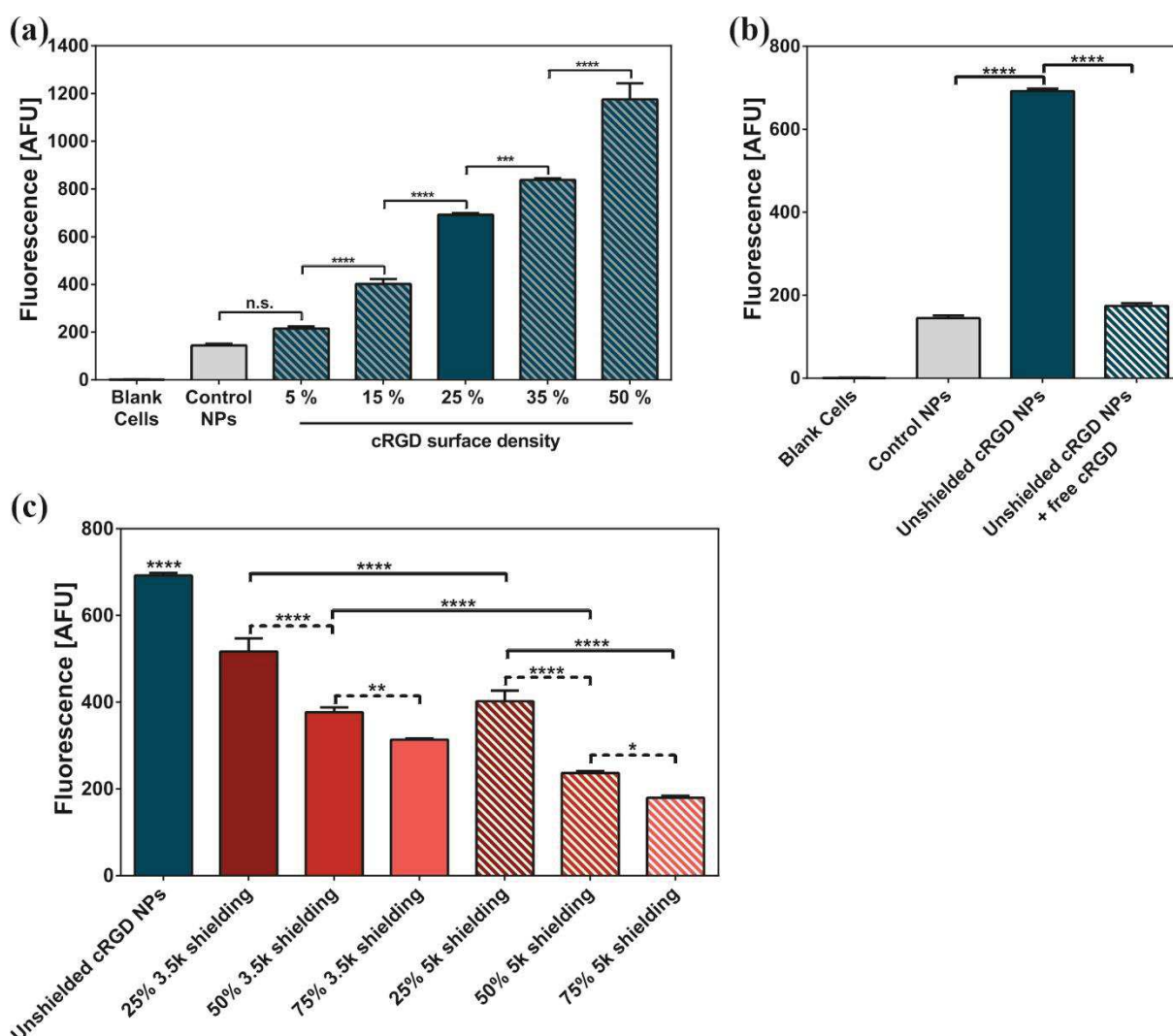

Figure 3. NP uptake under static conditions. **(a)** HUVEC uptake for unshielded, cRGD-functionalized NPs significantly increased with a greater cRGD density on the NP surface. **(b)** NP uptake for particles with a cRGD density of 25 % ("Unshielded cRGD NPs") was significantly higher than for unfunctionalized Control NPs. Addition of an excess of free ligand reversed this effect, thereby proving $\alpha_v\beta_3$-dependency of NP uptake. **(c)** While cell-associated fluorescence was highest for cRGD NPs without any additional shielding, the NP uptake gradually declined with higher surface density and length of the shielding elements. Results represent mean ± SD (n = 3). *P < 0.05. **P < 0.01. ***P <0.001 ****P < 0.0001. (n.s. not significant; AFU, arbitrary fluorescence units.)

To confirm flow cytometry results, the NP-associated fluorescence was further analyzed using confocal laser scanning microscopy (CLSM) **(Figure 4** and **Figure S3)**. For a better cell identification, HUVECs were additionally stained with CellMask^{TM} Deep Red (CellMask). Figure 4 displays the results for unshielded cRGD NPs (25 % cRGD) as well as NPs carrying 25-75 % of 3.5k shielding elements. While non-shielded cRGD NPs showed the highest extent of accumulation in endocytotic vesicles, cell-associated fluorescence was gradually declining for a higher surface density of 3.5k shielding elements.

Analysis of NPs carrying 5k shielding components showed even lower fluorescence levels (Figure S3) with NP accumulation being only marginal for 50-75 % of 5k shielding.

Both flow cytometry and CLSM analysis confirmed the practicability of our steric concept to shield cRGD from interaction with the targeted integrin by addition of longer PEG elements. While cRGD functionalization of NPs initially led to a sharp increase in HUVEC uptake compared to Control NPs, this effect could substantially be decreased by the addition of described shielding elements. However, as described shielded NP species carried a generally higher amount of PEG on their surface compared to unshielded cRGD NPs, we finally investigated, whether the experienced shielding was due to the postulated steric hindrance effect or merely because of a general increase in PEG surface amount, which could potentially also have an impact on the cRGD-integrin interaction or facilitate an extended NP circulation by lowering the tendency towards migration to the channel wall. To that end, unshielded cRGD NPs were manufactured not only with PEG chains of 2 kDa, but also with longer COOH-/cRGD-PEG-PLA (3.5k/5k). Flow cytometry analysis of endothelial NP uptake under static conditions thereby revealed only minor differences between all three unshielded cRGD NP species (**Figure S4).** Additionally, unshielded NP species (2k/3.5k/5k) showed a significantly greater cell endocytosis compared to NP types carrying shorter cRGD-PEG$_{2k}$-PLA$_{10k}$ and 75 % of either 3.5k or 5k shielding elements.

Because of this observation, we concluded that NP uptake was mainly lowered due to the described steric hindrance effect on the cRGD-integrin interaction and could therefore be regulated by control of the surface density and length of the implemented shielding components.
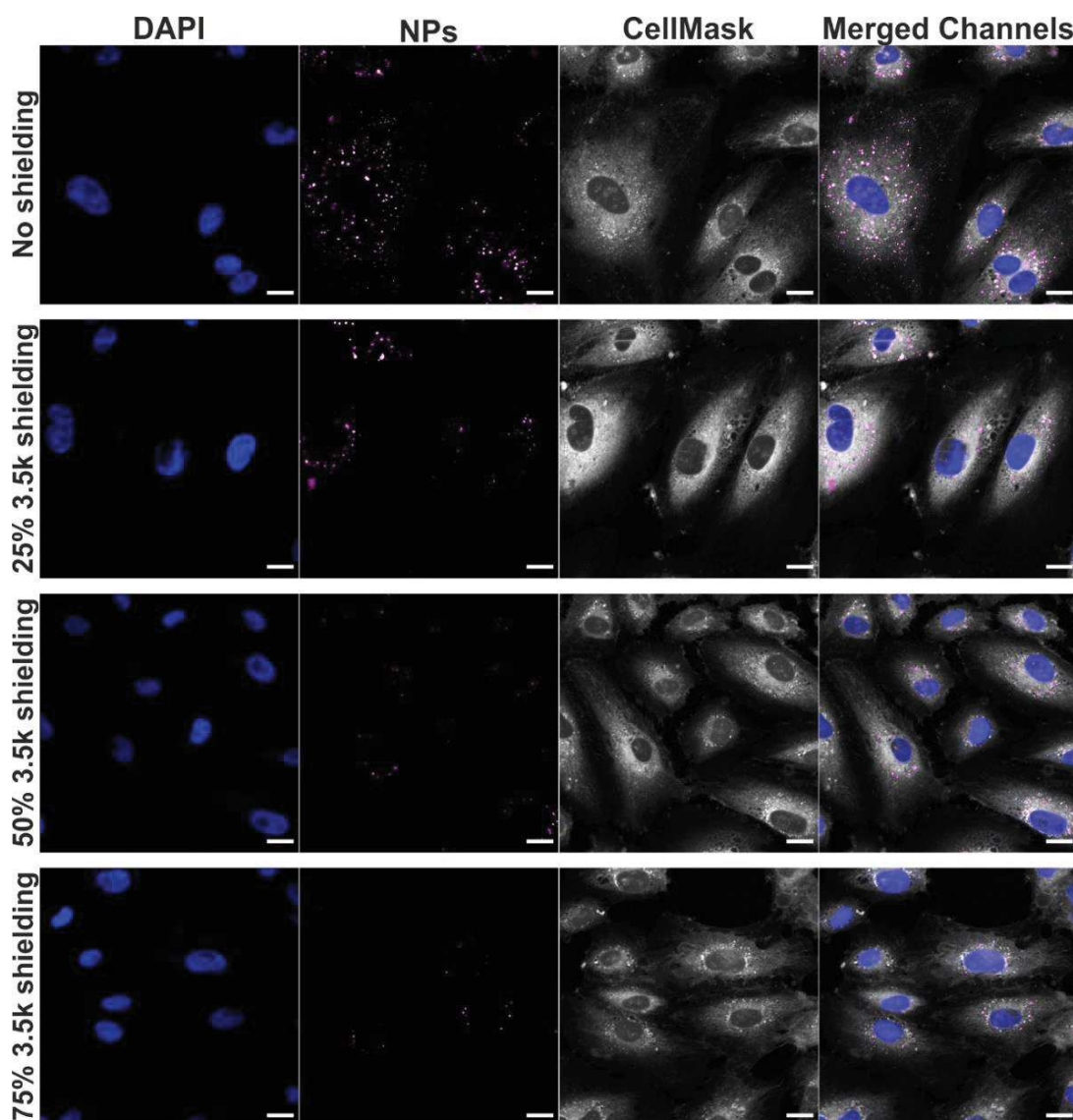
Figure 4. CLSM analysis of NP uptake under static conditions. Unshielded cRGD NPs (top row) showed a substantial accumulation in endocytotic vesicles (purple) within the HUVEC cytosol (grey). Addition of rising amounts of 3.5k shielding elements lead to a gradual decrease in cell-associated fluorescence, thereby proving flow cytometry results. (Scale bar 20 µm.)

3.2   Implementation of a physiological flow during cell culture to mimic *in vivo* conditions

As we were able to introduce a steric shielding strategy for satisfactory control of integrin-mediated NP uptake under static conditions, we were interested, whether this concept could be transferred to a set-up, that mimics actual *in vivo* conditions in a more realistic way.

Since endothelial cells are constantly subject to a significant blood flow and resulting shear stress in the vessel, we chose to initially culture HUVECs under respective flow conditions for 72 h to create a more accurate cell environment for later NP uptake studies. Endothelial cells were therefore exposed to a constant shear stress of 10 dyn cm^{-2}, which is in the range of physiological values and allows sufficient cell growth without excessive cell detachment or apoptosis.[51,52]

While endothelial cells showed a random orientation right after seeding, morphology drastically changed within 3 days of culture under flow conditions (**Figure 5a**). HUVECs thereby showed a gradual elongation as well as orientation along the applied flow, indicating the morphological reaction to the constant shear stress. To better visualize changes in cell morphology, immunocytochemistry of HUVECs cultured both under flow and static conditions was performed (**Figure 5b**). Antibody staining of intercellular junction protein vascular endothelial cadherin (VE-cadherin) indicated that HUVECs not only oriented along the applied flow, but also intensified cell-cell contacts to create a more stable cell layer and prevent detachment. F-actin staining also showed, that cytoskeletal filaments became more aligned, flow-oriented and enhanced. A subsequent image analysis of performed VE-cadherin staining of cultured endothelial cells confirmed this assessment by revealing considerable changes in cell morphology that HUVECs underwent, while being exposed to a constant shear stress for an extended period of time (**Figure S5**).
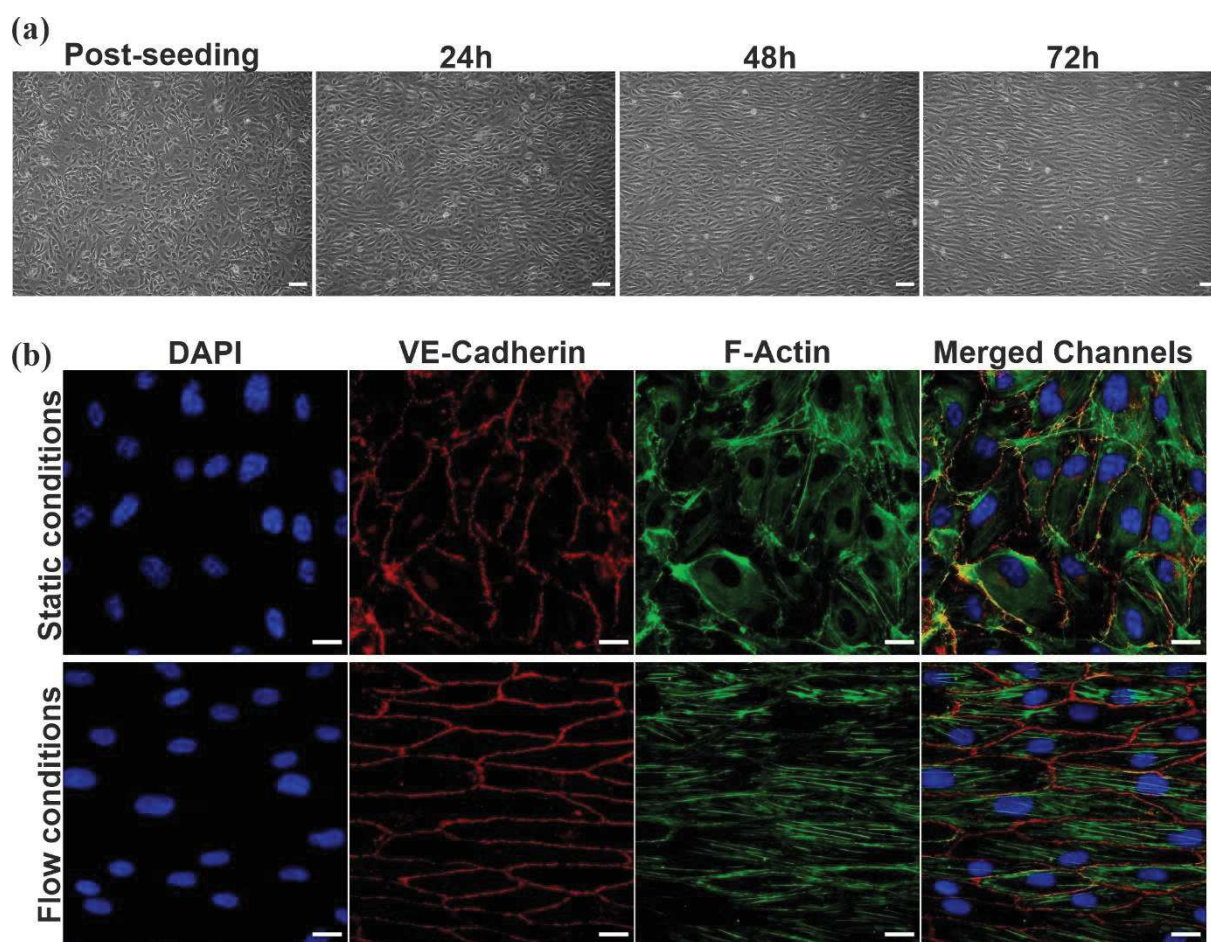

Figure 5. Changes in cell morphology due to the applied shear stress. **(a)** Brightfield images of HUVECS cultured under a constant shear stress (10 dyn cm^{-2}) revealed considerable elongation and orientation of cell bodies. (Scale bar 100 μm.) **(b)** CLSM analysis of HUVECs cultured under static (top row) and flow conditions (bottom row). Immunostaining for VE-cadherin (red) and F-actin (green) revealed substantial changes in cell morphology due to application of flow during cell culture. In all images for dynamic conditions, flow was applied from left to right. (Scale bar 20 μm.)

134

These results were in line with previous studies[35,53,54] and show the importance of adequate culturing conditions to create a realistic cell environment for further studies.[55] For all following NP uptake experiments, we decided to pre-culture HUVECs under the same flow conditions (10 dyn cm^{-2}; 72 h). This should on the one hand guarantee a realistic cell environment for the uptake studies, but on the other hand exclude any additional impact of different culturing parameters and resulting changes in cell phenotype on the actual NP endocytosis.

3.3   Steric shielding concept is transferable to more realistic flow conditions

Having implemented a cell culture model under constant physiological shear stress, we next intended to test the steric shielding concept on its transferability to flow conditions. In that context, numerous studies have previously shown, that NP-cell interaction can be significantly altered, if particles are subject to a constant flow during incubation.[35] Similar to the circulation in a blood vessel, NPs thereby not only have to migrate from the vessel or channel interior towards the wall (margination)[56], but also bind to the cell surface swiftly enough to prevent immediate detachment due to the applied flow.[57–59] Concerning our above-described shielding concept, it was particularly important to assess the impact of flow conditions not only on the actual ligand-receptor interplay, but also on the spatial organization of the polymeric shielding elements and their capacity to sufficiently camouflage the ligand activity. Therefore, we considered it essential to assess whether the discussed shielding of cRGD-integrin interaction is also maintainable once the particles are passing the endothelial cells at a certain flow rate.

To that end, HUVECs were initially cultured under flow conditions, triggering the above-described morphological changes (Figure 5). To realistically mimic NP circulation in the blood vessel, fluorescently labeled NPs were not pipetted on the culture slides but filled into the perfusion sets. This enabled the incubation of endothelial cells with NPs under various flow rates.

Figure 6 shows flow cytometry results of HUVECs after incubation with differently shielded NP species at a flow rate of 2 mL min^{-1} (equaling a shear stress of 1.8 dyn cm^{-2}) . In accordance with the results under static conditions (Figure 3), cRGD-mediated NP uptake was the highest for unshielded NPs and gradually decreased with a higher surface density and greater length of shielding elements. We therefore concluded that integrin-mediated particle uptake was similarly controllable as under static conditions.
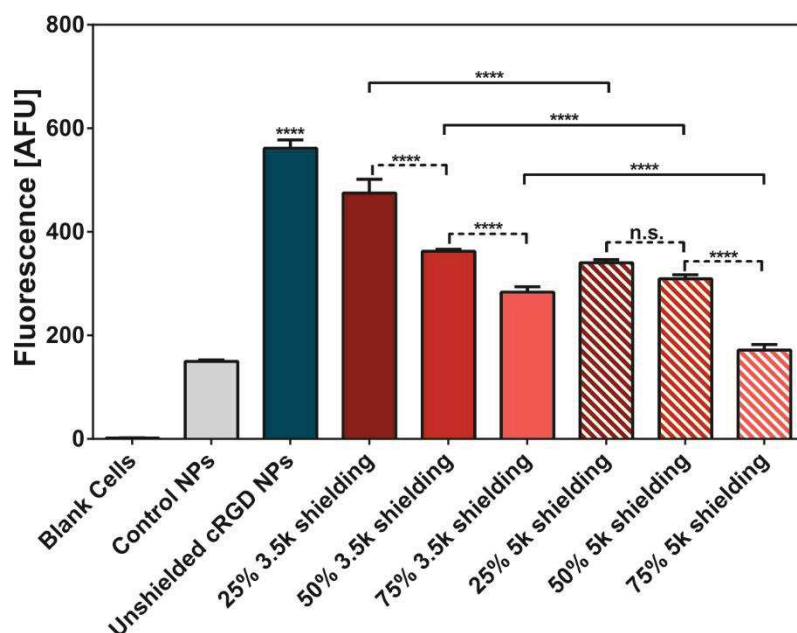
Figure 6. Flow cytometry analysis of NP uptake into HUVECs under flow conditions (flow rate = 2 mL min^{-1}; shear stress = 1.8 dyn cm^{-2}). Comparable to static conditions, cell-associated fluorescence for unshielded cRGD NPs was highest and gradually decreased with higher surface densities and chain lengths of respective shielding chains. NPs carrying 75 % of 5k shielding elements thereby showed no significant difference in cell uptake compared to ligand-free control NPs, indicating complete inhibition of ligand-receptor interplay. Results represent mean ± SD (n = 3). ****P < 0.0001. (n.s. not significant; AFU, arbitrary fluorescence units.)

CLSM analysis (**Figure 7**) further confirmed this observation with unshielded cRGD NPs showing the highest intracellular accumulation, while increasing amounts of 3.5k shielding elements lead to a substantial decline in fluorescence levels. This trend was even greater for longer 5k shielding elements, where only marginal fluorescence could be detected for higher amounts of 5k shielding (**Figure S6**). CellMask staining of HUVECs additionally showed the substantial elongation and alignment of cultured cells as a response to the previously applied shear stress. As the described concept of steric ligand shielding was also transferable to more realistic flow conditions, we were finally interested in the immediate impact of the applied flow rate on NP deposition. As the initially tested flow rate of 2 mL min^{-1} (shear stress = 1.8 dyn cm^{-2}) can be assigned to smaller vessels in the circulatory system with lower blood supply, we decided to additionally test higher flow rates of 10 and 15 mL min^{-1} (shear stress = 9.2/13.8 dyn cm^{-2}), which can be found in medium and larger arteries.[60]
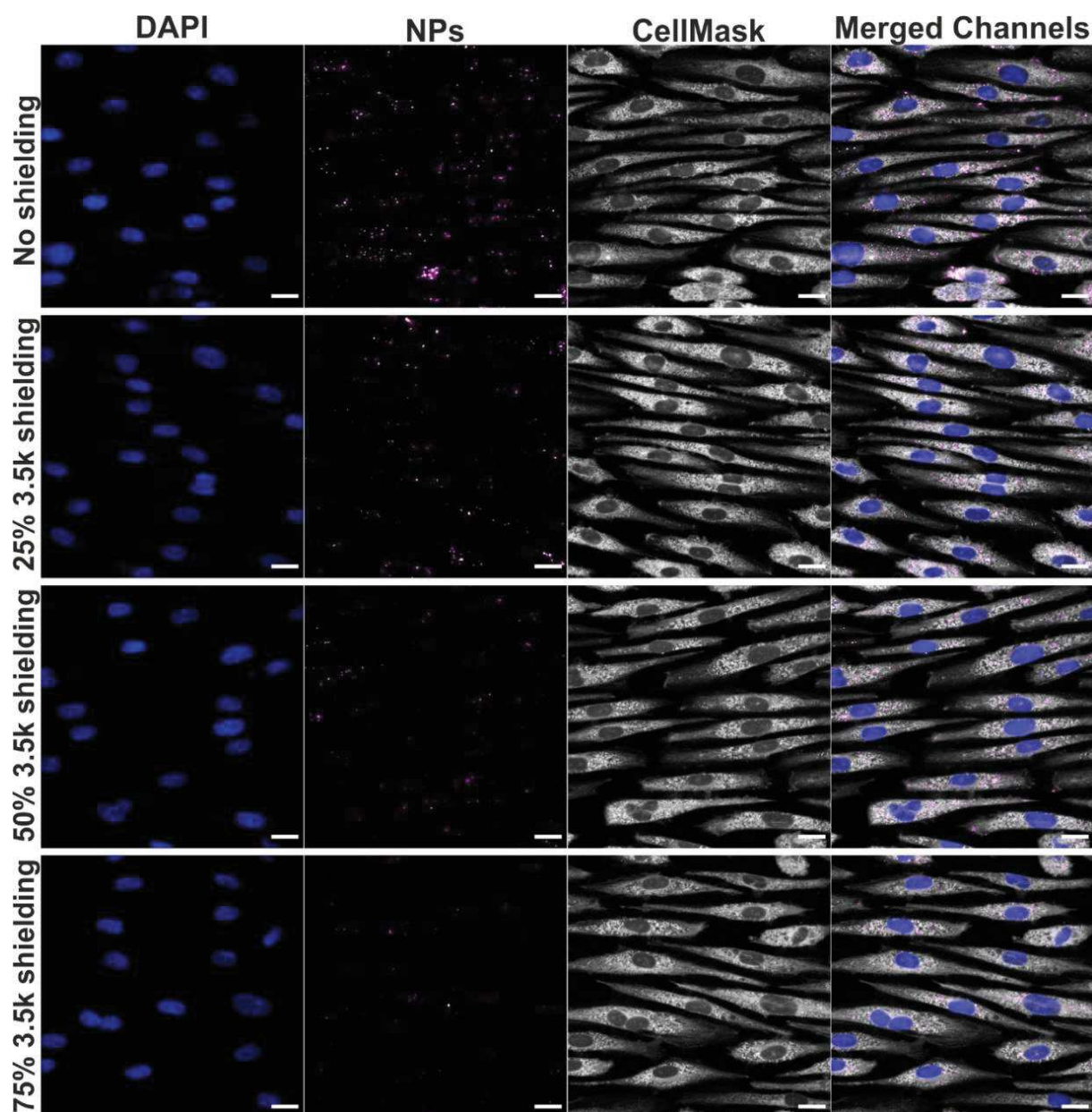
Figure 7. CLSM analysis of NP uptake under flow conditions. NP accumulation in endocytotic vesicles (purple) of the HUVEC cell cytosol (grey) was gradually decreasing with rising amounts of 3.5k shielding elements on the NP surface (top row to bottom row). CellMask staining also showed characteristic shear stress induced elongation of cultured cells as described above. (Scale bar 20 µm).

Our hypothesis thereby was, that the shielded NPs would show only neglectable endothelial deposition at these higher flow rates, which should correspond to the initial phase of NP circulation in larger blood vessels. At lower flow rates, on the contrary, NP uptake should increase in comparison, thereby facilitating particle accumulation at the actual target sites, where in most cases the corresponding blood flow is significantly lower.[61]
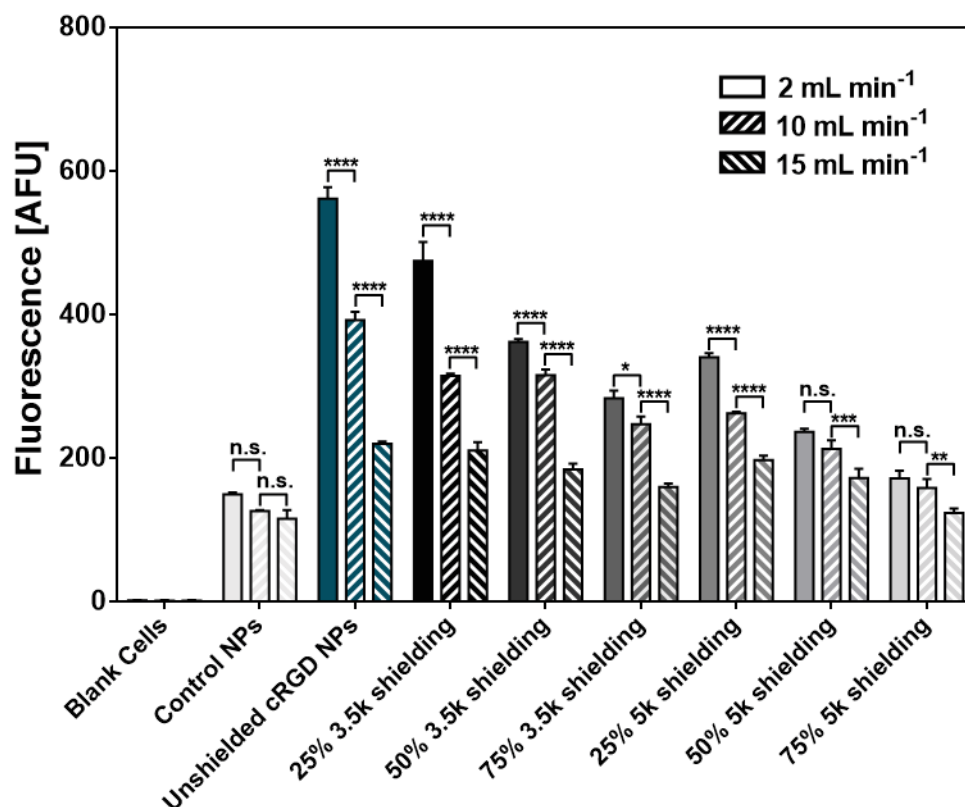
Figure 8. Flow cytometry analysis of NP uptake dependent on the applied flow rate. Cell-associated fluorescence for all flow rates gradually decreased with higher amounts and length of shielding elements. While cell uptake under a flow rate of 10 mL min^{-1} was significantly lower compared to a flow rate of 2 mL min^{-1} for almost all particle types, fluorescence levels for a high flow rate of 15 mL min^{-1} were considerably reduced with only marginal differences between the NP species. Results represent mean ± SD (n = 3). *P < 0.05. ****P < 0.0001. (n.s. not significant; AFU, arbitrary fluorescence units.)

Figure 8 shows the flow cytometry results of cells incubated with NPs under the above discussed flow rates. While the already described indirect proportionality of NP uptake and ligand shielding could also be found at flow rates of 10 and 15 mL min^{-1}, the absolute values of cell-associated fluorescence substantially decreased compared to the results at 2 mL min^{-1}. Interestingly, NP uptake into HUVECs was lower at higher flow rates even though the frequency and therefore the total amount of NPs passing by the cells was 5- and 7,5-fold higher. We therefore estimated, that due to the increased flow rate, cRGD-integrin interplay was additionally hindered, and NP were detached from the cell surface before they could initiate integrin-mediated endocytosis. This hypothesis was additionally supported by the observation, that levels of cell-associated fluorescence were minimal for the highest flow rate of 15 ml min^{-1}. Here, differences between the administered NP species were only marginal. However, this generally reduced cell uptake of all NP types at very high flow rates would be highly beneficial, considering that these conditions are merely present in very large vessels such as the aorta, where NP deposition is generally undesirable.

In summary, the introduced concept of steric ligand shielding was satisfactorily transferable to more realistic flow conditions and could also be maintained under application of higher shear forces, thereby proving its robustness regarding a possible *in vivo* application. The observed differences in cell uptake dependent on the applied flow rate are equally promising as they could be used to implement the above discussed targeting strategy for areas of lower blood flow, such as the initially mentioned mesangium. In this context, it would be valuable to also test the experienced effects for NPs with a varying diameter as a multitude of studies stress, that these characteristics can greatly influence particle migration towards the vessel wall or unspecific cell binding of NPs in general.[49,62]

Additionally, several further aspects would have to be assessed when it comes to the transferability of these results to an *in vivo* setting: First, in contrast to the applied continuous flow conditions, bigger arteries such as the aorta are subject to a pulsatile blood flow. However, it is important to mention, that cRGD-mediated NP deposition within these vessels would also be considerably hampered by to the substantial shear stress in these areas (Figure 8). Second, despite the above described low impact of the overall increased PEG surface amount on the actual cRGD-integrin interaction, NP *in vivo* circulation time would potentially be increased due to a general "stealth" effect, which even has been found for NP species with a very low PEG functionalization degree.[63] In the present study, this effect most probably only played a minor role due to the merely short incubation time of 45 min. Lastly, further blood components such as red blood cells[56,64], the constantly changing mixture of serum proteins as well as the MPS would certainly also have a significant impact on the transferability of this concept.

4 Conclusion

In this study, we were able to implement a steric shielding concept to efficiently control off-target accumulation of cRGD-functionalized NPs to integrin-positive endothelial cells *in vitro*. NP uptake could thereby be satisfactorily steered by addition of respective amounts of longer or shorter PEG-PLA components. Furthermore, the shielding concept was not only applicable under static conditions but could also be transferred to more realistic flow conditions. Interestingly, overall NP uptake was thereby decreasing with application of higher flow rates. Regarding possible *in vivo* applications, this fact could potentially be used to precisely target areas with lower blood supply like small arterioles or interstitial tissues such as the renal mesangium or the hepatic space of Disse. Thereby, partially shielded particles would initially be protected from off-target deposition in areas of high flow rates such as big arteries, which would increase the timespan for successful passive targeting strategies like extravasation through fenestrated endothelia in the kidney or liver.[65,66] Once the NPs would reach the area of interest, ligand-mediated endocytosis could be initiated due to the present lower flow rates and consequently greater timespan for the necessary cell-particle interaction. In that regard, we were already able to show, that partially shielded cRGD NPs still have a considerably enhanced mesangial target efficacy in contrast to ligand-free control NPs.[29]

To our estimation, the present study demonstrates, that novel concepts of actively targeted NPs should not only try to maximize on-target efficacy of manufactured systems, but also focus on a satisfactory steerability of the implemented targeting functionalities. This aspect becomes even more critical, when the targeted cell recognition sequences cannot be exclusively attributed to one single cell type, which is the case for the majority of all active targeting approaches. The shielding concept itself is thereby not limited to the presented materials as the general principle of a sterically hindered ligand-receptor interaction could also be realized with different polymers or other targeting sequences, provided that the visibility of the NP-bound ligand is lowered *via* the addition of longer protruding surface components. In our view, the above discussed results not only demonstrate the potential of described steric shielding concept, but also show, that transferability of *in vitro* experiments largely depends on a realistic reconstruction of actual *in vivo* conditions. Future approaches for efficient drug delivery applications should therefore not only focus on the profuse refining of targeting strategies but also scrutinize prevalent experimental set-ups. In this regard, approaches to mimic the actual geometry of the circulatory architecture play a pivotal role in facilitating more efficient drug delivery concepts.[34,67] Nevertheless, most concepts eventually still need to be tested in an *in vivo* setting, as the complex network of above mentioned physiological influence factors can hardly be mimicked *in vitro*.

References

(1) Friedman, A. D.; Claypool, S. E.; Liu, R. The Smart Targeting of Nanoparticles. *Current Pharmaceutical Design* **2013**, *35* (19), 6315–6329.

(2) Toy, R.; Roy, K. Engineering nanoparticles to overcome barriers to immunotherapy. *Bioengineering & translational medicine* **2016**, *1* (1), 47–62. DOI: 10.1002/btm2.10005.

(3) Petros, R. A.; Desimone, J. M. Strategies in the design of nanoparticles for therapeutic applications. *Nature reviews. Drug discovery* **2010**, *9* (8), 615–627. DOI: 10.1038/nrd2591.

(4) Park, W.; Na, K. Advances in the synthesis and application of nanoparticles for drug delivery. *Wiley interdisciplinary reviews. Nanomedicine and nanobiotechnology* **2015**, *7* (4), 494–508. DOI: 10.1002/wnan.1325.

(5) van der Meel, R.; Vehmeijer, L. J. C.; Kok, R. J.; Storm, G.; van Gaal, E. V. B. Ligand-targeted particulate nanomedicines undergoing clinical evaluation: current status. *Advanced Drug Delivery Reviews* **2013**, *65* (10), 1284–1298. DOI: 10.1016/j.addr.2013.08.012.

(6) Yoo, J.; Park, C.; Yi, G.; Lee, D.; Koo, H. Active Targeting Strategies Using Biological Ligands for Nanoparticle Drug Delivery Systems. *Cancers* **2019**, *11* (5), 640. DOI: 10.3390/cancers11050640.

(7) Modery-Pawlowski, C. L.; Gupta, A. S. Heteromultivalent ligand-decoration for actively targeted nanomedicine. *Biomaterials* **2014**, *35* (9), 2568–2579. DOI: 10.1016/j.biomaterials.2013.12.047.

(8) Ni, R.; Zhou, J.; Hossain, N.; Chau, Y. Virus-Inspired Nucleic Acid Delivery System: Linking Virus and Viral Mimicry. *Advanced Drug Delivery Reviews* **2016**, *106*, 3–26. DOI: 10.1016/j.addr.2016.07.005.

(9) Xiong, X.-B.; Uludağ, H.; Lavasanifar, A. Virus-Mimetic Polymeric Micelles for Targeted siRNA Delivery. *Biomaterials* **2010**, *31* (22), 5886–5893. DOI: 10.1016/j.biomaterials.2010.03.075.

(10) Wilhelm, S.; Tavares, A. J.; Dai, Q.; Ohta, S.; Audet, J.; Dvorak, H. F.; Chan, W. C. W. Analysis of Nanoparticle Delivery to Tumours. *Nature Reviews Materials* **2016**, *1* (5), 16014. DOI: 10.1038/natrevmats.2016.14.

(11) Dai, Q.; Wilhelm, S.; Ding, D.; Syed, A. M.; Sindhwani, S.; Zhang, Y.; Chen, Y. Y.; MacMillan, P.; Chan, W. C. W. Quantifying the Ligand-Coated Nanoparticle Delivery to Cancer Cells in Solid Tumors. *ACS nano* **2018**, *12* (8), 8423–8435. DOI: 10.1021/acsnano.8b03900.

(12) Moghimi, S. M.; Hunter, A. C.; Andresen, T. L. Factors Controlling Nanoparticle Pharmacokinetics:An Integrated Analysis and Perspective. *Annual review of pharmacology and toxicology* **2012**, *52*, 481–503. DOI: 10.1146/annurev-pharmtox-010611-134623.

(13) Barua, S.; Mitragotri, S. Challenges associated with Penetration of Nanoparticles across Cell and Tissue Barriers: A Review of Current Status and Future Prospects. *Nano today* **2014**, *9* (2), 223–243. DOI: 10.1016/j.nantod.2014.04.008.

(14) Shi, J.; Kantoff, P. W.; Wooster, R.; Farokhzad, O. C. Cancer nanomedicine: progress, challenges and opportunities. *Nature reviews. Cancer* **2017**, *17* (1), 20–37. DOI: 10.1038/nrc.2016.108.

(15) Yang, B.; Han, X.; Ji, B.; Lu, R. Competition Between Tumor and Mononuclear Phagocyte System Causing the Low Tumor Distribution of Nanoparticles and Strategies to Improve Tumor Accumulation. *Current Drug Delivery* **2016** (13), 1261–1274.

(16) Syed, A.; Chan, W. C. W. How nanoparticles interact with cancer cells. *Cancer treatment and research* **2015**, *166*, 227–244. DOI: 10.1007/978-3-319-16555-4_10.

(17) Alexis, F.; Pridgen, E.; Molnar, L. K.; Farokhzad, O. C. Factors Affecting the Clearance and Biodistribution of Polymeric Nanoparticles. *Molecular pharmaceutics* **2008**, *5* (4), 505–515. DOI: 10.1021/mp800051m.

(18) Hamidi, H.; Ivaska, J. Every step of the way: integrins in cancer progression and metastasis. *Nature reviews. Cancer* **2018**, *18* (9), 533–548. DOI: 10.1038/s41568-018-0038-z.

(19) Chen, K.; Chen, X. Integrin Targeted Delivery of Chemotherapeutics. *Theranostics* **2011** (1), 189–200.

(20) Winter, P. M.; Neubauer, A. M.; Caruthers, S. D.; Harris, T. D.; Robertson, J. D.; Williams, T. A.; Schmieder, A. H.; Hu, G.; Allen, J. S.; Lacy, E. K.; Zhang, H.; Wickline, S. A.; Lanza, G. M. Endothelial alpha(v)beta3 integrin-targeted fumagillin nanoparticles inhibit angiogenesis in atherosclerosis. *Arteriosclerosis, thrombosis, and vascular biology* **2006**, *26* (9), 2103–2109. DOI: 10.1161/01.ATV.0000235724.11299.76.

(21) Kluza, E.; van der Schaft, D. W. J.; Hautvast, P. A. I.; Mulder, W. J. M.; Mayo, K. H.; Griffioen, A. W.; Strijkers, G. J.; Nicolay, K. Synergistic Targeting of Alphavbeta3 Integrin and Galectin-1 with Heteromultivalent Paramagnetic Liposomes for Combined MR Imaging and Treatment of Angiogenesis. *Nano letters* **2010**, *10* (1), 52–58. DOI: 10.1021/nl902659g.

(22) Graf, N.; Bielenberg, D. R.; Kolishetti, N.; Muus, C.; Banyard, J.; Farokhzad, O. C.; Lippard, S. J. α(V)β(3) Integrin-Targeted PLGA-PEG Nanoparticles for Enhanced Anti-Tumor Efficacy of a Pt(IV) Prodrug. *ACS nano* **2012**, *6* (5), 4530–4539. DOI: 10.1021/nn301148e.

(23) van der Flier, A.; Sonnenberg, A. Function and interactions of integrins. *Cell and tissue research* **2001**, *305* (3), 285–298. DOI: 10.1007/s004410100417.

(24) Evans, R.; Patzak, I.; Svensson, L.; Filippo, K. de; Jones, K.; McDowall, A.; Hogg, N. Integrins in immunity. *Journal of cell science* **2009**, *122* (Pt 2), 215–225. DOI: 10.1242/jcs.019117.

(25) Katsumi, A.; Orr, A. W.; Tzima, E.; Schwartz, M. A. Integrins in mechanotransduction. *The Journal of biological chemistry* **2004**, *279* (13), 12001–12004. DOI: 10.1074/jbc.R300038200.

(26) Horton, M. A. The αvβ3 integrin "vitronectin receptor". *The International Journal of Biochemistry & Cell Biology* **1997**, *29* (5), 721–725. DOI: 10.1016/S1357-2725(96)00155-0.

(27) Hodivala-Dilke, K. Alphavbeta3 Integrin and Angiogenesis: a Moody Integrin in a Changing Environment. *Current opinion in cell biology* **2008**, *20* (5), 514–519. DOI: 10.1016/j.ceb.2008.06.007.

(28) Danhier, F.; Le Breton, A.; Préat, V. RGD-based strategies to target alpha(v) beta(3) integrin in cancer therapy and diagnosis. *Molecular pharmaceutics* **2012**, *9* (11), 2961–2973. DOI: 10.1021/mp3002733.

(29) Fleischmann, D.; Maslanka Figueroa, S.; Beck, S.; Abstiens, K.; Witzgall, R.; Schweda, F.; Tauber, P.; Goepferich, A. Adenovirus-Mimetic Nanoparticles: Sequential Ligand-Receptor Interplay as a Universal Tool for Enhanced In Vitro/In Vivo Cell Identification. *ACS applied materials & interfaces* **2020**, *12* (31), 34689–34702. DOI: 10.1021/acsami.0c10057. Published Online: Jul. 22, 2020.

(30) Knop, K.; Hoogenboom, R.; Fischer, D.; Schubert, U. S. Poly(ethylene glycol) in drug delivery:Pros and cons as well as potential alternatives. *Angewandte Chemie (International ed. in English)* **2010**, *49* (36), 6288–6308. DOI: 10.1002/anie.200902672.

(31) Gulati, N. M.; Stewart, P. L.; Steinmetz, N. F. Bioinspired Shielding Strategies for Nanoparticle Drug Delivery Applications. *Molecular pharmaceutics* **2018**, *15* (8), 2900–2909. DOI: 10.1021/acs.molpharmaceut.8b00292.

(32) Ziółkowska, K.; Kwapiszewski, R.; Brzózka, Z. Microfluidic devices as tools for mimicking the in vivo environment. *New J. Chem.* **2011**, *35* (5), 979. DOI: 10.1039/c0nj00709a.

(33) Valencia, P. M.; Farokhzad, O. C.; Karnik, R.; Langer, R. Microfluidic technologies for accelerating the clinical translation of nanoparticles. *Nature nanotechnology* **2012**, *7* (10), 623–629. DOI: 10.1038/nnano.2012.168.

(34) Gomez-Garcia, M. J.; Doiron, A. L.; Steele, R. R. M.; Labouta, H. I.; Vafadar, B.; Shepherd, R. D.; Gates, I. D.; Cramb, D. T.; Childs, S. J.; Rinker, K. D. Nanoparticle localization in blood vessels: dependence on fluid shear stress, flow disturbances, and flow-induced changes in endothelial physiology. *Nanoscale* **2018**, *10* (32), 15249–15261. DOI: 10.1039/c8nr03440k.

(35) Chen, Y. Y.; Syed, A. M.; MacMillan, P.; Rocheleau, J. V.; Chan, W. C. W. Flow Rate Affects Nanoparticle Uptake into Endothelial Cells. *Advanced materials (Deerfield Beach, Fla.)* **2020**, *32* (24), e1906274. DOI: 10.1002/adma.201906274.

(36) Cho, E. C.; Zhang, Q.; Xia, Y. The effect of sedimentation and diffusion on cellular uptake of gold nanoparticles. *Nature nanotechnology* **2011**, *6* (6), 385–391. DOI: 10.1038/nnano.2011.58.

(37) Krüger-Genge, A.; Blocki, A.; Franke, R.-P.; Jung, F. Vascular Endothelial Cell Biology: An Update. *International journal of molecular sciences* **2019**, *20* (18), 4411. DOI: 10.3390/ijms20184411.

(38) Model, M. A.; Omann, G. M. Ligand-receptor interaction rates in the presence of convective mass transport. *Biophysical journal* **1195**, *69*, 1712–1720.

(39) Binder, K.; Kreer, T.; Milchev, A. Polymer brushes under flow and in other out-of-equilibrium conditions. *Soft Matter* **2011**, *7* (16), 7159. DOI: 10.1039/c1sm05212h.

(40) Vonnemann, J.; Liese, S.; Kuehne, C.; Ludwig, K.; Dernedde, J.; Böttcher, C.; Netz, R. R.; Haag, R. Size dependence of steric shielding and multivalency effects for globular binding inhibitors. *Journal of the American Chemical Society* **2015**, *137* (7), 2572–2579. DOI: 10.1021/ja5114084.

(41) Jacobi, F.; Wilms, D.; Seiler, T.; Queckbörner, T.; Tabatabai, M.; Hartmann, L.; Schmidt, S. Effect of PEGylation on Receptor Anchoring and Steric Shielding at Interfaces: An Adhesion and Surface Plasmon Resonance Study with Precision Polymers. *Biomacromolecules* **2020.** DOI: 10.1021/acs.biomac.0c01060.

(42) Desgrosellier, J. S.; Cheresh, D. A. Integrins in cancer: biological implications and therapeutic opportunities. *Nature reviews. Cancer* **2010**, *10* (1), 9–22. DOI: 10.1038/nrc2748.

(43) Qian, H.; Wohl, A. R.; Crow, J. T.; Macosko, C. W.; Hoye, T. R. A Strategy for Control of "Random" Copolymerization of Lactide and Glycolide:Application to Synthesis of PEG-b-PLGA Block Polymers Having Narrow Dispersity. *Macromolecules* **2011**, *44* (18), 7132–7140. DOI: 10.1021/ma201169z.

(44) Abstiens, K.; Maslanka Figueroa, S.; Gregoritza, M.; Goepferich, A. M. Interaction of Functionalized Nanoparticles with Serum Proteins and its Impact on Colloidal Stability and Cargo Leaching. *Soft Matter* **2019**, *15* (4), 709–720. DOI: 10.1039/c8sm02189a.

(45) Abstiens, K.; Gregoritza, M.; Goepferich, A. M. Ligand Density and Linker Length are Critical Factors for Multivalent Nanoparticle-Receptor Interactions. *ACS applied materials & interfaces* **2019**, *11* (1), 1311–1320. DOI: 10.1021/acsami.8b18843.

(46) Valencia, P. M.; Hanewich-Hollatz, M. H.; Gao, W.; Karim, F.; Langer, R.; Karnik, R.; Farokhzad, O. C. Effects of Ligands with Different Water Solubilities on Self-assembly and Properties of Targeted Nanoparticles. *Biomaterials* **2011**, *32* (26), 6226–6233. DOI: 10.1016/j.biomaterials.2011.04.078.

(47) Abstiens, K.; Fleischmann, D.; Gregoritza, M.; Goepferich, A. M. Gold-Tagged Polymeric Nanoparticles with Spatially Controlled Composition for Enhanced Detectability in Biological Environments. *ACS Applied Nano Materials* **2019**, *2* (2), 917–926. DOI: 10.1021/acsanm.8b02165.

(48) Childs, C. E. The Determination of Polythethylene Glycol in Gamma Globulin Solutions. *Microchemical Journal* **1975**, *20*, 190–192.

(49) Albanese, A.; Tang, P. S.; Chan, W. C. W. The effect of nanoparticle size, shape, and surface chemistry on biological systems. *Annual review of biomedical engineering* **2012**, *14*, 1–16. DOI: 10.1146/annurev-bioeng-071811-150124.

(50) He, C.; Hu, Y.; Yin, L.; Tang, C.; Yin, C. Effects of Particle Size and Surface Charge on Cellular Uptake and Biodistribution of Polymeric Nanoparticles. *Biomaterials* **2010**, *31* (13), 3657–3666. DOI: 10.1016/j.biomaterials.2010.01.065.

(51) Reneman, R. S.; Hoeks, A. P. G. Wall shear stress as measured in vivo: consequences for the design of the arterial system. *Medical & biological engineering & computing* **2008**, *46* (5), 499–507. DOI: 10.1007/s11517-008-0330-2.

(52) Papaioannou, T. G.; Stefanadis, C. Vascular Wall Shear Stress: Basic Principles and Methods. *Hellenic journal of cardiology* **2005**, *46*, 9–15.

(53) McCue, S.; Dajnowiec, D.; Xu, F.; Zhang, M.; Jackson, M. R.; Langille, B. L. Shear stress regulates forward and reverse planar cell polarity of vascular endothelium in vivo and in vitro. *Circulation research* **2006**, *98* (7), 939–946. DOI: 10.1161/01.RES.0000216595.15868.55.

(54) Malek, A. M.; Izumi, S. Mechanism of endothelial cell shape change and cytoskeletal remodeling in response to fluid shear stress. *Journal of cell science* **1996**, *109*, 713–726.

(55) Chien, S. Effects of disturbed flow on endothelial cells. *Annals of biomedical engineering* **2008**, *36* (4), 554–562. DOI: 10.1007/s10439-007-9426-3.

(56) Müller, K.; Fedosov, D. A.; Gompper, G. Margination of micro- and nano-particles in blood flow and its effect on drug delivery. *Scientific reports* **2014**, *4*, 4871. DOI: 10.1038/srep04871.

(57) Samuel, S. P.; Jain, N.; O'Dowd, F.; Paul, T.; Kashanin, D.; Gerard, V. A.; Gun'ko, Y. K.; Prina-Mello, A.; Volkov, Y. Multifactorial determinants that govern nanoparticle uptake by human endothelial cells under flow. *International journal of nanomedicine* **2012**, *7*, 2943–2956. DOI: 10.2147/IJN.S30624.

(58) Mehrabadi, M.; Ku, D. N.; Aidun, C. K. Effects of shear rate, confinement, and particle parameters on margination in blood flow. *Physical review. E* **2016**, *93* (2), 23109. DOI: 10.1103/PhysRevE.93.023109.

(59) Khodabandehlou, K.; Masehi-Lano, J. J.; Poon, C.; Wang, J.; Chung, E. J. Targeting cell adhesion molecules with nanoparticles using in vivo and flow-based in vitro models of atherosclerosis. *Experimental biology and medicine (Maywood, N.J.)* **2017**, *242* (8), 799–812. DOI: 10.1177/1535370217693116.

(60) Seymour, R. S.; Hu, Q.; Snelling, E. P.; White, C. R. Interspecific scaling of blood flow rates and arterial sizes in mammals. *The Journal of experimental biology* **2019**, *222* (Pt 7). DOI: 10.1242/jeb.199554.

(61) Hunt, S. E.; Dorfman, K. D.; Segal, Y.; Barocas, V. H. A computational model of flow and species transport in the mesangium. *American journal of physiology. Renal physiology* **2016**, *310* (3), F222-9. DOI: 10.1152/ajprenal.00182.2015.

(62) Cooley, M.; Sarode, A.; Hoore, M.; Fedosov, D. A.; Mitragotri, S.; Sen Gupta, A. Influence of particle size and shape on their margination and wall-adhesion: implications in drug delivery vehicle design across nano-to-micro scale. *Nanoscale* **2018**, *10* (32), 15350–15364. DOI: 10.1039/c8nr04042g.

(63) Gref, R.; Lück, M.; Quellec, P.; Marchand, M.; Dellacherie, E.; Harnisch, S.; Blunk, T.; Müller, R. H. 'Stealth' corona-core nanoparticles surface modified by polyethylene glycol (PEG): influences of the corona (PEG chain length and surface density) and of the core composition on phagocytic uptake and plasma protein adsorption. *Colloids and Surfaces B: Biointerfaces* **2000**, *18*, 301–313.

(64) Müller, K.; Fedosov, D. A.; Gompper, G. Understanding particle margination in blood flow - A step toward optimized drug delivery systems. *Medical engineering & physics* **2016**, *38* (1), 2–10. DOI: 10.1016/j.medengphy.2015.08.009.

(65) Haraldsson, B.; Jeansson, M. Glomerular filtration barrier. *Current opinion in nephrology and hypertension* **2009**, *18* (4), 331–335. DOI: 10.1097/MNH.0b013e32832c9dba.

(66) Kang, J.-H.; Toita, R.; Murata, M. Liver cell-targeted delivery of therapeutic molecules. *Critical reviews in biotechnology* **2016**, *36* (1), 132–143. DOI: 10.3109/07388551.2014.930017.

(67) Khoury, M.; Epshtein, M.; Zidan, H.; Zukerman, H.; Korin, N. Mapping deposition of particles in reconstructed models of human arteries. *Journal of controlled release : official journal of the Controlled Release Society* **2019**, *318*, 78–85. DOI: 10.1016/j.jconrel.2019.12.004.

Chapter 4 – Supporting Information

Steric Shielding of cRGD-Functionalized Nanoparticles from Premature Exposition to Off-Target Endothelial Cells under a Physiological Flow
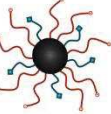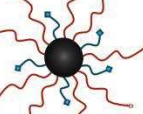
1   NP compositions

Figure S1. PEG-PLA composition of different NP species. While all NP types were manufactured with a PEG-PLA/PLGA ratio of 70/30, the composition of the respective PEG-PLA fraction was adjusted with regard to the intended particle features. Thereby, Control NPs contained 100 % of unfunctionalized $COOH-PEG_{2k}-PLA_{10k}$. To theoretically enable integrin-specific NP uptake, all other NP types were fabricated with an addition of 25 % $cRGD-PEG_{2k}-PLA_{10k}$. Besides, 25-75 % of either $COOH-PEG_{3.5k}-PLA_{10k}$ or $COOH-PEG_{5k}-PLA_{10k}$ were added to produce shielded NP species (3.5k/5k shielding).

2 $\alpha_v\beta_3$ expression
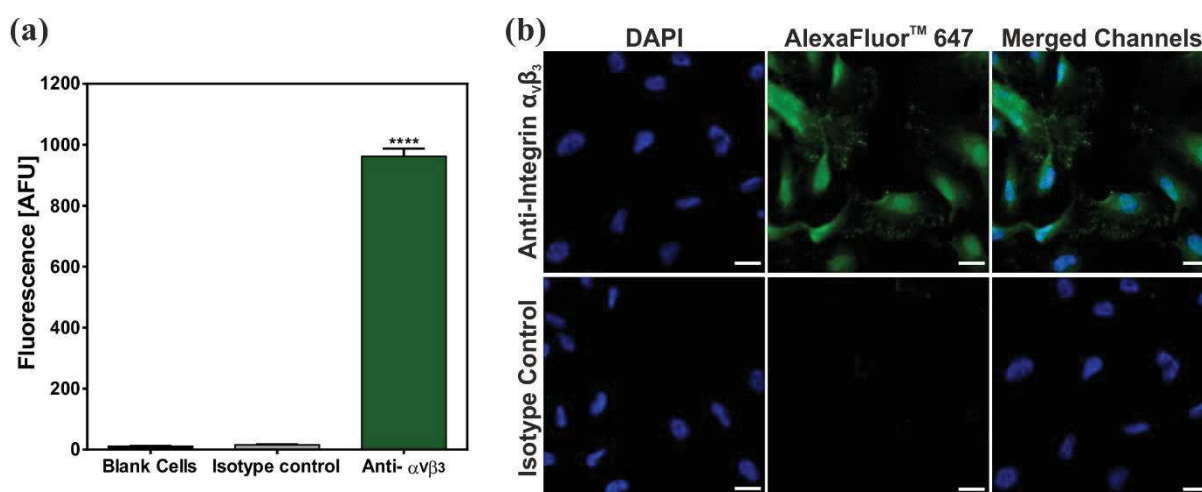
Figure S2. Quantification of $\alpha_v\beta_3$ expression by HUVECs. **(a)** Flow cytometry results. Antibody staining for $\alpha_v\beta_3$ integrin showed a significantly stronger fluorescence signal compared to both the isotype and blank control, proving a substantial integrin expression by HUVECs. Results represent mean ± SD (n = 3). **(b)** CLSM analysis confirmed flow cytometry results and showed a considerable cell surface fluorescence of respective integrin antibody, compared to the isotype control. (Scale bar 20 μm.)

3 CLSM uptake under static conditions
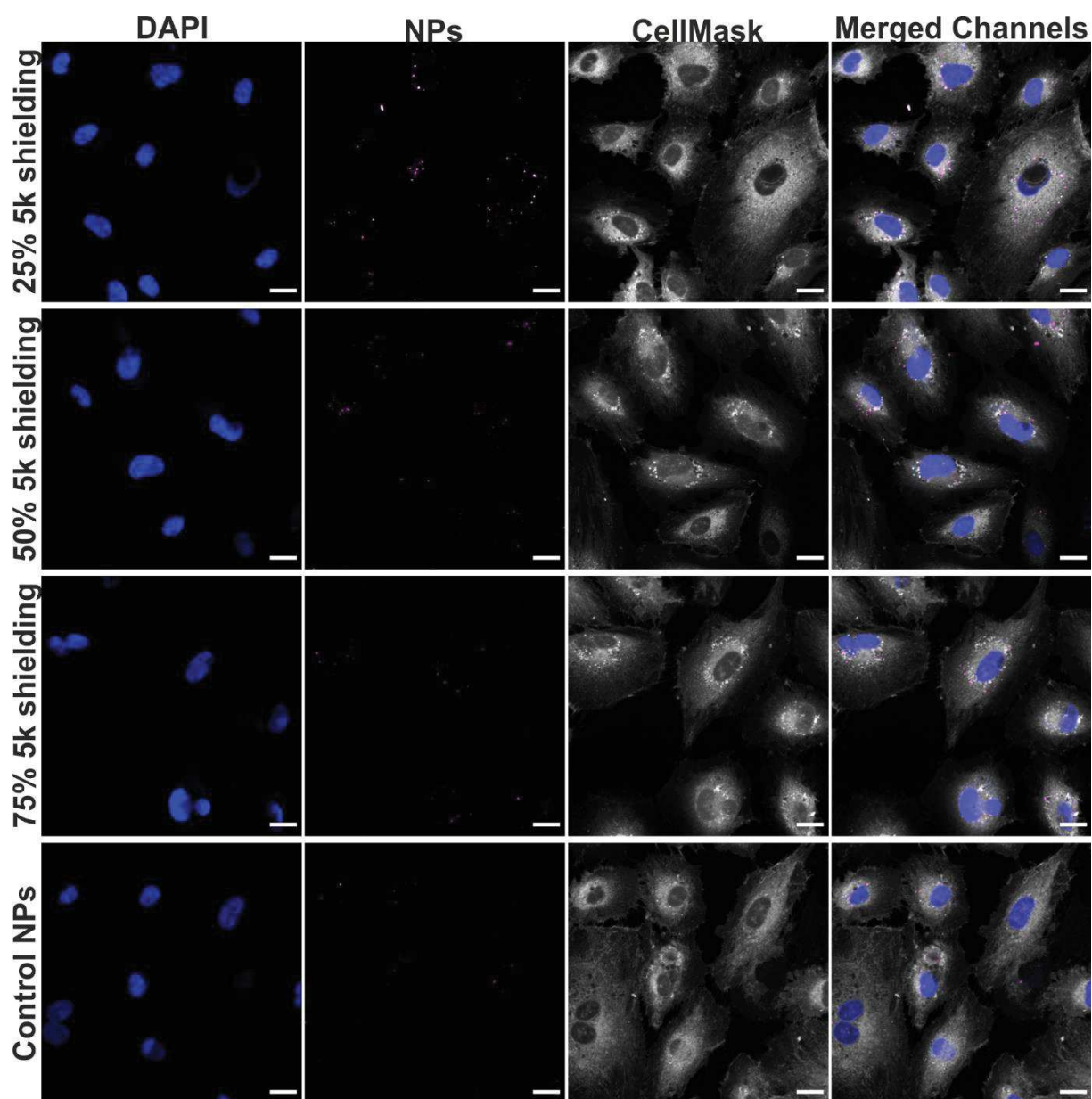
Figure S3. CLSM analysis of NP uptake under static conditions for 5k shielding and Control NPs. Addition of rising amounts of 5k shielding elements (row 1-3) lead to a gradual decrease in NP-associated fluorescence (purple) within the HUVEC cytosol (grey). NPs with 75 % 5k shielding showed only very weak NP uptake, which was comparable to the results for Control NPs (bottom row). (Scale bar 20 µm.)

4   Steric shielding effect
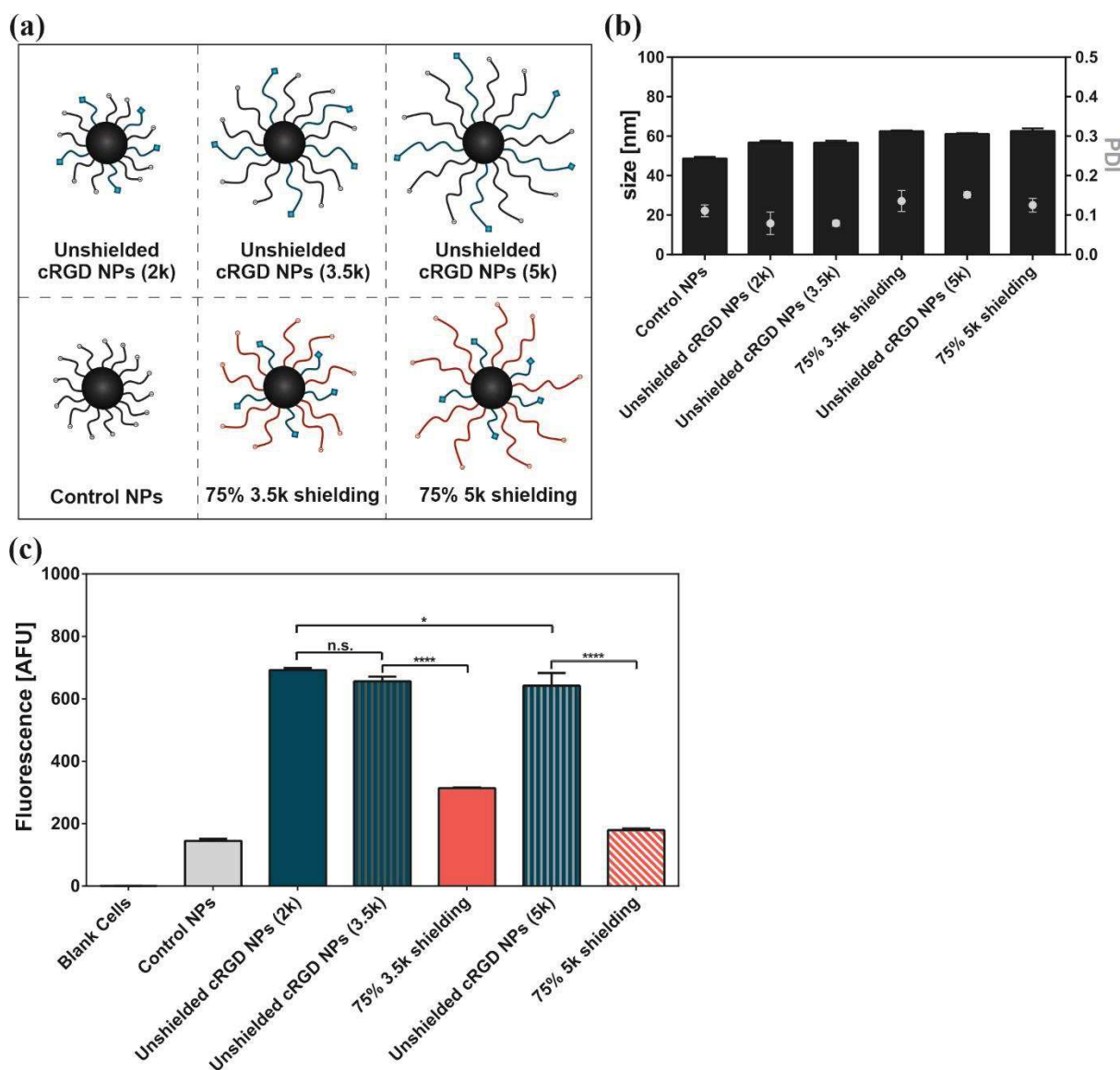
Figure S4. Confirmation of a steric shielding effect. **(a)** To assess a possible impact of the general composition of the NP PEG corona on the cRGD-integrin interaction and the resulting NP uptake, unshielded cRGD NPs (25 % cRGD) were manufactured not only with a PEG chain length of 2 kDa, but also with longer COOH-/cRGD-$PEG_{3.5k/5k}$-$PLA_{10k}$. **(b)** DLS analysis thereby revealed no considerable changes in NP diameter or size distribution. **(c)** Flow cytometry analysis of NP uptake under static conditions. While unshielded cRGD NPs (2k) showed a maximum endothelial cell uptake, fluorescence levels for unshielded cRGD NPs with longer PEG chain lengths (3.5k/5k) were comparably high, indicating that higher amounts of PEG on the NP surface had only a minor effect on the interaction between cRGD and integrin αvβ3. In contrast, sterically shielded NPs, that were manufactured with shorter cRGD-PEG_{2k}-PLA_{10k} but also carried 75 % of longer shielding chains (3.5k/5k), showed a significantly reduced endothelial cell uptake compared to all unshielded cRGD NP species (2k/3.5k/5k). Results represent mean ± SD (n = 3). *P < 0.05. ****P < 0.0001. (n.s. not significant; AFU, arbitrary fluorescence units.)

5 Morphological changes under flow incubation
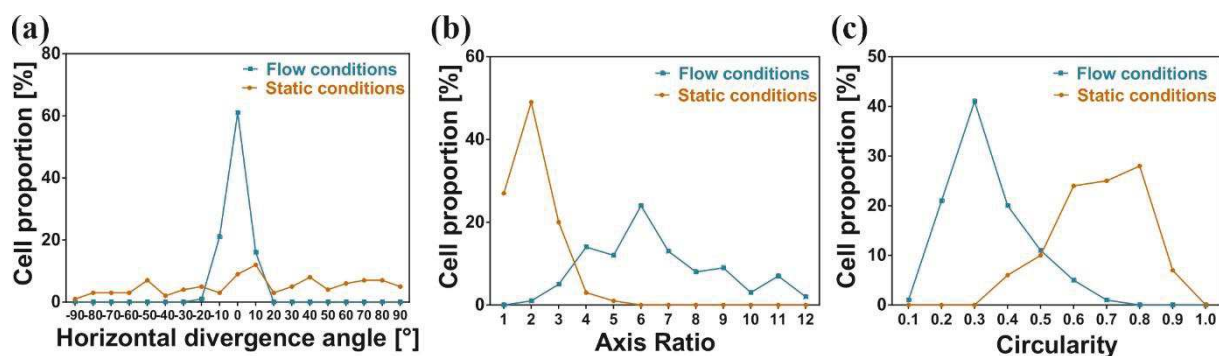
Figure S5. In order to quantify observed morphological changes between static and flow conditions, individual cell dimensions were assessed by image analysis of previously described VE-cadherin staining (Figure 5b). **(a)** Cells cultured under flow conditions showed only minimal divergence from the horizontal flow direction while cells cultured under static conditions were randomly spread without any apparent alignment. **(b)** Distribution of axis ratios for HUVECs cultured under flow showed a considerable right-shift compared to the static control, indicating substantial cell alignment. (Axis ratio = major axis/minor axis.) **(c)** Cell circularity under flow conditions was considerably decreased compared to static conditions. (Circularity value of 1.0 indicates a perfect circle.) (n = 100 cells for image analysis of each condition.)

6   CLSM uptake under flow conditions
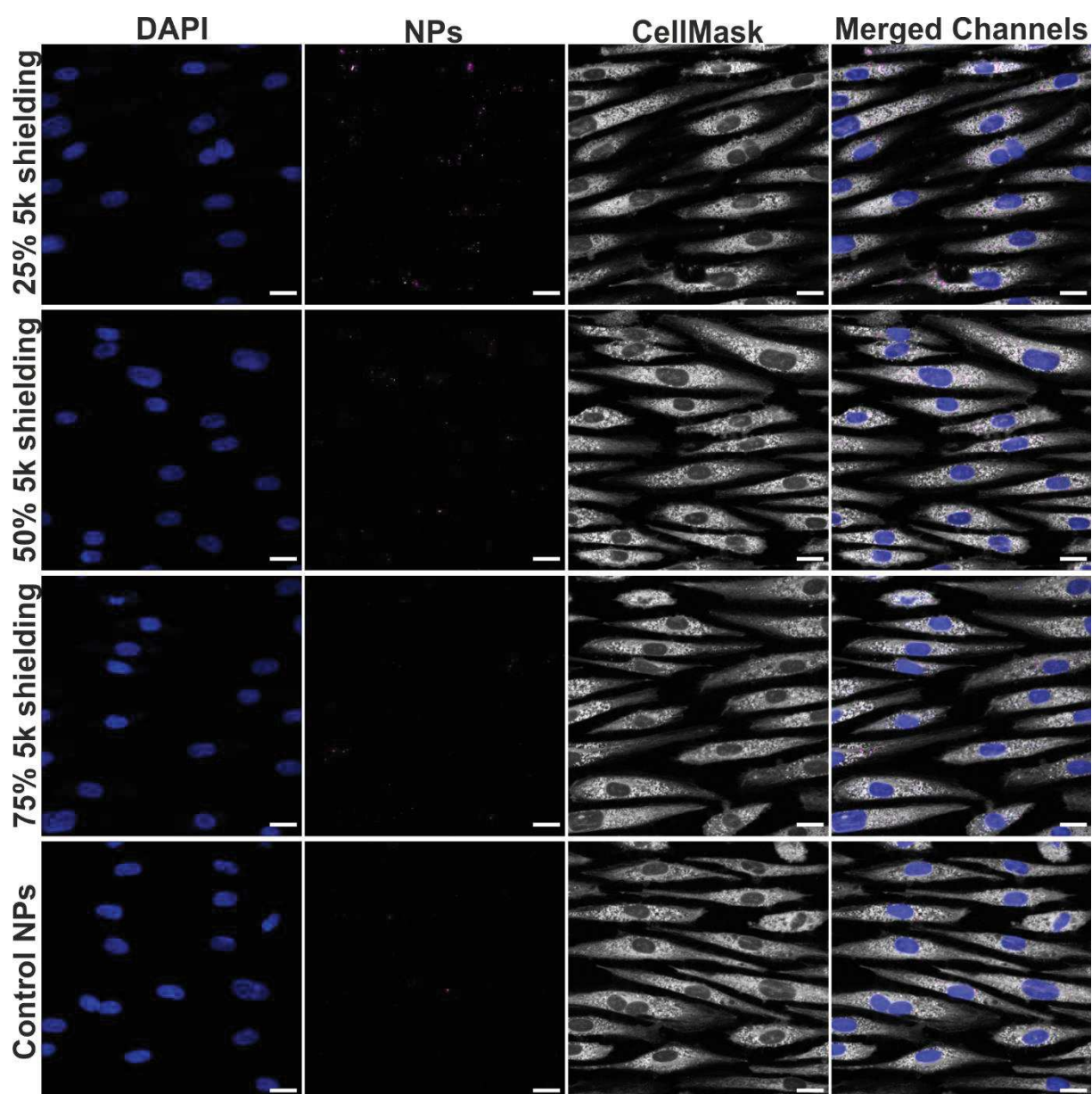
Figure S6. CLSM analysis of NP uptake under flow conditions (flow rate: 2 mL min^{-1}) for 5k shielding and Control NPs. NP-associated fluorescence (purple) within the HUVEC cell body (grey) gradually decreased for higher levels of shielding elements. NPs containing 50-75 % of 5k shielding did not show a considerably higher cell-associated fluorescence than unfunctionalized Control NPs. (Scale bar 20 μm.)

Chapter 5

Targeted Delivery of Soluble Guanylate Cyclase (sGC) Activator Cinaciguat to Renal Mesangial Cells *via* Virus-Mimetic Nanoparticles Potentiates Anti-Fibrotic Effects by cGMP-Mediated Suppression of the TGF-β Pathway

Abstract

Diabetic nephropathy (DN) ranks among the most detrimental long-term effects of diabetes, affecting more than 30% of all patients. Within the diseased kidney, intraglomerular mesangial cells play a key role in facilitating the pro-fibrotic turnover of extracellular matrix components and a progredient glomerular hyperproliferation. These pathological effects are in part caused by an impaired functionality of soluble guanylate cyclase (sGC) and a consequentially reduced synthesis of anti-fibrotic messenger 3´,5´-cyclic guanosine monophosphate (cGMP). Bay 58-2667 (cinaciguat) is able to re-activate defective sGC, however the drug suffers from poor bioavailability and its systemic administration is linked to adverse events such as severe hypotension, which can hamper the therapeutic effect. In this study, cinaciguat was therefore efficiently encapsulated into virus-mimetic nanoparticles (NPs) which are able to specifically target renal mesangial cells and therefore increase the intracellular drug accumulation. NP-assisted drug delivery thereby substantially increased *in vitro* potency of cinaciguat-induced sGC stabilization and activation as well as the related downstream signaling four- to five-fold. Also, administration of drug-loaded NPs provided a considerable suppression of the non-canonical transforming growth factor β (TGF-β) signaling pathway and the resulting pro-fibrotic remodeling by 50-100%, making the system a promising tool for a more refined therapy of DN and other related kidney pathologies.

1 Introduction

With an estimated number of almost 500 million cases worldwide and an ever-growing prevalence throughout all age groups, diabetes ranks among the top global causes of death.[1] While the imminent consequences of a poor blood sugar homeostasis are minor, long-term diabetic complications severely limit the life expectancy of patients. Among these, chronic kidney disease (CKD) and eventual end-stage renal disease (ESRD), i.e. the ultimate loss of kidney function, are regarded to be most critical.[2–4] Within the plentiful concomitants of CKD, diabetic nephropathy (DN) plays a central role, affecting more than 30% of diabetes patients.[5,6] When it comes to DN, a plethora of pathological renal processes are initiated by a prolonged state of hyperglycemia and eventually culminate in a progredient decline in glomerular filtration capacity.[7] Among these processes, increasing podocyte damage, basement membrane thickening as well as an increased glomerular hypertrophy and fibrosis have been found to play a substantial role.[8,9] In that context, the glomerular mesangium acts as a key player by facilitating a fundamentally altered production of extracellular matrix components as well as a broad range of paracrine interactions with glomerular endothelial cells and podocytes.[10–12] Within the highly complex network of molecular mechanisms, that are responsible for this pathological remodeling, progredient activation of transforming growth factor β (TGF-β) signal cascades has been shown to be a central element, especially regarding an increased ECM remodeling and glomerular hyperproliferation.[13–15] However, there is also unanimous evidence, that apart from other pathological triggers such as elevated oxidative stress or an enhanced activity of the renin angiotensin aldosterone system (RAAS), a dysfunctionality of nitric oxide (NO) and its downstream cascade plays a pivotal role.[16–18] Under physiological conditions, NO can bind the intracellularly located soluble form of the guanylate cyclase (sGC), that then transforms guanosine triphosphate (GTP) to 3′,5′-cyclic guanosine monophosphate (cGMP), a central messenger for the downregulation of excessive glomerular fibrosis and hyperproliferation.[19–21] Under hyperglycemic conditions, however, NO production is impaired due to a progrediently dysfunctional endothelium.[22] Also, the above mentioned, hyperglycemia-induced oxidative stress can lead to an oxidation or even loss of the sGC heme prosthetic group (Fe^{3+}-/Apo-sGC), making the enzyme unresponsive to any NO activation.[23,24] Initially, pharmacological research concerning the NO-cGMP cascade – particularly in the field of cardiovascular disease - was mainly focused on an increase of nitric oxide levels *via* NO-donating substances or an inhibition of cGMP-degrading phosphodiesterases.[25] However, the impact of these approaches as well as sGC stimulators such as riociguat relies on a sufficient residual activity of sGC and is therefore severely limited, if an sGC heme oxidation or loss has already taken place. In contrast, sGC activators such as Bay 58-2667 (cinaciguat; CCG) are able to specifically bind and thus re-activate defective Fe^{3+}-/Apo-sGC independently of the presence of NO. This characteristic provides the fundamental advantage, that a therapeutic effect is also achievable in a more advanced stage of disease. Initial research on CCG was mainly focused on its therapeutic effects regarding the cardiovascular system[26], however there is also promising evidence concerning a beneficial role in above discussed renal fibrosis and

hyperproliferation[27–29], whereby a CCG-mediated sGC activation has been shown to reduce TGF-β expression as well as non-canonical TGF-β signaling *via* extracellular-regulated protein kinase 1/2 (ERK 1/2).[30,31] While these results were highly encouraging, CCG can however also potentially cause unfavorable adverse events such as a strong hypotension due to its imminent effect on the vasculature after a systemic administration.[32] The application of the free drug is additionally complicated by its profound lipophilicity which could possibly hamper the therapeutic success due to a reduced solubility or a generally disadvantageous biodistribution.[33] To our estimation, CCG would therefore substantially profit from a drug delivery system, that is able to considerably increase the drug accumulation in target regions such as the above discussed mesangium while minimizing interactions with off-target sites like the vasculature.

When it comes to targeted drug delivery, nanoparticular approaches provide the considerable benefit, that they enable the differentiation of targeted tissues from un-favorable off-target sites via functionalization with cell-selective recognition sequences for target cell surface structures.[34,35] Implementation of this principle already led to a great number of nanoparticular devices with a substantial specificity for target cells within various tissues such as the colon, liver or also the kidney.[36–38] In that regard, we recently presented an actively targeted nanoparticle (NP) species, that enabled a highly specific mesangial *in vivo* targeting within the kidney.[39] The NP system is based on a virus-mimetic presentation of two ligands that selectively recognize mesangial surface components and enable a reliable discrimination of mesangial sites and possible off-targets. Inspired by its biological model, human adenovirus type 2[40], the NP thereby interacts with the cell surface in a sequential manner of initial binding to the angiotensin II receptor type 1 (AT1r) *via* an AT1r blocker (EXP3174), followed by a presentation of previously shielded cyclic amino acid sequence (cRGD), that activates mesangial surface integrin $\alpha_v\beta_3$ and eventually triggers cell endocytosis (**Figure 1a**).[41]

As this NP system provided excellent mesangial *in vivo* specificity, we hypothesized, that virus-mimetic NPs loaded with CCG (**Figure 1b**) could substantially increase drug delivery into intracellular compartments of target mesangial cells. After a subsequent processing and endolysosomal degradation of the NP system, the active substance would be released and then bind and thus stimulate cytosolic sGC, both in its oxidized and heme-free form, which would eventually lead to a significant rise in cGMP-mediated signaling (Figure 1a).

In this study, we therefore initially loaded our NP system with CCG and assessed, whether a therapeutically relevant amount of drug could be encapsulated while still preserving the described active mesangial NP targeting functionalities. In order to subsequently test the pharmacological impact of the NP-mediated drug delivery, we compared the effect of both free and NP-encapsulated CGG on its target as well as various further downstream elements of the sGC-cGMP cascade such as the cGMP-dependent activation of protein kinase 1 α (PKG1-α). Finally, we determined the anti-fibrotic potential of the system in a TGF-β induced *in vitro* fibrosis model (Figure 1a).
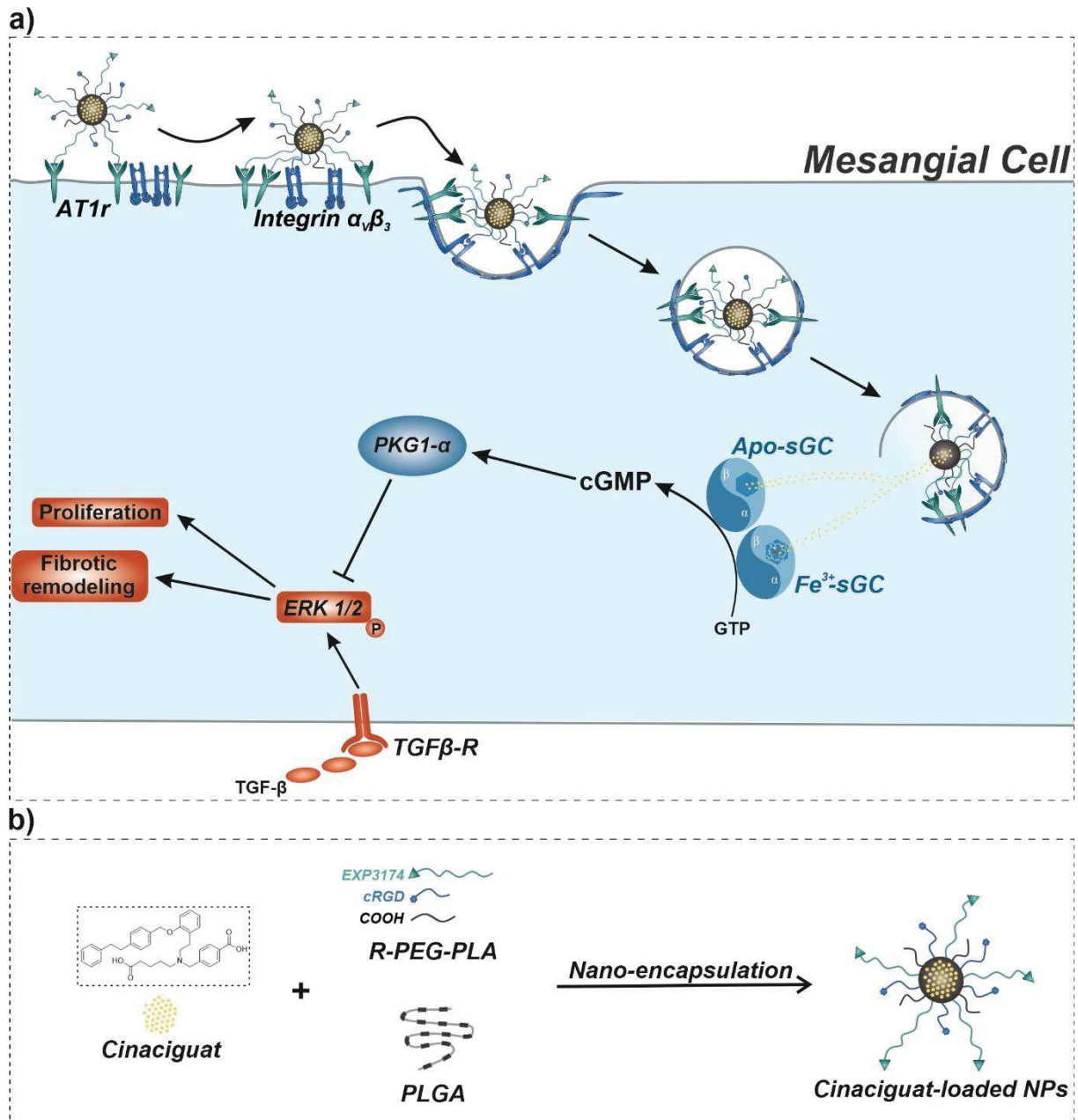
Figure 1. Therapeutic concept. a) NP-assisted CCG delivery to intracellular Apo-/Fe^{3+}-sGC of target mesangial cells. After a sequential and thereby highly cell-selective mesangial NP uptake, CCG is released into the cytosol due to endolysosomal degradation of the NP. Here, CCG binds and thus activates both oxidized and heme-free sGC, leading to an increased production of cGMP and a PKG1-α mediated inhibition of TGF-β induced pathological remodeling. **b)** Manufacturing principle for CCG-loaded virus-mimetic NPs.

2   Materials and Methods

2.1   Materials

BAY 58-2667 (Cinaciguat hydrochloride) was purchased from Axon Medchem BV (Groningen, Netherlands). For NP preparation, heterobifunctional poly(ethylene glycol) components were obtained from Jenkem Technology USA Inc. (Allen, TX, USA), while methoxy poly(ethylene glycol) and Resomer RG 502 (PLGA) were purchased from Sigma-Aldrich (Taufkirchen, Germany). EXP3174 (losartan carboxylic acid) was obtained from Santa Cruz (Heidelberg, Germany) and cyclic RGDfK (cRGD) was purchased from Synpeptide Co. Ltd. (Shanghai, China). AlexaFluor 568 Hydrazide (Alexa568) and CellTracker Deep Red Dye (CTDR) were purchased from Fisher Scientific GmbH (Schwerte, Germany). For Lowry protein determination and later western blot analysis, DC protein assay and Clarity™ Western ECL Blotting substrate were obtained from Bio-Rad Laboratories GmbH (Munich, Germany). Immobilon® PVDF membranes were purchased from Millipore GmbH (Schwalbach, Germany). For western blot analysis, the following primary antibodies and dilutions were used: sGC $\beta 1$ (ER19), rabbit, 1:500 (Sigma-Aldrich); phospho-VASP (Ser239), rabbit, 1:1000; VASP (9A2), rabbit, 1:1000; phospho-p44/42 MAPK (p-ERK1/2), rabbit, 1:1000; p44/42 MAPK (ERK1/2), rabbit, 1:1000; GAPDH, rabbit, 1:1000 (all from Cell Signaling Technology, Cambridge, UK); PKG1-α, rabbit, 1:500 (own production [42]); Col1α1, rabbit, 1:500; α-SMA, mouse, 1:500 (Abcam, Cambridge, UK); vinculin, mouse, 1:500 (R&D Systems, Wiesbaden-Nordenstadt, Germany). Secondary antibodies: mouse-IgG horse radish peroxidase-conjugated, 1:10000 (Sigma-Aldrich); rabbit-IgG horse radish peroxidase-conjugated, 1:25,000 (Dianova GmbH, Hamburg, Germany). Transforming growth factor-$\beta 1$ human (TGF-β) as well as all other utilized chemicals were purchased from Sigma-Aldrich in analytical grade if not stated differently. Immortalized, rat-derived mesangial cells (rMCs) were a kind gift from Prof. Dr. Armin Kurtz (Institute of Physiology, University of Regensburg, Regensburg, Germany). rMCs were isolated and cultured in RPMI 1640 medium containing 10% fetal bovine serum, insulin-transferrin-selenium (ITS) (1×), and 100 nM hydrocortisone as previously described.[43,44]

2.2   Synthesis and functionalization of NP polymer components

COOH-/NH$_2$-PEG$_{2k/5k}$-PLA$_{10k}$ block copolymers were synthesized and functionalized with EXP3174/cRGDfK as previously published by our working group[39,41,45–47], yielding longer EXP3174-PEG$_{5k}$-PLA$_{10k}$ and shorter cRGD-PEG$_{2k}$-PLA$_{10k}$. When needed, core component PLGA was additionally coupled to Alexa568 as described before to enable fluorescence imaging of NPs.[39]

2.3   NP manufacture and CCG encapsulation

Using above mentioned unfunctionalized/ligand-carrying block copolymers and core-forming PLGA, EXPcRGD NPs as well as ligand-free control NPs were manufactured *via* a well-established nanoprecipitation method[39,46,47]. In brief, all polymeric components were mixed in acetonitrile

162

(ACN), whereby different ratios of PEG-PLA/PLGA (70/30; 60/40; 50/50) were prepared to test the ideal composition for CCG encapsulation. For ligand-carrying EXPcRGD NPs, the PEG-PLA proportion thereby consisted of 25% EXP3174-PEG$_{5k}$-PLA$_{10k}$, 15% cRGD-PEG$_{2k}$-PLA$_{10k}$ and 60% COOH-PEG$_{2k}$-PLA$_{10k}$ (ligand-free NPs: 100% COOH-PEG$_{2k}$-PLA$_{10k}$), which had previously been found to be ideal for the desired stepwise targeting concept.[39] The polymer mix was finally added dropwise to vigorously stirring millipore water (mpH$_2$O), yielding above-described NP species.

For drug encapsulation, a stock solution of 2 mg mL^{-1} CCG in a mixture of ACN/dimethyl sulfoxide (DMSO) (21/1; V/V) was prepared and rising volumes of the CCG solution were added to the polymer mix prior to nanoprecipitation. The NP solution was stirred for 3 h at room temperature (RT) to remove all organic solvents and subsequently purified from non-encapsulated CCG *via* centrifugation using Pall Microsep filters (molecular weight cut-off, 30 kDa; Pall Corporation, NY, USA). The NPs were thereby centrifuged three times (1250g; 10 min) and washed with mpH$_2$O after every centrifugation step.

2.4 NP characterization

Manufactured NPs were analyzed regarding their hydrodynamic diameter with a Malvern Zetasizer Nano ZS (Malvern, Herrenberg, Germany). For a more thorough discussion of these aspects and the surface density of EXP3174 and cRGDfK on the NP surface, please refer to our previous publications.[39,41]

2.5 HPLC analysis of drug encapsulation

For a detailed analysis of CCG encapsulation, HPLC analysis was performed using a PLRP-S column (Agilent Technologies Inc., Santa Clara, CA, USA) at 40 °C. The mobile phase consisted of a 10 mM sodium phosphate buffered solution (pH 7.4; A) and ACN (B) (gradient: 0 min 95% A / 5% B; 9 min 65% A / 35% B; 25 min 20% A / 80% B; 45 min 20% A / 80% B; 50 min 95% A / 5% B), eluted at 1.0 mL min^{-1}.[48] CCG was detected at a wavelength of 230 nm (retention time = 12 min). For calibration, CCG dilutions of 0.0125 - 0.8 mg mL^{-1} in DMSO were prepared, injected in the HPLC system and the resulting peak area was analyzed (injection volume = 15 μL). To investigate drug encapsulation efficiency for the different NP types, freshly prepared particles were freeze-dried for 72 h, weighed, and subsequently dissolved in DMSO and injected into the HPLC system (injection volume = 15 μL), yielding a CCG peak at the same retention time (Figure 2a).

2.6 Calculatory determination of encapsulation parameters

For a detailed explanation of the calculation of the Flory-Huggins parameter, please refer to our previous publication.[49,50] The encapsulation efficiency (EE) was calculated as depicted in equation 1 (**E1**), whereby m_e is the mass of encapsulated drug and m_a is the mass of initially added CCG.

$$EE \ [\%] = \frac{m_e}{m_a} \times 100 \tag{E1}$$

For the lyophilized NP batches, we then assessed the amount of NPs (n_{NP}) using **E2**, whereby m_{NP} is the gravimetrically determined mass of the NP batch, $\rho_{(NP)}$ is the estimated density of the NPs (1.25 g cm^{-3}) [49], d_h is the experimentally determined hydrodynamic diameter and N_A is the Avogadro constant.[45]

$$n_{NP} = \frac{m_{NP}}{\rho_{(NP)}\frac{4}{3}\pi\left(\frac{d_h}{2}\right)^3} \times \frac{1}{N_A} \tag{E2}$$

Next, the amount of CCG molecules per batch (n_{CCG}) was calculated from the HPLC results and the number of CCG molecules per NP (N_{exp}) was determined with **E3**.

$$N_{exp} = \frac{n_{CCG}}{n_{NP}} \tag{E3}$$

We then calculated the theoretical volume of the NP core (V_{core}) for every NP sample as described before.[49] Assuming a maximum packing efficiency of 90%[51] as well as the molecular volume of CCG ($V_{CCG} = 0,725$ nm^3) [52], we then calculated the ideal number of CCG molecules per NP (N_{ideal}) using **E4**.

$$N_{ideal} = \frac{V_{core}}{V_{CCG}} \times 0,9 \tag{E4}$$

Finally, the CCG entrapment efficiency (E_{ET}) was determined using the experimentally determined N_{exp} and **E5**.

$$E_{ET}[\%] = \frac{N_{exp}}{N_{ideal}} \times 100 \tag{E5}$$

2.7 CLSM analysis of NP uptake

To confirm ligand-mediated NP uptake, target rMCs were initially stained with CTDR for 45 min (25 µM in serum-free medium, 37 °C, 5% CO$_2$), subsequently seeded into 8-well slides (Ibidi, Gräfelfing, Germany) at a density of 8000 cells well^{-1} and incubated for 48 h at 37 °C and 5% CO$_2$. CCG-loaded EXPcRGD NPs as well as ligand-free particles were prepared as described above, however with Alexa 568-labeled PLGA (40% PLGA; 10 µg CCG addition per batch). Resulting NPs were adjusted to a concentration of 0.4 nM using Leibovitz´s buffer supplemented with 0.1% bovine serum albumine (BSA) and added to the cells for 90 min. After, cells were washed with Dulbecco´s phosphate buffered saline (DPBS) and fixed with 4% paraformaldehyde (PFA) in DPBS for 10 min. To enable visualization of the cell nuclei, cells were thereafter stained for 5 min with a 1:200 dilution of 4′,6-diamidine-2′-phenylindole dihydrochloride (DAPI) in DPBS. Final samples were subsequently analyzed at a Zeiss LSM 710 (Carl Zeiss Microscopy GmbH, Jena, Germany).

2.8 Analysis of CCG effect on intracellular targets

To study the effect of free and NP-encapsulated cinaciguat on mesangial intracellular targets, cells were seeded into 6-well plates (Corning Inc., Corning, NY, USA) at a density of 200,000 cells well^{-1} and grown for 48 h (37 °C, 5% CO_2). Subsequently, cells were incubated for 1 – 24 h with either free CCG (c = 0.2/2 µM), CCG-loaded EXPcRGD NPs (c(NP) = 0.4 nM; c(CCG) = 0.2 µM) or CCG-free EXPcRGD NPs (c(NP) = 0.4 nM). All samples were thereby adjusted to the specified concentrations using serum-free RPMI 1640 medium. After incubation, samples were aspirated, and cells were processed as previously described. [53] In brief, cells were washed with DPBS and harvested by adding 80 µL of lysis buffer (2% Lubrol, 20 mM Tris, 150 mM NaCl; protease inhibitors: 0.5 µg mL^{-1} leupeptin, 1 mM benzamidine, 0.3 mM phenylmethylsulfonyl fluoride) and using a cell scraper. Cells were thereafter homogenized and centrifuged for 15 min at 16,500 g and 4 °C to remove cell remnants. For the following determination of the protein concentration of cell lysates, a modified method of Lowry was used.[54] Cell samples were thereafter denatured, separated using a 11.5% SDS-PAGE (30 µg protein lane^{-1}) and western blotted using above-described primary antibodies against sGC, (P-)VASP, PKG1-α as well as GAPDH. Horse radish peroxidase coupled secondary antibodies were added and finally, activity was assessed after addition of Clarity™Western ECL Blotting substrate, using a chemiluminescence detector (ChemiDoc MP System; Bio-Rad Laboratories) and ImageLab software. Results for both sGC and PKG1-α were thereby normalized to the GAPDH content per sample. For VASP, the ratio of P-VASP and VASP was determined and normalized to the P-VASP/VASP ratio of untreated control cells.

2.9 Analysis of anti-fibrotic CCG effects

To determine the anti-fibrotic potential of CCG-loaded EXPcRGD NPs, we implemented a fibrosis model, whereby rMCs were initially seeded into 6-well plates as described above and serum-starved after 24 h in order to exclude any impact of serum-derived TGF-β.[55] After another 24 h, free CCG, CCG-carrying or CCG-free EXPcRGD NPs were added as described above. After incubation for 3 h, 10 ng mL^{-1} of TGF-β per well was added to induce pro-fibrotic changes. Also, for a second group, free CCG/NPs and TGF-β were added simultaneously. Cells were thereafter incubated for either 1 h (ERK1/2 phosphorylation) or 72 h (α-SMA/Col1α1 content), depending on the intended read-out (see also Figure 6a). After incubation, cells were harvested as described above, followed by SDS-PAGE and western blot analysis with the respective antibodies. Resulting band intensities of α-SMA/Col1α1 were finally normalized to the respective vinculin content, while for ERK1/2, the ratio of P-ERK1/2 and ERK1/2 was determined and normalized to the P-ERK1/2/ERK1/2 ratio of untreated cells.

2.10 Cell proliferation assay

To assess the impact of discussed samples on a TGF-β induced mesangial hyperproliferation, a 3-(4,5-dimethylthiazol-2-yl)-2,5-diphenyltetrazolium bromide (MTT) reduction assay was performed. In brief,

rMCs were seeded into a 96 well plate (Corning Inc.) at a density of 3000 cells well^{-1} and incubated for 48 h, whereby cells were serum-starved after 24 h. Cells were thereafter incubated for 72 h with samples and TGF-β in serum-free RPMI medium, as described in the previous section. After 72 h, samples were removed and 50 μL of RPMI medium containing 1 mg mL^{-1} MTT were added per well. After 3 h of incubation, the MTT solution was aspirated and 100 μL of isopropanol were added for 30 min under light exclusion and gentle shaking. Finally, absorbance at 570 and 690 nm was assessed at a FluoStar Omega fluorescence microplate reader (BMG Labtech, Ortenberg, Germany). For cell viability, the difference in absorbance at 570 and 690 nm was determined. Results were finally normalized to untreated control cells.

2.11 CLSM analysis of α-SMA expression

For visualization of changes in α-SMA deposition, rMCs were initially seeded into 8-well Ibidi slides as described above. After 24 h, cells were serum-starved, and after another 24 h, cells were incubated with either free CCG, CCG-loaded or CCG-free EXPcRGD NPs for 3 h, followed by a TGF-β stimulation for 72 h (c = 10 ng mL^{-1}) in serum-free RPMI medium. Cells were thereafter washed, fixed with 4% PFA for 10 min at RT and permeabilized with 0.1% Triton-X in DPBS for 10 min at RT. After a washing step, unspecific binding sites were blocked by addition of a 1% solution of BSA in DPBS for 30 min. Subsequently, cells were incubated overnight with a mix of AlexaFluor® 488-coupled antibody against α-SMA (Sigma-Aldrich) and DAPI (1:500 in 0.1% BSA in DPBS), followed by CLSM analysis.

2.12 Statistical Analysis

Results are expressed as mean ± standard deviation (SD), whereby n represents technical replicates. Statistical parameters were calculated using GraphPad Prism 6 software. One-way analysis of variance (ANOVA) as well as Tukey post-test were performed for calculation of statistical differences between analyzed groups. The resulting p-values are stated in each individual figure.

3   Results and Discussion

3.1   Efficient and reproducible encapsulation of CCG into targeted NPs

To enable a NP-mediated, targeted delivery of CCG to mesangial sites, we initially assessed whether a pharmacologically sufficient amount of drug can be encapsulated into our NP system. The NP itself thereby consists of shell-forming poly(ethylene glycol)−poly(lactic acid) (PEG-PLA) block-copolymers carrying the above described targeting functionalities as well as poly(lactic-co-glycolic acid) (PLGA), which both stabilizes the NP core and can be used to encapsulate suitable active agents such as CCG (Figure 1b). In this regard, we recently presented a study discussing the necessary physicochemical properties of encapsulated compounds in order to achieve a satisfactory NP loading.[49] We therein found, that for a successful encapsulation, substances on the one hand need to possess a sufficient lipophilicity and on the other hand, the miscibility of encapsulated drug and core forming PLGA has to exceed a certain threshold in order to guarantee NP stability. With regard to these prerequisites, CCG was found to be a promising candidate for NP encapsulation, showing a substantial lipophilicity (logP ≈ 7) and a - calculatorily determined - high miscibility with PLGA. In that regard, the Flory-Huggins parameter for CCG and PLGA was found to be around 0.005, indicating that both components are excellently miscible.[50]

Based on these initial considerations, we decided to test three different NP compositions with a varying proportion of core PLGA (30/40/50%) to find an ideal compromise between high drug loading, satisfactory encapsulation efficiency and small NP diameter. It was thereby particularly important, that resulting NPs would not exceed 90 – 100 nm to still guarantee a sufficient *in vivo* extravasation through the fenestrated glomerular endothelium into mesangial areas.[56] For every NP composition, we then added rising levels of CCG to the polymer mix and - after nanoprecipitation and lyophilization of NPs - assessed the amount of encapsulated drug *via* high performance liquid chromatography (HPLC). Both free CCG and NP-derived CCG could thereby be reproducibly detected at a wavelength of 230 nm (**Figure 2a** and **Figure S1**).

As **Figure 2b** indicates, larger amounts of initially added drug led to a progredient rise in finally encapsulated CCG (CCG loading) for all three NP compositions, whereby NP quality (size/dispersity) still remained satisfactory (**Figure S2a-c**). However, an addition of more than 10 µg CCG per 4 mg NP batch did not produce any further rise in CCG loading, but rather increased the tendency of NPs to form larger aggregates, indicating that the general NP loading capacity was exceeded (**Figure S2d**). For the following analysis, we therefore decided to add 10 µg of drug during nanoprecipitation to both enable a maximum CCG loading and preserve the NPs´ stability.

In a next step, we determined several physicochemical parameters to assess the optimal PLGA proportion per particle (for a more detailed description, please also refer to the Methods section, **Figure S3a/b** as well as[49]). While the NPs´ hydrodynamic diameter was found to be below 100 nm for all three NP types (**Figure S2c**), the encapsulation efficiency was significantly rising with a greater

proportion of PLGA in the NP core (**Figure 2c**). This was expected due to the greater volume of the NP core as well as the excellent miscibility of CCG and PLGA. To enable a more realistic assessment of the actual amount of encapsulated drug per NP, we then calculated the number of CCG molecules per NP (**Figure 2d**), whereby a similar trend of rising levels of encapsulated substance could be found. Based on the hydrodynamic diameter of each NP type, we then calculated the respective NP core volume and determined the number of CCG molecules, that would ideally fit into one NP. Finally, this number was used to calculate the CCG entrapment efficiency, i.e. the ratio of the number of actually encapsulated and the ideally encapsulated CCG molecules. We thereby found a contrary trend for the tested NP compositions. Here, higher proportions of PLGA led to a generally decreasing entrapment efficiency, indicating that although NPs with a higher ratio of PLGA could generally encapsulate more drug, the actual rise in CCG molecule numbers was not as high as theoretically possible (**Figure S3c**). We therefore hypothesized, that the general composition of our NP system might not allow any higher CCG loading due to its substantial lipophilicity and a possible destabilizing effect of greater drug concentrations in the NP core. However, we estimated. that the successfully encapsulated amount of drug was already sufficient to enable a substantial pharmacological effect due to the considerable mesangial targeting capacity and the resulting drug delivery impact of the NP system.

We finally chose to proceed with the NP species consisting of 40% PLGA and 60% PEG-PLA, as this NP type showed a satisfactory encapsulation efficiency (~ 46%) and CCG loading (~ 600 CCG molecules per NP) while still possessing an ideal diameter of around 80 nm.
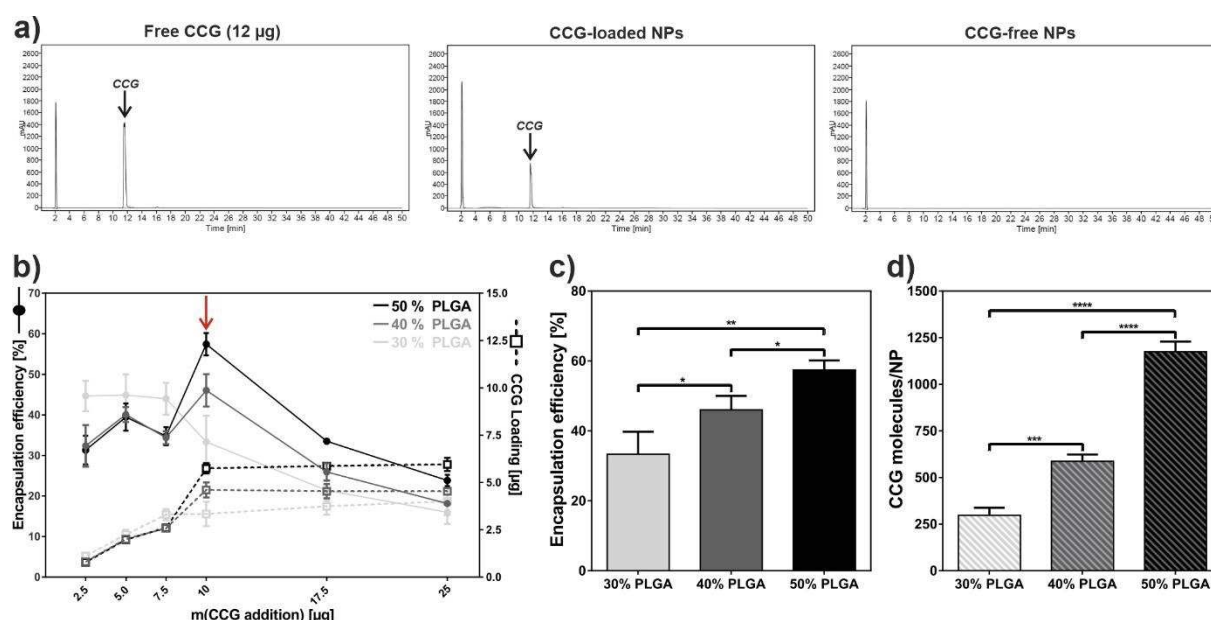
Figure 2. a) Representative HPLC chromatograms of free CCG as well as CCG-loaded or drug-free NPs. CCG could thereby be reproducibly detected at a retention time of 12 min (black arrow). **b)** CCG loading per NP batch and the respective encapsulation efficiency (EE) for NPs carrying either 30, 40 or 50% PLGA as core component. EE was thereby highest for an addition of 10 µG CCG per 4 mg NP batch (red arrow). **c)** EE (10 µg CCG addition) gradually increased with larger amounts of PLGA addition. **d)** Calculated number of CCG molecules per NP type. (see also Figure 3a/b). Results represent mean ± SD (n = 3). *P<0.05 **P<0.01 ***P<0.001 ****P<0.0001.

As we were able to reproducibly encapsulate a considerable amount of CCG into our NP system, we next intended to assess, whether these CCG-loaded NPs could still harness their attached ligands to enter intracellular regions of target mesangial cells. As described above, NP cell entry is thereby based on an initial AT1r binding and a subsequent presentation of previously shielded cRGD functionalities, that enable an integrin-mediated endocytosis.[39,41] We therefore used a rat-derived mesangial cell line (rMCs), that showed a substantial expression of both targets (AT1r/$\alpha_v\beta_3$ integrin), as our previous studies had already confirmed.[39]

In a first step, rat mesangial cells (rMCs) were incubated for 90 min with CCG-loaded NPs (10 µg per NP batch). The particles either carried both active ligands (EXPcRGD NPs) or were ligand-free control NPs. To enable a better visualization of particle uptake, a fluorescent label was covalently coupled to the PLGA prior to particle preparation and cell cytosol was stained using CellTracker® Deep Red dye (CTDR). As depicted in **Figure 3a**, ligand-functionalized EXPcRGD NPs showed a substantial mesangial accumulation, which corresponded to our previous results. [39] In contrast, no visible cellular uptake could be detected for ligand-free control NPs, indicating that the mesangial cell uptake of EXPcRGD NPs was mediated *via* described ligand-receptor interactions. However, as the CCG target sGC is located intracellularly, we finally also assessed the exact location of visible NP accumulations to further confirm NP endocytosis and exclude a mere binding to the cell surface. We therefore performed z-stack analysis of rMCs after 90 min of EXPcRGD NP incubation and found, that NP-associated fluorescence could almost entirely be found in sections representing intracellular segments of the cell body (**Figure 3b**). These observations were in line with our previous studies, that showed a maximum mesangial NP endocytosis after 90 – 120 min.[39]

Taken together, these results confirmed our hypothesis, that the active agent CCG can be efficiently transported into intracellular regions of mesangial cells *via* encapsulation in adenovirus-mimetic EXPcRGD NPs. The encapsulation process was thereby satisfactory and reproducible and did not interfere with the NPs´ ability to initially bind the AT1r *via* EXP3174 and subsequently initiate $\alpha_v\beta_3$ mediated cell endocytosis.
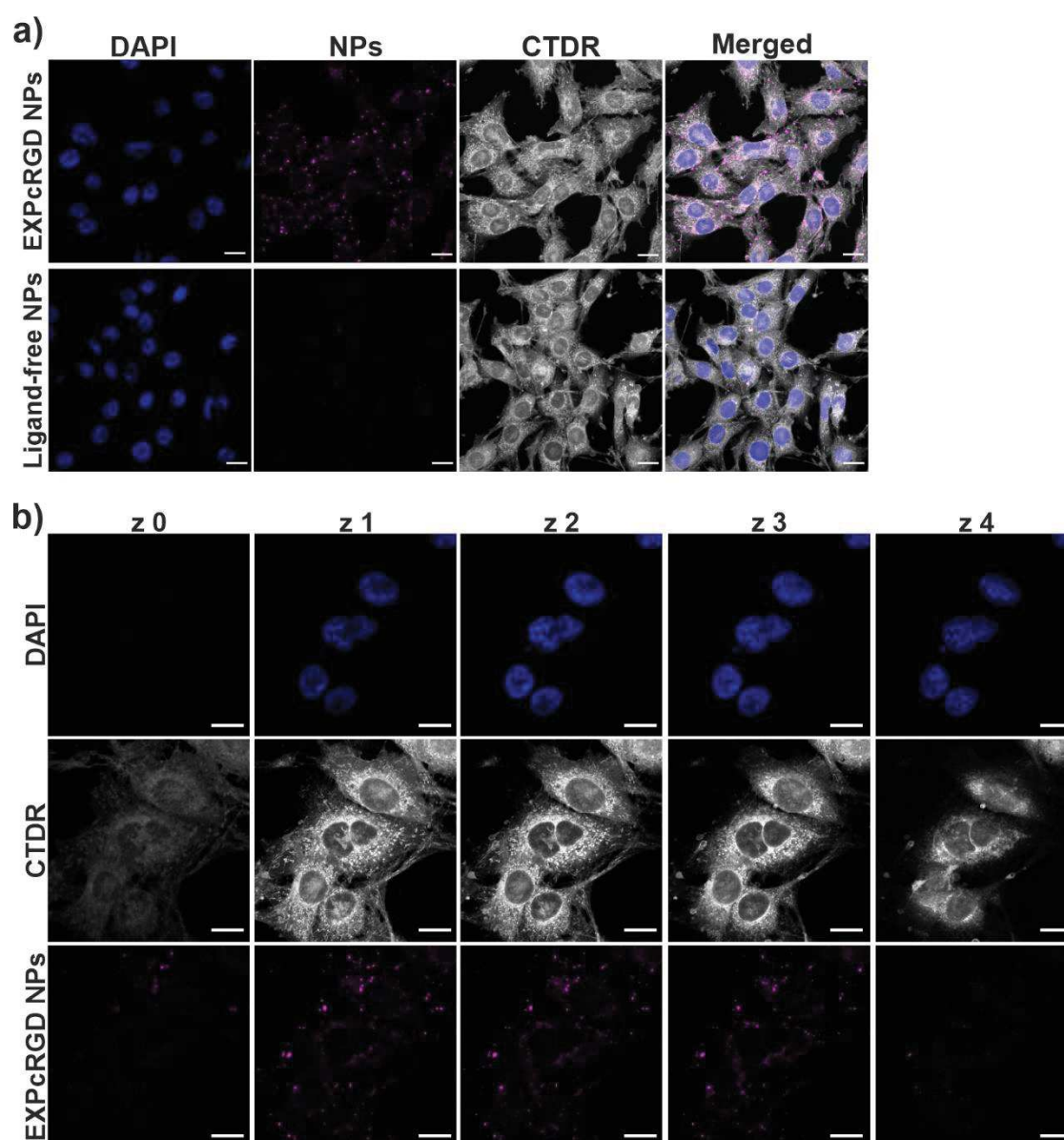
Figure 3. a) CLSM analysis of CCG-loaded NP-cell interaction. In contrast to ligand-free control NPs, targeted EXPcRGD NPs (purple) reached a substantial uptake into endocytotic vesicles of mesangial cells (cell cytosol = grey; cell nuclei = blue). **b)** z-stack analysis further confirmed the intracellular localization of targeted NPs (EXPcRGD NPs) (z0 - z4 = bottom to top z-plane). Scale bar = 20 µM.

3.2   Targeted CCG delivery potentiates sGC activation and stabilization

Having confirmed, that actively targeted EXPcRGD NPs can be loaded with a pharmacologically relevant amount of CCG, our next goal was to investigate, whether a more efficient transport of the active agent into the mesangial cytosol could possibly increase the drug´s potency due to a drug delivery effect. This hypothesis was based on the general assumption, that the cellular uptake and cytosolic accumulation of free CCG might be limited, partly because of its substantial lipophilicity and the resulting poor solubility in aqueous systems and because of a merely passive diffusion into the target cell, which requires a constant concentration gradient. In contrast, CCG-loaded EXPcRGD NPs would be able to enter intracellular compartments more efficiently and release the active agent due to an

endolysosomal degradation of the NP structure.[57,58] Also, the active targeting functionalities would enable a more selective *in vivo* transport of EXPcRGD NPs – and therefore also CCG – to mesangial sites within the kidney. This observation was already shown in our previous publication, where EXPcRGD NPs showed a considerably increased mesangial accumulation compared to ligand-free NPs.[39]

To test the above-described drug delivery effect, we therefore decided to compare four major groups (**Figure 4a**): First, free CCG was administered at a concentration of 2 µM. This concentration was chosen, as in previous studies, it had been shown to exhibit a satisfactory and reproducible activation of the sGC cascade, which also led to an anti-fibrotic effect. [31] The second group consisted of CCG-loaded EXPcRGD NPs at a concentration of 0.4 nM, which on the one hand was comparable to our previous *in vitro* studies, whereby no cell-toxic effects had been observed[39], and on the other hand contained CCG at approximately 10% of the free dose (0.2 µM *vs.* 2 µM). By administering merely a tenth of the free CCG dose, we wanted to test, whether the encapsulation in targeted NPs could increase the CCG potency as described above and eventually provide comparable effects with fewer drug needed. As a third group, we therefore also applied free CCG at a lower concentration of 0.2 µM, which was similar to the NP-delivered amount of drug and should theoretically provide a merely limited effect compared to the free drug at 2 µM.[31] Finally, CCG-free EXPcRGD NPs were administered in the same concentration as CCG-loaded NPs to exclude any possible impact of the NP-cell or ligand-receptor binding on the CCG effect.
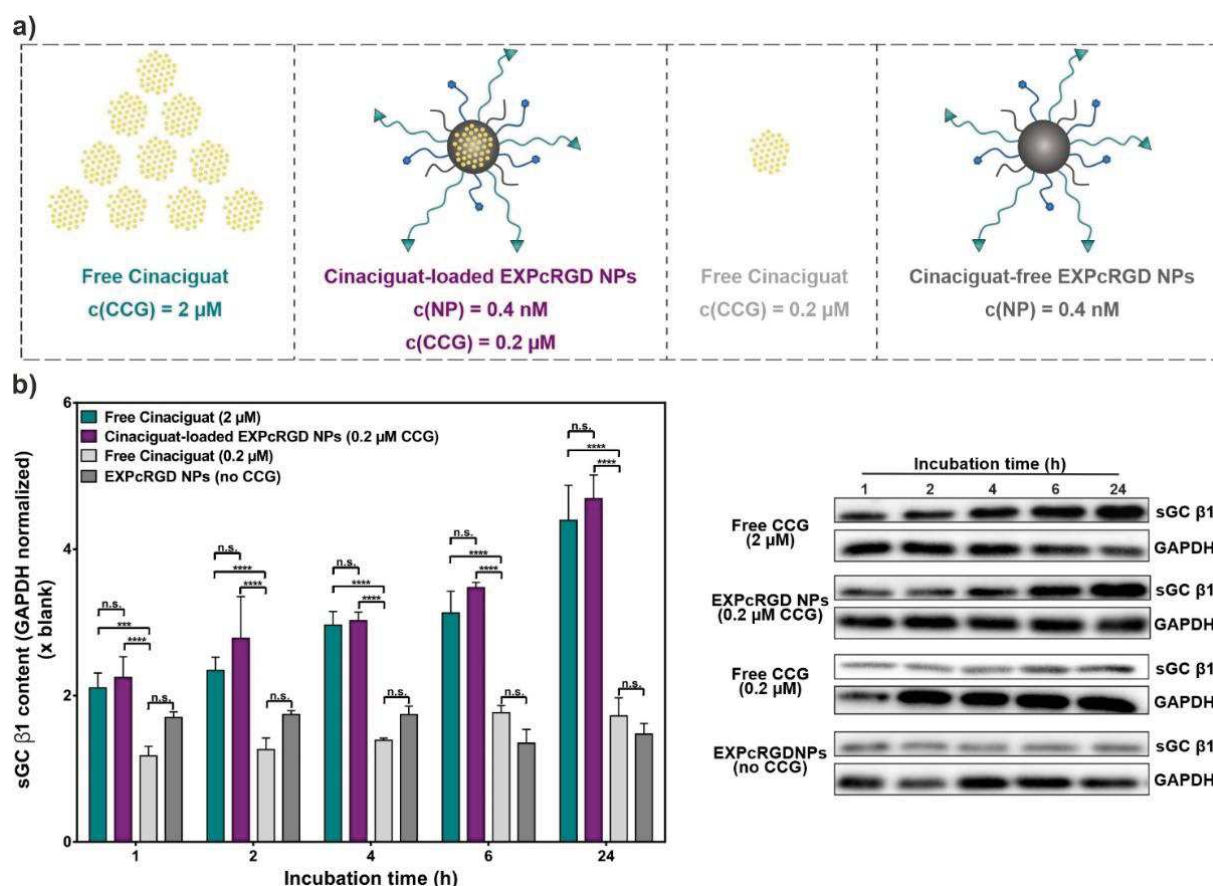
Figure 4. a) Experimental set-up. In contrast to free CCG (c = 2 µM), drug-loaded EXPcRGD NPs carried merely 10% of the CCG dose to assess a possible drug delivery effect. **b)** Western blot analysis of sGC β1 content upon sample incubation over 24 h showed significantly increased sGC β1 levels both for free CCG (2 µM) and the NP-encapsulated drug (0.2 µM), compared to a lower concentration of free CCG (0.2 µM) or drug-free NPs. Results represent mean ± SD (n = 3). ***P<0.001 ****P<0.0001. (n.s. not significant.)

We initially incubated rMCs with each of the four groups for 1 to 24 h and subsequently analyzed the sGC β1 content. Although CCG mainly acts as an activator of oxidized/heme-free sGC, previous studies indicated, that due to a stabilizing effect, CCG-bound sGC can also be prevented from undergoing proteasomal degradation.[59–61] In our case, a corresponding trend could be observed, as shown in **Figure 4b**: Incubation with 2 µM of free CCG led to a substantial increase in sGC β1 content over 24 h. Interestingly, CCG-loaded EXPcRGD NPs provided a comparable effect, even though here, merely 10% of drug was administered in total. In contrast, free CCG at a similarly low concentration of 0.2 µM only showed a slight increase in sGC β1 levels, supporting our hypothesis, that the NP-mediated CCG delivery can potentiate the pharmacological potency of the active substance. In this context, a possible impact of ligand-receptor or NP-cell interactions was negligible, as incubation with CCG-free NPs did not lead to an increase in sGC β1 content, but rather showed a constant or slightly declining trend.
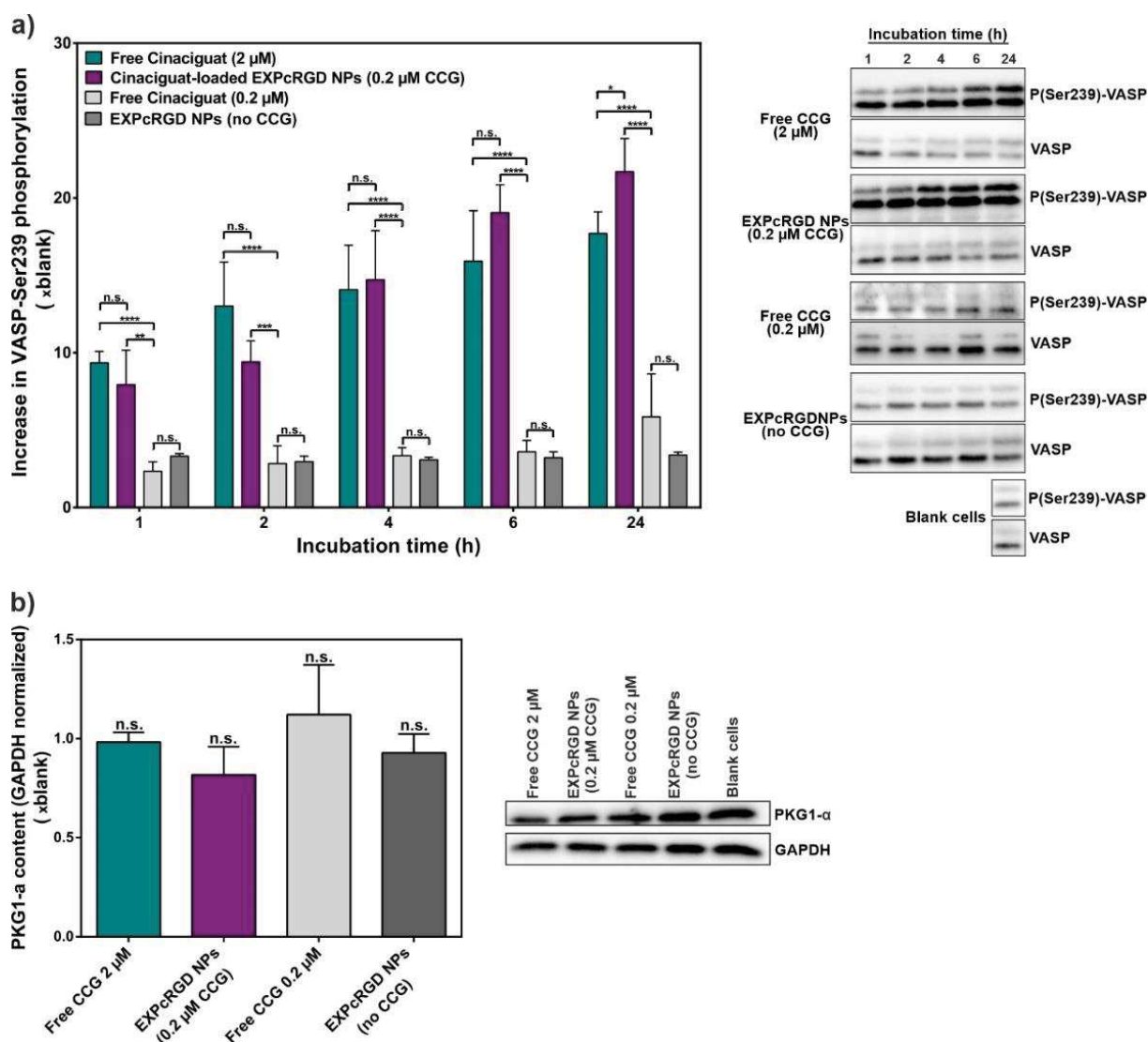
Figure 5. a) Phosphorylation of PKG1-α substrate VASP-Ser239 significantly increased over 24 h, both for free CCG (2 µM) and CCG-loaded EXPcRGD NPs (0.2 µM), indicating a substantial activation of the kinase. **b)** WB analysis of total PKG1-α levels after 24 h incubation showed no considerable changes in protein content for any sample. Results represent mean ± SD (n = 3). *P<0.05 **P<0.01 ***P<0.001 ****P<0.0001. (n.s. not significant.)

Since the main anti-fibrotic effect of sGC activators such as CCG is mediated *via* an eventual cGMP-derived activation of PKG1-α, we consequently also analyzed the respective impact of administered CCG/NPs on this kinase. In order to determine changes in activity, we chose to monitor the level of PKG1-α mediated phosphorylation of vasodilator-stimulated phosphoprotein (VASP) at serine 239 (P-VASP).[62] As shown in **Figure 5a**, VASP phosphorylation thereby increased substantially over 24 h of incubation, both for free CCG (2 µM) and CCG-loaded NPs, which again carried merely 10% of the free CCG dose. Interestingly, this trend was initially higher for the free drug while at later time points, CCG-loaded NPs had a significantly increased effect on PKG1-α activity. To our estimation, this observation can be explained by the endolysosomal degradation, that CCG-carrying NPs initially had to undergo until CCG was released into the cytosol. Again, incubation with a lower concentration of free CCG (0.2 µM) did not produce any noteworthy changes in VASP phosphorylation, even though here,

the same amount of drug was applied as with the NP delivery system. Also, CCG-free NPs did not provide any changes in P-VASP/VASP ratio. To confirm, that the observed upregulation of VASP phosphorylation was mediated *via* an enhanced PKG1-α activity, we additionally analyzed the PKG1-α content (**Figure 5b**). Here, no significant differences between any examined group could be found, supporting the hypothesis of a cGMP-mediated activation of PKG1-α.

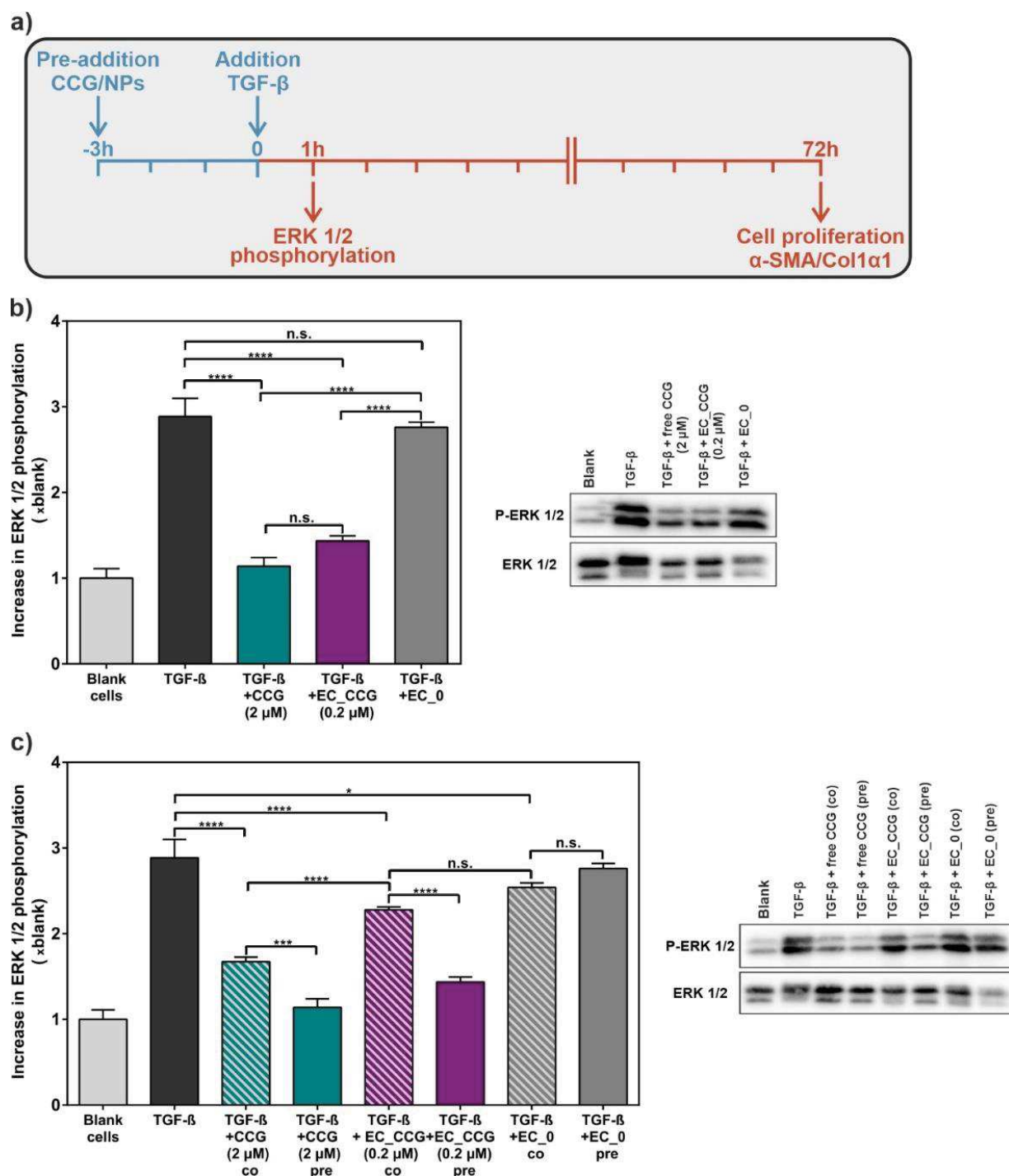The depicted results clearly confirmed our initial hypothesis, that CCG-loaded NPs can potentiate the agent´s pharmacological effect on sGC and its downstream cascade. The experienced sGC β1 activation/stabilization as well as the increase in PKG1-α activity was thereby comparable to the effect of the free drug, even though EXPcRGD NPs carried merely 10% of the dose. Remarkably, the free administration of the same CCG amount as in the NP system (0.2 μM) provided a considerably reduced pharmacological effect. In our view, this observation indicated, that highly lipophilic drugs such as CCG can substantially profit from a more efficient delivery into intracellular regions of their target cells and thereby reach a comparable therapeutic effect in a significantly reduced concentration range.

3.3 CCG-loaded NPs show a substantial anti-fibrotic effect *via* suppression of the non-canonical TGF-β pathway

As the NP-mediated CCG delivery led to a significantly potentiated activation of the sGC cascade, we lastly determined the anti-fibrotic potential of the system. In this context, previous studies had suggested, that CCG-mediated sGC activation can be harnessed to substantially alleviate glomerular pathologies caused by elevated levels of TGF-β associated fibrosis.[30,31] We therefore implemented a TGF-β based *in vitro* fibrosis model and analyzed the therapeutic potential of free CCG (2 μM) as well as CCG-loaded EXPcRGD NPs (0.2 μM) (**Figure 6a**), as these two samples had provided a sufficient activation of the sGC-cGMP cascade as described above. Again, drug-free EXPcRGD NPs served as a control to exclude any possible impact of the ligand-receptor or NP-cell interaction. Prior to cell incubation with described samples, rMC were starved from fetal bovine serum (FBS) for 24 h, as a significant amount of TGF-β is also present in FBS and could therefore have an impact on the later observed results.

Our first point of interest lay in ERK1/2, as previous studies had already indicated a substantial CCG-mediated suppression of the non-canonical TGF-β signaling pathway.[31] After 3 h of incubation with either free CCG (2 μM) or CCG-loaded EXPcRGD NPs (0.2 μM CCG), rMCs were therefore exposed to 10 ng mL^{-1} of TGF-β for 1 h and ERK1/2 phosphorylation was determined. Both for the free drug and CCG-loaded NPs, levels of P-ERK1/2 were thereby significantly reduced compared to a TGF-β control and CCG-free NPs. Similar to the experiments depicted in Figures 4 and 5, EXPcRGD NPs carried merely 10% of the drug dose, but provided a comparable result, thereby further supporting our initial hypothesis of a drug delivery effect. We additionally tested the impact of a pre-incubation on the inhibitory effect by adding CCG/NPs as well as TGF-β at the same time-point (**Figure 6c**). Here, reduction of ERK1/2 phosphorylation was significantly lower compared to the pre-incubation. This trend was most noticeable for CCG-loaded EXPcRGD NPs, where only a minor inhibitory effect could

be detected. To our estimation, these results indicated that the CCG-mediated effect was only possible after a successful intracellular uptake and degradation of NPs, thereby proving our hypothesized route of CCG delivery.

Figure 6. a) In order to assess the anti-fibrotic potential of CCG-loaded NPs, a TGF-β based fibrosis model was established, whereby fibrotic key elements were analyzed at different time points. **b)** Incubation of rMCs with free CCG (2 µM) or CCG-loaded EXPcRGD NPs (EC_CCG; 0.2 µM, 10% of the free drug dose) prior to TGF-β exposure significantly reduced ERK1/2 phosphorylation compared to CCG-free NP species (EC_0). **c)** In contrast to a pre-incubation ("pre"), co-addition ("co") of CCG/NPs and TGF-β led to a considerably lower reduction in ERK1/2 phosphorylation, especially for CCG-loaded NPs. Results represent mean ± SD (n = 3). *P<0.05 ***P<0.001 ****P<0.0001. (n.s. not significant.)

As another key element of a TGF-β associated remodeling is a substantial hyperproliferation of tissues, we next investigated the effect of our NP system on a possible reduction of cell proliferation. We therefore incubated rMCs with CCG/NPs as well as TGF-β similar to the experiments above, and after 72 h, performed an MTT proliferation assay. As depicted in **Figure 7a**, TGF-β induced hyperproliferation could thereby almost entirely be suppressed both with free CCG and EXPcRGD NPs, again carrying merely 10% of the free CCG dose. Drug-free NPs, in contrast, did not provide any significant anti-proliferative or cell-toxic effect. In this context, we also assessed a possible effect of the above-described serum starvation on the general cell viability of rMCs. As expected, deprivation of cells from FBS thereby led to a slight decrease in overall cell proliferation. However, no cell toxicity such as elevated levels of apoptosis could be observed, confirming the applicability of the model (**Figure S4**) in our set-up.

In a final step, we determined the inhibitory potential of the system on the expression of α-SMA as well as Col1α1, two key elements of a TGF-β derived, myofibroblast-like differentiation of cells. Antibody staining and CLSM analysis of α-SMA content thereby revealed a trend, which was similar to the above-described effects (**Figure 7b**): While stimulation of rMCs with TGF-β led to a considerable increase in α-SMA signal within the cell body of rMCs, pre-incubation with EXPcRGD NPs carrying CCG substantially suppressed this effect, especially compared to CCG-free NPs. These observations were further supported by western blot analysis of α-SMA content, where a similar anti-fibrotic effect was noticeable (**Figure 7c**). Accordingly, pre-incubation with CCG-loaded EXPcRGD NPs also significantly reduced expression of Col1α1 (**Figure 7d**). Again, the observed effect was comparable to the application of ten times as much free drug.

Taken together, we suggest that the presented results confirmed our initial hypothesis of a potentiated CCG effect due to a NP-derived drug delivery. Compared to the administration of the free drug, CCG-loaded NPs thereby showed a similar activation of the sGC pathway and suppression of the non-canonical TGF-β pathway, even though they carried merely 10% of the dose. To our estimation, this effect was mainly based on the fact, that EXPcRGD NPs could transport their cargo more efficiently into cytosolic compartments of the target cell in contrast to the highly lipophilic free drug.
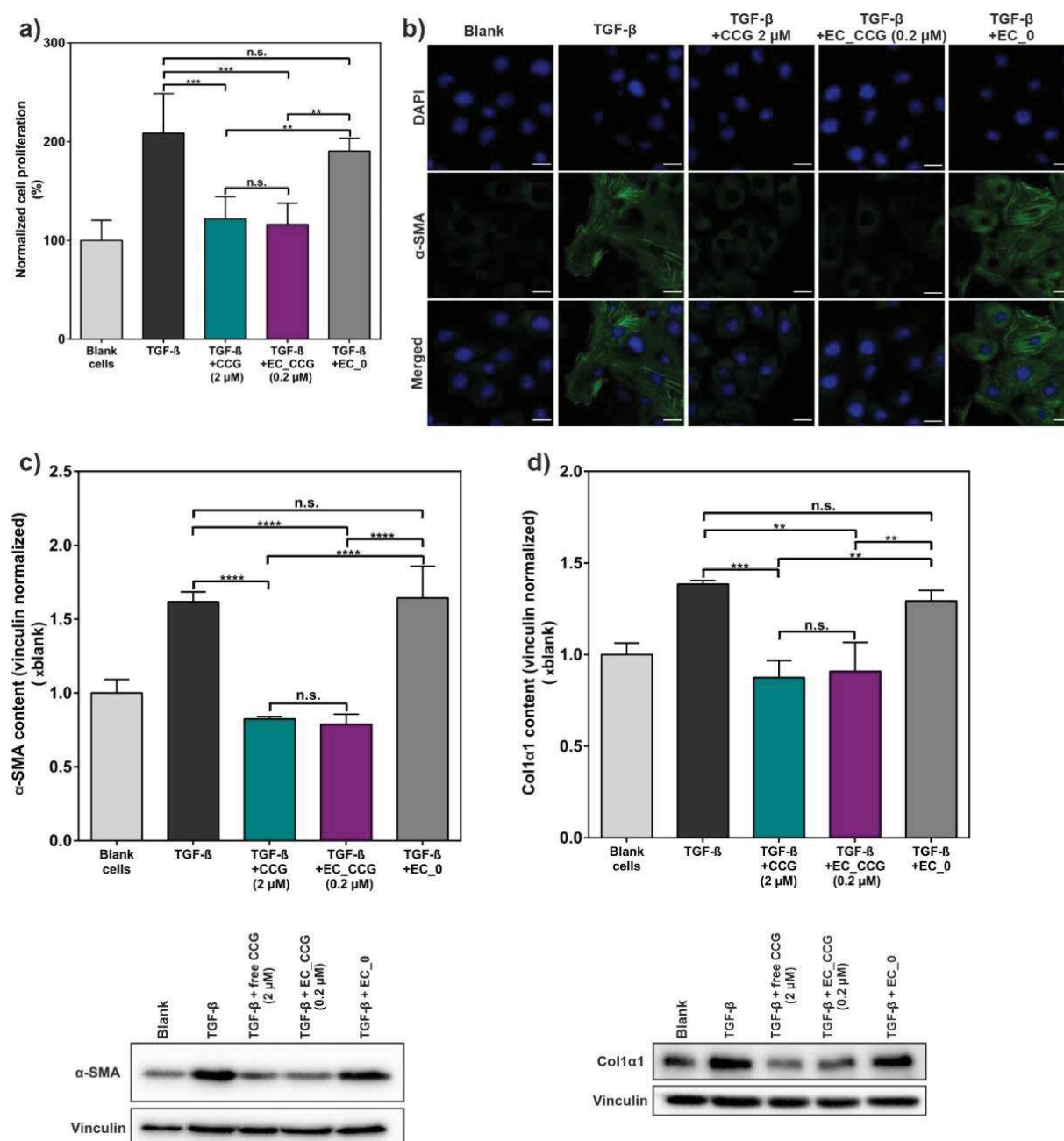
Figure 7. a) MTT cell proliferation assay revealed a significant reduction of TGF-β induced hyperproliferation by pre-incubation with CCG-loaded EXPcRGD NPs. **b)** CLSM analysis of α-SMA expression showed a considerable reduction of pro-fibrotic α-SMA (green) for free CCG as well as CCG-carrying NPs. Cell nuclei = blue. Scale bar = 20 µM. WB analysis of **c)** α-SMA and **d)** Colα1 expression proved the observation of a considerable anti-fibrotic potential of CCG-loaded EXPcRGD NPs. Results represent mean ± SD (n = 3). **P<0.01 ***P<0.001 ****P<0.0001. (n.s. not significant.)

4   Conclusion

The above discussed results of this study revealed three major outcomes: First, a pharmacologically relevant dose of CCG could be reproducibly encapsulated into our virus-mimetic NP system while still guaranteeing a highly efficient mesangial NP uptake due to the previously presented targeting functionalities. Second, NP-assisted delivery of CCG into the mesangial cytosol substantially potentiated the sGC activating effect of the drug. In this regard, NP-mediated transport of 10% of the original free dose led to a comparable pharmacological effect concerning sGC stabilization and activation. Remarkably, the same concentration did not provide any noteworthy effect, when it was not delivered *via* the NP system, but merely administered in its free form. As above mentioned, this outcome was possibly based on a more efficient and prolonged transport of NP-encapsulated CCG into cytosolic regions of the target cells. Lastly, activation of the sGC-cGMP cascade *via* CCG-loaded NPs led to a considerable reduction of non-canonical TGF-β signaling, resulting in significantly decreased levels of pro-fibrotic markers and a substantially reduced hyperproliferation. Again, the described effects could be realized with merely 10% of the free CCG dose, indicating the great potential of the NP system in the therapy of renal fibrosis and further pathologies. It would therefore be of utmost interest to test the described system in an *in vivo* disease model. In that regard, future studies would also have to elucidate, whether glomerular damage can not only be prevented, but also be reversed by the administration of CCG-loaded NPs. As this effect has already been shown repeatedly for the free CCG drug or for sGC stimulators[29–31], we suppose, a NP-mediated drug delivery could potentially even increase the observed therapeutic effect. In that regard, CCG transport *via* our virus-mimetic NP system would additionally provide the substantial advantage, that it can prevent an imminent interaction of CCG with the vasculature and thereby minimize possible adverse effects such as a drop in blood pressure. When it comes to diabetes and the related kidney pathologies, this new treatment option would be highly beneficial as it would not only be able to prevent further kidney damage like the currently predominant therapy options (control of blood sugar/pressure), but also have a substantial effect in the case of an already further progressed state of disease. In this regard, NP-assisted delivery of active substances such as CCG could be a decisive tool to increase target accumulation and drug bioavailability.

References

(1) Cho, N. H.; Shaw, J. E.; Karuranga, S.; Huang, Y.; da Rocha Fernandes, J. D.; Ohlrogge, A. W.; Malanda, B. IDF Diabetes Atlas: Global estimates of diabetes prevalence for 2017 and projections for 2045. *Diabetes research and clinical practice* **2018**, *138*, 271–281. DOI: 10.1016/j.diabres.2018.02.023. Published Online: Feb. 26, 2018.

(2) Romagnani, P.; Remuzzi, G.; Glassock, R.; Levin, A.; Jager, K. J.; Tonelli, M.; Massy, Z.; Wanner, C.; Anders, H.-J. Chronic kidney disease. *Nature reviews. Disease primers* **2017**, *3*, 17088. DOI: 10.1038/nrdp.2017.88. Published Online: Nov. 23, 2017.

(3) Hill, N. R.; Fatoba, S. T.; Oke, J. L.; Hirst, J. A.; O'Callaghan, C. A.; Lasserson, D. S.; Hobbs, F. D. R. Global Prevalence of Chronic Kidney Disease - A Systematic Review and Meta-Analysis. *PloS one* **2016**, *11* (7), e0158765. DOI: 10.1371/journal.pone.0158765.

(4) Webster, A. C.; Nagler, E. V.; Morton, R. L.; Masson, P. Chronic Kidney Disease. *The Lancet* **2017**, *389* (10075), 1238–1252. DOI: 10.1016/S0140-6736(16)32064-5.

(5) Thomas, M. C.; Brownlee, M.; Susztak, K.; Sharma, K.; Jandeleit-Dahm, K. A. M.; Zoungas, S.; Rossing, P.; Groop, P.-H.; Cooper, M. E. Diabetic kidney disease. *Nature reviews. Disease primers* **2015**, *1*, 15018. DOI: 10.1038/nrdp.2015.18. Published Online: Jul. 30, 2015.

(6) Umanath, K.; Lewis, J. B. Update on Diabetic Nephropathy: Core Curriculum 2018. *Am. J. Kidney Dis.* **2018**, *71* (6), 884–895. DOI: 10.1053/j.ajkd.2017.10.026.

(7) Magee, C.; Grieve, D. J.; Watson, C. J.; Brazil, D. P. Diabetic Nephropathy: a Tangled Web to Unweave. *Cardiovascular drugs and therapy* **2017**, *31* (5-6), 579–592. DOI: 10.1007/s10557-017-6755-9.

(8) Schena, F. P. Pathogenetic Mechanisms of Diabetic Nephropathy. *Journal of the American Society of Nephrology* **2005**, *16* (3_suppl_1), S30-S33. DOI: 10.1681/ASN.2004110970.

(9) Kanwar, Y. S.; Sun, L.; Xie, P.; Liu, F.-Y.; Chen, S. A glimpse of various pathogenetic mechanisms of diabetic nephropathy. *Annual review of pathology* **2011**, *6*, 395–423. DOI: 10.1146/annurev.pathol.4.110807.092150.

(10) Kolset, S. O.; Reinholt, F. P.; Jenssen, T. Diabetic Nephropathy and Extracellular Matrix. *J. Histochem. Cytochem.* **2012**, *60* (12), 976–986. DOI: 10.1369/0022155412465073.

(11) Scindia, Y. M.; Deshmukh, U. S.; Bagavant, H. Mesangial Pathology in Glomerular Disease:Targets for Therapeutic Intervention. *Adv. Drug Delivery Rev.* **2010**, *62* (14), 1337–1343. DOI: 10.1016/j.addr.2010.08.011.

(12) Schlöndorff, D.; Banas, B. The Mesangial Cell Revisited:No Cell Is an Island. *J. Am. Soc. Nephrol.* **2009**, *20* (6), 1179–1187. DOI: 10.1681/ASN.2008050549.

(13) Arora, M. K.; Singh, U. K. Molecular mechanisms in the pathogenesis of diabetic nephropathy:An update. *Vascular pharmacology* **2013**, *58* (4), 259–271. DOI: 10.1016/j.vph.2013.01.001.

(14) Chen, S.; Hong, S. W.; Iglesias-dela Cruz, M. C.; Isono, M.; Casaretto, A.; Ziyadeh, F. N. The Key Role of the Transforming Growth Factor-β System in the Pathogenesis of Diabetic Nephropathy. *Renal Failure* **2009**, *23* (3-4), 471–481. DOI: 10.1081/JDI-100104730.

(15) Zeng, L.-F.; Xiao, Y.; Sun, L. A Glimpse of the Mechanisms Related to Renal Fibrosis in Diabetic Nephropathy. *Advances in experimental medicine and biology* **2019**, *1165*, 49–79. DOI: 10.1007/978-981-13-8871-2_4.

(16) Ruggenenti, P.; Cravedi, P.; Remuzzi, G. The RAAS in the pathogenesis and treatment of diabetic nephropathy. *Nature reviews. Nephrology* **2010**, *6* (6), 319–330. DOI: 10.1038/nrneph.2010.58. Published Online: May. 4, 2010.

(17) Giacco, F.; Brownlee, M. Oxidative stress and diabetic complications. *Circulation research* **2010**, *107* (9), 1058–1070. DOI: 10.1161/CIRCRESAHA.110.223545.

(18) Tessari, P. Nitric oxide in the normal kidney and in patients with diabetic nephropathy. *Journal of nephrology* **2015**, *28* (3), 257–268. DOI: 10.1007/s40620-014-0136-2. Published Online: Sep. 13, 2014.

(19) Schinner, E.; Wetzl, V.; Schlossmann, J. Cyclic nucleotide signalling in kidney fibrosis. *International journal of molecular sciences* **2015**, *16* (2), 2320–2351. DOI: 10.3390/ijms16022320.

(20) Shen, K.; Johnson, D. W.; Gobe, G. C. The role of cGMP and its signaling pathways in kidney disease. *American journal of physiology. Renal physiology* **2016**, *311* (4), F671-F681. DOI: 10.1152/ajprenal.00042.2016. Published Online: Jul. 13, 2016.

(21) Krishnan, S.; Kraehling, J.; Eitner, F.; Bénardeau, A.; Sandner, P. The Impact of the Nitric Oxide (NO)/Soluble Guanylyl Cyclase (sGC) Signaling Cascade on Kidney Health and Disease: A Preclinical Perspective. *IJMS* **2018**, *19* (6), 1712. DOI: 10.3390/ijms19061712.

(22) Shi, Y.; Vanhoutte, P. M. Macro- and microvascular endothelial dysfunction in diabetes. *Journal of diabetes* **2017**, *9* (5), 434–449. DOI: 10.1111/1753-0407.12521. Published Online: Mar. 1, 2017.

(23) Adrian J. Hobbs; Johannes-Peter Stasch. Soluble Guanylate Cyclase.

(24) Murad, F. Nitric Oxide and Cyclic GMP in Cell Signaling and Drug Development. *The New England journal of medicine* **2006**, *355* (19), 2003–2011.

(25) Lundberg, J. O.; Gladwin, M. T.; Weitzberg, E. Strategies to increase nitric oxide signalling in cardiovascular disease. *Nature reviews. Drug discovery* **2015**, *14* (9), 623–641. DOI: 10.1038/nrd4623. Published Online: Aug. 7, 2015.

(26) Mátyás, C.; Németh, B. T.; Oláh, A.; Hidi, L.; Birtalan, E.; Kellermayer, D.; Ruppert, M.; Korkmaz-Icöz, S.; Kökény, G.; Horváth, E. M.; Szabó, G.; Merkely, B.; Radovits, T. The soluble guanylate cyclase activator cinaciguat prevents cardiac dysfunction in a rat model of type-1 diabetes mellitus. *Cardiovascular diabetology* **2015**, *14*, 145. DOI: 10.1186/s12933-015-0309-x.

(27) Kalk, P.; Godes, M.; Relle, K.; Rothkegel, C.; Hucke, A.; Stasch, J.-P.; Hocher, B. NO-independent activation of soluble guanylate cyclase prevents disease progression in rats with 5/6 nephrectomy. *British journal of pharmacology* **2006**, *148*.

(28) Hoffmann, L. S.; Kretschmer, A.; Lawrenz, B.; Hocher, B.; Stasch, J.-P. Chronic Activation of Heme Free Guanylate Cyclase Leads to Renal Protection in Dahl Salt-Sensitive Rats. *PloS one* **2015**, *10* (12), e0145048. DOI: 10.1371/journal.pone.0145048. Published Online: Dec. 30, 2015.

(29) Hohenstein, B.; Daniel, C.; Wagner, A.; Stasch, J.-P.; Hugo, C. Stimulation of soluble guanylyl cyclase inhibits mesangial cell proliferation and matrix accumulation in experimental glomerulonephritis. *American journal of physiology. Renal physiology* **2005**, *288* (4), F685-F693. DOI: 10.1152/ajprenal.00280.2004.

(30) Czirok, S.; Fang, L.; Radovits, T.; Szabó, G.; Szénási, G.; Rosivall, L.; Merkely, B.; Kökény, G. Cinaciguat ameliorates glomerular damage by reducing ERK1/2 activity and TGF-ß expression in type-1 diabetic rats. *Scientific reports* **2017**, *7* (1), 11218. DOI: 10.1038/s41598-017-10125-3.

(31) Beyer, C.; Zenzmaier, C.; Palumbo-Zerr, K.; Mancuso, R.; Distler, A.; Dees, C.; Zerr, P.; Huang, J.; Maier, C.; Pachowsky, M. L.; Friebe, A.; Sandner, P.; Distler, O.; Schett, G.; Berger, P.; Distler, J. H. W. Stimulation of the soluble guanylate cyclase (sGC) inhibits fibrosis by blocking non-canonical TGFβ signalling. *Annals of the rheumatic diseases* **2015**, *74* (7), 1408–1416. DOI: 10.1136/annrheumdis-2013-204508.

(32) Erdmann, E.; Semigran, M. J.; Nieminen, M. S.; Gheorghiade, M.; Agrawal, R.; Mitrovic, V.; Mebazaa, A. Cinaciguat, a soluble guanylate cyclase activator, unloads the heart but also causes hypotension in acute decompensated heart failure. *European heart journal* **2013**, *34* (1), 57–67. DOI: 10.1093/eurheartj/ehs196. Published Online: Jul. 9, 2012.

(33) Glassman, P. M.; Muzykantov, V. R. Pharmacokinetic and Pharmacodynamic Properties of Drug Delivery Systems. *The Journal of pharmacology and experimental therapeutics* **2019**, *370* (3), 570–580. DOI: 10.1124/jpet.119.257113. Published Online: Mar. 5, 2019.

(34) Yoo, J.; Park, C.; Yi, G.; Lee, D.; Koo, H. Active Targeting Strategies Using Biological Ligands for Nanoparticle Drug Delivery Systems. *Cancers* **2019**, *11* (5), 640. DOI: 10.3390/cancers11050640.

(35) Nag, O. K.; Delehanty, J. B. Active Cellular and Subcellular Targeting of Nanoparticles for Drug Delivery. *Pharmaceutics* **2019**, *11* (10). DOI: 10.3390/pharmaceutics11100543. Published Online: Oct. 18, 2019.

(36) Wang, K.; Wen, H.-F.; Yu, D.-G.; Yang, Y.; Zhang, D.-F. Electrosprayed hydrophilic nanocomposites coated with shellac for colon-specific delayed drug delivery. *Materials & Design* **2018**, *143*, 248–255. DOI: 10.1016/j.matdes.2018.02.016.

(37) Colino, C. I.; Lanao, J. M.; Gutierrez-Millan, C. Targeting of Hepatic Macrophages by Therapeutic Nanoparticles. *Frontiers in immunology* **2020**, *11*, 218. DOI: 10.3389/fimmu.2020.00218.

(38) Li, S.; Zeng, Y.-C.; Peng, K.; Liu, C.; Zhang, Z.-R.; Zhang, L. Design and evaluation of glomerulus mesangium-targeted PEG-PLGA nanoparticles loaded with dexamethasone acetate. *Acta pharmacologica Sinica* **2019**, *40* (1), 143–150. DOI: 10.1038/s41401-018-0052-4.

(39) Fleischmann, D.; Maslanka Figueroa, S.; Beck, S.; Abstiens, K.; Witzgall, R.; Schweda, F.; Tauber, P.; Goepferich, A. Adenovirus-Mimetic Nanoparticles: Sequential Ligand-Receptor Interplay

as a Universal Tool for Enhanced In Vitro/In Vivo Cell Identification. *ACS applied materials & interfaces* **2020**, *12* (31), 34689–34702. DOI: 10.1021/acsami.0c10057. Published Online: Jul. 22, 2020.

(40) Maslanka Figueroa, S.; Fleischmann, D.; Goepferich, A. Biomedical nanoparticle design: What we can learn from viruses. *Journal of controlled release : official journal of the Controlled Release Society* **2020**. DOI: 10.1016/j.jconrel.2020.09.045.

(41) Fleischmann, D.; Maslanka Figueroa, S.; Goepferich, A. Steric Shielding of cRGD-Functionalized Nanoparticles from Premature Exposition to Off-Target Endothelial Cells under a Physiological Flow. *ACS Appl. Bio Mater.* **2021**, *4* (1), 640–650. DOI: 10.1021/acsabm.0c01193.

(42) Geiselhöringer, A.; Gaisa, M.; Hofmann, F.; Schlossmann, J. Distribution of IRAG and cGKI-isoforms in murine tissues. *FEBS Letters* **2004**, *575* (1-3), 19–22. DOI: 10.1016/j.febslet.2004.08.030.

(43) Kurtz, A.; Jelkmann, W.; Bauer, C. Mesangial cells derived from rat glomeruli produce an erythropoiesis stimulating factor in cell culture. *FEBS Letters* **1982**, *137* (1), 129–132. DOI: 10.1016/0014-5793(82)80330-X.

(44) Pfeilschifter, J.; Schalkwijk, C.; Briner, V. A.; van den Bosch, H. Cytokine-stimulated secretion of group II phospholipase A2 by rat mesangial cells. Its contribution to arachidonic acid release and prostaglandin synthesis by cultured rat glomerular cells. *The Journal of clinical investigation* **1993**, *92* (5), 2516–2523. DOI: 10.1172/JCI116860.

(45) Maslanka Figueroa, S.; Fleischmann, D.; Beck, S.; Tauber, P.; Witzgall, R.; Schweda, F.; Goepferich, A. Nanoparticles Mimicking Viral Cell Recognition Strategies Are Superior Transporters into Mesangial Cells. *Adv. Sci.* **2020**, *7* (11), 1903204. DOI: 10.1002/advs.201903204.

(46) Abstiens, K.; Gregoritza, M.; Goepferich, A. M. Ligand Density and Linker Length are Critical Factors for Multivalent Nanoparticle-Receptor Interactions. *ACS applied materials & interfaces* **2019**, *11* (1), 1311–1320. DOI: 10.1021/acsami.8b18843.

(47) Maslanka Figueroa, S.; Veser, A.; Abstiens, K.; Fleischmann, D.; Beck, S.; Goepferich, A. Influenza A Virus Mimetic Nanoparticles Trigger Selective Cell Uptake. *Proc. Natl. Acad. Sci. U. S. A.States of America* **2019**. DOI: 10.1073/pnas.1902563116.

(48) Muenster, U.; Becker-Pelster, E.-M.; Mao, S.; Ni, R.; Liang, Z. Process for the Preparation of Porous Microparticles.

(49) Maslanka Figueroa, S.; Fleischmann, D.; Beck, S.; Goepferich, A. Thermodynamic, Spatial and Methodological Considerations for the Manufacturing of Therapeutic Polymer Nanoparticles. *Pharm Res* **2020**, *37* (3). DOI: 10.1007/s11095-020-2783-4.

(50) Thakral, S.; Thakral, N. K. Prediction of drug-polymer miscibility through the use of solubility parameter based Flory-Huggins interaction parameter and the experimental validation: PEG as model polymer. *Journal of Pharmaceutical Sciences* **2013**, *102* (7), 2254–2263. DOI: 10.1002/jps.23583. Published Online: May. 6, 2013.

(51) Kansal, A. R.; Torquato, S.; Stillinger, F. H. Computer generation of dense polydisperse sphere packings. *The Journal of chemical physics* **2002**, *117* (18), 8212–8218. DOI: 10.1063/1.1511510.

(52) Fedors, R. F. A method for estimating both the solubility parameters and molar volumes of liquids. *Polymer Engineering and Science* **1974**, *14* (2), 147–154.

(53) Schramm, A.; Mueller-Thuemen, P.; Littmann, T.; Harloff, M.; Ozawa, T.; Schlossmann, J. Establishing a Split Luciferase Assay for Proteinkinase G (PKG) Interaction Studies. *IJMS* **2018**, *19* (4), 1180. DOI: 10.3390/ijms19041180.

(54) Lowry, O. H.; Rosebrough, N. J.; Lewis Farr, A.; Randall, R. J. Protein Measurement With the Folin Phenol Reagent. *J. Biol. Chem.* **1951**, *193*, 265–275.

(55) Danielpour, D.; Kim, K. Y.; Dart, L. L.; Watanabe, S.; Roberts, A. B.; Sporn, M. B. Sandwich enzyme-linked immunosorbent assays (SELISAs) quantitate and distinguish two forms of transforming growth factor-beta (TGF-beta 1 and TGF-beta 2) in complex biological fluids. *Growth factors (Chur, Switzerland)* **1989**, *2* (1), 61–71. DOI: 10.3109/08977198909069082.

(56) Satchell, S. C.; Braet, F. Glomerular Endothelial Cell Fenestrations: an Integral Component of the Glomerular Filtration Barrier. *Am. J. Physiol. Renal Physiol.* **2009**, *296* (5), 947-956. DOI: 10.1152/ajprenal.90601.2008.

(57) Nam, H. Y.; Kwon, S. M.; Chung, H.; Lee, S.-Y.; Kwon, S.-H.; Jeon, H.; Kim, Y.; Park, J. H.; Kim, J.; Her, S.; Oh, Y.-K.; Kwon, I. C.; Kim, K.; Jeong, S. Y. Cellular uptake mechanism and intracellular fate of hydrophobically modified glycol chitosan nanoparticles. *Journal of controlled release : official journal of the Controlled Release Society* **2009**, *135* (3), 259–267. DOI: 10.1016/j.jconrel.2009.01.018.

(58) Seo, S.-J.; Chen, M.; Wang, H.; Kang, M. S.; Leong, K. W.; Kim, H.-W. Extra- and intra-cellular fate of nanocarriers under dynamic interactions with biology. *Nano today* **2017**, *14*, 84–99. DOI: 10.1016/j.nantod.2017.04.011.

(59) Meurer, S.; Pioch, S.; Pabst, T.; Opitz, N.; Schmidt, P. M.; Beckhaus, T.; Wagner, K.; Matt, S.; Gegenbauer, K.; Geschka, S.; Karas, M.; Stasch, J.-P.; Schmidt, Harald H. H. W.; Müller-Esterl, W. Nitric oxide-independent vasodilator rescues heme-oxidized soluble guanylate cyclase from proteasomal degradation. *Circulation research* **2009**, *105* (1), 33–41. DOI: 10.1161/CIRCRESAHA.109.198234. Published Online: May. 28, 2009.

(60) Evgenov, O. V.; Pacher, P.; Schmidt, P. M.; Hasko, G.; Schmidt, Harald H. H. W.; Stasch, J.-P. NO-independent stimulators and activators of soluble guanylate cyclase: discovery and therapeutic potential. *Nature reviews. Drug discovery* **2006**, *5* (9), 755–768.

(61) Martin, F.; Baskaran, P.; Ma, X.; Dunten, P. W.; Schaefer, M.; Stasch, J.-P.; Beuve, A.; van den Akker, F. Structure of cinaciguat (BAY 58-2667) bound to Nostoc H-NOX domain reveals insights into heme-mimetic activation of the soluble guanylyl cyclase. *The Journal of biological chemistry* **2010**, *285* (29), 22651–22657. DOI: 10.1074/jbc.M110.111559. Published Online: May. 12, 2010.

(62) Smolenski, A.; Burckhardt, M.; Eigenthaler, M.; Butt, E.; Gambaryan, S.; Lohmann, S. M.; Walter, U. Functional analysis of cGMP-dependent protein kinases I and II as mediators of NO/cGMP effects. *Naunyn-Schmiedeberg′s Archives of Pharmacology* **1998**, *358*, 134–139.

Chapter 5 – Supporting Information

Targeted Delivery of Soluble Guanylate Cyclase (sGC) Activator Cinaciguat to Renal Mesangial Cells *via* Virus-Mimetic Nanoparticles Potentiates Anti-Fibrotic Effects by cGMP-Mediated Suppression of the TGF-β Pathway

1 HPLC chromatograms
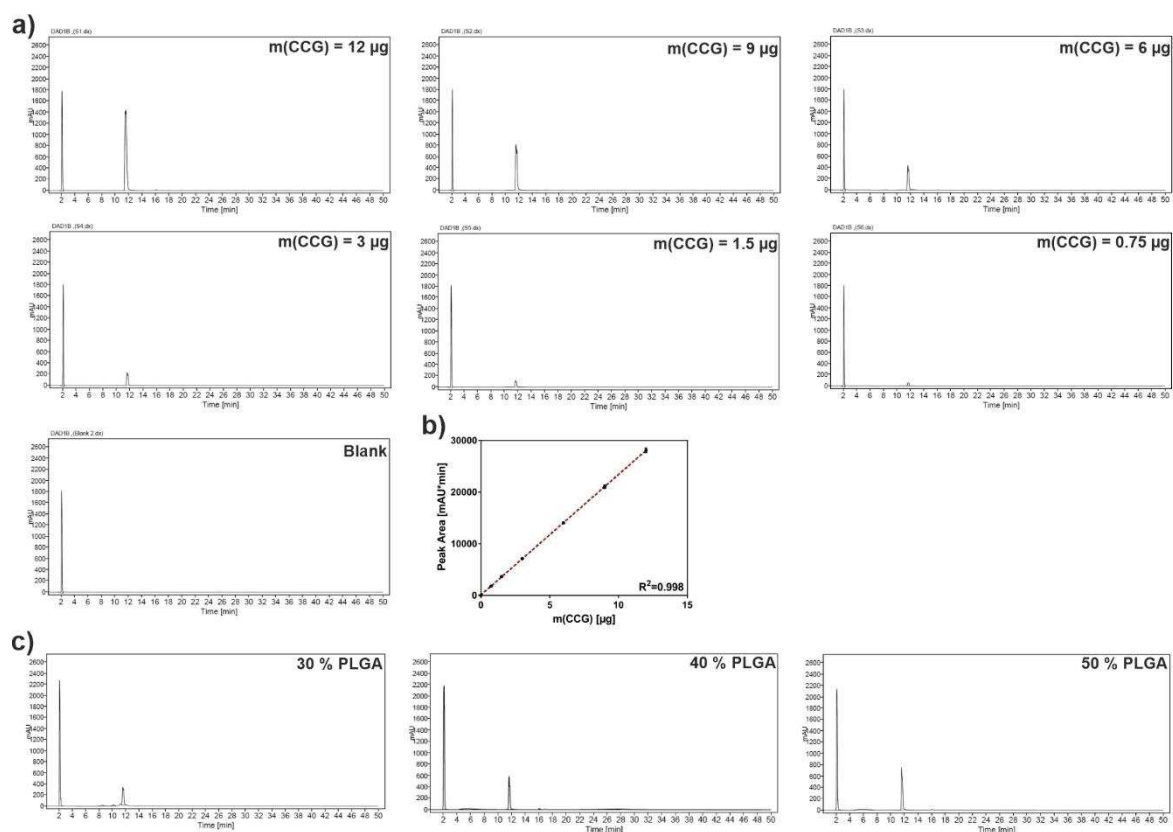
Figure S1. HPLC chromatograms. **a)** Representative HPLC chromatograms for the calibration of free Cinaciguat. **b)** HPLC calibration. Results represent mean ± SD (n = 3). **c)** Representative chromatograms for NP species carrying 30-50% PLGA and an initial CCG addition of 10 µg per 4 mg NP batch.

2 DLS data
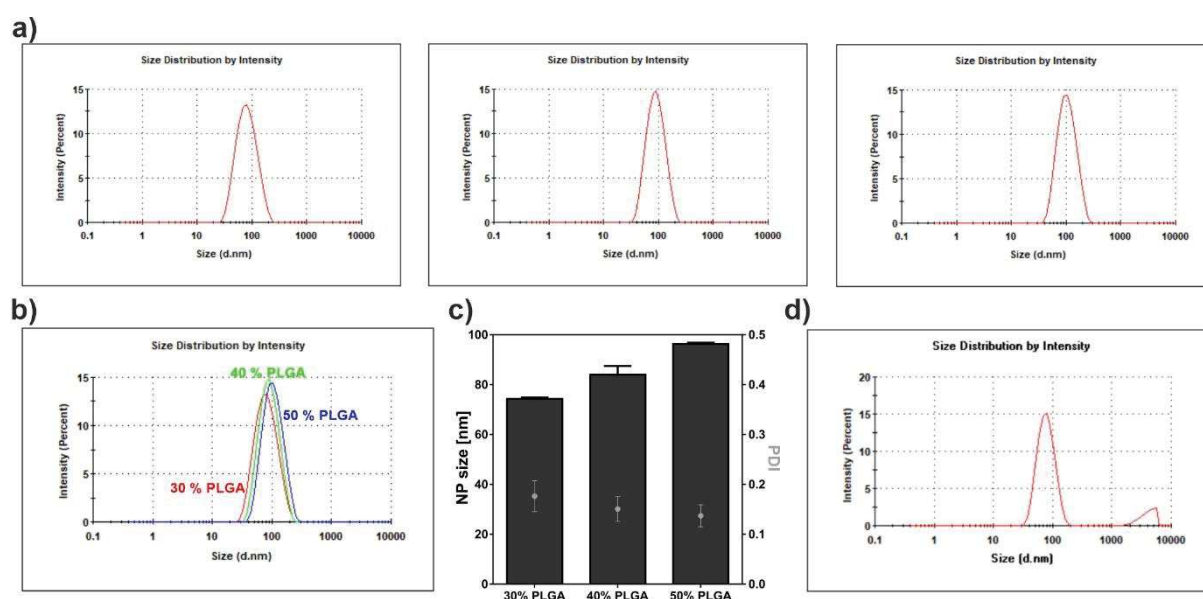
Figure S2. a) DLS size distribution of NP species containing 30/40/50% PLGA (from left to right). **b)** Merged DLS graphs. **c)** Size and polydispersity index (PDI) data for different NP species. **d)** Representative DLS graph

of 40% PLGA NPs and an addition of 17.5 µg per 4 mg NP batch, showing a strong tendency for larger aggregates (see right peak).

3 Physicochemical parameters

a)

	size NP [nm]	d(NP core) [nm]	V(NP core) [nm³]
30 % PLGA 1	75	11	697
30 % PLGA 2	74	10	523
30 % PLGA 3	74	10	523
40 % PLGA 1	82	18	3052
40 % PLGA 2	82	18	3052
40 % PLGA 3	88	19	3590
50 % PLGA 1	97	33	18807
50 % PLGA 2	96	32	17149
50 % PLGA 3	96	32	17149

b)

|	size NP [nm]	m(CCG) [µg]	N(CCG)	m(NP) [mg]	n(NP) [mol]	N(NP)	CCG molecules/NP	CCG molecules/NP(ideal)	Entrapment efficiency [%]	Encapsulation efficiency [%]
30 % PLGA 1	75	2,59	2,76E+15	2,99	1,80E-11	1,08E+13	254,74	865,22	29,44	25,90
30 % PLGA 2	74	3,72	3,96E+15	3,45	2,16E-11	1,30E+13	304,88	650,05	46,90	37,24
30 % PLGA 3	74	3,69	3,93E+15	3,12	1,95E-11	1,18E+13	334,05	650,05	51,39	36,90
40 % PLGA 1	82	4,73	5,04E+15	3,14	1,44E-11	8,70E+12	579,07	3791,11	15,27	47,31
40 % PLGA 2	82	4,93	5,24E+15	3,02	1,39E-11	8,36E+12	626,80	3791,11	16,53	49,25
40 % PLGA 3	88	4,16	4,43E+15	3,02	1,32E-11	7,96E+12	556,32	4458,72	12,48	41,59
50 % PLGA 1	97	6,05	6,44E+15	3,11	8,64E-12	5,20E+12	1237,84	23360,97	5,30	60,51
50 % PLGA 2	96	5,66	6,03E+15	3,05	8,74E-12	5,26E+12	1145,17	21300,95	5,38	56,64
50 % PLGA 3	96	5,52	5,88E+15	2,98	8,54E-12	5,14E+12	1142,50	21300,95	5,36	55,21

c)
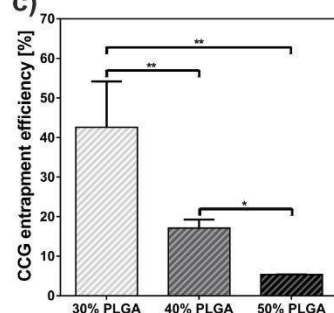
Figure S3. a) Results for calculation of NP core volume for each sample. **b)** Results for calculation of CCG encapsulation as well as entrapment efficiency. **c)** CCG entrapment efficiency per NP type. Results represent mean ± SD (n = 3). *P<0.05 **P<0.01.

4 Impact of serum starvation
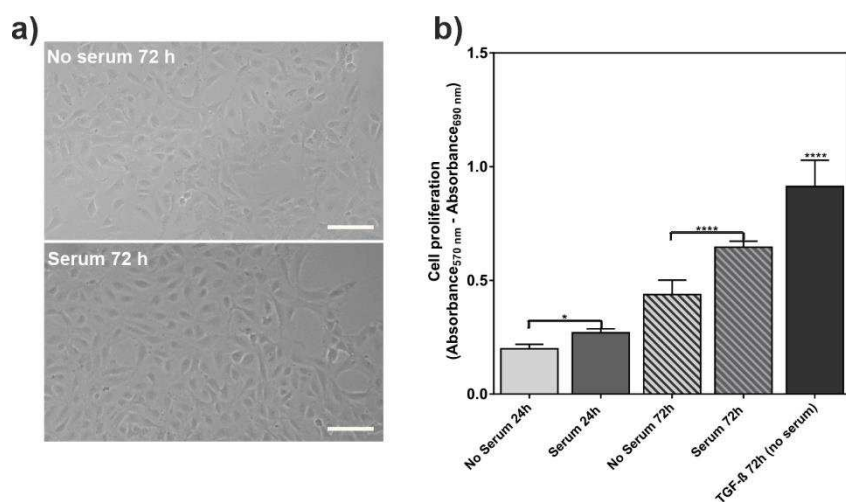
Figure S4. a) Brightfield images of rMCs cultured for 72 h during the cell proliferation assay either without (top) or with (bottom) addition of 10 % FBS. (Scale bar 100 μm). **b)** MTT assay results of rMC proliferation after 24 h and 72 h with and without addition of 10 % FBS. (Note: The results for samples "No serum 72 h" and "TGF-β 72 h (no serum)" represent the blank-normalized samples "Blank cells" and "TGF-β" in Figure 7a of the main manuscript.) Results represent mean ± SD (n = 3). *P<0.05 ****P<0.0001.

Chapter 6

Summary and Conclusion

1   Summary

Although modern pharmaceutical research is able to identify promising drugs for a plethora of existing diseases at a growing pace, a great number of possible therapeutic candidates show limited efficiency due to an unfavorable biodistribution or severe side effects in off-target tissues after administration. While nanoparticular drug delivery approaches could potentially provide a solution for this predicament, criticism over the disappointing outcome of many NP-assisted therapy approaches has intensified in recent years.[1] One key aspect is thereby the oftentimes low bioavailability, that (targeted) NP systems have shown despite the implementation of more and more complex materials.[2,3] Apart from a general clearance *via* the MPS, the majority of currently existing nanoparticular concepts thereby also suffer from a considerable off-target accumulation in the usual suspects, i.e. the liver, kidney, and the vascular system. It would therefore be a promising approach to harness this to some extent inevitable deposition and combine it with active targeting concepts to treat pathologically remodeled cell types within the respective tissues or organs (**Chapter 1**). NPs would thereby profit not only from their cell-selective recognition patterns, but also from a considerable passive targeting effect *via* the intravascular transport into respective regions.

Filtrating the entire blood volume for approximately 300 times a day, the kidney is thereby one particular interesting region for NP-mediated drug delivery as a substantial portion of intravenously administered NPs will inevitably pass the organ. Within the kidneys´ glomeruli, mesangial cells act as key players in controlling the structural support of the actual filtration apparatus consisting of podocytes, a basement membrane end glomerular endothelial cells.[4,5] However, various renal diseases such as diabetic nephropathy are accompanied by a progredient malfunction of described mesangial cells, leading to a pro-fibrotic turnover of extracellular matrix components and a pathological remodeling of the glomerular filtration barrier.[6] In this regard, NP-assisted drug delivery into the mesangium could offer a highly beneficial alternative to currently existing therapeutic options, as particles are able to passively accumulate in mesangial regions *via* extravasation through the fenestrated glomerular endothelium.[7]

In this work, mimicry of adenoviral host cell identification was used to substantially increase target cell specificity of NPs during their active recognition of mesangial surface structures (**Chapter 2**). Inspired by AdV2, NPs thereby initially bind mesangial AT1r to enable NP-cell attachment without immediate cell uptake. Only after a resulting spatial approach, NPs present a previously shielded second ligand, which triggers NP endocytosis *via* activation of mesangial surface integrin $\alpha_v\beta_3$ (**Chapter 3**). While functionalization of block-copolymer NPs with AT1r antagonist EXP3174 thereby led to an efficient binding of AT1r and thus the mesangial cell surface, attached integrin activator cRGDfK enabled a substantial receptor-mediated endocytosis of targeted NPs into the mesangial cytosol. Also, introduction of a steric shielding concept, that initially limited the visibility of the second ligand, led to an adenovirus-mimetic and therefore sequential NP-cell interaction of initial AT1r binding and subsequent integrin-

mediated NP uptake, thereby drastically increasing the NPs´ target cell specificity in an *in vitro* co-culture assay with off-target cells. Hetero-multivalent EXPcRGD NPs eventually also

showed a substantial *in vivo* accumulation within mesangial regions, proving the potential of a combination of passive and active targeting functionalities.

When it comes to the design of actively targeted NP systems, the impact of the actual particle transport within the blood vessels is generally overlooked. However, ligand-receptor interactions can be greatly influenced by the imminent dynamic blood flow, that administered NPs are subject to.[8–10] Also, off-target deposition into vascular endothelial cells can severely limit targeting efficiency of NPs, as the addressed cell surface structures such as integrins are to some extent also expressed in the endothelium. In this regard, the concept of sterically shielding cRGD sequences from premature presentation to off-targets such as vascular endothelial cells provided promising results as NP-cell interaction could be precisely regulated by the introduction of varying densities of longer protruding shielding elements (**Chapter 4**). The concept could thereby be maintained both under static and more realistic dynamic flow conditions. Also, cRGD-integrin interaction was minimal at higher flow rates and intensified at lower flow rates, where the timespan for NP-cell interaction and following ligand unveiling was increased. This observation could in part explain the successful *in vivo* targeting of mesangial regions with the adenovirus-mimetic NP system. Due to the shielding effect as well as the substantial blood flow in larger vessels, particles initially showed only marginal off-target deposition to vascular endothelial cells. Only after an extravasation into the mesangium, flow rate decreased, and NPs could interact with their target cells in the described sequential manner.

As mentioned above, the mesangium plays a central role in the fibrotic remodeling of the renal filtration apparatus during pathologies such as diabetic nephropathy.[11,12] Therefore, encapsulation of anti-fibrotic drug candidates into adenovirus-mimetic NPs could offer a substantial benefit for the therapy of respective renal diseases. In this regard, sGC activator cinaciguat is an ideal candidate for NP drug delivery, as it has previously shown a considerable therapeutic potential for pathologically affected mesangial cells but suffers from a poor biodistribution and unfavorable side effects after administration.[13–16] Based on its substantial lipophilicity and a sufficient miscibility with the NP core component PLGA, CCG could be reproducibly encapsulated into the adenovirus-mimetic NP system, whereby resulting NPs could maintain their active mesangial targeting functionalities (**Chapter 5**). Due to an efficient transport into cytosolic regions of mesangial cells, resulting CCG-loaded NPs could significantly increase the pharmacological potency of the drug regarding sGC stabilization and activation of the sGC-cGMP cascade. Also, therapeutic NPs showed beneficial results regarding an anti-fibrotic effect in a TGF-β model compared to the application of the free drug.

Taken together, the depicted results show the considerable potential of the combination of passive targeting strategies into general sites of NP biodistribution with virus-inspired active cell recognition patterns. It also became evident, that for a successful NP-assisted therapy, a greater focus has to be

placed on relevant physiological parameters such as blood flow dynamics or the microarchitecture of the target tissue.

2 Conclusion

This work led to the manufacture of an adenovirus-mimetic NP system, that is able to successfully imitate the sequential target cell recognition process of its viral model AdV2. The functionalization of block-copolymer NPs with two different ligands and, most importantly, the step-wise presentation of these ligands led to a substantial mesangial specificity both *in vitro* and *in vivo*. In this regard, the concept of a steric shielding of the second, uptake-mediating ligand could also be maintained under more realistic conditions of a dynamic flow cell culture and NP incubation. More so, the encapsulation of sGC activator cinaciguat into the adenovirus-mimetic NPs led to a substantially increased pharmacological potency and a considerably enhanced anti-fibrotic effect compared to the administration of the free drug.

Taken all together, the described findings demonstrate the immense potential of a NP-assisted therapy of kidney pathologies such as diabetic nephropathy. In this regard, future nanotherapeutic research will hopefully lead to a better treatability of these oftentimes detrimental long-term effects of diabetes, for which currently, merely unsatisfactory therapeutic options exist.

References

(1) Park, K. The beginning of the end of the nanomedicine hype. *Journal of controlled release : official journal of the Controlled Release Society* **2019**, *305*, 221–222. DOI: 10.1016/j.jconrel.2019.05.044.

(2) Wilhelm, S.; Tavares, A. J.; Dai, Q.; Ohta, S.; Audet, J.; Dvorak, H. F.; Chan, W. C. W. Analysis of Nanoparticle Delivery to Tumours. *Nature Reviews Materials* **2016**, *1* (5), 16014. DOI: 10.1038/natrevmats.2016.14.

(3) Dai, Q.; Wilhelm, S.; Ding, D.; Syed, A. M.; Sindhwani, S.; Zhang, Y.; Chen, Y. Y.; MacMillan, P.; Chan, W. C. W. Quantifying the Ligand-Coated Nanoparticle Delivery to Cancer Cells in Solid Tumors. *ACS nano* **2018**, *12* (8), 8423–8435. DOI: 10.1021/acsnano.8b03900.

(4) Schlöndorff, D. Roles of the Mesangium in Glomerular Function. *Kidney Int.* **1996**, *49* (6), 1583–1585. DOI: 10.1038/ki.1996.229.

(5) Schlöndorff, D.; Banas, B. The Mesangial Cell Revisited:No Cell Is an Island. *J. Am. Soc. Nephrol.* **2009**, *20* (6), 1179–1187. DOI: 10.1681/ASN.2008050549.

(6) Arora, M. K.; Singh, U. K. Molecular mechanisms in the pathogenesis of diabetic nephropathy:An update. *Vascular pharmacology* **2013**, *58* (4), 259–271. DOI: 10.1016/j.vph.2013.01.001.

(7) Choi, C. H. J.; Zuckerman, J. E.; Webster, P.; Davis, M. E. Targeting kidney mesangium by nanoparticles of defined size. *Proceedings of the National Academy of Sciences of the United States of America* **2011**, *108* (16), 6656–6661. DOI: 10.1073/pnas.1103573108.

(8) Chen, Y. Y.; Syed, A. M.; MacMillan, P.; Rocheleau, J. V.; Chan, W. C. W. Flow Rate Affects Nanoparticle Uptake into Endothelial Cells. *Advanced materials (Deerfield Beach, Fla.)* **2020**, *32* (24), e1906274. DOI: 10.1002/adma.201906274.

(9) Namdee, K.; Thompson, A. J.; Charoenphol, P.; Eniola-Adefeso, O. Margination propensity of vascular-targeted spheres from blood flow in a microfluidic model of human microvessels. *Langmuir : the ACS journal of surfaces and colloids* **2013**, *29* (8), 2530–2535. DOI: 10.1021/la304746p.

(10) Mehrabadi, M.; Ku, D. N.; Aidun, C. K. Effects of shear rate, confinement, and particle parameters on margination in blood flow. *Physical review. E* **2016**, *93* (2), 23109. DOI: 10.1103/PhysRevE.93.023109.

(11) Kolset, S. O.; Reinholt, F. P.; Jenssen, T. Diabetic Nephropathy and Extracellular Matrix. *J. Histochem. Cytochem.* **2012**, *60* (12), 976–986. DOI: 10.1369/0022155412465073.

(12) Kanwar, Y. S.; Sun, L.; Xie, P.; Liu, F.-Y.; Chen, S. A glimpse of various pathogenetic mechanisms of diabetic nephropathy. *Annual review of pathology* **2011**, *6*, 395–423. DOI: 10.1146/annurev.pathol.4.110807.092150.

(13) Czirok, S.; Fang, L.; Radovits, T.; Szabó, G.; Szénási, G.; Rosivall, L.; Merkely, B.; Kökény, G. Cinaciguat ameliorates glomerular damage by reducing ERK1/2 activity and TGF-ß expression in type-1 diabetic rats. *Scientific reports* **2017**, *7* (1), 11218. DOI: 10.1038/s41598-017-10125-3.

(14) Beyer, C.; Zenzmaier, C.; Palumbo-Zerr, K.; Mancuso, R.; Distler, A.; Dees, C.; Zerr, P.; Huang, J.; Maier, C.; Pachowsky, M. L.; Friebe, A.; Sandner, P.; Distler, O.; Schett, G.; Berger, P.; Distler, J. H. W. Stimulation of the soluble guanylate cyclase (sGC) inhibits fibrosis by blocking non-canonical TGFβ signalling. *Annals of the rheumatic diseases* **2015**, *74* (7), 1408–1416. DOI: 10.1136/annrheumdis-2013-204508.

(15) Geschka, S.; Kretschmer, A.; Sharkovska, Y.; Evgenov, O. V.; Lawrenz, B.; Hucke, A.; Hocher, B.; Stasch, J.-P. Soluble guanylate cyclase stimulation prevents fibrotic tissue remodeling and improves survival in salt-sensitive Dahl rats. *PloS one* **2011**, *6* (7), e21853. DOI: 10.1371/journal.pone.0021853.

(16) Erdmann, E.; Semigran, M. J.; Nieminen, M. S.; Gheorghiade, M.; Agrawal, R.; Mitrovic, V.; Mebazaa, A. Cinaciguat, a soluble guanylate cyclase activator, unloads the heart but also causes hypotension in acute decompensated heart failure. *European heart journal* **2013**, *34* (1), 57–67. DOI: 10.1093/eurheartj/ehs196. Published Online: Jul. 9, 2012.

Appendix

α-SMA	α-smooth muscle actin
ACE	Angiotensin converting enzyme
ACN	Acetonitrile
AdV2	Human adenovirus type 2
AFU	Arbitrary fluorescence unit
Alexa568	AlexaFluor568 hydrazide
ANOVA	Analysis of variance
Phalloidin	AlexaFluor 568 Phalloidin
ApoE	Apolipoprotein E
ASGPR	Asialoglycoprotein receptor
AT-I/-II	Angiotensin I/II
AT1r	Angiotensin II receptor type 1
ATTR	Amyloidogenic transthyretin
BME	β-mercaptoethanol
BSA	Bovine serum albumine
CAM	Cell adhesion molecule
CAR	Coxsackie and adenovirus receptor
CCG	Cinaciguat
CCR	CC chemokine receptor
CellMask	CellMask deep red plasma membrane stain
cGMP	3′,5′-cyclic guanosine monophosphate
CKD	Chronic kidney disease
CLSM	Confocal laser scanning microscopy
Col1α1	Collagen 1α1
COPD	Chronic obstructive pulmonary disease
CP	Cyclopentenone
CPP	Cell penetrating peptide
cRGDfC	Cyclo(-Arg-Gly-Asp-D-Phe-Cys)
cRGDfK	Cyclo(-Arg-Gly-Asp-D-Phe-Lys)
CTG	CellTracker Green

CTDR	CellTracker Deep Red
DAPI	4′,6-diamidine-2′-phenylindole dihydrochloride
DCC	N,N′-dicyclohexylcarbodiimide
DCM	Dichloromethane
DFG	German research foundation
DIPEA	N,N-diisopropylethylamine
DLS	Dynamic light scattering
DMSO	Dimethyl sulfoxide
DMTMM	4-(4,6-dimethoxy-1,3,5-triazin-2-yl)-4-methylmorpholinium chloride
DN	Diabetic nephropathy
DPBS	Dulbecco´s phosphate-buffered saline
EDC	3-(ethyliminomethyleneamino)-N,N-dimethylpropan-1-amine
ECM	Extracellular matrix
EE	Encapsulation efficiency
EGTA	Ethylene glycol-bis(2-aminoethylether)-N,N,N′,N′-tetraacetic acid
ERK1/2	Extracellular-regulated kinase 1/2
ESRD	End-stage renal disease
FBS	Fetal bovine serum
GAPDH	Glyceraldehyde 3-phosphate dehydrogenase
GBM	Glomerular basement membrane
GFB	Glomerular filtration barrier
GFP	Green fluorescent protein
GFR	Glomerular filtration rate
GTP	Guanosine triphosphate
HA	Hyaluronic acid
HBV	Hepatitis virus B
HDL	High-density lipoprotein
HPLC	High-performance liquid chromatography
HSA	Human serum albumine
HSC	Hepatic stellate cell
HUVEC	Human umbilical vein endothelial cell
HVJ	Hemagglutinating virus of Japan
IC_{50}	Half-maximal inhibitory concentration

ICAM	Intercellular adhesion molecule
IFN-γ	Interferon-γ
ITS	Insulin-transferrin-selenium
KC	Kupffer cell
LB	Leibovitz´s buffer
LDL	Low-density lipoprotein
LSEC	Liver sinusoidal endothelial cell
MC	Mesangial cell
M6P	Mannose 6-phosphate
mpH$_2$O	Millipore water
MPS	Mononuclear phagocyte system
MR	Mannose receptor
MRI	Magnet resonance imaging
mTOR	Mechanistic target of rapamycin
MTT	3-(4,5-dimethylthiazol-2-yl)-2,5-diphenyltetrazolium bromide
NAcGal	N-acetyl-D-galactosamine
NHS	N-hydroxysuccinimide
NK	Natural killer cell
NO	Nitric oxide
NP	Nanoparticle
NNM	Nanomedicine
oxLDL	Oxidized low-density lipoprotein
oxPC	Oxidized phosphatidylcholine
PAMAM	Polyamidoamine
PCL	Poly(caprolactone)
PDGFR	Platelet-derived growth factor receptor
PDI	Polydispersity index
PECAM-1	Platelet-endothelial cell adhesion molecule-1
PEG	Poly-(ethylene glycol)
PEI	Poly(ethylene imine)
PFA	Paraformaldehyde
PFD	Pirfenidone
PGK1-α	Protein-regulated kinase 1 α

PLGA	Poly(lactic-co-glycolic acid)
PPARγ	Peroxisome proliferator-activated receptor γ
PVA	Polyvinyl alcohol
RAAS	Renin-angiotensin-aldosterone system
RBPR	Retinol binding protein receptor
rMC	Rat mesangial cell
RT	Room temperature
SDS-PAGE	Sodium dodecyl sulfate polyacrylamide gel electrophoresis
sGC	Soluble guanylate cyclase
SD	Standard deviation
SR	Scavenger receptor
TAT	Transactivating transcriptional activator
TEM	Transmission electron microscopy
TFA	Trifluoroacetic acid
TGF-β	Transforming growth factor β
TLR-4	Toll-like receptor 4
VCAM-1	Vascular cell adhesion molecule 1
VEC	Vascular endothelial cell
VEGFR-2	Vascular endothelial growth factor receptor 2
vWF	Von Willebrand Factor
VE-cadherin	Vascular endothelial cadherin
VASP	Vasodilator-stimulated phosphoprotein
YFP	Yellow fluorescence protein

Name:	Daniel Fleischmann
Date of birth:	6th of November 1990
Place of birth:	Furth im Wald
Nationality:	German

Scientific education

07/2017 – 03/2021	PhD Candidate, Department of Pharmaceutical Technology, University of Regensburg
07/2017	Licensure as Pharmacist
11/2016 – 04/2017	Practical training, Neue Apotheke St. Josef, Regensburg
01/2016 – 07/2016	Visiting Scientist, Fischbach Lab, Department of Biomedical Engineering, Cornell University, Ithaca, NY, USA
	"Influence of Obesity-Mediated ECM Changes on Breast Cancer Stem Cell Properties"
10/2011 – 10/2015	Study of Pharmacy, University of Regensburg

School education

07/2010 – 04/2011	Community service, Fachklinik Furth im Wald
09/2001 – 06/2010	Grammar school, Joseph-von-Fraunhofer Gymnasium Cham
09/1997 – 08/2001	Primary school, Grundschule Furth im Wald

List of Publications

Peer-reviewed publications

1. <u>Fleischmann, Daniel</u>; Goepferich, Achim; *General Sites of Nanoparticle Biodistribution As a Novel Opportunity for Nanomedicine.* Submitted for publication. **(Chapter 1)**

2. <u>Fleischmann, Daniel</u>; Harloff, Manuela; Maslanka Figueroa, Sara; Schlossmann, Jens; Goepferich, Achim; *Targeted Delivery of Soluble Guanylate Cyclase (sGC) Activator Cinaciguat to Renal Mesangial Cells via Virus-Mimetic Nanoparticles Potentiates Anti-Fibrotic Effects by cGMP-Mediated Suppression of the TGF-β Pathway.* In: International Journal of Molecular Sciences 2021, 22, 5, 2557. **(Chapter 5)**

3. <u>Fleischmann, Daniel</u>; Maslanka Figueroa, Sara; Goepferich, Achim; *Steric Shielding of cRGD-Functionalized Nanoparticles from Premature Exposition to Off-Target Endothelial Cells under a Physiological Flow.* In: ACS Applied Bio Materials 2021, 4, 1, 640-650. **(Chapter 4)**

4. Maslanka Figueroa, Sara; <u>Fleischmann, Daniel (Shared First Author)</u>; Goepferich, Achim; *Biomedical nanoparticle design: What we can learn from viruses.* In: Journal of Controlled Release 2020, 329, 552-569.

5. <u>Fleischmann, Daniel</u>; Maslanka Figueroa, Sara; Beck, Sebastian; Abstiens, Kathrin; Witzgall, Ralph; Schweda, Frank; Tauber, Philipp; Goepferich, Achim; *Adenovirus-Mimetic Nanoparticles: Sequential Ligand-Receptor Interplay as a Universal Tool for Enhanced In Vitro/In Vivo Cell Identification.* In: ACS Applied Materials & Interfaces 2020, 12, 3469-34702. **(Chapter 3)**

6. Maslanka Figueroa, Sara; <u>Fleischmann, Daniel</u>; Beck, Sebastian; Tauber, Philipp; Witzgall, Ralph; Schweda, Frank; Goepferich, Achim; *Nanoparticles Mimicking Viral Cell Recognition Strategies Are Superior Transporters into Mesangial Cells.* In: Advanced Science 2020, 1903204.

7. Maslanka Figueroa, Sara; <u>Fleischmann, Daniel</u>; Beck, Sebastian; Goepferich, Achim; *Thermodynamic, Spatial and Methodological Considerations for the Manufacturing of Therapeutic Polymer Nanoparticles.* In: Pharmaceutical Research 2020, 37, 3, 59.

8. Maslanka Figueroa, Sara; <u>Fleischmann, Daniel</u>; Beck, Sebastian; Goepferich, Achim; *The Effect of Ligand Mobility on the Cellular Interaction of Multivalent Nanoparticles.* In: Macromolecular Biosciences 2020, 20, 2, 1900427.

9. Maslanka Figueroa, Sara; Veser, Anika; Abstiens, Kathrin; <u>Fleischmann, Daniel</u>; Beck, Sebastian; Goepferich, Achim; *Influenza A Virus Mimetic Nanoparticles Trigger Selective Cell Uptake.* In: PNAS 2019, 116, 9831-9836.

10. Abstiens, Kathrin; <u>Fleischmann, Daniel</u>; Gregoritza, Manuel; Goepferich, Achim; *Gold-tagged Polymeric Nanoparticles with Spatially-Controlled Composition for Enhanced Detectability in Biological Environments.* In: ACS Applied Nano Materials 2019, 2, 917-926.

Conference abstracts

1. <u>Fleischmann, Daniel</u>; Maslanka Figueroa, Sara; Goepferich, Achim; *Adenovirus-Mimetic Nanoparticles as a Novel Tool to Potentiate Anti-Fibrotic Effects of Soluble Guanylate Cyclase (sGC) Activators.* International PhD Student & Postdoc Meeting of the German Pharmaceutical Society, Virtual Meeting, 2021.

2. <u>Fleischmann, Daniel</u>; Maslanka Figueroa, Sara; Goepferich, Achim; *Hetero-Multivalent Block-Copolymer Nanoparticles Show Enhanced Mesangial Cell Selectivity in an In Vitro Co-Culture Assay.* Annual Meeting and Exposition of the Controlled Release Society, Valencia, Spain, 2019.

3. Maslanka Figueroa, Sara; <u>Fleischmann, Daniel</u>; Goepferich, Achim; *Tailoring the particle corona composition modulates the cellular interaction of multivalent-binding nanoparticles.* Annual Meeting and Exposition of the Controlled Release Society, Valencia, Spain, 2019.

4. <u>Fleischmann, Daniel</u>; Maslanka Figueroa Sara, Goepferich, Achim; *Enhanced Cell Recognition of Heteromultivalent Nanoparticles using a Biomimetic Approach.* Annual Meeting of the German Pharmaceutical Society, Hamburg, Germany, 2018.

5. Maslanka Figueroa, Sara; <u>Fleischmann, Daniel</u>; Goepferich, Achim; *Virus-mimetic nanoparticles for enhanced target-cell specificity.* Annual Meeting of the German Pharmaceutical Society, Hamburg, Germany, 2018.

6. Maslanka Figueroa, Sara; <u>Fleischmann, Daniel</u>; Goepferich, Achim; *Virus-mimetic multistep-binding nanoparticles for enhanced target-cell specificity.* 6th Galenus Workshop. Würzburg, Germany, 2018.

7. Maslanka Figueroa, Sara; <u>Fleischmann, Daniel</u>; Goepferich, Achim; *Strategies for Enhancing the Target Specificity and Affinity of Nanomaterials.* Biomaterials International, Tokyo, Japan, 2018.

8. Maslanka Figueroa, Sara; Abstiens, Kathrin; <u>Fleischmann, Daniel</u>; Goepferich, Achim; *Angiotensin-I decorated nanoparticles target mesangial cells after enzymatic activation.* 11th World Meeting on Pharmaceutics Biopharmaceutics and Pharmaceutical Technology, Granada, Spain, 2018.

Acknowledgements

First of all, I would like to thank Prof. Achim Göpferich for making it possible to start this PhD project in his working group. During the past four years, he constantly supported our research and most importantly gave me the necessary freedom to also pursue my own ideas. Throughout all our conversations, meetings, and seminars, he always showed great enthusiasm for the project while creating a friendly atmosphere, which I deeply enjoyed and certainly will miss.

Furthermore, I would like to thank Prof. Miriam Breunig for her continuous support and sharing her excellent scientific expertise with me.

I also would like to express my gratitude to Prof. Frank Schweda for his support of our animal studies, which certainly would not have been possible without his guidance. In this context, I also thank Dr. Philipp Tauber for an insightful cooperation, the skillful handling of our *in vivo* experiments and his pleasant demeanor.

Moreover, I thank Prof. Jens Schlossmann and Manuela Harloff for the excellent support during our successful cooperation and their great expertise in all pharmacological aspects of my project. In this regard, I would like to also thank Astrid Seefeld, Michael Majer, Sally Prüschenk and Simon Kerler for their technical advice and the always pleasant atmosphere in their working group.

I also want to express my gratitude to all former and present members of the department as they were not only highly motivated and professional colleagues, but also created a relaxed and enjoyable atmosphere.

A special thanks goes out to the following people:

My project partner Dr. Sara Maslanka Figueroa for saving my experiments more than once with her impressive expertise, work ethic and great collegiality. Much of the content of this manuscript would not have been possible without her, for which I am deeply grateful. I also enjoyed our conference trips and the nights out with our gang! 😊

Heike Lehr for bearing with me as a lab-mate, helping me out in countless situations and being an always enjoyable conversation and conference partner.

Christian Ziegler for 10 years of studies, research, sharing a flat and all the related madness. 😉

Sebastian Beck for countless hilarious conversations, his great help as the master of good scientific practice and the great conference trips.

Moritz Graf for his great expertise in any scientific field and his continuous helpfulness.

Jonas Groner for many funny and insightful conversations on history, politics, and the latest meme trends.

Oliver Zimmer for his enthusiasm for the project and the great help during practical courses.

Renate Liebl, Viktoria Eismann, Silvia Babl, Andrea Blaimer and Stefan Kolb for their excellent technical advice and support during all my experiments and always having a smile on their face.

Margit Schimmel for enduring my hopeless efforts in preparing TEM ultrathin sections and her great expertise in cell imaging.

Uwe de Vries for his dedicated help in fluorescence microscopy.

As this dissertation marks the preliminary completion of my scientific education, I also wanted to thank Franz Rackl for his inspiring introduction into chemistry and biology at a very early stage. Throughout my following studies and this project, I always kept in mind his memorable wisdoms and the love for natural sciences, that he successfully passed on to me and many more of his students.

A big thank you goes out to my family for always supporting me throughout my entire education and the work on this project.

More so, I want to thank my dear friends for all the great memories of the past years and creating a sometimes much-needed refuge from science.

The last and most important thank goes to Anna for being my best friend, lockdown buddy and the most wonderful partner one could imagine.

I hereby declare that I have completed the dissertation presented without the impermissible help of third parties, without the use of resources other than those indicated, and that any data and concepts stemming directly or indirectly from other sources are indicated with citations to the literature.

No further persons were involved with the creation of the contents of the dissertation presented. In particular, I have not made use of the assistance of a doctoral consultant or other person in return for payment. No-one has received payment in kind either directly or indirectly for work which is associated with the content of the dissertation submitted.

The dissertation has not been submitted in the same or similar form to another examining authority, neither in Germany nor abroad.

Regensburg, 29.03.2021

_____

(Daniel Fleischmann)